SYNTHESIZING NEW

$[(SnSe)_{1.15}]_m(TSe_2)_n$, $[(SnSe)_{1.16}]_m(VSe_2)_n[(SnSe)_{1.16}]_p(TaSe_2)_q$,

AND $(SnSe)_{1.16}(V_{.51}Ta_{.49}Se_2)$

INTERGROWTH COMPOUNDS (T = V AND Ta)

by

RYAN ELLIOT ATKINS

A DISSERTATION

Presented to the Department of Chemistry
and the Graduate School of the University of Oregon
in partial fulfillment of the requirements
for the degree of
Doctor of Philosophy

June 2013

DISSERTATION APPROVAL PAGE

Student: Ryan E. Atkins

Title: Synthesizing New $[(SnSe)_{1.15}]_m(TSe_2)_n$, $[(SnSe)_{1.16}]_m(VSe_2)_n[(SnSe)_{1.16}]_p(TaSe_2)_q$, and $(SnSe)_{1.16}(V_{.51}Ta_{.49}Se_2)$ Intergrowth Compounds (T = V and Ta)

This dissertation has been accepted and approved in partial fulfillment of the requirements for the Doctor of Philosophy degree in the Department of Chemistry by:

Dr. Mark C. Lonergan	Chairperson
Dr. David C. Johnson	Advisor
Dr. Kenneth M. Doxsee	Core Member
Dr. Richard Taylor	Institutional Representative

and

Kimberly Andrews Espy	Vice President for Research and Innovation; Dean of the Graduate School

Original approval signatures are on file with the University of Oregon Graduate School.

Degree awarded June 2013

DISSERTATION ABSTRACT

Ryan E. Atkins

Doctor of Philosophy

Department of Chemistry

June 2013

Title: Synthesizing New $[(SnSe)_{1.15}]_m(TSe_2)_n$, $[(SnSe)_{1.16}]_m(VSe_2)_n[(SnSe)_{1.16}]_p(TaSe_2)_q$, and $(SnSe)_{1.16}(V_{.51}Ta_{.49}Se_2)$ Intergrowth Compounds (T = V and Ta)

A modification of the modulated elemental reactants synthetic technique was developed and used to synthesize several new layered compounds. Several TSe_2, $[(SnSe)_{1+y}]_m(TSe_2)_n$, $[(SnSe)_{1+y}]_m(TSe_2)_n[(SnSe)_{1+y}]_p(T'Se_2)_q$, and $(SnSe)_{1+y}(V_{1-x}Ta_xSe_2)$ layered compounds were synthesized by the new modulated elemental reactant (MER) technique with T = V, Ta, and Ti. The MER approach is a low-temperature synthesis that allows the kinetic trapping of metastable compounds, allowing a designed synthesis with control over the value of *m*, *n*, *p*, and *q*. These layered compounds were structurally characterized by X-ray diffraction and transmission electron microscopy studies. Each integer increase of *m*, *n*, *p*, and *q* resulted in a linear increase in thickness, representing the single structural units of SnSe (a Sn/Se atomic bilayer) and TSe_2 (an X-T-X trilayer sandwich). All of the compounds contained preferentially oriented layering, with the layer's (00*l*) plane parallel to the substrate surface. From Bragg-Brentano and in-plane X-ray diffraction studies, the layers are found to be regularly spaced along *c* with abrupt interfaces and contain crystallinity in their *ab*-plane. Many of these layered compounds were found to exhibit turbostratic disorder, a random rotational disorder that is usually present in materials made by the MER technique. The presence of turbostratic disorder

was found to be dependent on the polytypes that exist in the bulk form of the TSe_2 constituent. The electrical properties of the layered compounds were studied by means of temperature-dependent resistivity and Hall measurements. Interesting electrical properties were found as a result of the turbostratic disorder, including a charge density wave transition found in the $[(SnSe)_{1.15}]_m(VSe_2)$ ferecrystal. The onset temperature of the CDW transition was found to be a sensitive function of the layering sequence, increasing with higher *m* values. The CDW transition was attributed to the VSe_2 constituent and was found in all the composite crystals that contained VSe_2. It was found that the $[(SnSe)_{1+y}]_m(VSe_2)_n$ and $[(SnSe)_{1+y}]_m(TaSe_2)_n$ intergrowths could be combined into an ABCB layered $[(SnSe)_{1+y}]_m(VSe_2)_n[(SnSe)_{1+y}]_p(TaSe_2)_q$ intergrowth, with chemical separation of the VSe_2 and $TaSe_2$ constituents.

This dissertation includes previously published and unpublished co-authored material.

CURRICULUM VITAE

NAME OF AUTHOR: Ryan E. Atkins

GRADUATE AND UNDERGRADUATE SCHOOLS ATTENDED:

University of Oregon, Eugene
Central Washington University, Ellensburg

DEGREES AWARDED:

Doctor of Philosophy, Chemistry, 2013, University of Oregon
Bachelor of Science, Biochemistry, 2008, Central Washington University

GRANTS, AWARDS, AND HONORS

IGERT Fellowship, University of Oregon, 2011

PUBLICATIONS:

Grosse, C.; Atkins, R.; Kirmse, H.; Mogilatenko, A.; Neumann, W.; Johnson, D.C. Local structure and defect chemistry of $[(SnSe)_{1.15}]_m(TaSe_2)$ ferecrystals – a new type of layered intergrowth compound. Submitted to *Journal of Alloys and Compounds* **2013**.

Atkins, R.; Moore, D.B.; Johnson, D.C. Insights into the self-assembly of designed amorphous precursors into targeted ferecrystalline compounds. Accepted by *Chemistry of Materials* **2013**.

Atkins, R.; Disch, S.; Jones, Z.; Haeusler, I.; Grosse, C.; Fischer, S.F.; Neumann, W.; Zschack, P.; Johnson, D.C. Synthesis, structure, and electrical properties of new tin vanadium selenide. *Journal of Solid State Chemistry* **2013**, 202, 128-133.

Atkins, R.; Wilson, J.; Zschack, P.; Grosse, C.; Neumann, W.; Johnson, D.C. Synthesis of $[(SnSe)_{1.15}]_m(TaSe_2)_n$ ferecrystals: structurally tunable metallic compounds. *Chemistry of Materials* **2012**, 24, 4594-4599.

Moore, D.B.; Stolt, M.J.; Atkins, R.; Sitts, L.; Jones, Z.; Disch, S.; Beekman, M.; Johnson, D.C. Structural and electrical properties of $(PbSe)_{1.16}TiSe_2$. *Emerging Materials Research* **2012**, 1, 292-298.

Beekman, M.; Heideman, C.; Anderson, M.; Smeller, M.; Atkins, R.; Lin, Q.; Nguyen, N.; Johnson, D.C. Design and realization of nanostructured inorganic intergrowths. Modules, Systems, and Applications in Thermoelectrics, CRC Press **2012**, Boca Raton, 2.1-2.19.

Neumann, W.; Kirmse, H.; Häusler, I.; Grosse, C.; Moeck, P.; Rouvimov, S.; Beekman, M.; Atkins, R.; Johnson, D.C.; Volz, K. Methods of electron crystallography as tools for materials analysis. *Solid State Phenomena* **2012**, 186, 1-6.

Atkins, R.; Anderson, M.; Anderson, I.; Zschack, P.; Johnson, D.C. Synthesis of new ferecrystals $(SnSe)_y(TSe_2)$ where T = V and Ta. IEEE-NANO Proceedings **2011**, 1230-1234.

Rouvimov, S.; Grosse, C.; Beekman, M.; Atkins, R.; Kirmse, H.; Zschack, P.; Johnson, D.C.; Neumann, W. Structural incestigations of ferecrystals $[(SnSe)_{1+\delta}]_m[TSe_2]$ (T = Mo, Ta) by means of transmission electron microscopy. IEEE-NANO Proceedings **2011**, 398-403.

Beekman, M.; Moore, D.B; Atkins, R.; Heideman, C.; Lin, Q.; Hill, K.; Anderson, M.; Johnson, D.C. New compounds consisting of turbostratic intergrowths: ultra-low thermal conductivities and tunable electric properties. MRS Proceedings **2011**, 1329.

Atkins, R.; Diaz, A.L. Investigation of host-to-activator energy transfer and surface losses in $SrY_2O_4:Eu^{3+}$ under VUV Excitation. *Journal of Luminescence* **2008**, 128, 1463-1470.

ACKNOWLEDGMENTS

I would like to acknowledge my Advisor Prof. David C. Johnson for letting me work in his research laboratory, as well as the advice and support he has provided throughout my doctorate work. I would like to thank my thesis committee for the constructive advice they have provided; their comments have always helped to improve my research.

I have collaborated with many graduate students during my work at the University of Oregon that I would like to acknowledge, including Daniel Moore, Dr. Matt Beekman, Dr. Colby Heideman, Dr. Mike Anderson, Dr. Ngoc Nguyen, Richard Westover, Ines Haeusler, Devin Merrill, Matti Alemayehu, Noel Gunning, Corinna Grosse, Dr. Sabrina Disch, Dr. Mary Smeller, and Dr. Qiyin Lin. I have worked with several undergraduates that I would like to acknowledge, including Jason Wilson, Zachery Jones, Patrick Hennaghan, James Kunert, Chun Lee and Nicholas McDowell. I have collaborated with several Professors from institutions other than the University of Oregon that I would like to acknowledge, including Prof. Wolfgang Neumann, Prof. Saskia F. Fischer, and Prof. Michael Hietschold. I would like to thank Dr. Paul Zschack and Dr. Evguenia Karapetrova from the Advanced Photon Source for their assistance in X-ray diffraction analyses at Beamline 33BM. I would like to acknowledge Jeffrey Ditto and Joshua Razink for their work in focused ion beam and transmission electron microscopy at the Center for Advanced Materials Characterization in Oregon (CAMCOR).

I would like to acknowledge funding from the National Science Foundation under Grant DMR 0907049, Grant MRI 0923577, and CCI Grant CHE-1102637. Support from the Oregon's National Science Foundation IGERT Fellowship Program under Grant No.

DGE-0549503. Use of the Advanced Photon Source was supported by the U.S. Department of Energy, Office of Science, Office of Basic Energy Sciences, under Contract No. DE-AC02-06CH11357.

Last, but certainly not least, I would like to thank my wife Stephanie, my family, and my Lord Jesus Christ; without their support I would not have finished my Graduate work.

I dedicate this work to my wife Stephanie, our daughter Chloe, and the developing next member of our family; may we grow together in love.

"And now these three remain: faith, hope, and love. But the greatest of these is love"
1 Corinthians 13:13

TABLE OF CONTENTS

Chapter	Page
I. MISFIT LAYER COMPOUNDS	1
I.1. Introduction	1
I.2. Misfit Layer Compounds	2
I.3. Misfit Ratio	3
I.4. Structural Characteristics	5
I.5. Electronic Structure	9
I.6. Electrical Properties	10
II. FERECRYSTALS	13
II.1. Introduction	13
II.2. Ferecrystals	14
II.3. Structural Characterization	17
II.4. Turbostratic Disorder in $[(MX)_{1+y}]_m(TX_2)_n$ Ferecrystals	25
III. SYNTHESIS	29
III.1. Physical Vapor Deposition	29
III.2. Calibrating a Precursor to $[(MX)_{1+y}]_m(TX_2)_n$	31
III.3. X-ray Diffraction Peak Splitting	39
III.4. Modeling Peak Splitting	45
III.5. Annealing Study	49
III.6. Bridge	52

Chapter Page

IV. SYNTHESIS OF $[(SnSe)_{1.15}]_m(TaSe_2)_n$ FERECRYSTALS: STRUCTURALLY TUNABLE METALLIC COMPOUNDS 54

IV.1. Introduction 54

IV.2. Experimental Details 57

IV.3. Results and Discussion 59

IV.4. Bridge 69

V. SYNTHESIS, STRUCTURE, AND ELECTRICAL PROPERTIES OF A NEW TIN VANADIUM SELENIDE 70

V.1. Introduction 70

V.2. Experimental Details 73

V.3. Results and Discussion 75

V.4. Bridge 89

VI. SYNTHESIS, STRUCTURE, AND ELECTRICAL CHARACTERIZATION OF $[(SnSe)_{1.15}]_m(VSe_2)$, m = 1, 2, 3, and 4 90

VI.1. Introduction 90

VI.2. Experimental Details 93

VI.3. Results and Discussion 96

VII. ABCB LAYERED FERECRYSTALS 113

VII.1. Introduction 113

VII.2. Results and Discussion 116

VII.3. Bridge 129

Chapter Page

VIII. INSIGHTS INTO THE SELF-ASSEMBLY OF FERECRYSTALLINE COMPOUNDS FROM DESIGNED AMORPHOUS PRECURSORS 130

VIII.1. Introduction 130

VIII.2. Experimental Details 135

VIII.3. Results and Discussion 136

IX. CONCLUSION 151

APPENDICES 153

A. LIST OF MISFIT LAYER COMPOUNDS 153

B. LIST OF FERECRYSTALS 162

REFERENCES CITED 165

Chapter I 165

Chapter II 169

Chapter III 171

Chapter IV 172

Chapter V 174

Chapter VI 177

Chapter VII 181

Chapter VIII 182

LIST OF FIGURES

Figure Page

I.1. An in-plane view of the theoretical crystal structure for a $[(MX)_{1+y}]_m(TX_2)_n$ superlattice 4

I.2. The non-equivalent *a*-lattice parameters of MX and TX_2 in the $(MX)_{1+y}(TX_2)$ superlattice can be visualized as the stacking of two different building blocks. 5

I.3. An example for calculating the misfit ratio $1+y$ in $[(MX)_{1+y}]_m(TX_2)_n$. 6

II.1. A theoretical image of an $(MX)_{1+y}(TX_2)$ misfit layer compound (left) and ferecrystal (right). 14

II.2. X-ray reflection (top) and diffraction (bottom) patterns of a $(SnSe)_{1.15}(TaSe_2)$ ferecrystal..... 18

II.3. Two plots of the *c*-lattice parameter vs. *m* or *n* 19

II.4. An in-plane X-ray diffraction pattern from a representative $(SnSe)_{1.15}(TaSe_2)$ ferecrystal. 21

II.5. A STEM-HAADF image of a representative $(SnSe)_{1.15}(TaSe_2)$ sample. 23

II.6. High resolution STEM-HAADF (a,b,d) and TEM (c) images of several $[(MX)_{1+y}]_m(TX_2)_n$ ferecrystals. 26

II.7. Grazing incidence X-ray diffraction by a representative $(SnSe)_{1.15}VSe_2$ specimen. 27

III.1. Schematic for two custom built physical vapor deposition chambers 30

III.2. An ideal self-assembly scenario 32

III.3. Schematic of depositing a precursor to $[(MX)_{1+y}]_1(TX_2)_1$ 33

III.4. Example precursors to five different $[(MX)_{1+y}]_m(TX_2)_n$ compounds 33

III.5. An example of five Sn_xSe samples 35

III.6. A plot of Sn/Se composition (determined by EPMA) vs. Sn shutter open 35

III.7. A example of five $(MX)_x(TX_2)$ samples 36

Figure Page

III.8. A plot of Sn/Ta composition (determined by EPMA) vs. Sn shutter open 37

III.9. θ-2θ locked coupled X-ray diffraction patterns of precursors annealed at 400 °C for 30 min 38

III.10. HRSTEM-HAADF images of two annealed precursors. a) from an ideal precursor to $(SnSe)_{1.15}(TaSe_2)$ and b) a non-ideal precursor 40

III.11. Resulting XRR patterns from Bede Refes using the above layering 41

III.12. Bragg-Brentano XRD patterns from intergrowth structures prepared using the XRR modeling layering sequences 42

III.13. Theoretical scenario of diffracting X-rays on the Bragg condition of the (001) reflection for layer spacing *d* 43

III.14. Theoretical non-ideal scenario of diffracting X-rays on the Bragg condition of the (001) (left) and (002) (right) reflection for layer spacing *d*. 44

III.15. Modeled XRD intensity profile 47

III.16. Modeled XRD intensity profile 48

III.17. Modeled XRD intensity profile 49

III.18. A Bragg-Brentano XRD pattern of an annealed precursor that was designed to form $(PbSe)_{1+y}(TiSe_2)_3$ 50

III.19. Bragg-Brentano XRD patterns from an annealing study on the $(SnSe)_{1+y}(Mo_{1-x}Nb_xSe_2)$ compound 52

IV.1. A schematic of the structure for $[(SnSe)_{1.15}]_1(TaSe_2)_1$ which forms after annealing the precursor 56

IV.2. θ-2θ locked coupled X-ray diffraction patterns of several $[(SnSe)_{1.15}]_m(TaSe_2)_n$ ferecrystals 63

IV.3. Cross-sectional HR-STEM-HAADF image of a $[(SnSe)_{1.15}]_1(TaSe_2)_1$ specimen. 65

IV.4. In-plane electrical resistivity of $[(SnSe)_{1.15}]_m(TaSe_2)_n$ ferecrystals 68

Figure Page

V.1. A schematic of the self-assembly process by which an amorphous modulated Se-V-Se-Sn layer sequence (left) self-assembles into $(SnSe)_{1.15}(VSe_2)$ 77

V.2. X-ray diffraction patterns (θ-2θ locked-coupled scan geometry) of a $(SnSe)_{1.15}(VSe_2)$ precursor annealed at several temperatures 78

V.3. In-plane grazing incidence X-ray diffraction data of a representative $(SnSe)_{1.15}(VSe_2)$ sample 80

V.4. Cross-sectional transmission electron microscope image of a representative area of a $(SnSe)_{1.15}(VSe_2)$ sample 82

V.5. Diffraction data and associated Rietveld refinement of a $(SnSe)_{1.15}(VSe_2)$ 83

V.6. Temperature-dependent resistivity and carrier concentration for two different $(SnSe)_{1.15}(VSe_2)$ samples 87

VI.1. Bragg-Brentano X-ray diffraction patterns of (left) $[(SnSe)_{1.15}]_3(VSe_2)$ and (right) $[(SnSe)_{1.15}]_2(VSe_2)$ ferecrystals 98

VI.2. Bragg-Brentano X-ray diffraction patterns of $[(SnSe)_{1.15}]_1(VSe_2)$ ferecrystal ... 99

VI.3. In-plane X-ray diffraction patterns of $[(SnSe)_{1.15}]_m(VSe_2)$ ferecrystals 101

VI.4. 2D X-ray diffraction pattern of representative $[(SnSe)_{1.15}]_m(VSe_2)$ ferecrystals. Families of reflections 103

VI.5. A cross-sectional HR-TEM image of a $[(SnSe)_{1.15}]_3(VSe_2)$ ferecrystal 104

VI.6. A cross-section STEM-HAADF image of a $[(SnSe)_{1.15}]_3(VSe_2)$ ferecrystal 105

VI.7. A visual representation of the atomic spacing for each $[(SnSe)_{1.15}]_m(VSe_2)$ ferecrystal 107

VI.8. Temperature-dependent electrical resistivity for $[(SnSe)_{1.15}]_m(VSe_2)$ ferecrystals. The transition temperatures 109

VI.9. Temperature-dependent Hall coefficient and carrier concentration (assuming a single band model and a single carrier type) for the $[(SnSe)_{1.15}]_m(VSe_2)$ 110

Figure Page

VII.1. A theoretical image of a (left) alloyed $[(MX)_{1+y}]_1(T_{.5}T'_{.5}X_2)_1$ and (right) ABCB layered $[(MX)_{1+y}]_1(TX_2)_1[(MX)_{1+y}]_1(T'X_2)_1$ ferecrystal 115

VII.2. X-ray diffraction patterns, Bragg-Brentano scan geometry, of an ABCB layered precursor annealed at several different temperatures 117

VII.3. X-ray diffraction patterns, Bragg-Brentano scan geometry, of two ABCB layered ferecrystals. 118

VII.4. X-ray diffraction patterns from in-plane scan geometries for several ferecrystals. The (*hk*0) reflections 121

VII.5. 2D X-ray diffraction pattern of an ABCB layered ferecrystal 122

VII.6. *c*-lattice parameters of several $[(SnSe)_{1.16}]_m(VSe_2)_n[(SnSe)_{1.16}]_p(TaSe_2)_q$ ferecrystals plotted as a function of *m* 124

VII.7. A STEM-HAADF image of a $[(SnSe)_{1.16}]_4(VSe_2)_4[(SnSe)_{1.16}]_4(TaSe_2)_4$ ferecrystal. Due to the *z*-contrast 125

VII.8. Temperature-dependent electrical resistivity from a $(SnSe)_{1.16}(V_{.51}Ta_{.49}Se_2)$ and $[(SnSe)_{1.16}]_1(VSe_2)_1[(SnSe)_{1.16}]_1(TaSe_2)_1$ ferecrystal. 126

VII.9. Temperature-dependent absolute Hall coefficient data. 127

VIII.1. High resolution STEM *z*-contrast image of $[(PbSe)_{1.00}]_3(MoSe_2)_1$ 131

VIII.2. X-ray diffraction patterns (θ-2θ locked coupled scan geometry) collected as a function of temperature for a representative precursor containing modulated V-Se bilayers 139

VIII.3. Diffraction intensity of the (001) reflection for VSe_2 and $TaSe_2$ films as a function of the deposition time 141

VIII.4. X-ray diffraction patterns (θ-2θ locked coupled scan geometry) obtained for $TaSe_2$, $TiSe_2$, and VSe_2 samples 142

VIII.5. In-plane grazing incidence diffraction pattern obtained for a representative VSe_2 sample 144

Figure Page

VIII.6. Cross-sectional transmission electron microscope image of VSe_2 (top) and $TaSe_2$ (bottom) 146

VIII.7. Grazing incidence X-ray diffraction by representative $TaSe_2$, $TiSe_2$, and VSe_2 specimens 147

LIST OF TABLES

Table Page

III.1. *c*-lattice parameters from an annealing study on the $(SnSe)_{1+y}(Mo_{1-x}Nb_xSe_2)$ compound 53

III.2. Full width half maximum (FWHM) determined by the (00*l*) reflections 53

IV.1. In-plane *a*-lattice parameters of the SnSe (square) and $TaSe_2$ (hexagonal) constituents and *c*-lattice parameters for several $[(SnSe)_{1.15}]_m(TaSe_2)_n$ 62

IV.2. Summary of resistivity ratios for $[(SnSe)_{1.15}]_m(TaSe_2)_n$ ferecrystals 68

V.1. The repeat thicknesses of as-deposited precursors, *c*-lattice parameters of annealed samples 79

V.2. Results from Rietveld and LeBail refinements on $(SnSe)_{1.15}(VSe_2)$ 84

VI.1. Atomic spacing along the *c*-axis using fractional coordinates from the Rietveld refinement 106

VII.1. A compilation of *c*-lattice parameters 119

VIII.1. Summary of composition, unit cell size perpendicular to the substrate, and line width collected as a function of annealing temperature 140

CHAPTER I

MISFIT LAYER COMPOUNDS

I.1. Introduction

The generic formula $[(MX)_{1+y}]_m(TX_2)_n$ refers to a very large collection of layered compounds. Since the 1970's, ninety three $[(MX)_{1+y}]_m(TX_2)_n$ crystalline compounds have been synthesized.[1-29] In 2008, the Johnson research group began synthesizing ferecrystal versions of $[(MX)_{1+y}]_m(TX_2)_n$ intergrowths through non-traditional techniques.[30-42] In this work, crystalline $[(MX)_{1+y}]_m(TX_2)_n$ intergrowths are referred to as misfit layer compounds (Chapter I) and all non-crystalline, non-amorphous $[(MX)_{1+y}]_m(TX_2)_n$ intergrowths as ferecrystals (Chapter II). The main structural difference between the two categories is turbostratic disorder. Turbostratic disorder is a rotational disorder between the MX and TX_2 layers that disrupts the coherence of translational symmetry in the supercell; so that the intergrowth cannot be defined by a continuous crystal lattice and is therefore not a crystal. The synthetic technique used to create the $[(MX)_{1+y}]_m(TX_2)_n$ intergrowth can promote the presence of turbostratic disorder. The typical synthetic technique for misfit layer compounds is high-temperature synthesis, leading to thermodynamic, crystalline products; discussed in this chapter. Later, Johnson et al used a low-temperature physical vapor deposition synthetic technique, known as the modulated elemental reactants technique, to create misfit layer compounds with turbostratic disorder, otherwise known as ferecrystals (Chapter III). In this work, the MER technique was used to create $[(SnSe)_{1.15}]_m(TaSe_2)_n$, $[(SnSe)_{1.15}]_m(VSe_2)$, $(SnSe)_{1+y}(V_{1-x}Ta_xSe_2)$, and $[(SnSe)_{1.15}]_m(VSe_2)_n[(SnSe)_{1.15}]_p(TaSe_2)_q$ ferecrystals; their

structural and electrical characterization is reported in Chapters IV, V, VI, and VII. Chapter IV is previously published work on the $[(SnSe)_{1.15}]_m(TaSe_2)_n$ ferecrystals with co-authors Jason Wilson, Paul Zschack, Corinna Grosse, Wolfgang Neumann, and David C. Johnson. Chapter V is previously published work on the $(SnSe)_{1.15}(VSe_2)$ ferecrystal with co-authors Sabrina Disch, Zachary Jones, Paul Zschack, and David C. Johnson. Chapter VI is unpublished work on the $[(SnSe)_{1.15}]_m(VSe_2)$ ferecrystals with co-authors Michelle Dolgos, Andreas Fiedler, Corinna Grosse, Saskia F. Fischer, and David C. Johnson. To further understand why the MER synthetic technique encourages turbostratic disorder, an investigation into the self-assembly growth mechanism was done using ferecrystalline and crystalline TSe_2 layered compounds (Chapter VIII). Chapter VIII is previously published material with co-authors Daniel B. Moore and David C. Johnson.

I.2. Misfit Layer Compounds

In this work, the term misfit layer compounds (MLCs) refers to $[(MX)_{1+y}]_m(TX_2)_n$ intergrowth structures that are fully crystalline; they contain translational symmetry in three dimensions. Chapter II will discuss ferecrystals, which lack a symmetrical modulation of their interleaved layers; i.e. lacking crystallinity along (*hkl*). In its entirety, the term misfit layer compounds can refer to several types of layered structures but the scope of this work is focused on the $[(MX)_{1+y}]_m(TX_2)_n$ compounds. An extensive review on the misfit layer compounds was done by Wiegers.[2] The largest subset of MLCs is $(MX)_{1+y}(TX_2)$, or $m = n = 1$, and has been synthesized with a very large variety of elements; M = Sn, Pb, Sb, Bi, and rare earth metals; T = Ti, V, Cr, Nb, and Ta; and X = S and Se.[1-29] Since the creation of $LaCrS_3$ in 1971 (determined to be the misfit layer

compound $(LaS)_{1.20}(CrS_2)$ in 1985),[26] one hundred and two $[(MX)_{1+y}]_m(TX_2)_n$ MLCs have been reported over the last forty years, compiled in Appendix A. Most of these compounds are sulfides with both *m* and *n* equal to 1; though there are twenty eight with *m*:*n* = 1:2, two with m:n = 1:3, five with *m*:*n* = 1.5:1, two with *m*:*n* = 2:1, and nineteen of these have been made with selenium instead of sulfur. The basic intergrowth structure is shown in Figure I.1, the MLC superlattice consists of interleaved MX and TX_2 layers. The individual MX and TX_2 layers are crystalline with independent crystal lattices and a continuous, symmetrical modulation of the layers throughout the superlattice exists; defining these compounds as crystalline. A single MX unit represents a bilayer, two atomic planes of (100) distorted NaCl type structure, essentially two atomic layers of a (100) oriented face centered cubic unit cell. A single TX_2 unit consists of three atomic planes, a X-T-X trilayer sandwich, with hexagonal oriented T atoms. Depending on the element, the T-atoms will have trigonal prismatic (Ta, Nb) or octahedral (Ti, V, and Cr) coordination. The bulk form of TX_2 is a layered structure, X-T-X sandwiches separated by van der Waals gaps; the $[(MX)_{1+y}]_m(TX_2)_n$ intergrowth both structurally and electronically can be described as an intercalation of MX units into the van der Waals gap of the TX_2 structure.

I.3. Misfit Ratio

The term "misfit" was given to these compounds for in the intergrowth structure there is a non 1:1 ratio of M:T. Originally this non-integer stoichiometry was unknown and these compounds were identified as ternary compounds or MTX_3; however, later structural and compositional studies revealed the non-integer ratio between the MX and

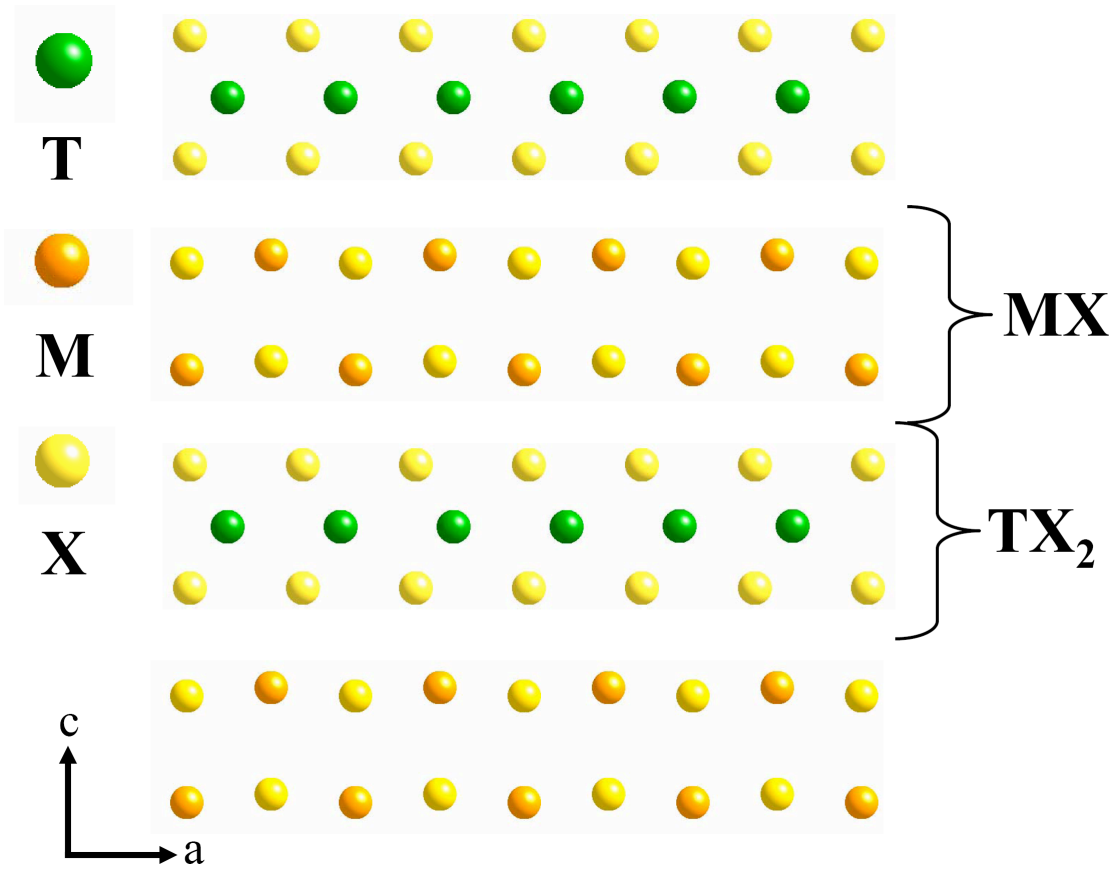

Figure I.1. An in-plane view of the theoretical crystal structure for a $[(MX)_{1+y}]_m(TX_2)_n$ superlattice, where $m = n = 1$. The single MX and TX_2 structural units are indicated and represent sheets that continue along the *ab*-axis. Two units of the $(MX)_{1+y}(TX_2)$ layering sequence are shown, this sequence is continuous along the *c*-axis.

TX_2 constituents. The non 1:1 ratio of M:T is a result of the two constituents having incommensurate *a*-lattice parameters; their *c*- and *b*-lattice parameters are usually equivalent. The simplest representation of this is the stacking of two different building blocks, shown in Figure I.2. The resulting misfit between the two constituents is represented as the *y* value; within $[(MX)_{1+y}]_m(TX_2)_n$ MLCs, *y* ranges between 0.07 and 0.28.[1-29] Some reports of MLCs still represent the compound as MTX_3; possibly this is because the structural characterization required to determine *y* wasn't obtained. An

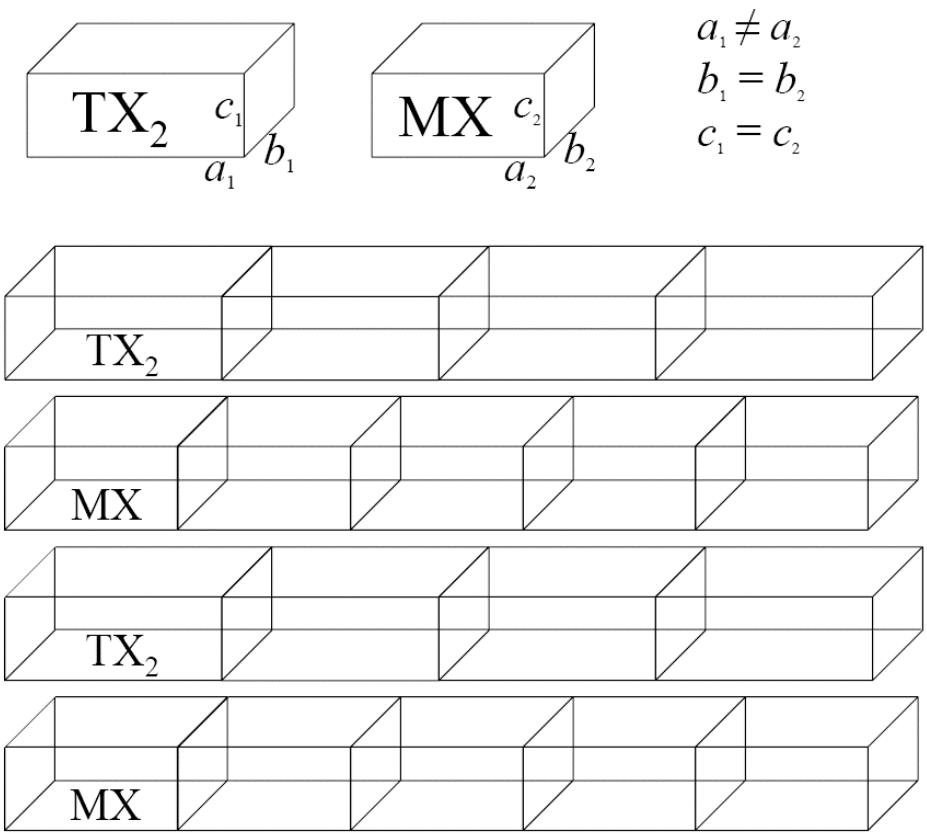

Figure I.2. The non-equivalent *a*-lattice parameters of MX and TX_2 in the $(MX)_{1+y}(TX_2)$ superlattice can be visualized as the stacking of two different building blocks. The building blocks form continuous layering but the non-equivalency of a_1 and a_2 results in a non-integer ratio of MX to TX_2 blocks along the *a*-axis.

example of calculating the misfit parameter is shown in Figure I.3. The misfit parameter doesn't significantly change when going between the sulfide and selenide analogues; making predictions of the value of the misfit parameter based on sulfides useful when synthesizing the selenides.

I.4. Structural Characteristics

The misfit layer compounds are very unique in their ability to incorporate many different elements into the same base structure. However, MLCs are limited in their

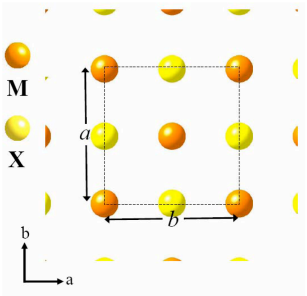

Four M atoms per square or rectangle
Two from each the top and bottom atomic layer

area of a square

$$area = a \times b$$

M atoms per area

$$atoms / area = 4/(a \times b)$$

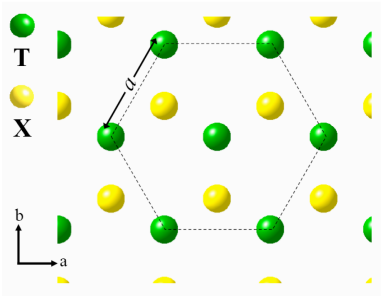

Three T atoms per Hexagon

area of a hexagon

$$area = \frac{3\sqrt{3}}{2} a^2$$

T atoms per area

$$atoms / area = 3/(\frac{3\sqrt{3}}{2} a^2)$$

M atoms per T atoms

$$misfit = (atoms / area)_{MX} /(atoms / area)_{TX_2} = (4/(a_{MX} \times b_{MX}))/(3/(\frac{3\sqrt{3}}{2} a_{TX_2}^2))$$

Figure I.3. An example for calculating the misfit ratio $1+y$ in $[(MX)_{1+y}]_m(TX_2)_n$. The atomic models are a cross-plane or top-down view of the individual MX and TX_2 structures.

layering sequence; that is, there are limitations to the different values of *m* and *n* that can be stabilized in $[(MX)_{1+y}]_m(TX_2)_n$. Though there are examples of MLCs with $m = 1.5$ or 2 and $n = 2$ or 3, the majority of them are restricted to *m* and *n* equal to 1. The reason for this is the high-temperature synthetic technique used in creating MLCs. Typically, MX and TX_2 binary reactants are combined in an evacuated ampoule and heated to minimal temperatures of 700° C or more for days to weeks,[2] combining the reactants into the intergrowth compound by solid diffusion. The result of a high-temperature synthesis is a thermodynamic product, suggesting that the $[(MX)_{1+y}]_1(TX_2)_1$ compound is usually the most thermodynamically stable layer sequence, since it is most common. With a few

MLCs, $(SbS)_{1+y}(NbS_2)_2$ and $[(EuS)_{1.15}]_{1.5}(NbS_2)$ for example,[12,9] the 1:1 compound is not the most stable, based on the lack of a reported 1:1 compound. Also, one MLC was successfully made as a series; $(PbSe)_{1.14}(NbSe_2)_n$ was made with n = 1, 2, and 3, unfortunately this is the only example of its kind with MLCs.[15] Even so, it showed that variations in layer sequence are possible and provide a potential path for tuning physical properties. In chapter II, ferecrystalline $[(MX)_{1+y}]_m(TX_2)_n$ compounds are synthesized with much greater control over the value of m or n through the use of a low-temperature synthetic technique, obtaining metastable compounds.

In a solid compound, containing only one phase, there is a single crystal lattice that yields X-ray diffraction data corresponding to a single space group. In a composite crystal, like MLCs, there is still just one phase, the intergrowth superlattice, but the two constituents maintain their independent, incommensurate crystal lattices. This results in a diffraction pattern that resembles two phases and can be indexed to the separate MX and TX_2 constituents. At first, this made it very difficult to accurately refine the superlattice of MLCs because there was no matching ternary phase. As a result, the structure reported for most MLCs is that for two separate lattices. The MX and TX_2 constituents are refined separately, determining space groups and lattice parameters for each; reported in appendix A.[1-29] Although this does accurately describe the structural relationships of the individual MX and TX_2 constituents, it does not shed light on the structural characteristics of the $[(MX)_{1+y}]_m(TX_2)_n$ superlattice. Typically, within the $[(MX)_{1+y}]_m(TX_2)_n$ superlattice the MX and TX_2 constituents conform to one another ($b_{MX} = b_{TX2}$, $c_{mx} = c_{TX2;}$ $a_{MX} \neq a_{TX2}$), resulting in a consistent interlayer modulation and thereby three dimension translational symmetry of the superlattice. It is possible to characterize

the superlattice symmetry through diffraction studies, along with the reflections arising from the MX and TX_2 constituents a set of reflections are identifiable as belonging to the superlattice. The only way to accurately refine the superlattice reflections is through the use of a superspace group, which defines the symmetry of the two constituents and their interlayer modulations.[43-45]

The generic crystal structure for the misfit layer compounds is referred to as the combination of a distorted rock-salt like MX constituent and a hexagonal TX_2 transition metal dichalcogenide constituent. For the MX constituent, the term "rock-salt like" is used because when viewing a cross-section of the superlattice each atomic plane of the MX atomic bilayer conforms to the periodicity of two face centered cubic (001) oriented atomic planes, Figure I.1; in a single atomic row the periodicity of M and X atoms is every other and between rows is staggered just as it is in the rock-salt structure. For the TX_2 constituent, the arrangement of atoms in the transition metal dichalcogenide lattice is very similar to the TX_2 structure in the MLC superlattice form. The MX constituent is distorted from the rock-salt like structure both by its non-equivalent lattice parameters and by what is commonly referred to as a "puckering" distortion. If the MX structure were cubic rock-salt, we would expect $a = b = c$; the non-equivalent lattice parameters, $a \neq b$, are clearly recorded in appendix A along with corresponding space groups. The puckering distortion is where the cation and anion of a MX atomic plane distort along the *c*-axis, the metal cation will move towards the X plane of the neighboring X-T-X trilayer while the anion will move away; clearly visible in Figure I.1. Another interesting structural feature of the $[(MX)_{1+y}]_m(TX_2)_n$ superlattice is the so called van der Waals gap between layers that is typically reported as having little to no interlayer bonding.

I.5. Electronic Structure

The natural occurrence and synthetic abundance of misfit layer compounds containing many different elements implies that the $[(MX)_{1+y}]_m(TX_2)_n$ superlattice structure is a very stable arrangement of the two constituents. This is even more evident when considering that the thermodynamic product of combining the binary components, MX and TX_2, is the $(MX)_{1+y}(TX_2)$ superlattice. Such a stable superlattice may be expected to contain a strong bonding environment; although there is strong intralayer covalent bonding in both the MX and TX_2 constituents, interlayer bonding, or interactions between the MX and TX_2 layers, is reportedly much weaker for M = Sn, Pb, Sb, and Bi.[2] MLCs whose M element is a rare earth have comparable intralayer and interlayer bond distances; as a result they more readily form stronger, covalent interlayer bonding.[2] To further investigate the potential stabilizing interactions between the MX and TX_2 layers the electronic structure of MLCs has been investigated by several spectroscopic techniques, including X-ray photoemission spectroscopy (XPS), angle resolved photoelectron spectroscopy (ARPES), optical spectroscopy, and Raman.[2,9,46-54] In these studies the spectra from MLCs is compared to that of several bulk compounds with similar valence and bonding environments of the M or T atoms (such as bulk MX, TX_2, M_2X_3, MX_2, and others); thereby indirectly studying the electronic structure of MLCs. Many similarities between bulk solids and MLCs are found in these comparisons as would be expected given that the MX and TX_2 constituents maintain independent crystal structures within the MLC. The remaining subtle differences found in the spectra comparisons are attributed to interlayer interactions. Most reports now attribute these interactions as charge transfer between the MX and TX_2 constituents. According to a

rigid band model, carriers are donated from the M s and X p orbitals of the MX constituent into the T d orbitals of the TX_2 with the relative amount of charge transferred dependent on the particular M and T elements present in the MLC. Although, a couple reports do disagree with charge transfer, their findings support the presence of stronger covalent or macroionic interlayer bonding in the MLCs,[48,54] the majority of and most recent publications support charge transfer. Most studies have investigated the $[(MX)_{1+y}]_m(TX_2)_n$ layering scheme of $m = n = 1$, but one study on $(PbS)_{1.18}(TiS_2)_n$ was done with $n = 1$ and 2.[47] Finding that features in the XPS spectra attributed to interlayer charge transfer were reduced when going from $n = 1$ to 2, corresponding to a smaller transfer of carriers per Ti atom. These results are understandable when considering each TiS_2 layer has two neighboring PbS layers donating charge in the $n = 1$ MLC but only one neighboring PbS layer in the $n = 2$ MLC. If MLCs could be made with variable m and n values, then further assumptions regarding charge transfer could be tested.

I.6. Electrical Properties

The misfit layer compounds incorporate a large variety of elements into the common $[(MX)_{1+y}]_m(TX_2)_n$ structure, providing an opportunity to combine the many different physical properties found in the bulk MX and TX_2 compounds. It has already been discussed that within the $[(MX)_{1+y}]_m(TX_2)_n$ intergrowth the two constituents maintain a physical structure similar to that of their bulk form and therefore similar density of states. Assuming a rigid band model, the suggested charge donation between the MX and TX_2 constituents can be estimated or used to explain resulting physical properties of the $[(MX)_{1+y}]_m(TX_2)_n$ MLCs.[2] Ideally, for specific applications one could

then intelligently select $[(MX)_{1+y}]_m(TX_2)_n$ compounds based on combination of the parent constituents. There are MLCs where this idea works and often analyzing possible interlayer charge donation explains results in transport properties. As an example, $[(MX)_{1+y}]_m(TX_2)_n$ compounds that contain TaX_2, TiX_2 and NbX_2 as their TX_2 constituent have metallic transport properties, although bulk TaX_2 and NbX_2 are metallic, TiS_2 is a semiconductor and $TiSe_2$ is a semimetal. To achieve conduction in the $(SnS)_{1.20}(TiS_2)$ superlattice, carriers from the filled 3p orbital of SnS are donated into the vacant 3d band of TiS_2; this allows for conduction through a partially filled 3d band, in agreement with the aforementioned ARPES studies.[2,47] Many of the MX constituents are semiconductors, therefore the transport properties are often attributed to the conduction in the d-band of the TX_2 constituent. However, charge donation from the MX constituent to the TX_2 does play an important role in the outcome of transport properties, such as for the conductive $(MX)_{1+y}(TiX_2)$ MLCs, and makes the MX constituent a potential tool for adjusting transport properties. Other physical phenomena also exist in both the TX_2 and $[(MX)_{1+y}]_m(TX_2)_n$ form that are attributed to the pseudo two-dimensionality of TX_2 in both forms. In the transition metal dichalcogenides, superconductivity and charge density wave transitions exist and are dependent on intercalation of different molecules into the van der Waals gaps between the TX_2 layers. Since $[(MX)_{1+y}]_m(TX_2)_n$ is essentially a symmetrical intercalation of MX into the TX_2 structure,[55] one might expect similar results. Superconductivity has been found in several $[(MX)_{1+y}]_m(TX_2)_n$ MLCs whose TX_2 constituent is TaS_2, $NbSe_2$, $TiSe_2$ or NbS_2.[1,2,4,5,12,15,24,29] However, charge density waves have not been seen in MLCs; it is suggested that slight structural distortions of the TX_2 structure in $[(MX)_{1+y}]_m(TX_2)_n$ eliminates the conditions found in the bulk TX_2 compound

that allow for a CDW transition.[2] Attempts at tailoring physical properties in MLCs may be improved if a more versatile layering sequence for $[(MX)_{1+y}]_m(TX_2)_n$ compounds could be achieved.

CHAPTER II

FERECRYSTALS

II.1. Introduction

Ferecrystalline $[(MX)_{1+y}]_m(TX_2)_n$ compounds, usually referred to as ferecrystals, share many structural characteristics with crystalline misfit layer compounds (MLCs), including compositionally abrupt interfaces, in-plane crystallinity, structural misfit, and separate crystal lattices for the individual MX and TX_2 constituents. The key difference is that ferecrystals contain interlayer rotational disorder called turbostratic disorder, shown in Figure II.1. With MLCs, the MX and TX_2 constituents conform to one another by straining their crystal lattices; this produces a specific and consistent interlayer modulation that results in translational symmetry in three dimensions of the $[(MX)_{1+y}]_m(TX_2)_n$ superlattice.[1] With ferecrystals, a random rotational disorder occurs at MX-TX_2 interfaces and, depending on T, at the TX_2-TX_2 interfaces as well, where the *ab*-planes of the two layers are rotationally disordered relative to one another; the disorder doesn't appear at MX-MX interfaces.[2] This disorder is known as turbostratic disorder and it eliminates the interlayer modulations that are usually found in MLCs. Without interlayer modulations the superlattice does not contain translational symmetry in three dimensions and thereby is not a crystal. However, the intergrowth does contain a great deal of crystalline features and we cannot define it as amorphous. To define this new type of pseudo-superlattice (compositionally abrupt interfaces, in-plane crystallinity, structural misfit, and turbostratic disorder) the term ferecrystals, from the Latin "*fere*" meaning almost, is used to describe these ordered but not fully crystalline materials. This

chapter describes the discovery of turbostratically disordered $[(MX)_{1+y}]_m(TX_2)_n$ compounds and the characterization that has been used in confirming ferecrystallinity.

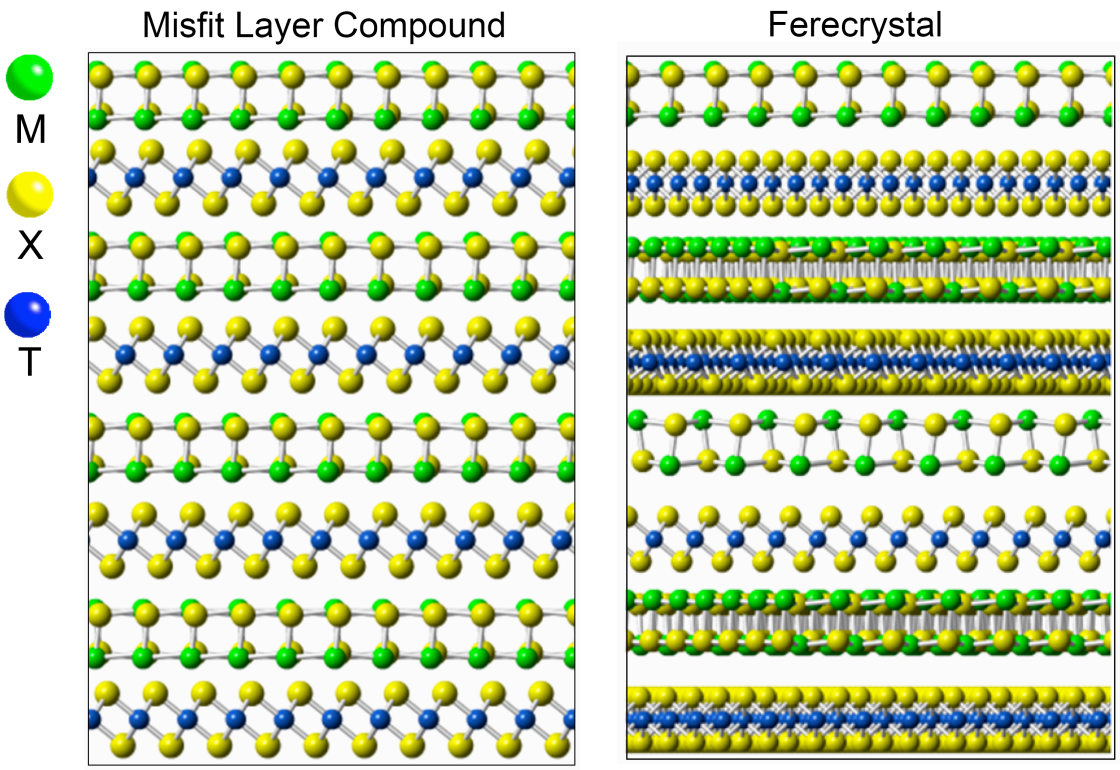

Figure II.1. A theoretical image of an $(MX)_{1+y}(TX_2)$ misfit layer compound (left) and ferecrystal (right). In the ferecrystal, the crystallographic alignment of each MX and TX_2 layers is inconsistent due to random rotational disorder at MX – TX_2 interfaces, whereas in the MLC there is consistent interlayer modulation throughout the superlattice.

II.2. Ferecrystals

The first literature observation of turbostratic disorder in a $[(MX)_{1+y}]_m(TX_2)_n$ intergrowth compound was the $[(VSe_2)_{1.06}]_m(TaSe_2)_n$ compounds created by Ngoc Nguyen in 2007.[3] Although these compounds contain two different TX_2 constituents instead of the usual MX and TX_2, the synthetic technique and structural characteristics are equivalent to those with the layering of $[(MX)_{1+y}]_m(TX_2)_n$ compounds. In the report on

$[(VSe_2)_{1.06}]_m(TaSe_2)_n$, a disorder amongst the layers was identified; observing the area diffraction of $[(VSe_2)_{1.06}]_m(TaSe_2)_n$ it was noticed that the intensity of certain (*hkl*) reflections was smeared along *l* ($hk \neq 0$, $l \neq 0$), producing a large amount of diffuse scattering. However, the material yielded relatively sharp (00*l*) and (*hk*0) reflections, reflecting the regular and abrupt interfaces of the layering and the in-plane crystallinity of the two constituents, respectively. In X-ray diffraction, very small coherence lengths cause diffuse scattering, because the full width half maximum of a reflection peak broadens as particle size diminishes. It was concluded that the diffuse scattering occurred because the TX_2 layers had no continuous interlayer modulation; they were regularly and abruptly spaced with individual crystallinity within each layer but they did not structurally conform to one another. Without a consistent interlayer modulation, any (*hkl*) reflection that required a coherence length longer than *m* or *n* TX_2 layers would have diffuse scattering; this corresponded to the (*hkl*) reflections with ($hk \neq 0$, $l \neq 0$). Diffuse scattering occurs along the axis of limited coherence length, therefore the disorder is about the *c*-axis. The disorder was comparable to turbostratic disorder frequently seen in layered clay minerals[4] but the term turbostratic disorder wasn't mentioned with the report on $[(VSe_2)_{1.06}]_m(TaSe_2)_n$. Following this report, many turbostratically disordered $[(MX)_{1+y}]_m(TX_2)_n$ compounds were created by the Dave Johnson lab; these compounds were made with more variable stacking sequences and found to contain extremely low thermal conductivities in comparison to their crystalline counterparts.[5-16] For quite some time, the term ferecrystals was not used and these compounds were referred to as misfit layer compounds with turbostratic disorder. It was not until 2012, when the full extent of

these materials was realized, that $[(MX)_{1+y}]_m(TX_2)_n$ compounds containing turbostratic disorder were renamed as ferecrystals.[2]

Many $[(MX)_{1+y}]_m(TX_2)_n$ ferecrystals have been made by the Dave Johnson Lab; with M = Pb, Bi, Ce, and Sn; T = W, Mo, Nb, Ta, and Ti; and X = Se and Te; where the misfit parameter *y* varies between -0.1 and 0.18.[5-16] All of these compounds are formed using physical vapor deposition (PVD) and the modulated elemental reactant (MER) synthetic approach, more details on the synthesis are provided in chapter III. The MER technique uses amorphous precursors with sub-nanometer layers, deposited in a layering sequence that mimics a desired $[(MX)_{1+y}]_m(TX_2)_n$ product. These precursors so closely mimic the product that very little solid diffusion is required to crystallize the as-deposited sample, and at low annealing temperatures (300-500 ºC) the amorphous modulated layers of the precursor self-assemble into the ferecrystal. The MER technique does not produce a thermodynamic product, like high-temperature synthesis does, but instead kinetically stabilized structures corresponding to local free-energy minima. Based on what materials have been successfully made, $[(MX)_{1+y}]_m(TX_2)_n$ structures that correspond to a local free-energy minima are those with integer values of *m* and *n*; although there are cases of half integer values for *m*.[9,10] With the MER synthetic technique, 155 different $[(MX)_{1+y}]_m(TX_2)_n$ ferecrystals have been synthesized with no apparent layer sequence limitations (Appendix B). The ability to control the layering sequence, the values of *m* and *n*, is a direct result of the MER synthetic technique; by kinetically trapping meta-stable compounds, $[(MX)_{1+y}]_m(TX_2)_n$ ferecrystals have been produced with *m* and *n* independently equal to integer values as high as 21.[2]

II.3. Structural Characterization

X-ray reflection and diffraction (XRR and XRD) are non-invasive and cost-effective analysis techniques for studying solids, and are readily applied for many different structural investigations of ferecrystals. All the $[(MX)_{1+y}]_m(TX_2)_n$ ferecrystals were synthesized by PVD, and as a result they are all thin-films (typically around 50 nm thick). Often the thin-film nature and preferred orientation of the samples leads to difficulties in analysis when trying to apply classical powder diffraction techniques. Using X-ray diffraction, several structural characteristics of the $[(MX)_{1+y}]_m(TX_2)_n$ layering can be identified; such as the atomic separation of the layers along the *c*-axis, in-plane lattice parameters, and the presence of turbostratic disorder. A representative XRR and XRD scan of a $(SnSe)_{1.15}(TaSe_2)$ ferecrystal is shown in Figure II.2; the X-ray diffraction scan was gathered by Bragg-Brentano geometry after aligning the sample so that the incident angle is normal to the substrate surface. Viewing the XRR scan, the many small maxima between approximately 1 and 10 º2θ are referred to as Kiessig fringes. They arise from constructive interference of X-rays reflecting off the atmosphere-film and film-substrate interfaces and can be used to calculate the total thickness of the film. The XRR scan also contains lower angle (00*l*) reflections from the intergrowth and only the (001) reflection from the $(SnSe)_{1.15}(TaSe_2)$ layering is present. Viewing the XRD scan in Figure II.2, all the maxima can be indexed as (00*l*) reflections from the $(SnSe)_{1.15}(TaSe_2)$ layering, suggesting that the $(SnSe)_{1.15}(TaSe_2)$ intergrowth is textured with its (001) planes parallel to the substrate; i.e. the SnSe and $TaSe_2$ layers are all parallel to the substrate. This is an expected result, because the amorphous layers put down in the PVD process are parallel to the substrate and the nano-architecture of those

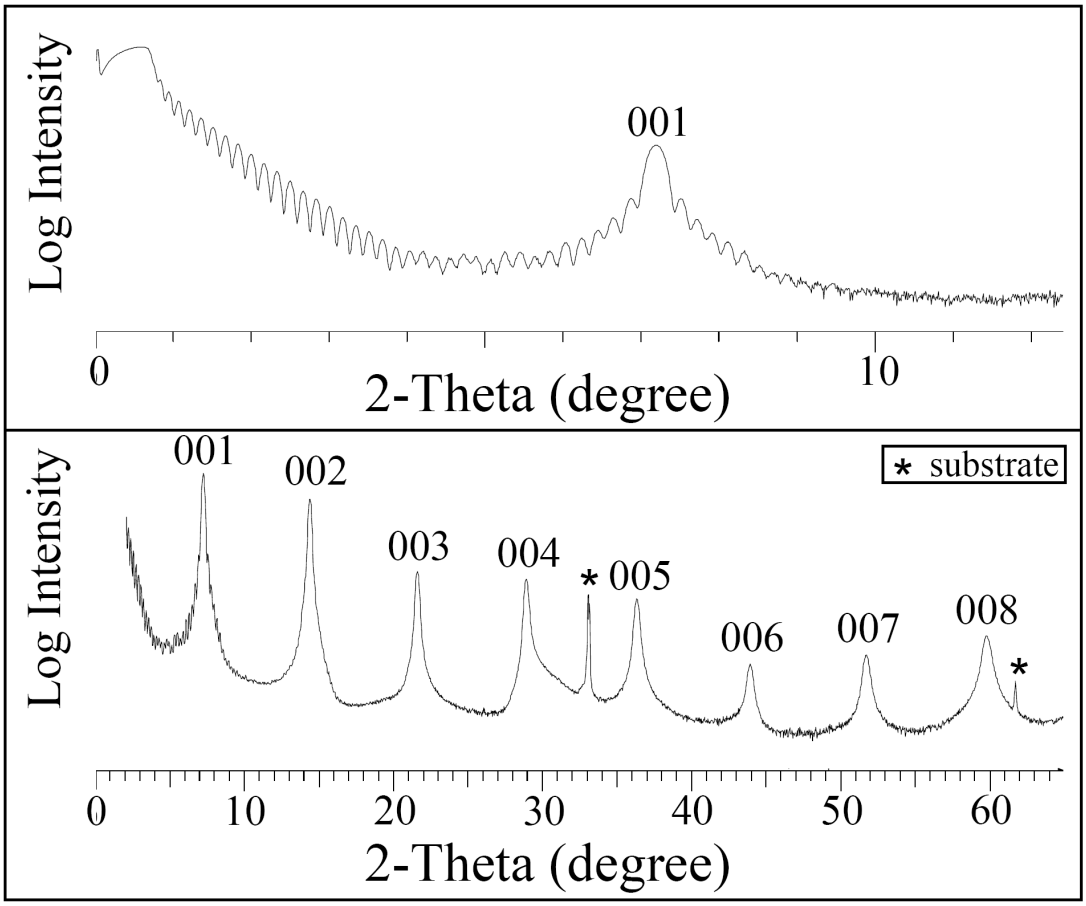

Figure II.2. X-ray reflection (top) and diffraction (bottom) patterns of a $(SnSe)_{1.15}(TaSe_2)$ ferecrystal, Bragg-Brentano scan geometry. The (00*l*) reflections are indexed, the substrate is silicon.

layers is maintained through the self-assembly process. After indexing the (00*l*) reflections, the *c*-lattice parameter for the ferecrystal is determined from the positions of these reflections. Further information regarding the fractional coordinates of atomic planes along the *c*-axis can be attained from the Bragg-Brentano geometry scans by means of Rietveld refinement.[3,5,7,11,13,14,16] No information regarding atomic positions along the *a*- or *b*-axis is attainable from this data due to the lack of (*hkl*) reflections ($hk \neq 0$). To determine the thickness of a single MX or TX_2 unit, a series of $[(MX)_{1+y}]_m(TX_2)_n$ must be made where either *m* or *n* is constant, shown in Figure II.3. Plotting the *c*-lattice

parameter versus *m* or *n* for one of these series results in a linear trend with a slope equal to either the thickness of a single MX unit (if *x*-axis equals *m*) or TX_2 unit (if *x*-axis equals *n*). Typically the thickness per MX or TX_2 unit stays constant for all *m* and *n* values, reflecting the local free-energy minima of a single MX bilayer or TX_2 monolayer. If there are any size dependent structural features in either constituent, such as interfacial straining of lattice parameters, then it may be expected that plotting thickness vs. *m* or *n* would result in a non-linear slope as the lattice relaxes further from the interface.

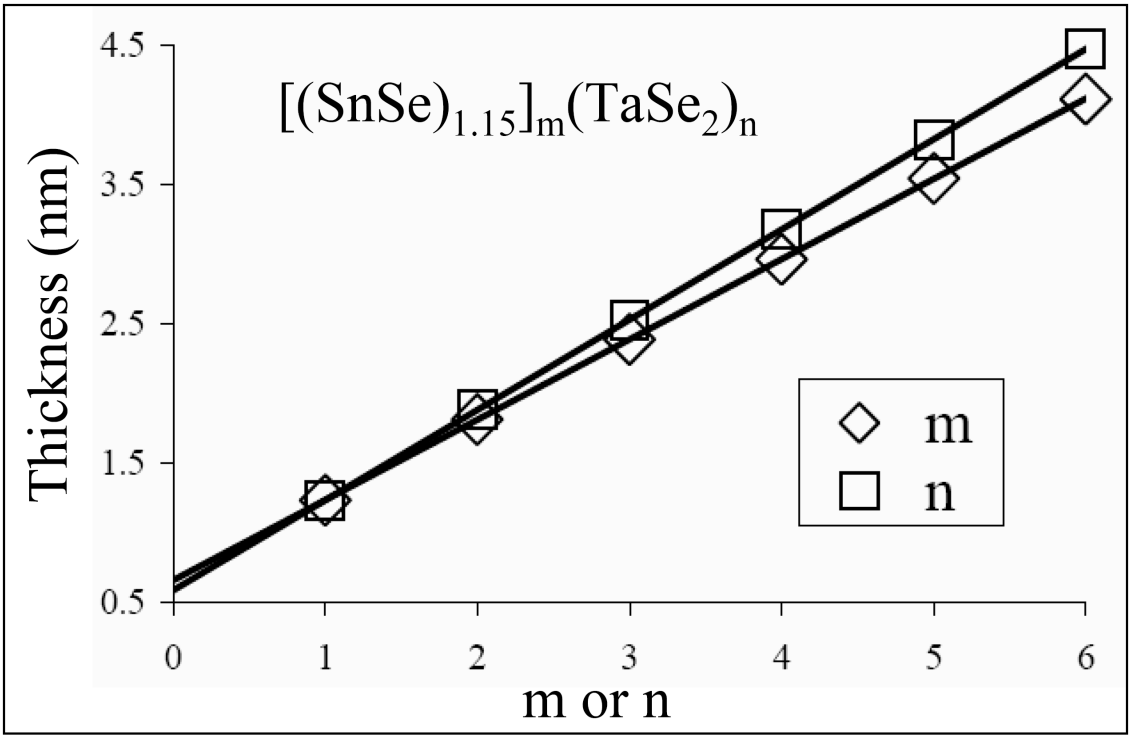

Figure II.3. Two plots of the *c*-lattice parameter vs. *m* or *n* for either several $[(SnSe)_{1.15}]_m(TaSe_2)$ or $(SnSe)_{1.15}(TaSe_2)_n$ specimens, indicated in the legend by *m* or *n* respectively. Thicknesses were calculated from the positions of Bragg maxima in the Bragg-Brentano XRD patterns for individual specimens.

Due to the $[(MX)_{1+y}]_m(TX_2)_n$ intergrowth's preferred orientation, a different XRD geometry than Bragg-Brentano is required to analyze the in-plane structural features of the $[(MX)_{1+y}]_m(TX_2)_n$ layering. Using a very low incident angle (normal to the substrate surface) and scanning the detector angle parallel to the substrate, the representative XRD pattern of a $(SnSe)_{1.15}(TaSe_2)$ ferecrystal was obtained, shown in Figure II.4. For completely textured $[(MX)_{1+y}]_m(TX_2)_n$ samples, with layers parallel to the substrate surface, all maxima in these scan geometries can be indexed as (*hk*0) reflections belonging to two separate crystal lattices. For the $[(MX)_{1+y}]_m(TX_2)_n$ ferecrystals and MLCs, reflections belonging to two separate crystal systems are expected because the MX and TX_2 constituents have independent crystal lattices. These data also confirm that the $[(MX)_{1+y}]_m(TX_2)_n$ layering is parallel to the substrate surface, with the (*hk*0) plane parallel to the substrate; in agreement with previous Bragg-Brentano scan geometries. Typically for $[(MX)_{1+y}]_m(TX_2)_n$ ferecrystals, a square and hexagonal lattice are refined for the MX and TX_2 constituents, respectively.[5-16] Unlike with MLCs, the lattice parameters of the MX and TX_2 constituents do not conform to one another and remain independent, $a_{MX} \neq a_{TX2}$, $b_{MX} \neq b_{TX2}$, $c_{MX} \neq c_{TX2}$. The *a*-lattice parameters of the two constituents can be determined from (*hk*0) reflections by simply determining peak positions and using the geometric equation relating *d*-spacing and a (*hkl*) plane for a cubic and hexagonal lattice (equations II.1 and II.2). However, for several $[(MX)_{1+y}]_m(TX_2)_n$ ferecrystals, such as the one in Figure II.4, several of the peaks overlap and require a modeling program to distinguish the peak positions. For several ferecrystal studies, the general structure analysis system (GSAS) was used to model the (*hk0*) diffraction data by a LeBail fit. The GSAS can accurately fit the overlapping diffraction maxima and thereby produce more

(cubic) $$\frac{1}{d^2} = \frac{h^2 + k^2 + l^2}{a^2}$$ Equation II.1.

(hexagonal) $$\frac{1}{d^2} = \frac{4}{3} \cdot \frac{h^2 + k^2 + hk}{a^2} + \frac{l^2}{c^2}$$ Equation II.2.

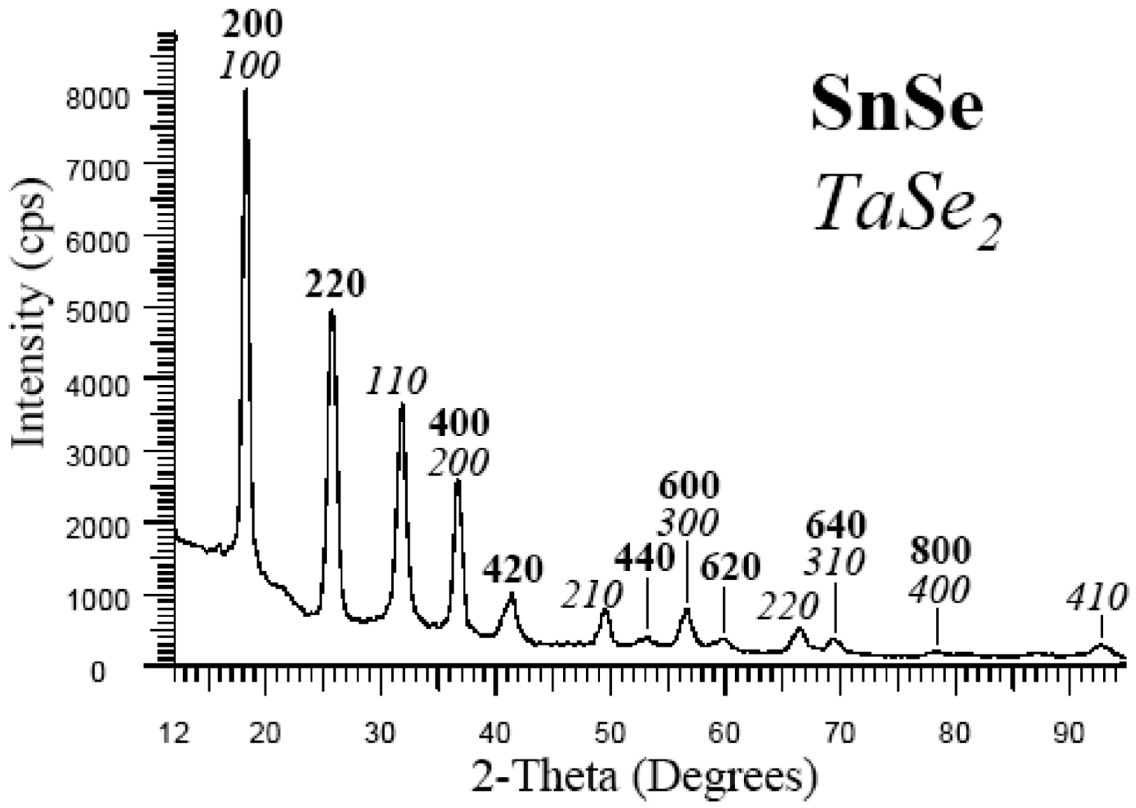

Figure II.4. An in-plane X-ray diffraction pattern from a representative $(SnSe)_{1.15}(TaSe_2)$ ferecrystal. Diffraction maxima are indexed for cubic SnSe, **bold,** and hexagonal $TaSe_2$, *italic*.

accurate in-plane lattice parameters. Although most of the ferecrystalline $[(MX)_{1+y}]_m(TX_2)_n$ compounds have been reported with a square basal plane for their MX constituent, recent studies on the $[(SnSe)_{1+y}]_m(MoSe_2)_n$ ferecrystal report a size dependent transition of the SnSe basal plane.[17] As *m* is increased from 1 to 21 the SnSe basal plane undergoes a continuous transition from square to rectangular. Interestingly, bulk SnSe undergoes a similar structural transition but as a function of temperature where the crystal basis continuously changes from tetragonal to orthorhombic as temperature is lowered.[18] Further studies by collaborator Corinna Grosse on the $[(SnSe)_m]_{1.15}(TaSe_2)$ ferecrystal revealed several structural characteristics of the SnSe constituent for $m = 3$ and 6 that are consistent with the orthorhombic structure of bulk SnSe, suggesting that size constraints on the SnSe system have similar effects to those of elevated temperature.[19]

To gain further understanding into what the $[(MX)_{1+y}]_m(TX_2)_n$ layering looks like and to extend the structural characterization, transmission electron microscopy (TEM) and scanning transmission electron microscopy (STEM) have been used. A representative STEM image of a $(SnSe)_{1.15}(TaSe_2)$ ferecrystal is shown in Figure II.5; this point of view is referred to as an in-plane view because it is down the individual MX and TX_2 sheets or parallel to the (001) plane. The sample was prepared by a focused ion beam (FIB) and lift-out technique; because the FIB cut across the intergrowth layers these TEM or STEM samples are called cross-sections. The FIB preparation technique was used for most of the TEM or STEM work on ferecrystals,[5-8,10-14] but there is also a more traditional TEM preparation technique of cleaving the sample, followed by dimple grinding and polishing that was used by collaborator Corinna Grosse's research on $[(SnSe)_{1.15}]_m(TaSe_2)$

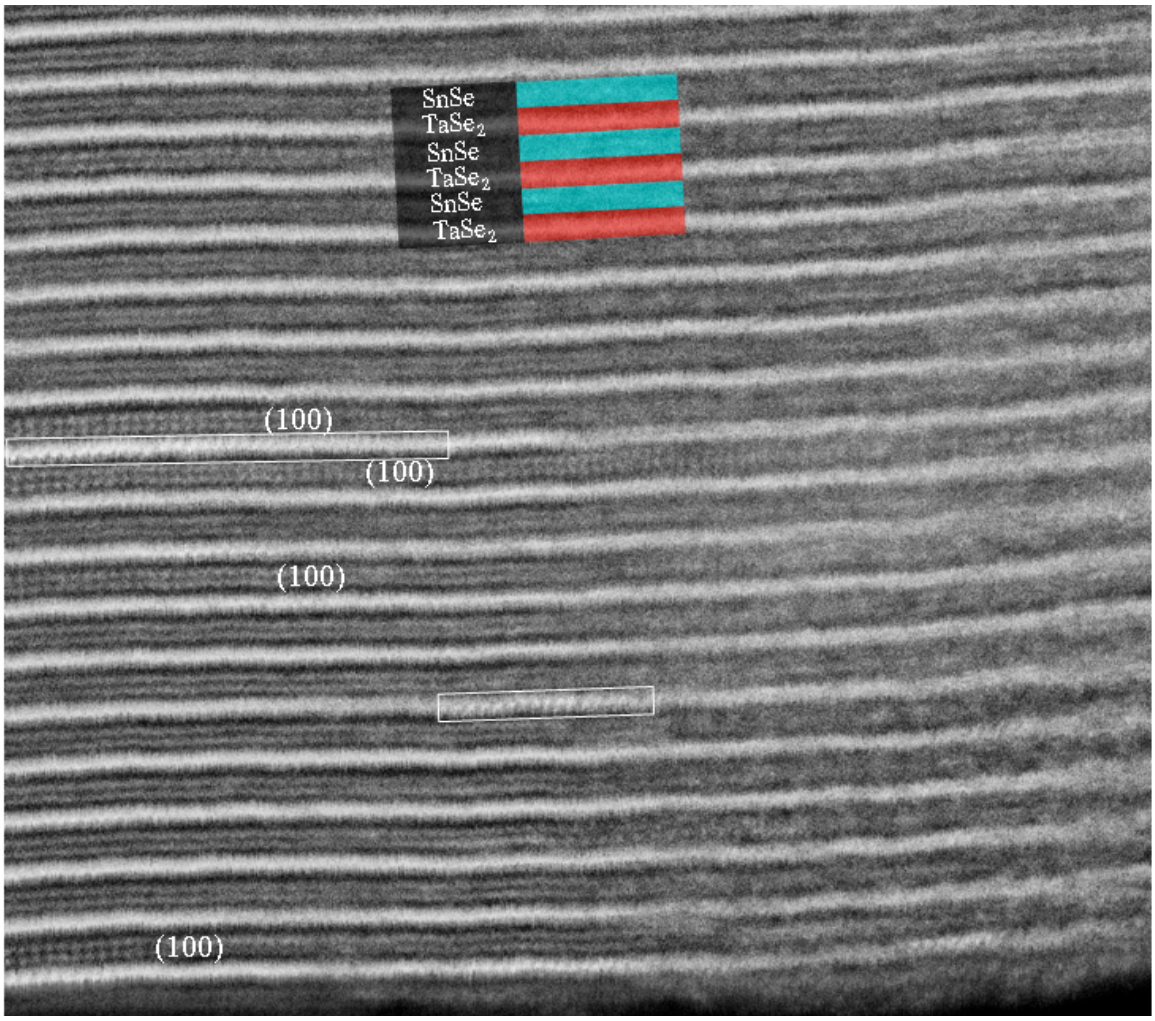

Figure II.5. A STEM-HAADF image of a representative $(SnSe)_{1.15}(TaSe_2)$ sample. Several SnSe sections are labeled (100), the resolved atoms in these sections conform to the known (100) zone axis found for the FCC NaCl type structure. The boxed-in $TaSe_2$ sections represent areas where atoms are resolved but inadequate resolution is present for axis identification.

ferecrystals.[19] The STEM image in Figure II.5 is of a $(SnSe)_{1.15}(TaSe_2)$ sample, prepared by the FIB technique, and clearly confirms the regularly spaced, un-interrupted, and chemically abrupt layering of the $m = n = 1$ intergrowth. These features appear continuous throughout the entire image and are in agreement with the sharp diffraction maxima seen in the Bragg-Brentano geometry XRD. The consistent layering in this image confirms that the MER precursor was properly calibrated. When the MER

precursors are not calibrated properly, the layers will still form, but contain several types of layering defects (discussed further in chapter III). The image in Figure II.5 is a scanning tunneling electron microscope (STEM) high-angle annular dark-field (HAADF) image of $(SnSe)_{1.15}(TaSe_2)$, therefore the brightest layer corresponds to the Ta atomic row of the $TaSe_2$ constituent and in between these rows is the bilayer of the SnSe constituent. The STEM image shows a repeating layering scheme of -(SnSe-$TaSe_2$)- that is continuous throughout the entire image, as is expected for the $(SnSe)_{1.15}(TaSe_2)$ ferecrystal with $m = n = 1$. Although, the layering does not align to a consistent zone axis, which would be expected for a crystalline MLC; the image is like patch-work with several visible zone axes scattered about. In these regions, atoms are resolved and a particular zone axis can be identified, as indicated in the image, but these zone axes appear to change both between and along the layering. This is consistent with the sample having turbostratic disorder, because between the layers the constituent's *ab*-plane is randomly rotated, creating different zone axes in neighboring layers. In most of the image the individual atoms are not resolved, instead where rows of atoms are expected there are streaks of intensity. Figure II.1 shows several different possible zone axes of MX and TX_2, including several that would resolve atoms and others that would yield streaks of intensity. Of the possible zone axes, those that show streaks of intensity outnumber those that resolve atoms. Since the in-plane crystallinity is randomly disordered, most of the layers in the STEM image are intensity streaks and not resolved atoms.

II.4. Turbostratic Disorder in $[(MX)_{1+y}]_m(TX_2)_n$ Ferecrystals

The turbostratic disorder within the $[(MX)_{1+y}]_m(TX_2)_n$ layering creates disorder by randomly rotating the *ab*-planes of the individual layers about the *c*-axis. The point at which the rotation occurs is at interfaces between layers; however, rotation does not occur at all types of interfaces and it does not behave the same for all $[(MX)_{1+y}]_m(TX_2)_n$ ferecrystals. Figures II.6a-d are STEM and TEM images of several ferecrystals; together they encompass the different possibilities of where the rotation of turbostratic disorder will occur. Figure II.6-a and II.6-b are both STEM images with $m = 3$, both showing three bilayer thick coherent sections of the MX constituent but on either side of the TX_2 layer the coherence of the MX constituent is interrupted. In this ferecrystal, at MX-MX interfaces there is no rotational disorder but at MX-TX_2 interfaces there is. Figure II.6-c shows a TEM image of a $(LaSe)_{1.17}(VSe_2)_4$ ferecrystal. In-between the LaSe layers the individual blocks of VSe_2 conform to a particular zone axis (in this case a block would be 4 VSe_2 monolayers thick); in this sample rotational disorder does not occur at TX_2-TX_2 interfaces, but again does occur at the MX-TX_2 interfaces. Figure II.6-d is a STEM image of $[(PbSe)_{1.00}]_5(MoSe_2)_5$, this sample shows that no rotation occurs at the MX-MX interfaces but does occur at the MX-TX_2 and TX_2-TX_2 interfaces; based on the lack of any zone axis in the TX_2 blocks. These studies suggest that the point of rotation for the turbostratic disorder occurs at the MX-TX_2 and, depending on T, at TX_2-TX_2 interfaces as well, but not at MX-MX interfaces. The self-assembly growth mechanism that leads to these results is further investigated in chapter VIII.

To further investigate the extent of turbostratic disorder in the ferecrystals, samples were studied by X-ray and transmission electron diffraction (TED) with the use

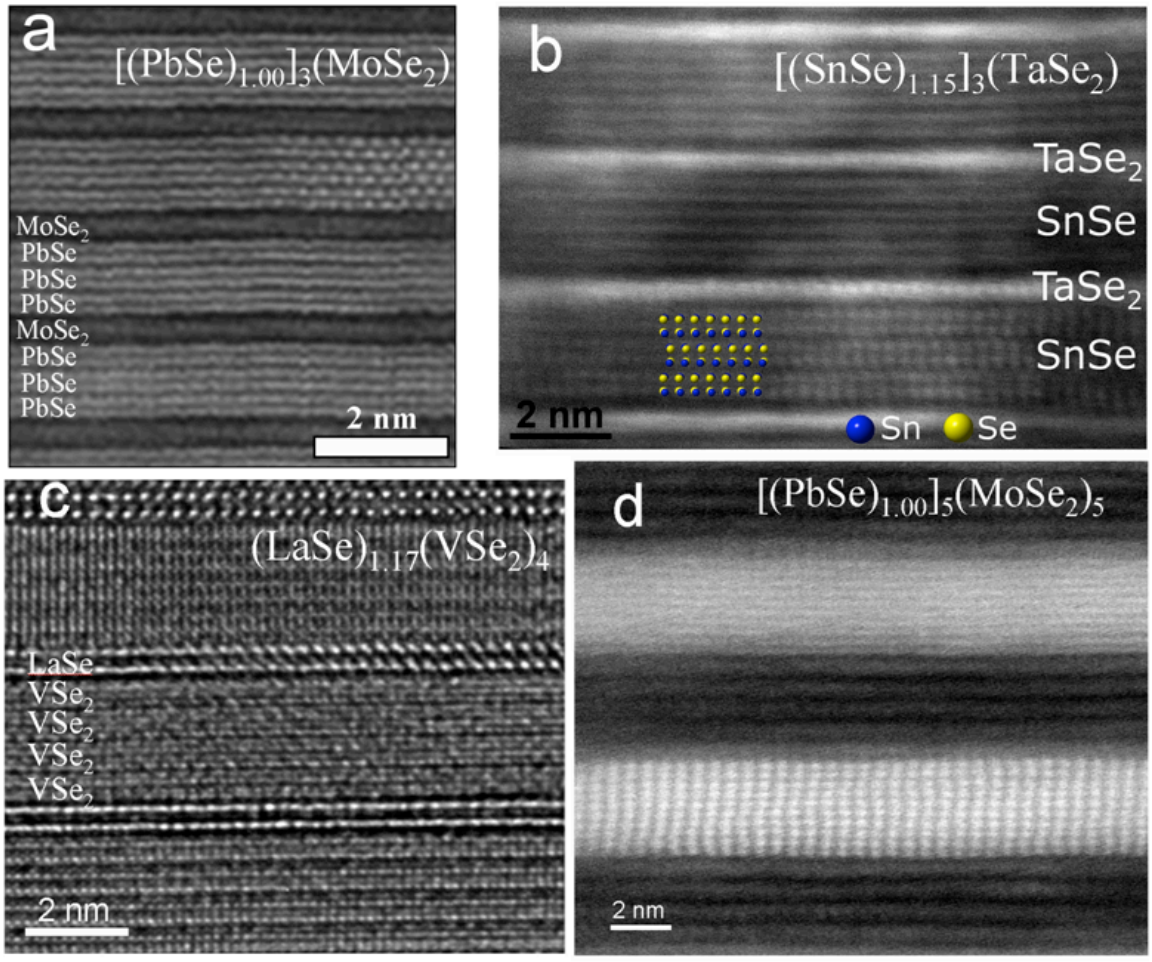

Figure II.6. High resolution STEM-HAADF (a,b,d) and TEM (c) images of several $[(MX)_{1+y}]_m(TX_2)_n$ ferecrystals. a) $[(PbSe)_{1.00}]_3(MoSe_2)$ and b) $[(SnSe)_{1.15}]_3(TaSe_2)$, both showing rotational disorder at MX-TX_2 interfaces but not at MX-MX interfaces, c) $(LaSe)_{1.17}(VSe_2)_4$ showing rotational disorder at MX-TX_2 interfaces but not at TX_2-TX_2 interfaces, and d) $[(PbSe)_{1.00}]_5(MoSe_2)_5$ showing rotational disorder at TX_2-TX_2 and MX-TX_2 interfaces but not at MX-MX interfaces.

of 2D area detectors. The 2D diffraction data reveals any remaining (*hkl*) reflections not visible in the Bragg-Brentano or in-plane scan geometries. Figure II.7 contains 2D diffraction images from a representative $(SnSe)_{1.15}(VSe_2)$ sample. The XRD scan was gathered using an incident angle of 0.6 ºθ while the TED image was gathered from the FIB cross-section sample. In the 2D diffraction images, the positions of (*hk*0) and (00*l*)

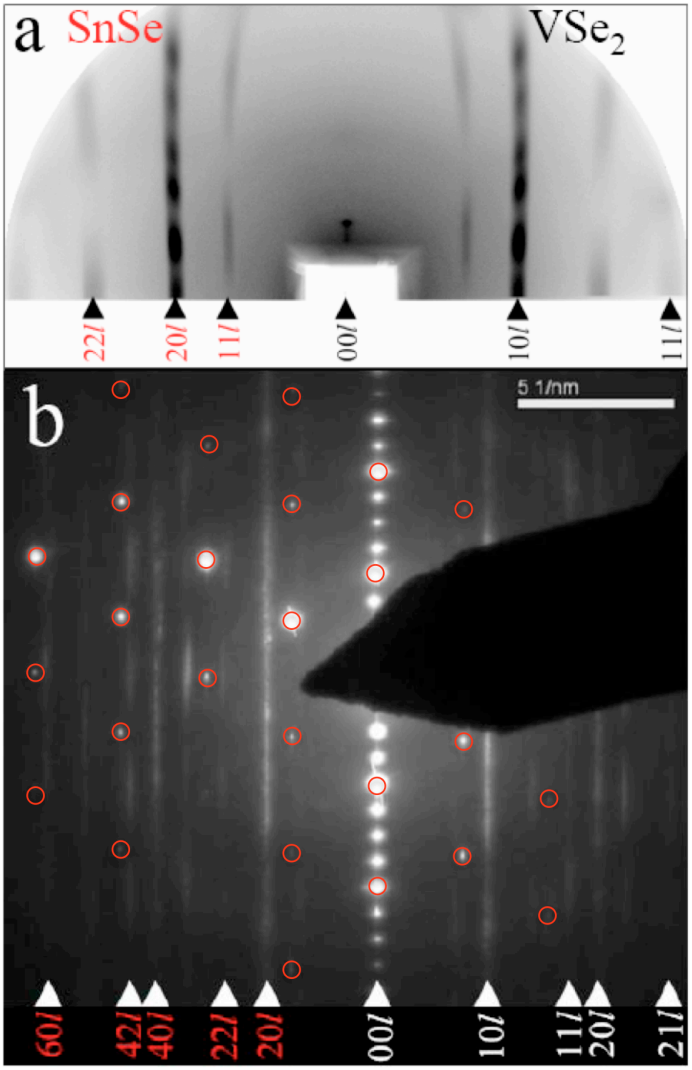

Figure II.7. a) Grazing incidence X-ray diffraction by a representative $(SnSe)_{1.15}(VSe_2)$ specimen. b) Electron diffraction image taken through a cross section of a representative $(SnSe)_{1.15}(VSe_2)$ specimen, Si substrate maxima are circled in red. The pronounced streaking is in the *c*-direction, indicating extremely short coherence lengths along the *c*-axis. Families of reflections are indexed for a square in-plane unit cell for SnSe on the left side, and for a hexagonal in-plane unit cell for VSe_2 on the right side. reflections are consistent with the previous Bragg-Brentano and in-plane scans;

confirming the preferred orientation of the intergrowth. However, for all of the visible (*hkl*) reflections ($hk \neq 0$, $l \neq 0$) there is a large amount of diffuse scattering along *l*. The extensive diffuse scattering arises from a very short coherence length in the crystal lattice

for that particular reflection; the diffuse scattering being only along *l* signifies a short coherence length along the *c*-axis. In the 2D diffraction images, the particular (*hkl*) reflections that contain diffuse scattering are those corresponding to planes not perpendicular or parallel to the layering. For these planes to have a short coherence length requires that the SnSe and VSe_2 layering contains inconsistent interlayer modulations that would limit the coherence length to a single $(MX)_m$ or $(TX_2)_n$ block. Turbostratic disorder eliminates consistency in the interlayer modulations and therefore limits the coherence length of the superlattice to single $(MX)_m$ or $(TX_2)_n$ blocks. These data suggest that the $(SnSe)_{1.15}(VSe_2)$ superlattice is turbostratically disordered and therefore is not a crystal but instead a ferecrystal.

The combined analytical techniques confirmed a $[(MX)_{1+y}]_m(TX_2)_n$ intergrowth structure of regularly spaced MX and TX_2 layering with chemically abrupt interfaces and preferentially oriented layers parallel to the substrate. The individual MX and TX_2 layers contain two different crystal types with non-equivalent in-plane lattice parameters, leading to a non-integer cation ratio between MX and TX_2. Between MX and TX_2 layers, and sometimes between TX_2 layers, there is a random rotational disorder about the *c*-axis that disrupts translational symmetry of the superlattice along (*hkl*) ($hk \neq 0$, $l \neq 0$) by creating inconsistent interlayer modulations. All of these structural characteristics are signs of a $[(MX)_{1+y}]_m(TX_2)_n$ compound not being crystalline and is therefore referred to as a ferecrystal.

CHAPTER III

SYNTHESIS

III.1. Physical Vapor Deposition

All ferecrystalline $[(MX)_{1+y}]_m(TX_2)_n$ intergrowths from the Dave Johnson Lab were made by physical vapor deposition (PVD) using custom built vacuum deposition chambers made by Thermionics™.[1] Two of these chamber's diagrams are shown in Figure III.1. The samples in this work were made using the chamber in Figure III.1-a. In this chamber, sources with higher vapor pressures are evaporated by an effusion cell (Se and Te) and sources with lower vapor pressures by an electron beam gun (Ta, V, Sn, and others). Typical deposition rates are between 0.2 and 0.5 Å/sec, depending on the element; the more difficult to evaporate elements, like Ta and W, are deposited at lower rates. Substrates are held above the sources; typically (100) oriented polished silicon is used, but polished quartz slides are used when preparing samples for electrical measurements to eliminate substrate interactions with the measurements. A pneumatic shutter and quartz crystal monitor are located between the substrate and source. The pneumatic shutter is a physical barrier to control deposition onto the substrate while the quartz crystal monitor measures the rate of deposition. A motorized carousel holds the substrates so that they may be selectively rotated between sources, in this way a specific sequence of elements can be deposited onto any substrate. A custom LabVIEW program commands the deposition rates, movement of substrates, sequence of deposition, and deposition amounts; thereby depositing any desired combination of elemental layers.

The PVD process for creating $[(MX)_{1+y}]_m(TX_2)_n$ precursors is not an epitaxial process, the substrate is unheated and no structural relationship between film and substrate or between individual layers is achieved during deposition, resulting in the

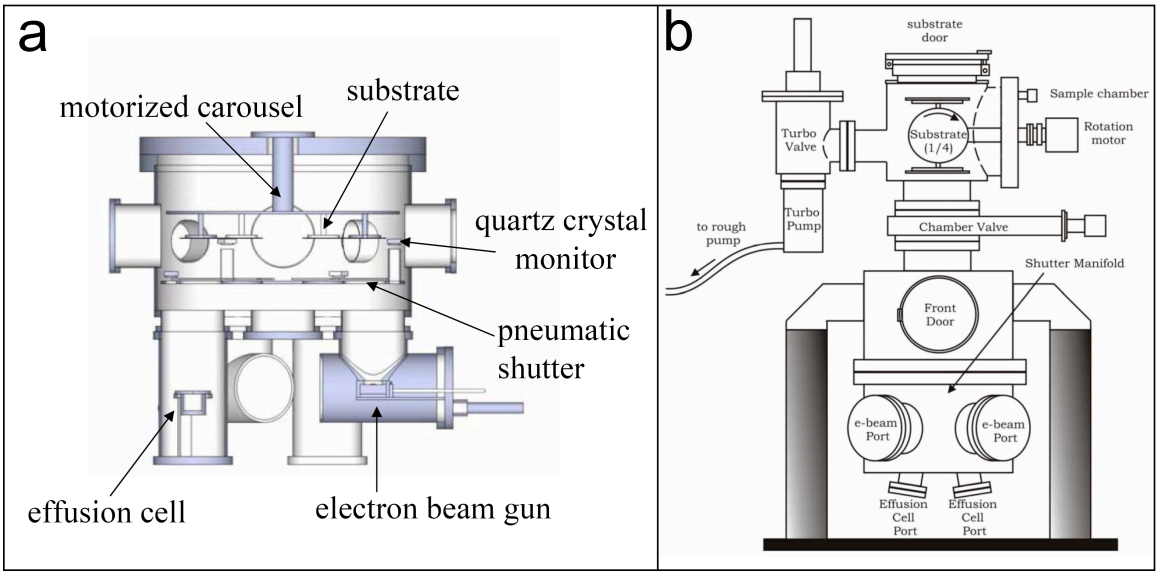

Figure III.1. Schematic for two custom built physical vapor deposition chambers; courtesy of Michael Anderson and Fred Harris.

deposition of amorphous modulated elemental layers. These layers are deposited in a sequence that mimics a desired product and are referred to as precursors, for when calibrated properly they will self-assemble into the desired product at low annealing temperatures (Figure III.2). For example, to create a precursor to the $[(MX)_{1+y}]_1(TX_2)_1$ ferecrystal would require a deposition of four elements per $\{[(MX)_{1+y}]_1(TX_2)_1\}$ unit; the deposition order would be X-M-X-T and repeated until the desired film thickness is achieved (Figure III.3). To create other $[(MX)_{1+y}]_m(TX_2)_n$ precursors with different values of *m* and *n* only requires changing the number of layers in the precursor's layering sequence without any additional calibration (Figure III.4). In order to repeatedly make

ideal precursors, or to make variations of m and n from the calibration of a single $m = n = 1$ intergrowth, requires that the deposition be reproducible. The maximum variation in composition and absolute amount of material of an ideal precursor's modulated layers has sub-angstrom tolerances. Keeping the deposition consistent is made even more difficult by the lack of a load lock (chamber in Figure III.1-a) and the regular interchanging of different elemental sources, both introduce contaminates to the deposition chamber that effect deposition. Cleaning the electron beam guns between exchanging elemental sources reduces cross-contamination, but to achieve a reproducible deposition requires a constant point source (the shape and physical location of the evaporating source). For effusion cells and electron beam guns, a constant point source is achieved by reproducing the physical position and build of the effusion cell crucible or electron beam emitter each time the equipment is removed for cleaning or exchanging sources. The electron beam guns are removed more often than the effusion cells. It is best that the electron beam emitters are not altered unless broken; this will help to keep a consistent point source. An additional feature to electron beam guns that aids in a consistent point source is their rastering ability, which can be equipped on most electron beam guns. A raster allows the user to move and shape the electron beam's projection onto the source, thereby reproducing the point source regardless of subtle alterations to the electron beam emitter.

III.2. Calibrating a Precursor to $[(MX)_{1+y}]_m(TX_2)_n$

Obtaining a precursor that will self-assemble into a targeted $[(MX)_{1+y}]_m(TX_2)_n$ ferecrystal without excessive defects, requires precise calibration of the composition and absolute amount of materials deposited. A successful precursor will contain in each of its

as-deposited M-X and T-X bilayers the exact quantities for crystallizing a single MX unit (two MX atomic planes, i.e. a MX bilayer) and TX_2 unit (a X-T-X trilayer sandwich, i.e. a TX_2 monolayer), respectively. If the as-deposited M-X and T-X bilayers of the precursor contain an excess or lack of material than what is required to form single MX or TX_2 units, then material must be excreted or obtained from elsewhere to continue a growth front of the desired $[(MX)_{1+y}]_m(TX_2)_n$ ferecrystal. Excreting or obtaining atoms can only be done by solid diffusion, which requires a great deal of energy; the self-assembly process uses low annealing temperatures far below the energy required for driving solid diffusion. Therefore, the tolerances for an ideal precursor's composition and absolute amount of material are very small and even slight inaccuracies in the calibration will result in the formation of untargeted layering schemes and secondary phases.

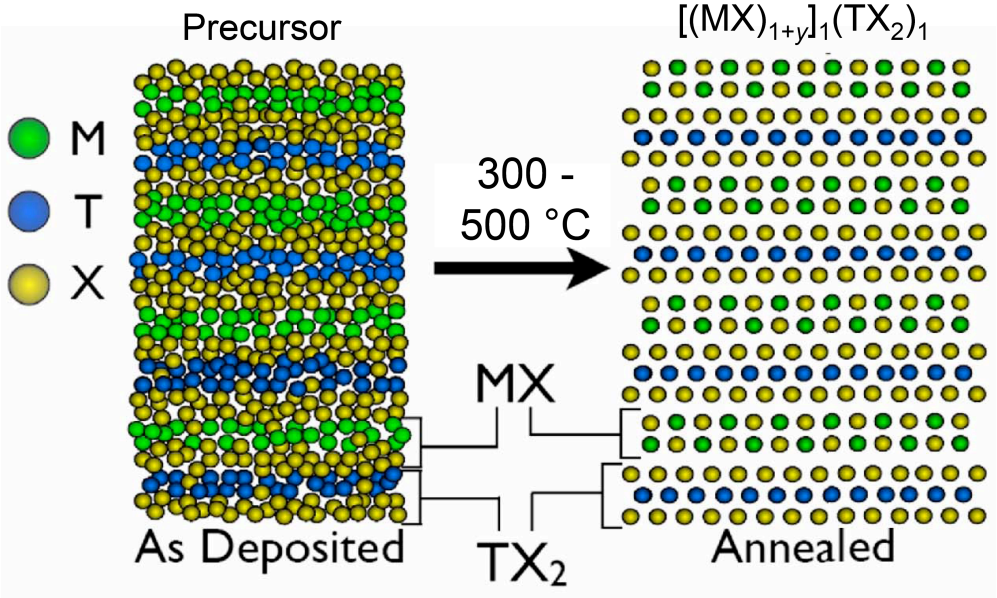

Figure III.2. An ideal self-assembly scenario, in the precursor (left) atoms are short distances from their final destination in the $[(MX)_{1+y}]_1(TX_2)_1$ compound (right); therefore, low annealing temperatures are sufficient to self-assemble the product.

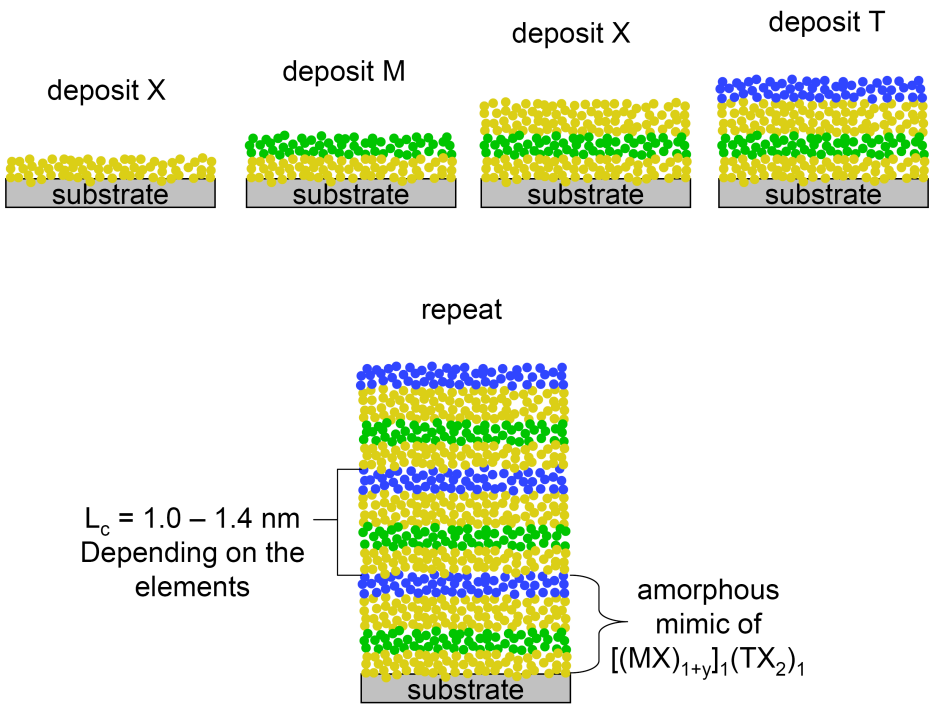

Figure III.3. Schematic of depositing a precursor to $[(MX)_{1+y}]_1(TX_2)_1$, $m = n = 1$.

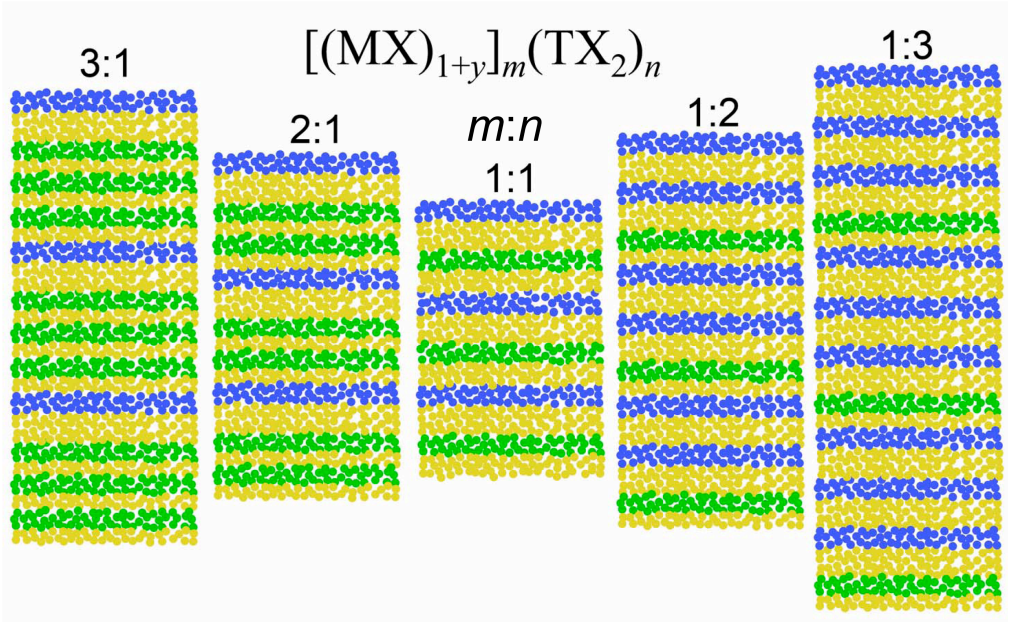

Figure III.4. Example precursors to five different $[(MX)_{1+y}]_m(TX_2)_n$ compounds, all can be made from the ideal deposition parameters determined in the $[(MX)_{1+y}]_1(TX_2)_1$ or 1:1 compound calibration.

Originally, obtaining a particular precursor's ideal conditions was done through an iterative calibration approach, where one would repeatedly make adjustments to the precursor's MX or TX_2 constituents compositions and absolute amount of materials until ideal $[(MX)_{1+y}]_m(TX_2)_n$ compounds were produced. Often this required much iteration as the calibration slowly circled in on the correct deposition parameters. To minimize iterations and design a more generic synthetic approach, a three step calibration process was developed that directly determines the ideal deposition parameters for any new $[(MX)_{1+y}]_m(TX_2)_n$ compound. The first calibration step is to determine the deposition parameters for creating stoichiometric MX and TX_2. For the MX constituent an M/X ratio of 1 is targeted, for this is the empirical composition of the face centered cubic structure expected for MX. To determine the deposition parameters that deposit an M/X ratio of 1, a series of M_xX films is deposited where x is trended over the empirical value of 1 (Figure III.5). In each precursor a different M_xX composition was achieved by changing the amount of M deposited per M-X bilayer while keeping the amount of X constant. Plotting the trend between M shutter time ("shutter time" is the amount of time that the pneumatic shutter is held open and is directly related to how much material is deposited) and M/X composition (determined by EPMA)[2] results in a linear trend that can be interpolated to determine the deposition parameters for M and X that produce an M/X atomic ratio of 1 (Figure III.6). Typically, a slight excess of X (3-6 atomic %) is used to compensate for X loss during annealing, and subsequently adjusted based on EPMA composition studies of pre- and post-annealed precursors. Equivalent studies are used for calibrating the TX_2 constituent, except with a targeted T/X ratio of 0.5.

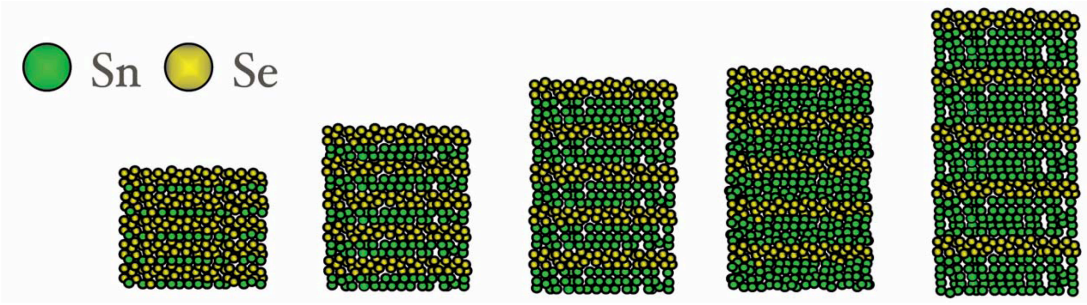

Figure III.5. An example of five Sn_xSe samples, deposited with the same Se open shutter time but different Sn open shutter times per M-X bilayer.

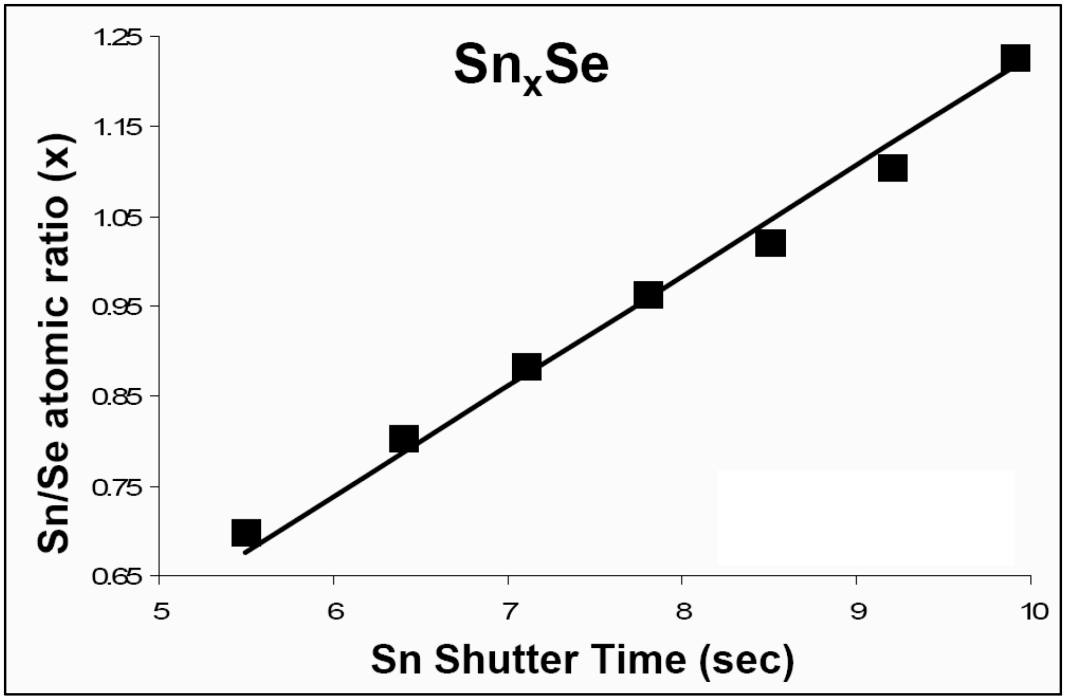

Figure III.6. A plot of Sn/Se composition (determined by EPMA) vs. Sn shutter open time (shutter open time is directly related to the amount of material deposited); interpolating the linear trend provides the Sn/Se shutter open time ratio that produces a 1:1 composition ratio of Sn:Se.

The second calibration step determines the deposition parameters required to prepare a precursor with an M/T cation ratio that corresponds to the misfit of the desired $[(MX)_{1+y}]_1(TX_2)_1$ compound. Since many ferecrystals are new compounds and therefore have no previously reported misfit value, a y must be estimated from either the MX and TX_2 bulk structures or a structurally similar misfit layered compound. A series of $(MX)_x(TX_2)$ layered precursors are prepared by alternatively depositing elemental bilayers of M-X and T-X, as described in Figure III.7, while using the calibrated deposition time ratios determined in step one so that the empirical formulas of MX and TX_2 are maintained. Between precursors x is varied by changing the layer thicknesses of the M-X bilayer while holding the layer thickness for T-X constant. Plotting the M shutter open time (M shutter open time is directly related to the M-X bilayer thickness) vs. M/T atomic ratio (determined by EPMA) the resulting trend is linear and can be interpolated to determine the deposition parameters that deposit the desired misfit ratio (Figure III.8). Later, the data from (hk0) XRD studies on the resulting $[(MX)_{1+y}]_m(TX_2)_n$ compounds can be used to determine the experimental misfit parameter and the composition of the precursors is subsequently adjusted.

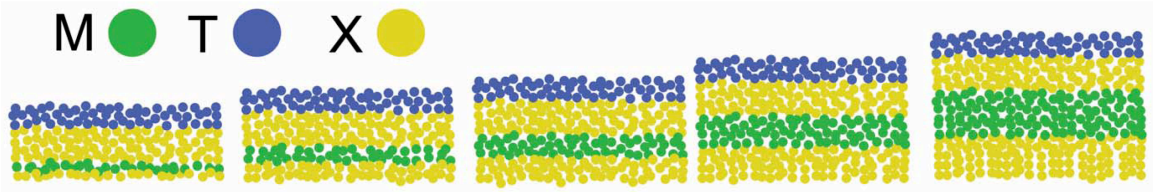

Figure III.7. A example of five $(MX)_x(TX_2)$ samples, deposited with the same shutter open times per T-X bilayer but different shutter open times per M-X bilayer; the shutter open time ratios calibrated in step one were used so that the empirical MX and TX_2 compositions were maintained.

The third calibration step is to simultaneously scale the M-X and T-X bilayer thicknesses, while maintaining the calibrated composition ratios previously determined in steps one and two for M/X, T/X, and M/T, to determine the correct absolute amount of material per repeating sequence that yields a single unit cell of the targeted $[(MX_{1+y})]_m(TX_2)_n$ ferecrystal. In this manner, a series of precursors was made and annealed to self-assemble the as-deposited modulated layers, with average annealing conditions of 400 ºC for 30 min. The diffraction patterns of the resulting films were used to access the correct thickness; a representative sample series from the calibration of $(SnSe)_{1.15}(TaSe_2)$ is shown in Figure III.9. In each pattern, the position of the first diffraction peak is at the same angle, independent of the precursor's repeating elemental

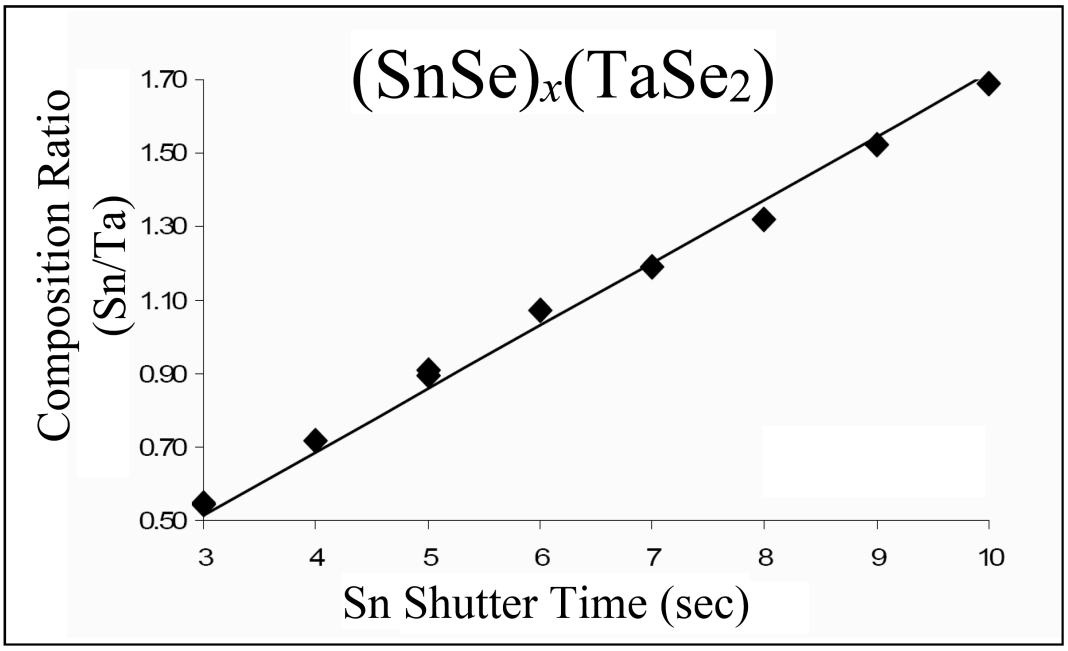

Figure III.8. A plot of Sn/Ta composition (determined by EPMA) vs. Sn shutter open time (shutter open time is directly related to the amount of material deposited); interpolating the linear trend provides the Sn/Ta shutter open time ratio that produces the desired misfit value *x*. The shutter open time ratios calibrated in step one were maintained so that the empirical MX and TX_2 compositions were maintained.

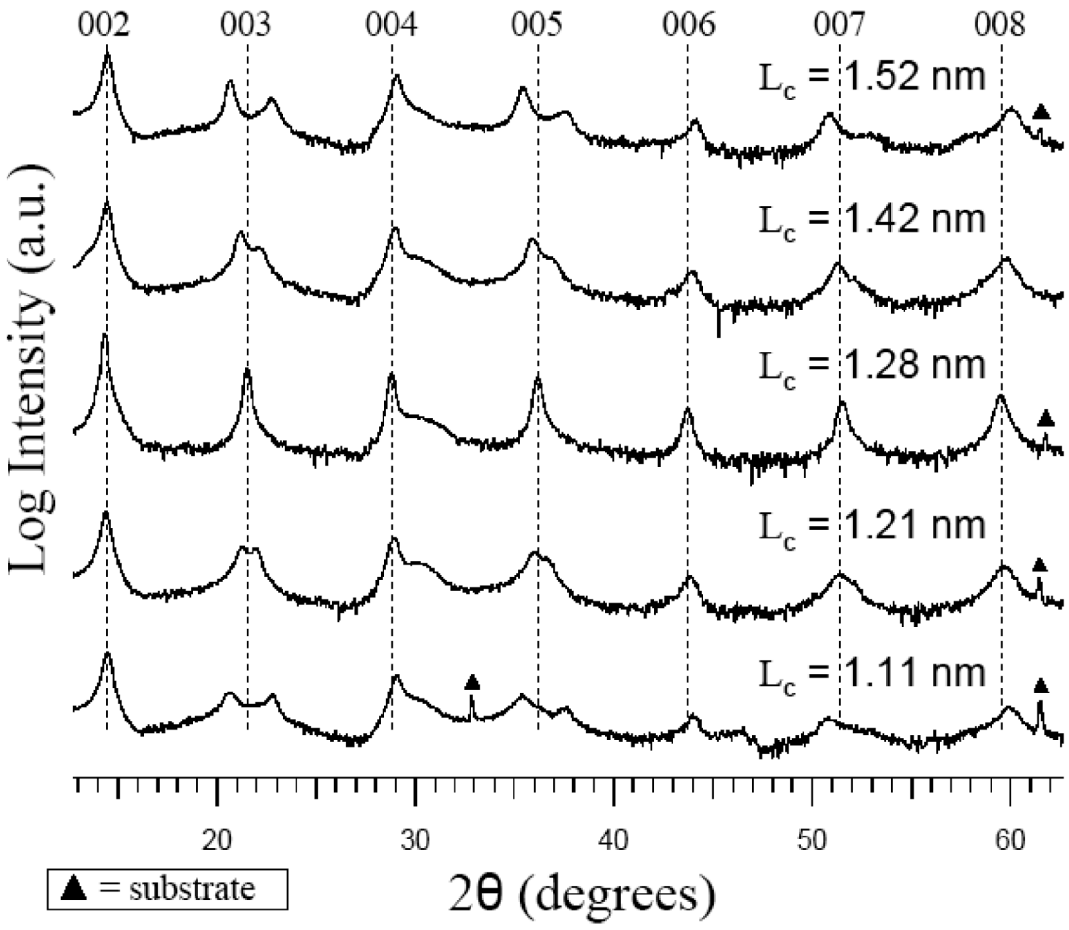

Figure III.9. θ-2θ locked coupled X-ray diffraction patterns of precursors annealed at 400 °C for 30 min, plotted as log intensity versus °2θ and arbitrarily offset for clarity. The modulation wavelengths, L_c, associated with the as-deposited precursor of each pattern are shown on the right above each of the diffraction patterns. For comparison clarity the position of each (00*l*) maxima are indexed relative to the ideal pattern.

sequence thickness (L_c), suggesting that there is a specific, favored structure being formed by all of the samples. In the middle diffraction pattern, from a precursor L_c = 1.28(1) nm, all of the diffraction maxima can be indexed as consecutive (00*l*) reflections arising from a single unit cell of *c* = 1.238(1) nm with no visible secondary phases; suggesting that this is the correct precursor thickness L_c to prepare the targeted $(SnSe)_{1.15}(TaSe_2)$ ferecrystal. The diffraction patterns with smaller or larger L_c contain extra diffraction features, suggesting that more complex intergrowths of the constituent

structures have formed. The reduction in thickness, L_c compared to *c*, during annealing is attributed to the more efficient arrangement of atoms in the product and evaporation of excess selenium.

III.3. X-ray Diffraction Peak Splitting

Examining the more complex diffraction patterns in Figure III.9, every expected odd indexed (00*l*) reflection peak is roughly split into a doublet and this systematic peak splitting becomes broader as the thickness of the precursor's L_c deviates from the ideal 1.28 nm precursor. To help decipher these unusual diffraction patterns, cross-section high-resolution scanning transmission electron microscope (STEM) high-angle annular dark-field (HAADF) images were obtained from several annealed precursors; two representative images are shown in Figure III.10. Figure III.10-a, from a 1.28 nm precursor, contains alternating SnSe bilayers and $TaSe_2$ monolayers as is expected for the $(SnSe)_{1.15}(TaSe_2)$ ferecrystal and consistent with the X-ray diffraction patterns which contain only (00*l*) reflections from a single *d*-spacing. The non-ideal precursor in Figure III.10-b contains small domains with the ideal SnSe and $TaSe_2$ layering, separated by domains with extra layers of SnSe or $TaSe_2$; suggesting that the precursor's M-X and T-X bilayers contained improper amounts of materials. The size in the *c*-direction of these ideal $[(SnSe)_{1.15}]_1(TaSe_2)_1$ domains decreases as L_c deviates further from 1.28 nm, suggesting that as the $[(SnSe)_{1.15}]_1(TaSe_2)_1$ domains grow, the excess atoms not involved in the superlattice growth segregate to the grain boundaries where they form extra layers of a binary constituent. The more incorrect the absolute amount of materials the more layering defects are present and the smaller the domains of ideal layering are.

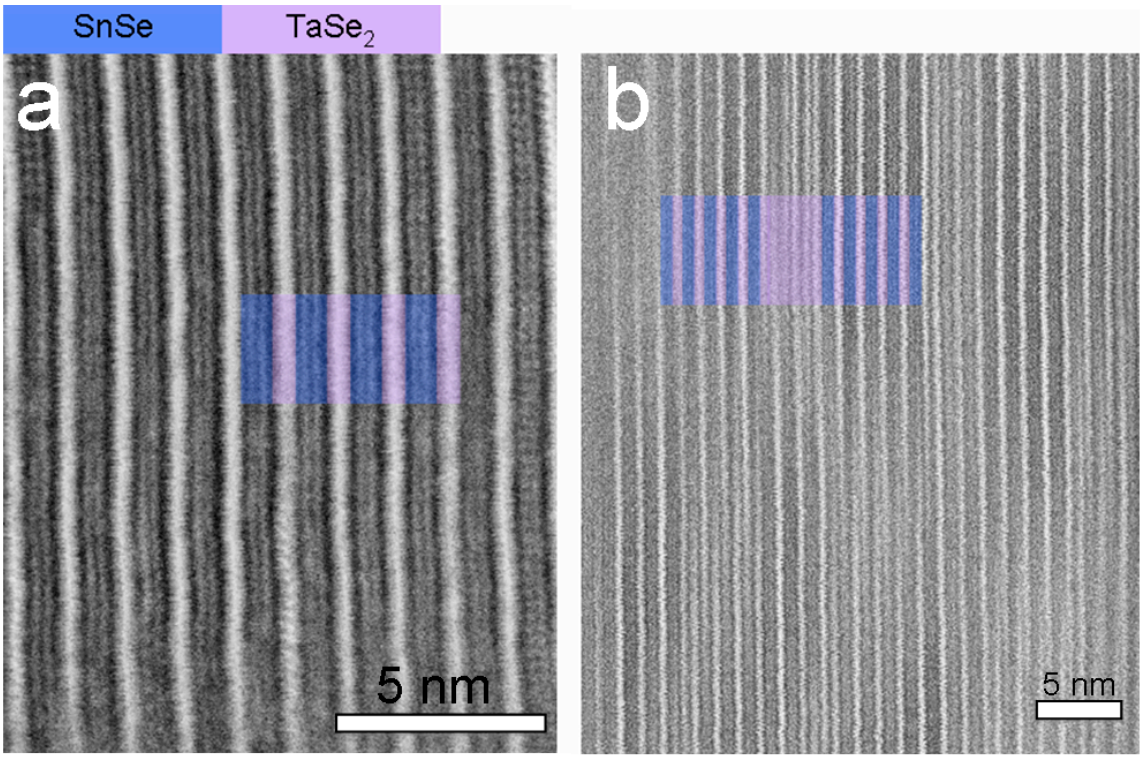

Figure III.10. HRSTEM-HAADF images of two annealed precursors. a) from an ideal precursor to $(SnSe)_{1.15}(TaSe_2)$ and b) a non-ideal precursor that has correct composition for the MX, TX_2, and M/T but has a incorrect absolute amount of materials.

To further explore the relationship between the non-ideal layering of Figure III.10-b and the peak splitting in Figure III.9, the XRR modeling program Bede Refs was used. Simulating XRR patterns of two finite crystals of $[(SnSe)_{1.15}]_1(TaSe_2)_1$ separated by one bilayer of SnSe or a monolayer of $TaSe_2$ results in a reflection pattern where all odd (00*l*) reflections are split into doublets (Figure III.11). Figure III.12 contains three samples prepared with the structures used in the XRR simulations, but with $(SnSe)_{1.15}(VSe_2)$ instead of $(SnSe)_{1.15}(TaSe_2)$ because the *c*-lattice parameter of SnSe and VSe_2 are more equivalent. The qualitative agreement between the experimental and simulated diffraction patterns and the change in the peak splitting as the $\{[(SnSe)_{1.15}(VSe_2)\}_n$ domains change in size supports our interpretation of this unusual

diffraction phenomenon. Fundamentally, the splitting effect arises from the interference of coherent X-rays diffracting from the individual domains of ideal layering, and the fact that there are only a finite number of unit cells within these domains. When two finite $\{(MX)_{1+y}(TX_2)\}_n$ domains are separated by a distance not corresponding to the superlattice *c*-lattice parameter, the diffracted X-rays from each domain will potentially become out of phase. This is caused by the incorrect *d*-spacing between the two domains that disrupts the Bragg condition normally found for a single domain of consistent layering.

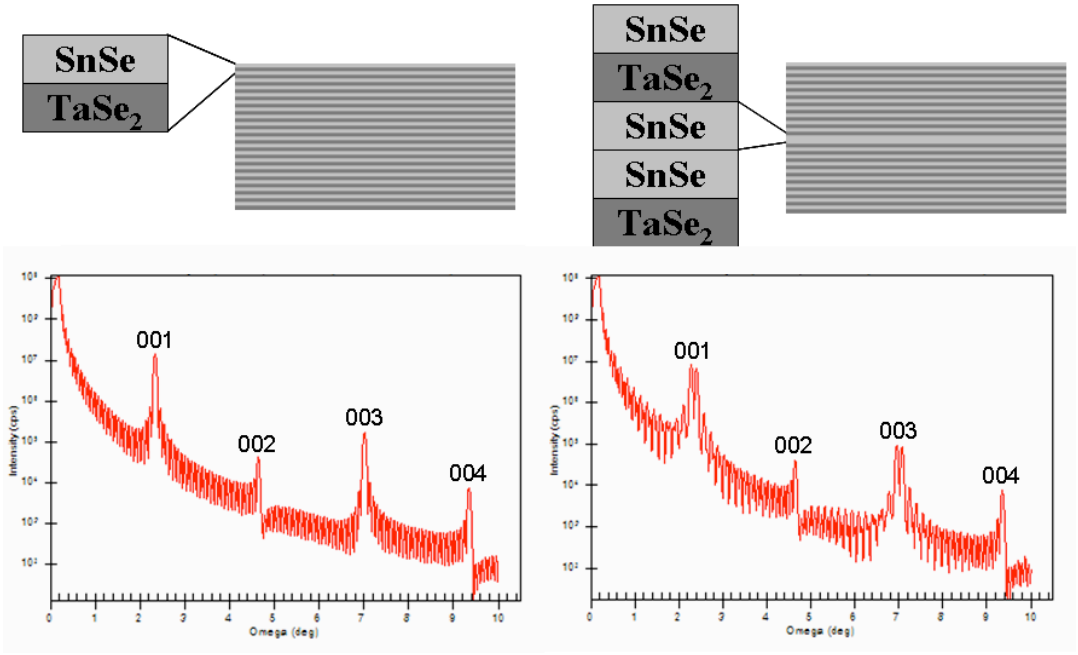

Figure III.11. Top) two theoretical models where on the top-left is the ideal superlattice scenario of $(SnSe)_{1.15}(TaSe_2)$ and on the top-right are two finite crystallites of $(SnSe)_{1.15}(TaSe_2)$ separated by one layer of SnSe. Bottom) resulting XRR patterns from Bede Refes using the above layering scenarios, the maxima are indexed for the expected (00*l*) reflections.

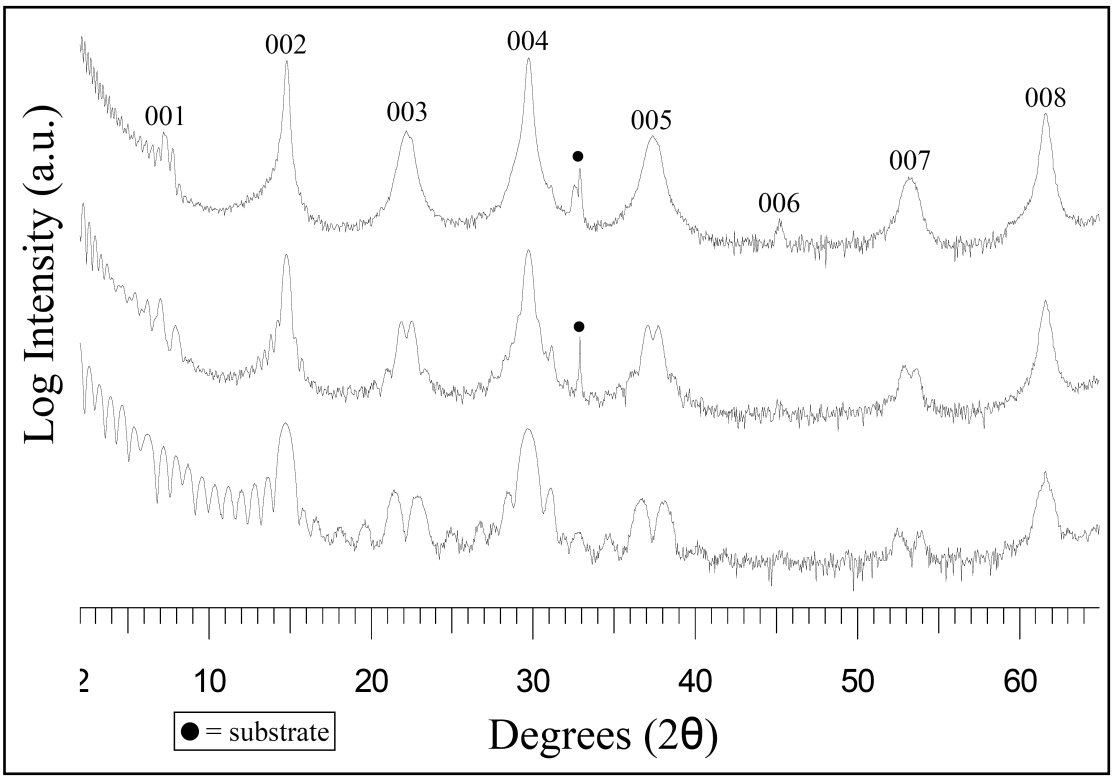

Figure III.12. Bragg-Brentano XRD patterns from intergrowth structures prepared using the XRR modeling layering sequences that produced peak splitting. The intergrowths each contained two finite sections of $(SnSe)_{1.15}(VSe_2)$ layering separated by one VSe_2 layer with the following layering sequences: top) $\{(SnSe)_{1.15}(VSe_2)\}_{20}$-$(VSe_2)_1$-$\{(SnSe)_{1.15}(VSe_2)\}_{20}$; middle) $\{(SnSe)_{1.15}(VSe_2)\}_{10}$-$(VSe_2)_1$-$\{(SnSe)_{1.15}(VSe_2)\}_{10}$; bottom) $\{(SnSe)_{1.15}(VSe_2)\}_5$-$(VSe_2)_1$-$\{(SnSe)_{1.15}(VSe_2)\}_5$.

To further understand the peak splitting, consider an ideal system with several layers of equivalent spacing (*d*), shown in Figure III.13. In this ideal scenario, a Bragg-Brentano geometry XRD pattern would consist of (00*l*) reflections from the consistent layering; such as the pattern from an annealed precursor with L_c = 1.28(1) nm in Figure III.9. Next, consider the same scenario but containing one anomalous layer with a spacing of *d*/2 (Figure III.13); we now have two finite domains of ideal layering separated by a spacing of *d*/2. In this case, for the Bragg condition of the (001) reflection, individually the two finite crystals would produce diffraction equivalent to the ideal scenario.

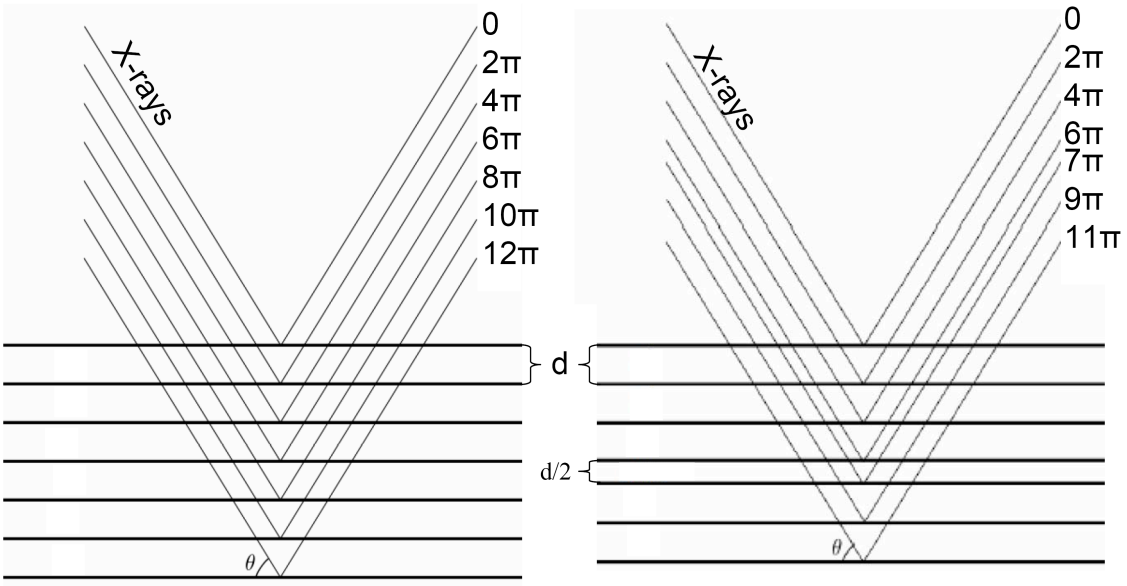

Figure III.13. Theoretical scenario of diffracting X-rays on the Bragg condition of the (001) reflection for layer spacing *d*. (left) Ideal superlattice scenario of a consistent *d*-spacing. (right) Two finite domains of consistent *d*-spacing separated by a distance of *d*/2.

However, due to the spacing of *d*/2 between the finite sections, X-rays diffracting from the second domain would have a phase shift of π relative to X-rays diffracting off the first domain; resulting in complete destructive interference at the Bragg condition. The reason that the diffraction intensity for odd (00*l*) reflections is split and even (00*l*) reflections is not split can be understood by Bragg's law and comparing the (001) and (002) reflections in the non-ideal scenario of Figure III.13 (Figure III.14). For the Bragg condition of the (001) reflection, the phase shift between the 4th and 5th X-ray is π. This results in all X-rays diffracted from the top domain to be out-of phase by half a wavelength with the diffracted X-rays from the bottom domain; causing destructive interference on the (001) Bragg condition. On the Bragg condition for the (002) reflection, the phase shift between the 4th and 5th X-ray is 2π, resulting in a phase shift between the two domain's diffracted

X-rays of one wavelength, causing constructive interference on the (002) Bragg condition. This explanation is true for all odd and even (00*l*) reflections and explains the periodicity of peak splitting.

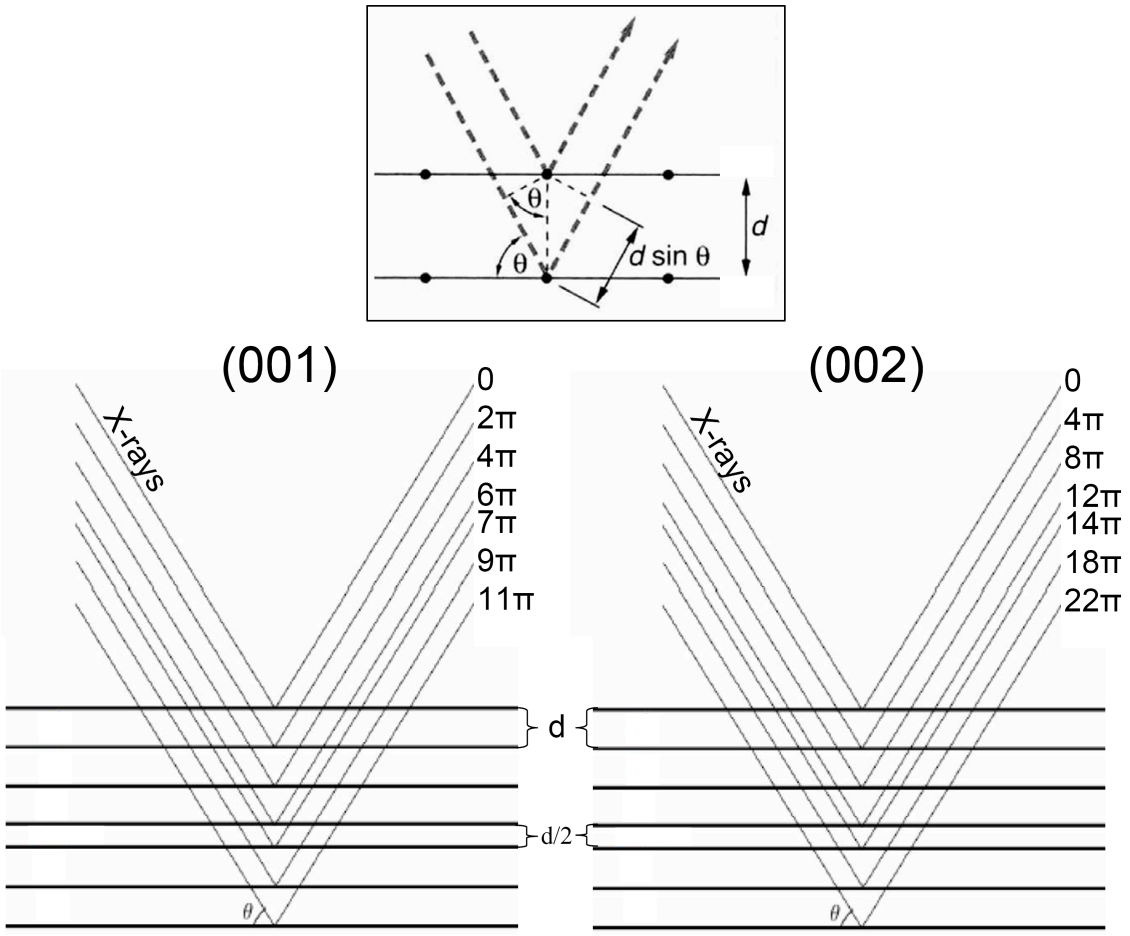

Figure III.14. Theoretical non-ideal scenario of diffracting X-rays on the Bragg condition of the (001) (left) and (002) (right) reflection for layer spacing *d*. On the (001) reflection the phase of the 4th and 5th X-ray are shifted by π (out of phase) while they are shifted by 2π for the (002) reflection (in phase).

III.4. Modeling Peak Splitting

The non-ideal layering scenario of two finite $\{(MX)_{1+y}(TX_2)\}_n$ domains separated by a spacing of $d/2$ is only one example of a layering defect. In reality, experimental results during the calibration of a new $[(MX)_{1+y}]_m(TX_2)_n$ precursor can contain a plethora of different layering defects, each with individual XRD interference characteristics. To rapidly analyze the diffraction patterns of any possible non-ideal layering sequence, a matlab program was designed in collaboration with James Kunert that produces a theoretical XRD intensity profile for any given combination of layering sequences. The matlab script was set up to calculate diffracted intensity as a function of θ, using equation III.1:

$$I(\theta) \propto \left| \sum_{n=0}^{N} e^{i2kd_n \sin\theta} \right|^2 \qquad \text{Equation III.1.}$$

Where θ is the incident angle, d_n is the n^{th} layer depth from the surface, k is the wave number ($k = 2\pi/\lambda$), N is the number of layers, and n is the n^{th} layer. Assuming a beam of parallel plane waves of constant wavelength and constant amplitude, this equation is used to display coherent and incoherent interactions of X-rays diffracting from any theoretical layering scheme. The path length difference between X-rays is given by equation III.2:

$$\Delta x_n = 2d_n \sin\theta \qquad \text{Equation III.2.}$$

Here the variables are the same as in equation III.1. Equation III.2 aids in understanding the matlab program's relationship to Bragg's law. Using this program, it is apparent that the broadness and symmetry of peak splitting is not limited to the aforementioned cases (symmetrical splitting and only odd (00*l*) reflections split) but instead is a function of the location and size of the layering defect. Figure III.15 contains XRD patterns from models containing the structures used in the designed peak splitting case of Figure III.12; the broadening of peak splitting as the domain size decreases is in agreement between the matlab program, Bede Refs, and experimental. In Figure III.16, two finite domains of ideal layering with *c*-lattice spacing of *d* are separated by a distance slightly more or less than *d*/2; this results in asymmetrical peak splitting. Figure III.17 contains the modeled XRD pattern of two finite ideal domains with *c*-lattice spacing of *d* separated by a spacing of *d*/3; this results again in non-symmetrical peak splitting but now the periodicity of split peaks has changed from every other to two thirds of the peaks split.

Possibly the greatest potential of the matlab program is how it can assist in the calibration process; Figure III.18 shows how the matlab program can be used to identify layering defects in annealed non-ideal precursors. A precursor was made whose desired product is the $[(PbSe)_{1+y}]_1(TiSe_2)_3$ compound; upon annealing the sample, Bragg-Brentano XRD patterns reveal (00*l*) reflections from a layering of a consistent *d*-spacing but every fourth reflection's intensity is split into a doublet. Using the matlab program, a model of two finite ideal domains with *c*-lattice spacing of *d* separated by a spacing of *d*/4 also had peak splitting with every 4^{th} peak split; revealing that approximately one extra PbSe bilayer or $TiSe_2$ monolayer exists within the desired $[(PbSe)_{1+y}]_1(TiSe_2)_3$ layering, since the thickness of one PbSe bilayer or $TiSe_2$ monolayer is approximately

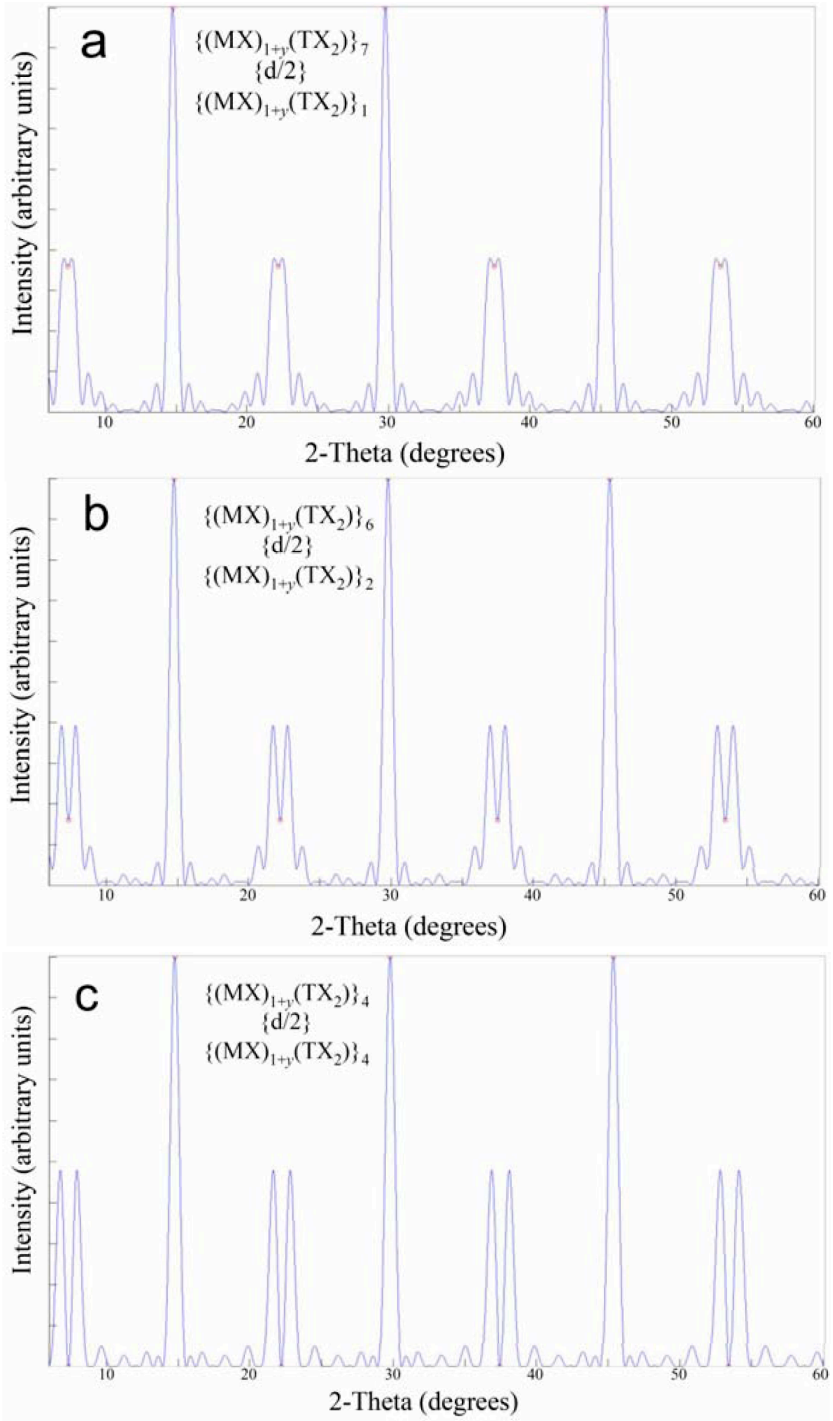

Figure III.15. Modeled XRD intensity profile from the matlab program using a layering sequence of two finite domains of ideal $(MX)_{1+y}(TX_2)$ layering separated by a distance equal to ½ the *c*-lattice parameter of the $(MX)_{1+y}(TX_2)$ superlattice. The layering sequence of each figure is the following: (a) $\{(MX)_{1+y}(TX_2)\}_7$-$\{d/2\}$-$\{(MX)_{1+y}(TX_2)\}_1$ (b) $\{(MX)_{1+y}(TX_2)\}_6$-$\{d/2\}$-$\{(MX)_{1+y}(TX_2)\}_2$ (c) $\{(MX)_{1+y}(TX_2)\}_4$-$\{d/2\}$-$\{(MX)_{1+y}(TX_2)\}_4$.

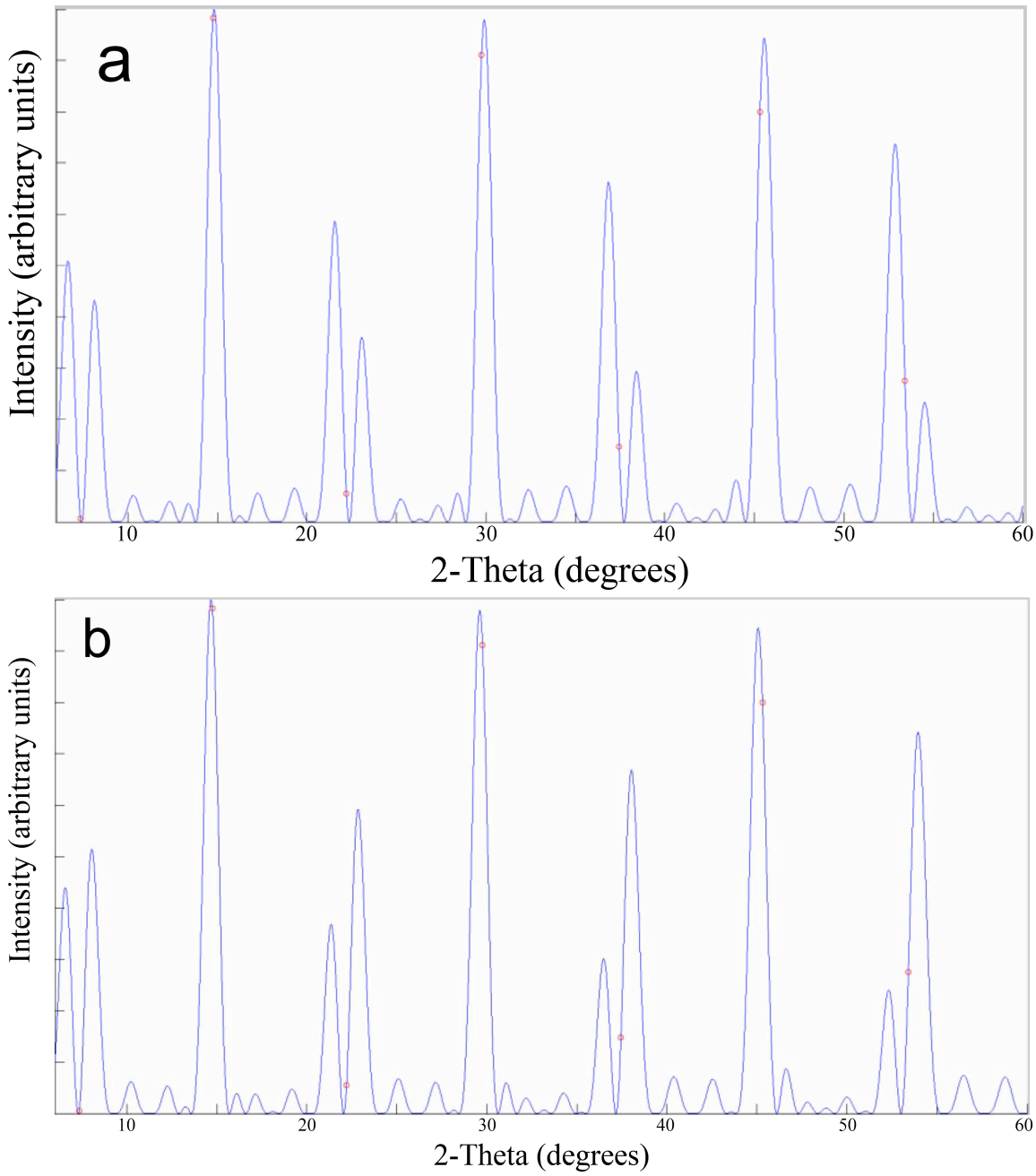

Figure III.16. Modeled XRD intensity profile from the matlab program using a layering sequence of two finite domains of ideal $(MX)_{1+y}(TX_2)$ layering separated by a distance slightly smaller (a) or larger (b) than ½ the *c*-lattice parameter of the $(MX)_{1+y}(TX_2)$ superlattice.

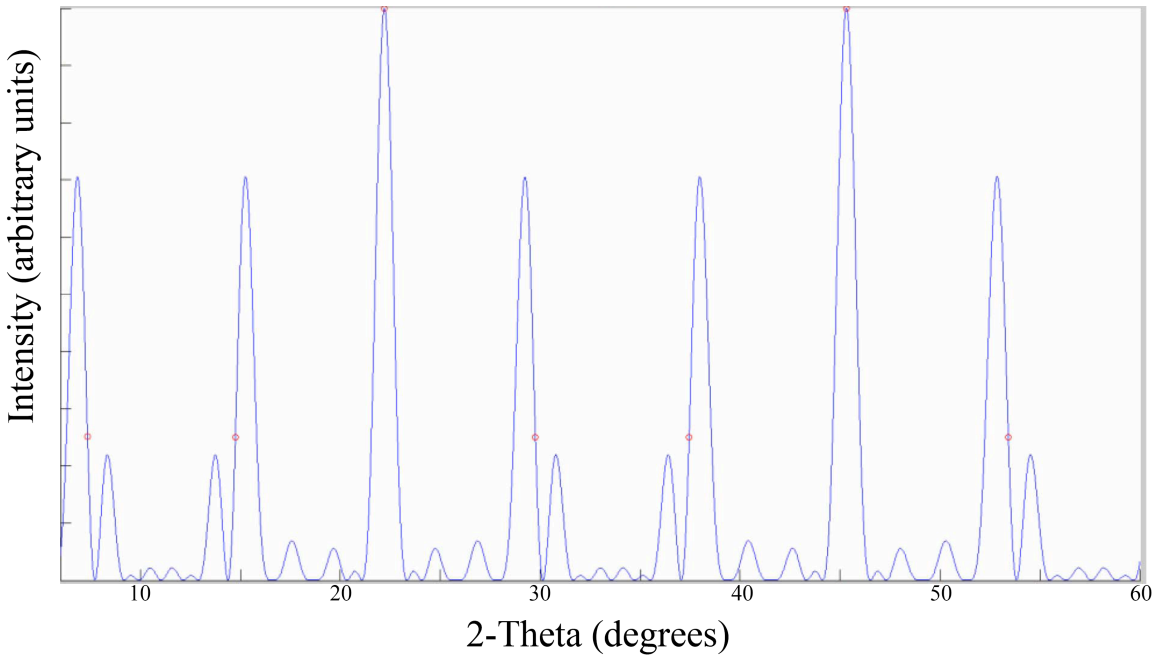

Figure III.17. Modeled XRD intensity profile from the matlab program using a layering sequence of two finite domains of ideal $(MX)_{1+y}(TX_2)$ layering separated by ⅓ the *c*-lattice parameter of the $(MX)_{1+y}(TX_2)$ superlattice.

d/4. Because this sample contains three $TiSe_2$ layers ($n = 3$), it is more likely that a small excess in each deposited Ti-Se bilayer has become enough material to form an extra $TiSe_2$ in the final product. Using the matlab model to understand the peak splitting, adjustments to the precursor's deposition can then be made for forming a ideal $[(PbSe)_{1+y}]_1(TiSe_2)_3$ compound.

III.5. Annealing Study

During the calibration process, generic annealing conditions of 400 ºC for 30 minutes were used; these conditions will promote self-assembly of precursors into $(MX)_{1+y}(TX_2)$ intergrowths for most compounds. There are a few examples where these conditions do not work; Te containing compounds require a much shorter annealing time

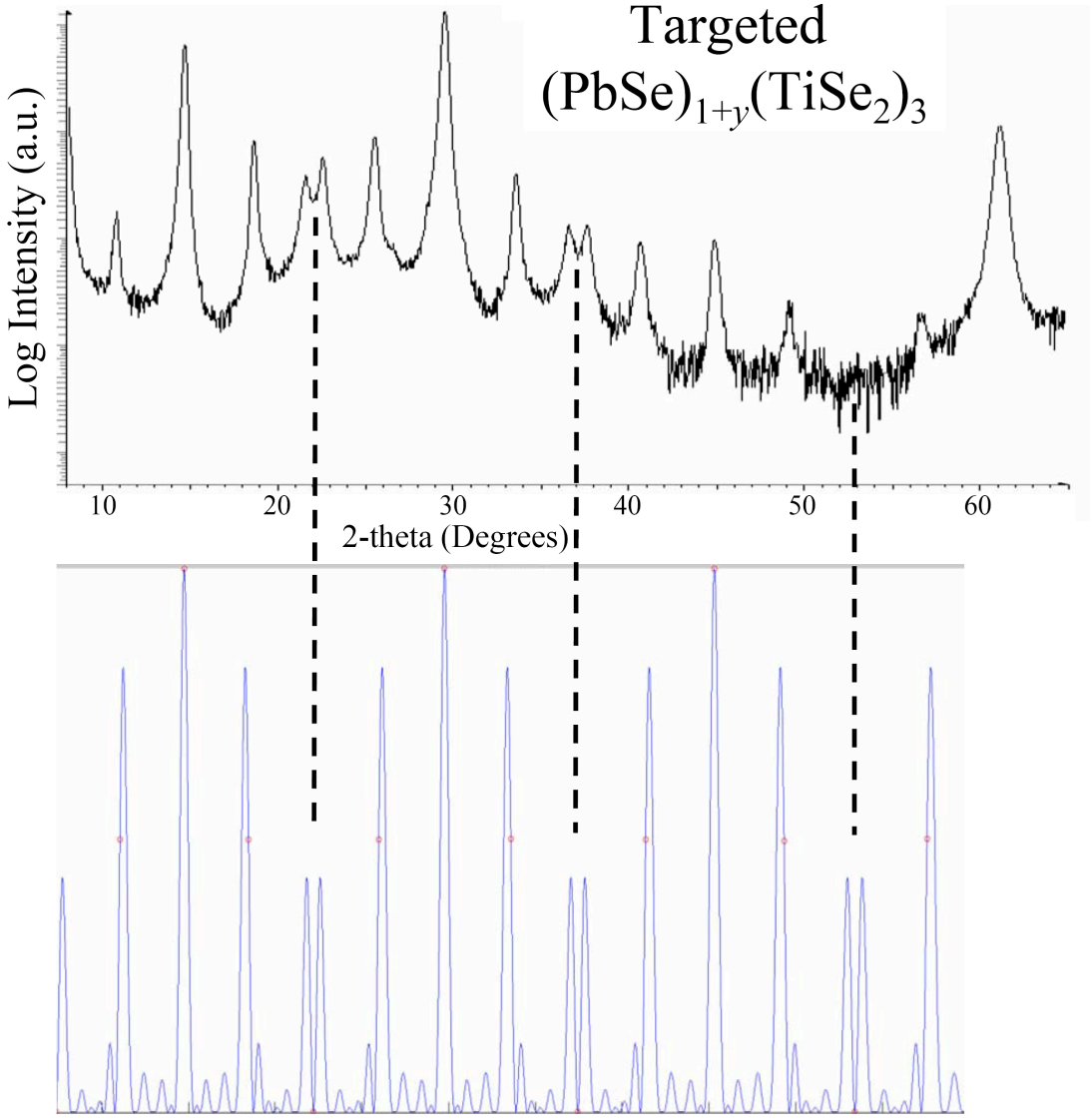

Figure III.18. (top) A Bragg-Brentano XRD pattern of an annealed precursor that was designed to form $(PbSe)_{1+y}(TiSe_2)_3$. (bottom) Modeled intensity profile from the matlab program using a layering sequence of two finite domains of ideal $(PbSe)_{1+y}(TiSe_2)_3$ layering separated by ¼ the *c*-lattice parameter of $(PbSe)_{1+y}(TiSe_2)_3$.

and La containing compounds require a much higher annealing temperature. To determine the optimal annealing temperature for a new $[(MX)_{1+y}]_m(TX_2)_n$ compound requires an annealing study. After a precursor is calibrated it is annealed as a function of

temperature and time and the resulting diffraction data are used to judge the ideal annealing conditions. Bragg-Brentano geometry XRD patterns are shown in Figure III.19 for a representative annealing study on the $(SnSe)_{1+y}(Mo_{1-x}Nb_xSe_2)$ compound. Annealing the as-deposited sample at temperatures between 300-500 ºC increases the number of (00*l*) reflections and their intensity, showing that the layered structure of the deposited precursor is conserved and the expected intergrowth layering has formed with a coherent *d*-spacing. Annealing at 500 ºC resulted in the formation of a SnSe impurity phase, determined by XRD, and annealing below 350 ºC resulted in less intense and broader (00*l*) reflections. In Figure III.19, It is difficult to tell qualitatively which annealing temperature is ideal. The XRD patterns from annealing at 350-450 ºC all have sharp and intense (00*l*) reflections as would be expected for an ideal $(SnSe)_{1+y}(Mo_{1-x}Nb_xSe_2)$ superlattice. Tables III.1 and III.2 have compiled the *c*-lattice parameters and full width half maximum (FWHM) of the (00*l*), l = 1-4, reflections for each XRD pattern between 350-500 ºC. Observing the data, the results from annealing at 400 ºC for 30 min appear to give the lowest FWHM and most consistent parameters, representing the most coherent layering. Also, there is no evidence that annealing for longer than 10 minutes has improved the coherence of $(SnSe)_{1+y}(Mo_{1-x}Nb_xSe_2)$ layers. From these results, ideal annealing conditions of 400 ºC for 30 min were chosen for self-assembling $(SnSe)_{1+y}(Mo_{1-x}Nb_xSe_2)$ compounds; the longer annealing time was chosen for it doesn't appear to degrade the sample while providing more time to reach an equilibrium.

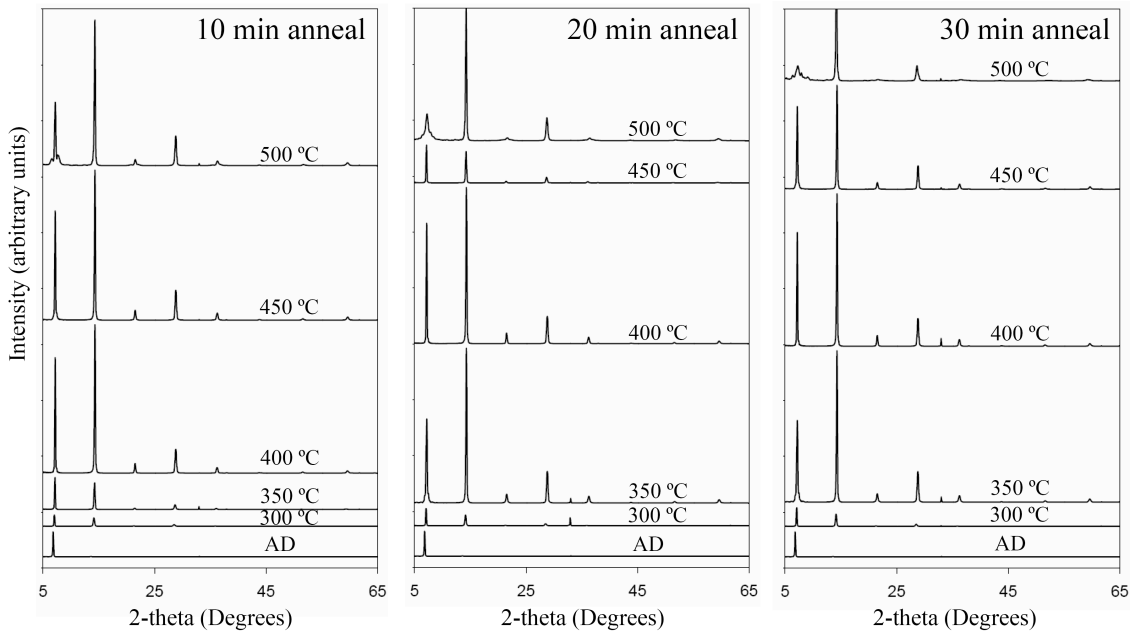

Figure III.19. Bragg-Brentano XRD patterns from an annealing study on the $(SnSe)_{1+y}(Mo_{1-x}Nb_xSe_2)$ compound. Intensity units are CPS but the patterns are offset along the *y*-axis for clarity.

III.6. Bridge

After completing the synthetic approach and calibration techniques mentioned above, a stoichiometric $[(MX)_{1+y}]_1(TX_2)_1$ compound is obtained. From this one compound's calibration, all other $[(MX)_{1+y}]_m(TX_2)_n$ compounds can be made with no further adjustments. Even if changes in the deposition chamber occur, resulting in a loss of calibration; techniques such as the peak splitting analysis matlab program will aid in determining the necessary minute adjustments needed to quickly regain ideal deposition parameters. These techniques will aid in the rapid production of new $[(MX)_{1+y}]_m(TX_2)_n$ compounds as more extravagant layering schemes and elements are used for investigating the structural and property tuning capability of ferecrystals. To demonstrate this calibration techniques capability, a case study was done for the $[(SnSe)_{1.15}]_m(TaSe_2)_n$

family of ferecrystals; this along with a full structural characterization is reported in Chapter IV.

Table III.1. *c*-lattice parameters from an annealing study on the $(SnSe)_{1+y}(Mo_{1-x}Nb_xSe_2)$ compound in Figure III.19.

Anneal	*c*-lattice parameter		
Temperature	10 min Anneal	20 min Anneal	30 min Anneal
350C	12.43(2)	12.36(4)	12.50(2)
400C	12.37(4)	12.37(4)	12.36(4)
450C	12.37(5)	12.42(3)	12.35(4)
500C	12.34(8)	12.3(1)	12.3(2)

Table III.2. Full width half maximum (FWHM) determined by the (00*l*) reflections in Figure III.19 (FWHM determined for only *l* = 1, 2, 3, and 4).

	Full Width Half Max (2-Theta)		
	350C		
(00*l*)	10 min	20 min	30 min
(001)	0.183	0.256	0.186
(002)	0.231	0.203	0.263
(003)	0.292	0.305	0.323
(004)	0.327	0.298	0.370
	400C		
(00*l*)	10 min	20 min	30 min
(001)	0.184	0.187	0.189
(002)	0.203	0.204	0.205
(003)	0.255	0.256	0.262
(004)	0.302	0.297	0.298
	450C		
(00*l*)	10 min	20 min	30 min
(001)	0.203	0.179	0.219
(002)	0.204	0.233	0.213
(003)	0.279	0.296	0.305
(004)	0.298	0.313	0.303
	500C		
(00*l*)	10 min	20 min	30 min
(001)	0.280	0.521	0.622
(002)	0.218	0.228	0.238
(003)	0.339	0.542	0.732
(004)	0.319	0.356	0.375

CHAPTER IV

SYNTHESIS OF $[(SnSe)_{1.15}]_m(TaSe_2)_n$ FERECRYSTALS: STRUCTURALLY TUNABLE METALLIC COMPOUNDS

This work was published in volume 24 of Chemistry of Materials in 2012 with co-authors Jason Wilson, Paul Zschack, Corinna Grosse, Wolfgang Neumann, and David C. Johnson. Jason Wilson performed research assistance in the synthesis process, Paul Zschack assisted in X-ray diffraction analysis at the Advanced Photon Source, Corinna Grosse and her advisor Wolfgang Neumann performed transmission electron microscopy analysis, David C. Johnson is my advisor and research group leader, and I am the primary author.

IV.1. Introduction

Naturally occurring and synthetic misfit layer compounds (MLCs) are stable intergrowths of two different crystal structures with incommensurate *ab*-plane lattice parameters. Traditional high-temperature synthesis has been used to produce thermodynamically stable $[(MX)_{1+y}]_m(TX_2)_n$ compounds, where M = Sn, Pb, Sb, Bi and rare earth metals; T = Ti, V, Cr, Nb, and Ta; X = S and Se; with y being the extent of misfit between the structures in their *ab*-plane.[1-5] Typically MX is a distorted rock-salt type crystal structure, and TX_2 is hexagonal with trigonal prismatic or octahedral coordination of T; the magnitude of *ab*-plane misregistration between the two constituents ranges from $0.07 \leq y \leq 0.28$. The values for m and n using high-temperature

synthesis are limited to $m = n = 1$ except for a few cases where $m = 1$ and $n = 2$ or 3. Although these compounds have been known for a considerable time and there has been extensive research activity because of their properties, including intercalation/deintercalation reactions, magnetism, and superconductivity, there is still debate about why they are stable and how these properties are correlated with their unusual layered structures.[1,6-8]

Recently, we described a synthetic procedure which permitted m and n to be independently and systematically varied between 1 and 16, producing numerous metastable $[(MX)_{1+y}]_m(TX_2)_n$ compounds within a specific elemental family of compounds.[9-15] The synthetic approach uses physical vapor deposition to create a compositionally modulated multilayer thin-film precursor. A precursor that mimics the composition and layer thickness of each layer within the desired product was found to self-assemble into that product on annealing. This enables the selective preparation of specific metastable compounds within a family (Figure IV.1). New metastable compounds prepared using this approach are structurally distinct from misfit layer compounds prepared through traditional high-temperature synthetic techniques by having extensive rotational disorder between the MX and TX_2 layers and between individual TX_2 layers, which results in a lack of (*hkl*) reflections with $h,k \neq 0$ and $l \neq 0$. Therefore, the term ferecrystals, from the Latin "*fere*" meaning almost, has been introduced to describe this ordered, but not crystalline state of matter.

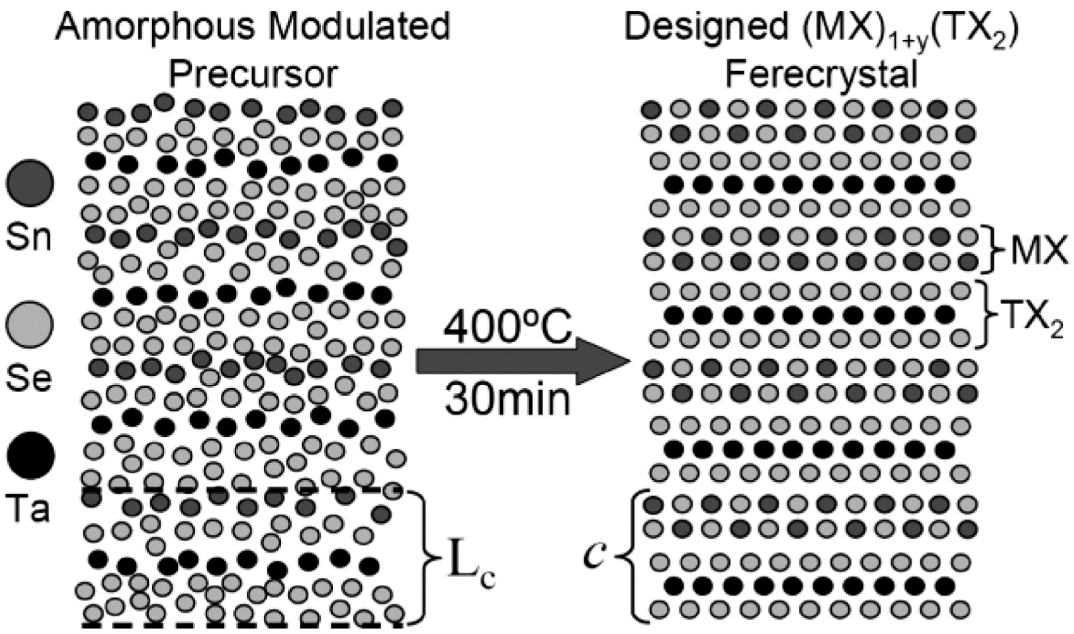

Figure IV.1. On the left is a schematic of an as-deposited precursor showing four L_c periods with a layering scheme designed to form the $[(SnSe)_{1.15}]_1(TaSe_2)_1$ ferecrystal. On the right is a schematic of the structure for $[(SnSe)_{1.15}]_1(TaSe_2)_1$ which forms after annealing the precursor.

Here we present a more efficient optimization strategy for calibrating modulated elemental reactant (MER) precursors and demonstrate its utility by preparing a new family of ferecrystals, $[(SnSe)_{1.15}]_m(TaSe_2)_n$. In the prior synthesis approach composition and layer thicknesses of the precursor's M-X and T-X bilayers were treated as two components with individual adjustments being made to each bilayer and then iteratively adjusted yielding a two-dimensional optimization problem. In our new approach, we fix the M to T ratio and the elemental sequence while varying the absolute thicknesses of the precursor's repeating elemental sequence, L_c. Observing the change in X-ray diffraction patterns as a function of thickness enables us to simultaneously optimize both constituents, more rapidly identifying the deposition parameters required to prepare targeted compounds. The $[(SnSe)_{1.15}]_m(TaSe_2)_n$ ferecrystals prepared were structurally

characterized, and their electrical transport properties were analyzed as a function of *m* and *n*.

IV.2. Experimental Details

All thin-film samples were deposited by physical vapor deposition (PVD) in a custom-built high vacuum chamber evacuated to a base pressure of 1×10^{-7} Torr. Elemental sources were evaporated from spatially separate positions, Ta (99.95% purity) and Sn (99.98% purity), were evaporated using a Thermionics 3 kW electron beam gun. Se (99.999% purity) was evaporated from a custom-built effusion cell. Quartz crystal monitors positioned approximately 25 cm above each source were used to monitor and control deposition rates. Approximate rates of 0.4 Å/s for Sn and Se and 0.2 Å/s for Ta were used for the samples prepared in this study. Pneumatically powered shutters separated the evaporating sources (below the shutter) from the substrates, typically polished (100) orientated silicon wafers (above the shutter). Substrates were mounted on a motorized, computer controlled carrousel. A custom-made LabVIEW program automatically rotated the samples into position above a deposition source, opened the shutter for the length of time required to deposit the desired amount of the element, and then closed the shutter. This process was repeated, building up the compositionally modulated precursor layer by layer.

The repeating elemental sequence, L_c, consists of four or more separately deposited elemental layers and is repeated until a total thickness between 400 and 600 Å is reached. This layer by layer deposition process enables $[(SnSe)_{1.15}]_m(TaSe_2)_n$ compounds to be prepared by depositing a Sn-Se bilayer *m* times and a Ta-Se bilayer *n*

times, using the parameters calibrated for the $[(SnSe)_{1.15}]_1(TaSe_2)_1$ precursor. Electron probe micro-analysis (EPMA) on a Cameca SX-50 was used to determine elemental compositions through a thin-layer technique described previously.[16] The composition analysis was used to dictate the adjustments of deposition parameters during the precursor calibration period. The amorphous as-deposited precursors require annealing under a nitrogen atmosphere (0.3 ppm O_2) to promote self-assembly of the modulated elemental reactants into the ferecrystal structure. For the $[(SnSe)_{1.15}]_m(TaSe_2)_n$ ferecrystals prepared here, 400 °C and 30 min were determined to be optimal annealing conditions as determined by X-ray diffraction data.

High resolution X-ray reflection (XRR) and X-ray diffraction (XRD) analysis was performed on a Bruker D8 Discover diffractometer equipped with Cu K_α radiation and Göbel mirror optics. Locked θ-2θ scan geometry was used to acquire low angle, 0−10 °2θ, and high angle, 10−65 °2θ, diffraction patterns for determination of total film thickness, repeating elemental sequence thickness, and ferecrystal formation. Synchrotron X-ray diffraction data were acquired from the Advanced Photon Source (APS), Argonne National Laboratory (beamline 33BM). The high flux X-ray source was used to determine the *ab*-plane lattice parameters.

High-resolution scanning transmission electron microscopy (HRSTEM) was performed on a FEI Titan 80−300 TEM/STEM equipped with a high angle annular dark field (HAADF) detector. HR-STEM samples were prepared at the Humboldt-Universität zu Berlin by a conventional dimple grinding and ion-milling technique and imaged at the Center for Advance Materials Characterization in Oregon (CAMCOR) of the University of Oregon (UO).

Electrical measurement specimens were deposited onto polished, electrically insulating quartz slides, to minimize any influence of the substrate on the measurement. Using a contact mask, the specimens were deposited in the shape of a 1 cm by 1 cm cross. The van der Pauw technique was used to measure sheet resistance of the thin-film by creating contacts with indium to each arm of the cross. Temperature dependent measurements were made by cooling the sample with a cryogenic cold head between room temperature and 20 K while under a vacuum of approximately 5×10^{-6} Torr. Data were collected both while cooling and warming the sample.

IV.3. Results and Discussion

Our approach to the synthesis of $[(SnSe)_{1+y}]_m(TaSe_2)_n$ family members requires a modulated precursor with designed elemental layer sequence and thicknesses that promote the self-assembly of the desired ferecrystalline product. To make a specific $[(SnSe)_{1+y}]_m(TaSe_2)_n$ compound, we deposit m bilayers of Sn + Se and n bilayers of Ta + Se. Three calibration steps are required to determine the composition and thickness of these elemental bilayers in the precursor that will anneal into structural units of SnSe (a bilayer) and $TaSe_2$ (a Se-Ta-Se trilayer sandwich). The first calibration step is to determine deposition parameters that create a stoichiometric composition for each of the binary constituents, SnSe and $TaSe_2$, by capitalizing on the systematic trend between the ratio of deposition times and composition. Samples were made holding the thickness of Se constant while systematically increasing the Sn or Ta thickness, creating two series of samples spanning the desired composition ranges. The proper ratios of deposition times for a stoichiometric sample of SnSe and $TaSe_2$ were found through interpolation of the

linear trend in composition (determined by EPMA) with Sn or Ta deposition times. To compensate for the expected loss of Se through evaporation during annealing a slight excess of Se (3−6 atomic%) was used and subsequently adjusted based on EPMA compositional analysis of pre- and post-annealed specimens.

The second calibration step determines the deposition parameters required to prepare a precursor with a Sn:Ta composition ratio that corresponds to the misfit of the desired 1:1 compound $[(SnSe)_{1+y}]_1(TaSe_2)_1$. Since this compound had not been previously reported, a y value of 0.16 was estimated from the structurally similar misfit layer compound $(SnSe)_{1.16}(NbSe_2)$.[3] A series of layered precursors was prepared by alternatively depositing elemental bilayers of Sn:Se and Ta:Se, using the calibrated deposition time ratios determined in step one. We varied the thickness of the Sn:Se bilayer while holding the layer thickness for Ta:Se constant. The ratio of Sn:Ta deposition times that yields a Sn/Ta composition ratio of 1.16 was determined by interpolation of the linear relationship between the Sn/Ta composition ratio and the thickness of the SnSe bilayer. (hk0) XRD studies of the resulting $[(SnSe)_{1+y}]_m(TaSe_2)_n$ compounds yielded y = 0.15 and the composition of the precursors was subsequently adjusted.

The third calibration step is to simultaneously scale the Sn:Se and Ta:Se thicknesses, while maintaining the calibrated composition ratios previously determined for Sn:Se, Ta:Se, and Sn/Ta, to determine the correct repeating sequence that yields a single unit cell of the targeted $[(SnSe)_{1.15}]_1(TaSe_2)_1$ ferecrystal. The deposited samples were annealed to self-assemble, and the resulting diffraction patterns were used to access the correct thickness. Figure III.9 contains the X-ray diffraction patterns of a series of

annealed precursors with varying thicknesses of their repeating elemental sequence, L_c. In each pattern, the position of the first diffraction peak is at the same angle, independent of the repeating elemental sequence thickness, suggesting that there is a specific, favored structure being formed by all of the samples. In the middle diffraction pattern, from a precursor L_c = 1.28(1) nm, all of the diffraction maxima can be indexed as consecutive (00*l*) Bragg reflections arising from a single unit cell of *c* = 1.238(1) nm with no visible secondary phases, suggesting that this is the correct precursor thickness L_c to prepare the $[(SnSe)_{1.15}]_1(TaSe_2)_1$ ferecrystal. The diffraction patterns with smaller or larger L_c contain extra diffraction features, suggesting that more complex intergrowths of the constituent structures have formed, which will be the topic of a subsequent paper. The reduction in thickness, L_c compared to *c*, during annealing is attributed to the more efficient arrangement of atoms in the product and evaporation of excess selenium. The *c*-lattice parameter for $[(SnSe)_{1.15}]_1(TaSe_2)_1$ is slightly larger than that found for the $(SnSe)_{1.16}(NbSe_2)$ misfit layer compound, *c* = 1.228 nm.[3]

To determine the optimal annealing temperature, diffraction data was collected as a function of annealing temperature for a precursor designed to produce $[(SnSe)_{1.15}]_1(TaSe_2)_1$. The number of (00*l*) reflections and their intensity increased on annealing, showing that the layered structure of the deposited precursor is conserved. Annealing at 400 °C for 30 min resulted in the sharpest Bragg maxima, suggesting this as the optimal annealing temperature. Annealing at higher temperatures resulted in the formation of a SnSe impurity phase, determined by XRD.

The deposition parameters obtained via the three step calibration procedure enabled us to prepare $[(SnSe)_{1.15}]_m(TaSe_2)_n$ compounds by preparing precursors with *m*

Sn:Se and *n* Ta:Se bilayers. The resulting diffraction patterns of the $[(SnSe)_{1.15}]_m(TaSe_2)_n$ ferecrystals formed on annealing are shown in Figure IV.2. The *c*-lattice parameters were calculated from the positions of the (00*l*) maxima for each ferecrystal and are summarized in Table IV.1. The *c*-lattice parameter increases by 0.579(1) nm per bilayer of SnSe and 0.649(1) nm per monolayer of $TaSe_2$. The increase per $TaSe_2$ monolayer is slightly larger than that found for bulk $TaSe_2$ polytypes, which range from a low of 0.6272 nm for the 1T to a high of 0.6392 nm for the 3R polytype.[17] The increase per SnSe bilayer agrees well with the 0.5785 nm expected from bulk orthorhombic SnSe but is smaller than the 0.599 nm found in the thin-film cubic phase.[18-20]

Table IV.1. In-plane *a*-lattice parameters of the SnSe (square) and $TaSe_2$ (hexagonal) constituents and *c*-lattice parameters for several $[(SnSe)_{1.15}]_m(TaSe_2)_n$ ferecrystals[a].

m	*n*	*c*-parameters $[(SnSe)_{1.15}]_m(TaSe_2)_n$	*a*-parameter SnSe	*a*-parameter $TaSe_2$
6	1	4.137(8)	0.604(3)	0346(3)
5	1	3.546(2)		
3	1	2.972(2)	0.603(2)	0.346(2)
2	1	1.818(2)		
1	1	1.238(1)	0.6015(8)	0.3456(4)
1	2	1.887(3)		
1	3	2.531(4)	0.605(9)	0.345(1)
1	5	3.182(4)		
1	6	4.481(4)	0.60(1)	0.345(3)

[a]Error in parentheses and units in nanometers (nm).

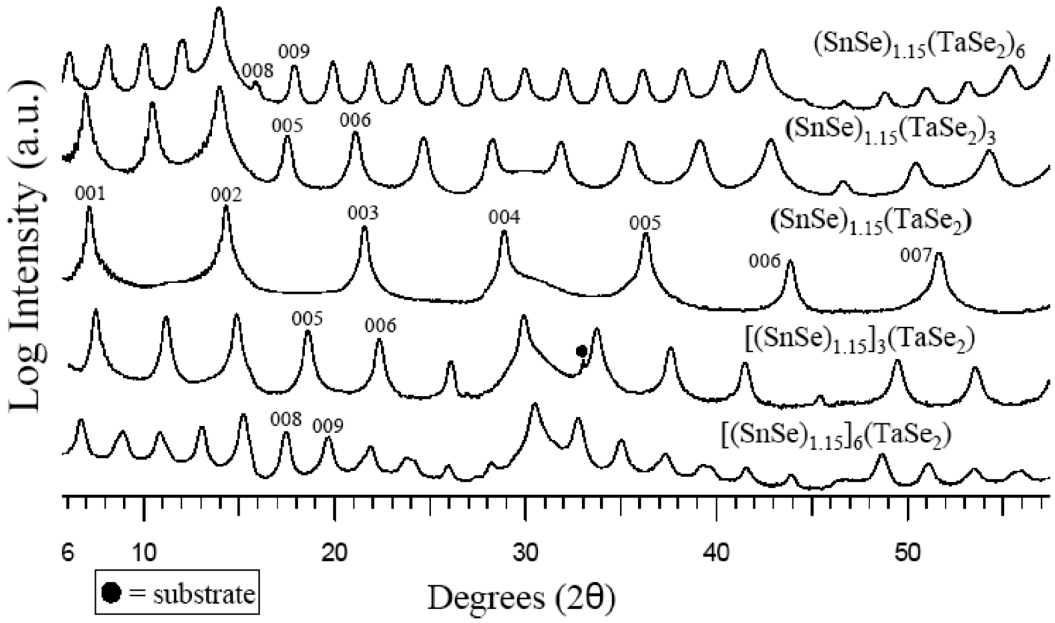

Figure IV.2. θ-2θ locked coupled X-ray diffraction patterns of several $[(SnSe)_{1.15}]_m(TaSe_2)_n$ ferecrystals, *m* and *n* indicated above each pattern.

The in-plane structural characteristics of several compounds were obtained from (*hk*0) X-ray diffraction patterns collected using grazing incidence scan geometry at the Advanced Photon Source (APS). A representative (*hk*0) diffraction pattern for $[(SnSe)_{1.15}]_1(TaSe_2)_1$ is shown in Figure II.4. All of the in-plane diffraction maxima can be indexed as (*hk*0) reflections of a square basal plane for SnSe or hexagonal $TaSe_2$. The resulting *a*-lattice parameters for several $[(SnSe)_{1.15}]_m(TaSe_2)_n$ specimens are summarized in Table IV.1. For the $[(SnSe)_{1.15}]_1(TaSe_2)_1$ ferecrystal, the $TaSe_2$ *a*-lattice parameter, 0.3456(4) nm, is within a range of literature values for different $TaSe_2$ polytypes (0.34348−0.34769 nm) with the 6R, $a = 0.34558$ nm, being the closest match.[17] The 0.6015(8) nm *a*-lattice parameter of SnSe agrees with that expected from a thin-film cubic SnSe phase (0.599 nm).[18-20] The full width at half-maximum of the SnSe (220)

reflection of $[(SnSe)_{1.15}]_6(TaSe_2)_1$ is slightly larger (0.889 °2θ) than that measured for $[(SnSe)_{1.15}]_1(TaSe_2)_1$ (0.857 °2θ), which might result from the beginning of peak splitting because of a square-to-rectangular transition as *m* is increased.

A representative cross-sectional HR-STEM-HAADF image is shown in Figure IV.3 for a $[(SnSe)_{1.15}]_1(TaSe_2)_1$ specimen. The entire image displays continuous parallel layering of SnSe bilayers and $TaSe_2$ monolayers, as inferred from the presence of intense (00*l*) X-ray diffraction maxima from the $[(SnSe)_{1.15}]_m(TaSe_2)_n$ specimens. The average position of each atomic plane was estimated through a gray value profile of the entire image; calculating a *c*-lattice parameter of 1.2(1) nm, in agreement with earlier calculations from (00*l*) Bragg maxima. The presence of turbostratic disorder is clearly seen in the image by the randomization of zone axes when translating both parallel and perpendicular to the *c*-axis. This turbostratic disorder is supported by the lack of (*hkl*) reflections with $h,k \neq 0$ and $l \neq 0$ and peak streaking along the *c*-axis in X-ray diffraction area detector scans gathered at the APS. In the boxed section, expanded on the right-hand side of Figure IV.3, ball-and-stick models of a (110) zone axis of orthorhombic SnSe next to a (10.0) zone axis of $TaSe_2$ are overlaid.[17,20] The resolution of the HRSTEM-HAADF cross-sectional image is not sufficient to distinguish the local symmetry of the SnSe constituent. The (10.0) $TaSe_2$ projection contains the symmetrical chevron pattern characteristic of a trigonal prismatic coordinated Ta center.[17]

The $[(SnSe)_{1.15}]_m(TaSe_2)_n$ intergrowth compounds have a consistent trend in structural properties. XRD and STEM studies confirm that they are all layered intergrowths with a defined periodicity along their *c*-axis. The modulated elemental reactants synthetic method results in a preferred orientation of the intergrowths with their

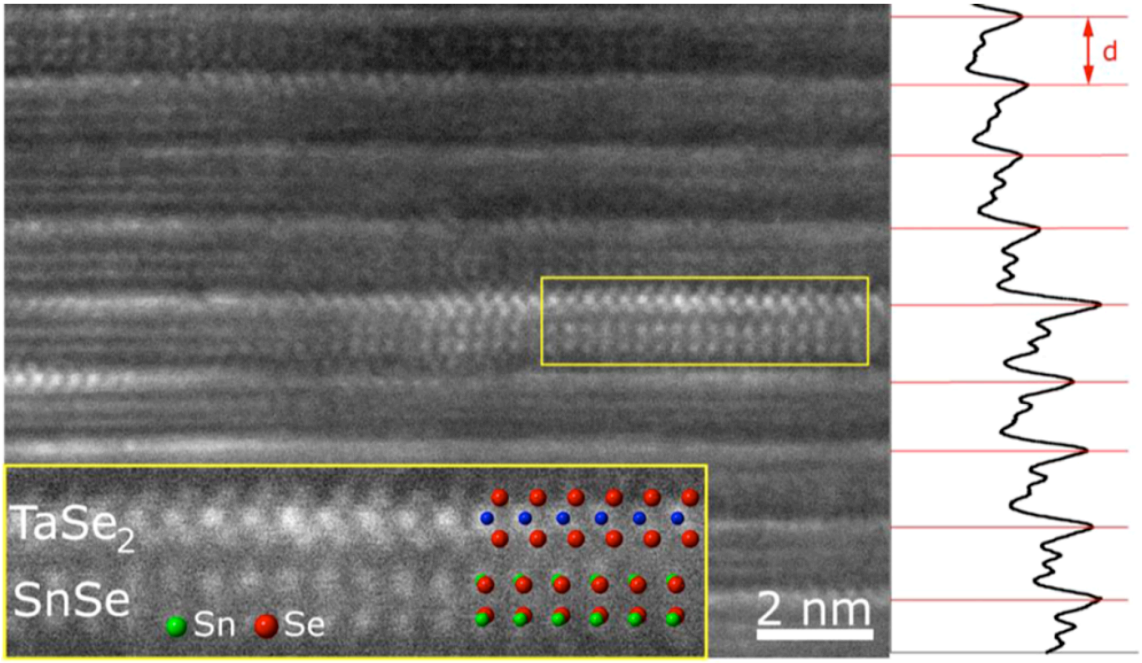

Figure IV.3. Cross-sectional HR-STEM-HAADF image of a $[(SnSe)_{1.15}]_1(TaSe_2)_1$ specimen. The expanded region clearly shows crystal orientations of (110) α-SnSe and (10.0) 2H-$TaSe_2$.

ab-plane parallel to the substrate. The SnSe and $TaSe_2$ layers are crystallographically independent with a consistent thickness along the *c*-axis for each constituent. STEM imaging is consistent with trigonal prismatic coordination of the Ta in $TaSe_2$. Turbostratic disorder is clearly present in both the STEM images and the XRD area diffraction data. The structural characterization confirms that specific $[(SnSe)_{1.15}]_m(TaSe_2)_n$ compounds were selectively synthesized and have the turbostratic disorder characteristic of ferecrystals.

The ability to prepare $[(SnSe)_{1.15}]_m(TaSe_2)_n$ with different *m* and *n* values provides an opportunity to probe for systematic variations in electrical transport properties as a function of the thickness of constituents and the density of interfaces. Figure IV.4 is the start of this systematic investigation, containing the temperature dependent in-plane

resistivity of three ferecrystals, $[(SnSe)_{1.15}]_1(TaSe_2)_1$, $[(SnSe)_{1.15}]_1(TaSe_2)_2$, and $[(SnSe)_{1.15}]_2(TaSe_2)_2$. The resistivity curves have metallic temperature dependences, with resistivity decreasing as temperature is decreased, until low temperatures where impurities and defects determine the mean free path of the charge carriers. The magnitude of the resistivity of our ferecrystalline compounds (3−9 μΩm, between 20 and 280 K), is within the range (0.1−10 μΩm, between 4 and 300 K) of literature reports on MLCs containing TaX_2 or NbX_2 constituents (X = S, Se).[1] The change in resistivity with temperature for the samples studied here, ρ280K/ρ20K = 1.4−1.5 for $[(SnSe)_{1.15}]_m(TaSe_2)_n$, is smaller than prior reports for MLCs containing TaX_2 or NbX_2, ρ300K/ρ4K = 16.0−2.0 for MLCs containing Sn, Pb, and Bi in their MX constituent and ρ300K/ρ4K = 5.0−1.9 for MLCs containing rare-earth elements.[1] The spread in the temperature dependence of resistivity in MLCs has been rationalized as variations in scattering from the incommensurate interfaces between constituents, with lower scattering from PbX, SnX, and BiX containing MLCs and higher scattering from rare-earth containing MLCs. This significant scattering of carriers from the incommensurate structure is thought to raise the low-temperature residual resistivity, which decreases the importance of temperature dependent phonon scattering.[1] The data in Figure IV.4 is consistent with this explanation, as the ferecrystalline structure presents a more disordered interface between constituents, further decreasing the importance of temperature dependent scattering mechanisms.

The ability to independently change *m* and *n* allows us to test the prior rigid band models for electrical conduction in MLCs, where transport through the TX_2 constituent is thought to be the dominant conductor, and also to explore the effect of incoherent

interfaces between constituents on mobility. In the simplest model, the conductivity of a $[(MX)_{1+y}]_m(TX_2)_n$ compound can be described by an equivalent circuit of parallel resistors with different resistivity values for each constituent, that is, $1/R_{total} = 1/R'_{MX} + 1/R'_{TX2}$ leading to $1/R_{total} = (m/R_{MX} + n/R_{TX2})(m + n)^{-1}$ where R_{MX} and R_{TX2} are the resistances of a single structural unit of a constituent. Assuming that $R_{MX} >> R_{TX2}$, then $1/R_{total} \approx (n/R_{TX2})(m + n)^{-1}$ or $R_{total} \approx (R_{TX2}(m + n))/n$. For different ratios of m:n in $[(MX)_{1+y}]_m(TX_2)_n$ compounds, the simple parallel resistor model predicts that 1:1 and 2:2 compounds will have the same resistivity and that the ratio of resistivity values for 1:1 and 1:2 compounds would be 1:1/1:1 = 1 and 1:2/1:1 = 3/4 as summarized in Table IV.2. $(PbS)_{1.14}(NbS_2)_1$ and $(PbS)_{1.14}(NbS_2)_2$ MLCs were previously prepared, and single resistivity values at 300 K were 3.2 μΩm and 2.0 μΩm for n = 1 and 2, respectively.[1] The ratio of ρ1:2/ρ1:1 is 0.63, suggesting that the conductivity of a $(NbS_2)_2$ unit is greater than two NbS_2 units reflecting the greater number of incoherent interfaces in the 1:1 compound relative to the 1:2 compound. Table IV.2 contains the resistivity ratios for the $[(SnSe)_{1.15}]_m(TaSe_2)_n$ compounds measured as part of this study. Within this model, the measured ratios suggest that the conductivity of a $(TX_2)_2$ unit is significantly larger than two TX_2 units perhaps because of the difference between commensurate and incommensurate interfaces on scattering as the 1:1 compound has a larger number of incoherent interfaces relative to the 1:2 and 2:2 compounds. Interestingly, the simple model correctly predicts the resistivity ratio between the 1:2 and 2:2 compounds, suggesting that the conductivity is primarily through the $(TaSe_2)_2$ unit and is similar in both compounds. The conductivity values measured for these $[(SnSe)_{1.15}]_m(TaSe_2)_n$ compounds supports the prior conclusions that the majority of conduction occurs through

the TX_2 structural unit and that incoherent interfaces increase scattering of carriers. This simple analysis suggests that it may be possible to quantify an interfacial scattering term by expanding this investigation to larger *m* and *n* compounds.

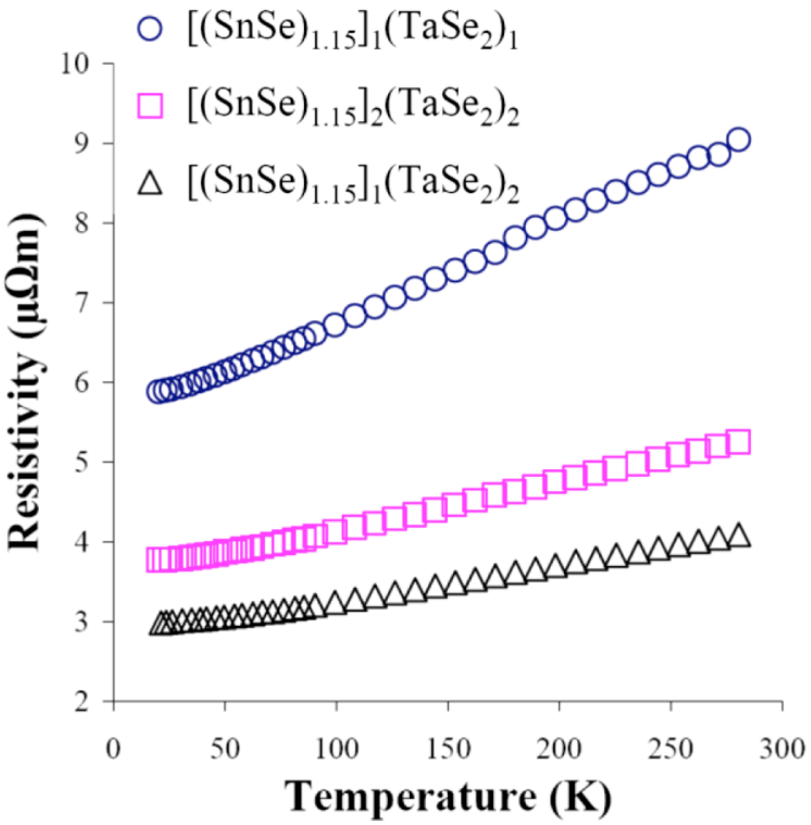

Figure IV.4. In-plane electrical resistivity of $[(SnSe)_{1.15}]_m(TaSe_2)_n$ ferecrystals.

Table IV.2. Summary of resistivity ratios for $[(SnSe)_{1.15}]_m(TaSe_2)_n$ ferecrystals

Ferecrystal $[(SnSe)_{1.15}]_m(TaSe_2)_n$	expected resistivity ratio ($R_{m:n}/R_{1:1}$)	measured resistivity ratio ($R_{m:n}/R_{1:1}$) 280 K	measured resistivity ratio ($R_{m:n}/R_{1:1}$) 20 K	expected resistivity ratio ($R_{m:n}/R_{2:2}$)	measured resistivity ratio ($R_{m:n}/R_{2:2}$) 280 K	measured resistivity ratio ($R_{m:n}/R_{2:2}$) 20 K
$[(SnSe)_{1.15}]_1(TaSe_2)_1$	1	1	1	1	1.72	1.56
$[(SnSe)_{1.15}]_1(TaSe_2)_2$	3/4	0.45	0.51	3/4	0.78	0.79
$[(SnSe)_{1.15}]_2(TaSe_2)_2$	1	0.58	0.64	1	1	1

IV.4. Bridge

The enhancement of the modulated elemental reactant synthetic technique described in Chapter III and IV successfully produced $[(SnSe)_{1.15}]_m(TaSe_2)_n$ intergrowth compounds with *m* and *n* independently equal to 1−6. The intergrowths have highly oriented, regular stacking along their *c*-axis, are crystalline in their *ab*-plane, and contain structural traits characteristic of ferecrystals. After completing the calibration of $[(SnSe)_{1.15}]_m(TaSe_2)_n$ ferecrystals, the transition metal was exchanged for V and the calibration process repeated so that $[(SnSe)_{1.15}]_m(VSe_2)_n$ ferecrystals could be synthesized (Chapter V).

CHAPTER V

SYNTHESIS, STRUCTURE, AND ELECTRICAL PROPERTIES OF A NEW TIN VANADIUM SELENIDE

This work was published in volume 202 of the Journal of Solid State Chemistry in 2013 with co-authors Sabrina Disch, Zachary Jones, Ines Haeusler, Corinna Grosse, Saskia F. Fischer, Wolfgang Neumann, Paul Zschack and David C. Johnson. Sabrina Disch and Zachary Jones worked with the Rietveld Refinement, Ines Haeusler and Wolfgang Neumann provided analysis of the electron diffraction, Corinna Grosse and her advisor Saskia F. Fischer performed electrical measurements, Paul Zschack assisted in X-ray diffraction analysis at the Advanced Photon Source, David C. Johnson is my advisor and research group leader, and I am the primary author.

V.1. Introduction

Low dimensional solids are an active area of materials research in part because their properties are more complicated than predicted by simple band theory that considers only weakly interacting electrons. A charge density wave (CDW), a periodic modulation of a material's conduction electron density, is one example of a temperature-dependent transition that occurs as electrons interact with one another, mediated by phonons and the underlying crystal lattice or by electron-electron interactions.[1] CDW transitions are more prevalent in two-dimensional layered structures, such as transition metal dichalcogenides, and have been extensively investigated as a function of alloying,[2] stoichiometry,[3]

inorganic and organic intercalation,[4,5] and poly- type.[6] The dependence of charge density waves on these parameters reflects the importance of both electrons and phonons in determining the CDW transition's onset temperature, number of electrons localized, and structure of both the commensurate and incommensurate states.

Layered compounds containing two or more intergrown structures are surprisingly common, occurring naturally in minerals and in synthetic products.[7,8] The misfit layer compounds (MLCs) containing an intergrowth of a distorted rock-salt type structured constituent (MX) and hexagonal structured, transition metal dichalcogenide constituent (TX_2) are perhaps the largest subset of synthetically prepared intergrowth compounds. MLCs have the general formula $[(MX)_{1+y}]_m(TX_2)_n$; where M = Sn, Pb, Sb, Bi, and rare earth metals; T = Ti, V, Cr, Nb, and Ta; X = S and Se; *y* is the misfit parameter reflecting the different densities of cations in the *ab*-planes of the constituents; and *m* and *n* are integers describing the number of MX bilayers and X–T–X trilayers in the unit cell.[9-22] The incommensurate structural relationship between the constituents and the large number of elements that can be incorporated into this family of compounds results in a wide range of physical properties; including intercalation reactions,[23] superconductivity,[19,20] unusual two-dimensional magnetic phenomena,[4,11] and promising thermoelectric properties.[22]

Several transition metal dichalcogenides with known CDW transitions, such as VSe_2, $TaSe_2$, and TaS_2, have been incorporated as the TX_2 constituent in $(MX)_{1+y}(TX_2)$ compounds, however, a CDW transition has not yet been found in any of these misfit layer compounds. Wiegers suggested that the irregular potential created by the periodic interlayer bonding of the two constituents in MLCs frustrates the formation of a charge

density wave superlattice transition.[4] Recently we reported using modulated elemental reactant (MER) precursors to prepare many new, metastable $[(MSe)_{1+y}]_m(TSe_2)_n$ intergrowth compounds; M = Pb, Bi, Ce, and Sn; T = W, Mo, Nb, Ta, and Ti; where the misfit parameter y varies between −0.1 and 0.16.[24-31] These compounds differ from MLCs by the constituents having independent crystallographic *ab*-plane structures and having rotational disorder between the constituent layers; also known as turbostratic disorder. We have referred to this very large class of $[(MX)_{1+y}]_m(TX_2)_n$ compounds as ferecrystals,[28] from the Latin "*fere*" meaning almost, and have found unique properties that result from the layer to layer rotational disorder, such as ultra-low thermal conductivity.[25] This turbostratic disorder might preserve the conditions necessary for a charge density wave transition by eliminating the long range periodic potential created in MLCs through epitaxial interlayer bonding and consequent periodic distortion of the two constituent structures. To explore this possibility, we chose VSe_2 as the transition metal dichalcogenide structured constituent because a CDW is observed over a wide range of $V_{1+x}Se_2$ compositions, and the transition onset temperature has been shown to vary with the extent of filled interstitial vanadium vacancies.[3,32–34]

Herein, we report the synthesis of $(SnSe)_{1.15}(VSe_2)$ using the MER technique, and characterize its structure and electrical properties. Rietveld refinement of (00*l*) diffraction data depicted planes of atoms, corresponding to the two constituent layers, separated along the *c*-axis with a *c*-lattice parameter in agreement to that reported for the analogous misfit layer compound, $SnVSe_3$.[35] Analysis of the (*hk*0) diffraction data yielded independent *ab*-plane lattice parameters for the two constituents; consistent with the proposed $(MX)_{1+y}(TX_2)$ intergrowth structure. Diffraction scans for (*hkl*) ($h,k \neq 0$; $l \neq 0$)

indicate the presence of very short coherence lengths along the *c*-axis and transmission electron microscope (TEM) imaging shows both the independent crystalline layers of the two constituents and turbostratic disorder between them. Temperature-dependent transport measurements revealed a reversible anomaly existing between approximately 50 and 100 K. An upturn in resistivity with decreasing temperature correlates with a drop in carrier concentration. These transport properties are consistent with either a CDW or a SDW transition. To our knowledge this is the first report of a possible CDW or SDW transition in a $[(MX)_{1+y}]_m(TX_2)_n$ intergrowth compound.

V.2. Experimental Details

The samples used in this study were formed through physical vapor deposition using a custom built high-vacuum deposition system,[36] evacuated to a base pressure of $1x10^{-7}$ mbar. Sources were purchased from Alfa Aesar®. Selenium (99.999% purity) was evaporated using a custom-built resistive heated effusion cell. Tin (99.98% purity) and vanadium (99.7% purity) were deposited using a Thermionics™ 3 kW electron beam gun. The films were deposited on (100) oriented silicon substrates positioned approximately 25 cm above the sources on a motorized carousel. Pneumatic powered shutters, located between each source and substrate, were used to control deposition times of each element onto the substrate. A custom LabVIEW program controls the positioning of substrates, the opening and closing of shutters, and the order of deposited layers. A quartz microbalance crystal monitoring system is used to control deposition rates. Se, Sn, and V were each deposited at approximately 0.4 Å/s. The deposition of $(SnSe)_{1.15}(VSe_2)$ specimens was done via a layer-by-layer process, constructing samples by repeatedly

depositing a four element sequence of Se–Sn–Se–V. The film total thickness is determined by the number of $(SnSe)_{1.15}(VSe_2)$ repeating units deposited and typically we targeted total film thicknesses near 50 nm. Calibration of the deposition parameters is necessary to determine the amount of each element required for a Se–Sn–Se–V unit to self-assemble into a single $(SnSe)_{1.15}(VSe_2)$ unit cell after annealing.[27,31] Composition of the films was analyzed by electron probe microanalysis (EPMA) using a thin-film technique described elsewhere.[37] Precursors were annealed under a nitrogen atmosphere (less than 1 ppm O_2). Optimal annealing conditions for $(SnSe)_{1.15}(VSe_2)$ were found to be 400ºC for 20 min. X-ray reflection (XRR) and X-ray diffraction (XRD) data were obtained on a Bruker D8 Discover diffractometer, using Cu Kα radiation and Göbel mirror optics. θ-2θ locked coupled scan geometry was used to acquire XRR scans between 0-10 º2θ and XRD scans between 10-65 º2θ of the precursors and annealed samples. High-resolution synchrotron X-ray diffraction data were acquired on beamline 33-BM of the Advanced Photon Source (APS), Argonne National Laboratory. A point detector was used for acquisition of diffraction scans in (00*l*) direction (specular diffraction) as well as (*hk*0) direction (in-plane diffraction) of the scattering wave vector *Q*, using an X-ray energy of 12.501 keV. The General Structure Analysis System (GSAS) was used to refine the (00*l*) reflections. An image plate detector (mar345) was used for collection of (*hkl*) reflection data.

High-resolution transmission electron microscopy (HR-TEM) and selected area electron diffraction (SAED) was obtained on an objective lens c_s-corrected FEI Titan 80-300 kV TEM, equipped with a high angle annular darkfield (HAADF) detector. HR-TEM samples were prepared at the Center for Advanced Materials Characterization in Oregon

(CAMCOR) of the University of Oregon (UO) on a FEI Helios Nanolab D600 Dual Beam focused ion beam (FIB) by an in-situ lift-out and thinning method, followed by low voltage ion beam polishing.

Electrical measurements were conducted both at the University of Oregon and Humboldt-Universität zu Berlin. For both measurements a contact mask was used to deposit the film in the shape of a cross or a four leaf clover. Forming contacts with indium, the van der Pauw technique was used to measure the sheet resistance and resistivity was calculated using film thickness determined from XRR data. Measurements at the University of Oregon used a 1 cm by 1 cm cross, deposited on a quartz substrate, and analyzed under vacuum between room temperature and 20 K on a lab built, labview controlled closed cycle helium transport measurement system. Measurements at Humboldt-Universität zu Berlin used a 0.5 cm by 0.5 cm four leaf clover, deposited on a silicon substrate topped with an electrically insulating thermally grown SiO_2 layer, and analyzed between room temperature and 1.4 K on a helium cryostat system. Bragg-Brentano XRD measurements were taken on films deposited on all substrates to confirm that the samples all formed the same compound with similar degrees of crystallographic alignment, as confirmed by the matching (00*l*) diffraction patterns.

V.3. Results and Discussion

Successfully synthesizing intergrowth compounds using the modulated elemental reactant (MER) approach requires precursors that mimic the composition and layering sequence of the desired $(MX)_{1+y}(TX_2)$ compound (Figure V.1).[31] Briefly, deposition parameters required to deposit layers of Sn:Se and V:Se with compositions of 1:1 and

1:2, respectively are determined via a sequence of calibration samples and EPMA measurements. A second set of calibration samples containing sequential Sn:Se and V:Se layers with varying relative thicknesses of the two binary constituent is then deposited. EPMA measurements of the composition of these samples allows us to interpolate the ratio of thicknesses required to make the ratio of Sn/V equal to the targeted composition. Since the misfit between the two constituents was not known, we estimated the ratio of the two metals would be 1.16 based on the structurally similar MLC compound $(SnSe)_{1.16}(NbSe_2)$.[10] Subsequent determination of in-plane lattice parameters yield a value of 1.15 for the $(SnSe)_{1.15}(VSe_2)$ misfit parameter. Finally, we varied the total thickness of the repeating four element sequence of Se-Sn-Se-V by scaling all of the deposition parameters determined in the first two calibration steps to determine the absolute amount of material required so each four element sequence of Se-Sn-Se-V self-assembled on annealing into a single structural unit of $(SnSe)_{1.15}(VSe_2)$ containing a SnSe bilayer and a trilayer Se-V-Se. The diffraction patterns of the annealed samples were used to determine the optimal thickness for the Se-Sn-Se-V sequence.[31]

The diffraction pattern of a representative precursor was examined as a function of annealing temperature and time (Figure V.2) to determine if the desired product formed and optimum annealing conditions to self-assemble the precursor into the target $(SnSe)_{1.15}(VSe_2)$ compound. Examining the as-deposited precursor films by XRR and XRD we found that the modulated SnSe and VSe_2 layers produce intense (00*l*) reflections below 20 º2θ, reflecting the expected periodic structure of elemental layers. When precursors are annealed at temperatures up to 400 ºC, the (00*l*) reflections sharpen, grow in intensity, and additional (00*l*) diffraction maxima grow in at higher angles. This reflects

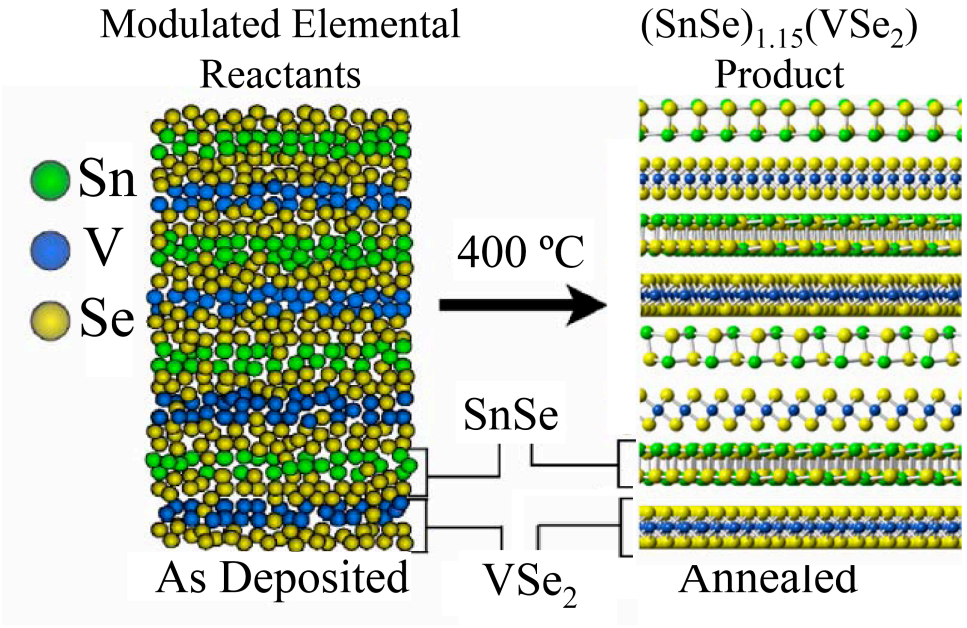

Figure V.1. A schematic of the self-assembly process by which an amorphous modulated Se-V-Se-Sn layer sequence (left) self-assembles into $(SnSe)_{1.15}(VSe_2)$ (right) on annealing at 400 ºC.

the self-assembly of the precursor into crystallized intergrowths containing planes of atoms separated by specific and regular distances parallel to the substrate. All the visible peaks in the XRD can be indexed as (00*l*) reflections yielding a single *c*-lattice parameter with no secondary phases, suggesting that the originally estimated misfit parameter is close to the actual value of the target compound. At temperatures above 400 ºC the intergrowth structure is degraded and impurity phases appear in the diffraction patterns, suggesting that $(SnSe)_{1.15}(VSe_2)$ is not thermodynamically stable at higher temperatures. The annealing data indicate that 400 ºC for 20 min are the optimal annealing conditions for $(SnSe)_{1.15}(VSe_2)$.

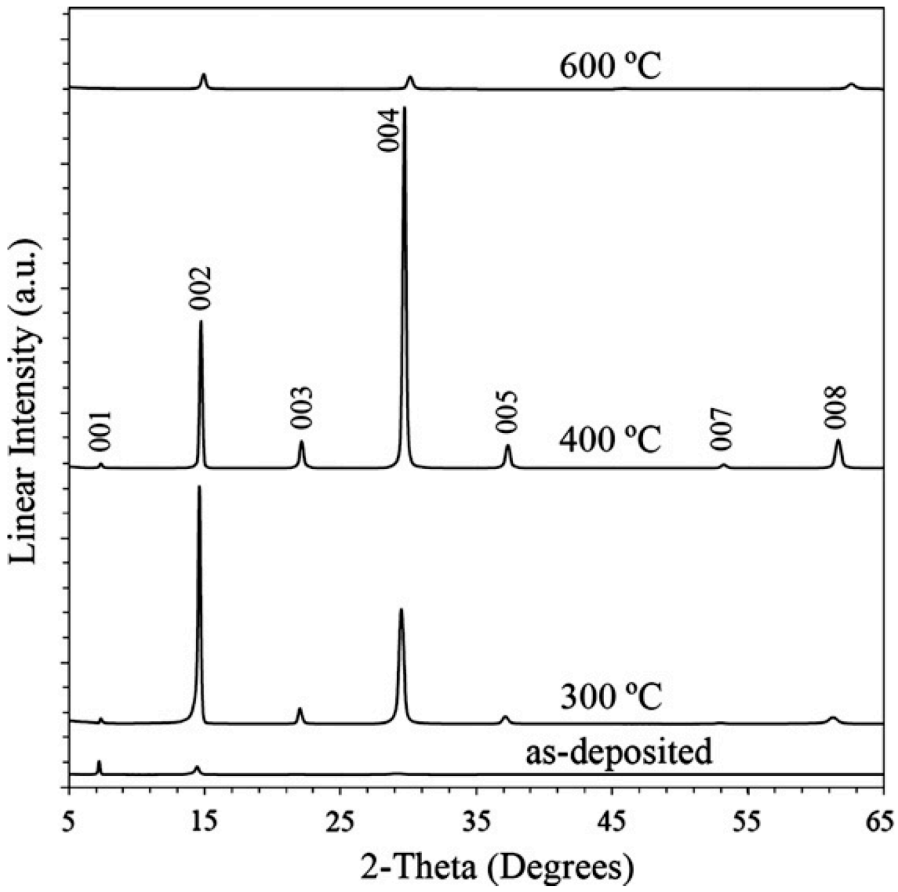

Figure V.2. X-ray diffraction patterns (θ-2θ locked-coupled scan geometry) of a $(SnSe)_{1.15}(VSe_2)$ precursor annealed at several temperatures for 20min.The (00*l*) reflections are indexed for the 400 ºC scan.

Using the calibrated deposition parameters, we created six precursors whose composition and thicknesses bracketed the values expected for the targeted composition. XRD and XRR patterns were collected before and after annealing. Indexing the (00*l*) reflections, we calculated the repeat thicknesses of the precursors and the *c*-lattice parameters of the resulting intergrowth products and show these values along with composition data in Table V.1. While the precursors vary in thickness for their as-deposited repeating units and have correspondingly different compositions, after annealing all samples have the same *c*-lattice parameter, within the error of the

measurement, suggesting a single intergrowth compound is being formed. Variation in the *c*-lattice parameter might be expected to result from variations in composition, which would produce different defect distributions. The Sn/V and Se/V ratios are all smaller than expected, presumably due to the oxygen found in the films after annealing in a 0.5 ppm oxygen containing inert atmosphere. We assume the oxygen reacts with V to form an impurity oxide phase not visible in the X-ray diffraction data, reducing the amount of V available to react with Se. The average *c*-lattice parameter of the six annealed samples is slightly smaller than that reported previously for the *c*-lattice parameter of the misfit layer compound $SnVSe_3$ (1.210 nm).[35]

Table V.1. The repeat thicknesses of as-deposited precursors, *c*-lattice parameters of annealed samples, and the composition ratios determined using electron probe microanalysis (EPMA) of the annealed samples are summarized.

Sample	As—deposited repeat thickness (nm)	Annealed *c*-axis lattice parameter (nm)	Sn/V	Se/V	O/V
Ideal			1.15	3.15	0
a	1.265(2)	1.2028(9)	1.15(4)	2.9(1)	0.35(5)
b	1.271(2)	1.2030(7)	1.08(4)	2.94(7)	0.25(4)
c	1.230(3)	1.2030(9)	1.05(5)	2.84(8)	0.72(7)
d	1.233(1)	1.2027(7)	1.03(4)	2.78(7)	0.33(3)
e	1.251(2)	1.2032(7)	1.07(5)	2.88(9)	0.33(4)
f	1.251(8)	1.2031(6)	1.07(4)	2.90(8)	0.26(3)

Further structural information regarding the individual SnSe and VSe_2 layers was obtained from in-plane X-ray diffraction data (Figure V.3). All of the peaks in the in-plane diffraction data can be indexed as (*hk*0) reflections from two separate crystal systems, a square SnSe or a hexagonal VSe_2. For the SnSe constituent, our square in-

plane *a*-lattice parameter of 0.5935(4) nm is consistent with that reported for the $(SnSe)_{1.16}(NbSe_2)$ misfit layer compound[10] and is also comparable to the 0.600 nm reported for a SnSe thin-film cubic phase.[38] For the VSe_2 constituent, our *a*-lattice parameter of 0.3414(3) nm is in good agreement with the bulk *a*-lattice parameter of $V_{1+x}Se_2$, which increases from 0.334(8) to 0.3556(1) nm as more interstitial V-vacancies are filled.[3,32-34] While there is no *a*-lattice parameter reported for $SnVSe_3$,[35] for the MLC $(La_{.95}Se)_{1.21}(VSe_2)$ a larger *a*-lattice parameter of 0.3576(3) nm was found for the VSe_2 constituent, perhaps as a result of greater charge donation from LaSe to the VSe_2

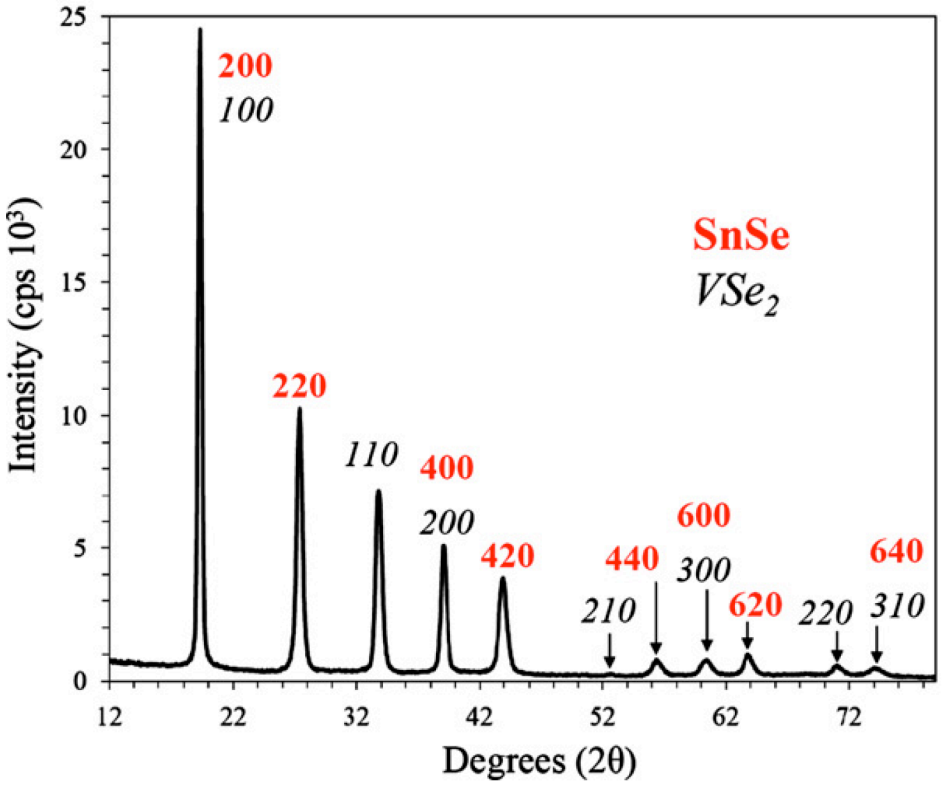

Figure V.3. In-plane grazing incidence X-ray diffraction data of a representative $(SnSe)_{1.15}(VSe_2)$ sample. Reflections are indexed as (*hk*0) reflections of a square in plane structured SnSe, (red), and (*hk*0) reflections of a hexagonal in-plane structured VSe_2, (black). Incident X-ray wavelength was 0.0992nm.

constituent.[21] From our *a*-lattice parameters we calculated a misfit parameter of 1.15 between SnSe and VSe_2, close to our original estimate used to calibrate the precursors. The misfit of $(SnSe)_{1.15}(VSe_2)$ lies within the range of literature reports for other MLCs which range from 1.07 to 1.28.[9-22]

Cross-sectional HR-TEM was performed on a representative $(SnSe)_{1.15}(VSe_2)$ specimen to examine the structure and quality of the intergrowth layering. Figure V.4 clearly reveals the parallel layering of two separate constituents with no layering defects or substitutions, as is expected for a $(SnSe)_{1.15}(VSe_2)$ intergrowth compound and is in agreement with the sharp (00*l*) reflections seen in the XRD data. The consistent repeating layer sequence consists of interleaved SnSe bilayers and Se–V–Se trilayers. The V layer in the expected Se-V-Se trilayer is not observed due to the weaker scattering resulting from its smaller atomic number. The thickness of the repeating sequence was measured as 1.2(1) nm, in agreement with the *c*-lattice parameter calculated from XRD. Throughout the image, both along and across the layers, there is no uniform crystal orientation of either constituent, suggesting that a rotational disorder, referred to as turbostratic disorder, is present in the sample. These structural features, layered structures with in-plane crystallinity, chemically and structurally abrupt interfaces, layer-to-layer misregistration, and turbostratic disorder, are consistent with $(SnSe)_{1.15}(VSe_2)$ being a ferecrystal.

To further access the extent of 3D crystallinity in the $(SnSe)_{1.15}(VSe_2)$ compound, additional diffraction studies were performed using X-rays and electrons; representative images are shown in Figure II.7. The X-ray diffraction image was obtained through a grazing incidence geometry and the electron diffraction was gathered while examining

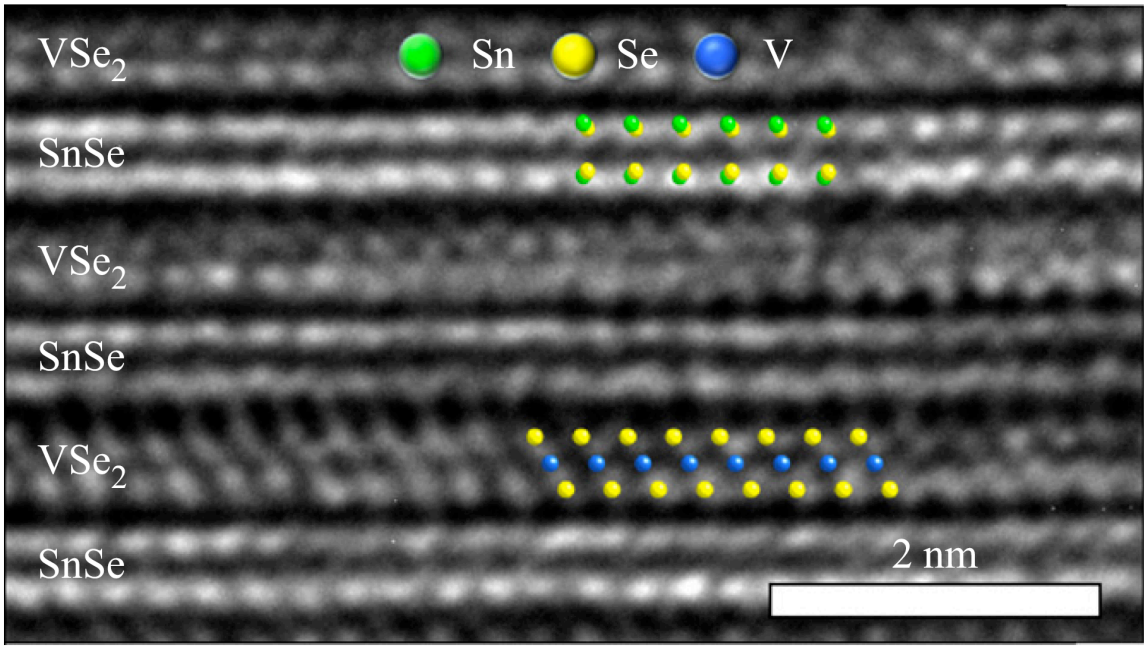

Figure V.4. Cross-sectional transmission electron microscope image of a representative area of a $(SnSe)_{1.15}(VSe_2)$ sample. Superimposed on the TEM image are the atom positions of the structures of the constituents. Due to the turbostratic disorder only small regions are orientated along a zone axis.

the cross-sectional HR-TEM. The positions of the (*hkl*) reflections in both images agree with those calculated from the aforementioned (*hk*0) diffraction data. In both images streaking in the (00*l*) direction is clearly visible for the (*hkl*) families of peaks. This results from extremely short coherence lengths, which is attributed to the random rotational disorder present between the SnSe and VSe_2 layers about the *c*-axis. The streaking of intensity along the *c*-axis and lack of supercell reflections are characteristic signs that the $(SnSe)_{1.15}(VSe_2)$ misfit layered compound has extensive turbostratic disorder.

High-resolution diffraction scans using 12.501 keV X-rays were collected on a representative $(SnSe)_{1.15}(VSe_2)$ specimen and the positions of atomic planes along the *c*-axis were refined from the intensities of the (00*l*) reflections. The Rietveld method was

used to determine the atomic plane positions based on a model where the relative atomic occupancies were fixed to the ideal misfit value, determined from the in-plane lattice parameters, to limit the number of refined parameters. The quality of the fit of the model is depicted in Figure V.5; additional refinement parameters are included in Table V.2 The refinements reveal that Sn and Se planes are separated by 19(3) pm, with the Se in each of the distorted (00*l*) planes of the rock-salt structure displaced further from the selenium of the dichalcogenide. This interfacial distortion or layer puckering is within the range (20–60 pm) previously reported.[9-22] The average interplanar distance between the distorted (00*l*) planes of the rock-salt bilayer was 0.276(3) nm, which is similar to the structure of $(SnSe)_{1.16}(NbSe_2)$.[10] The interplanar distance between the average position of

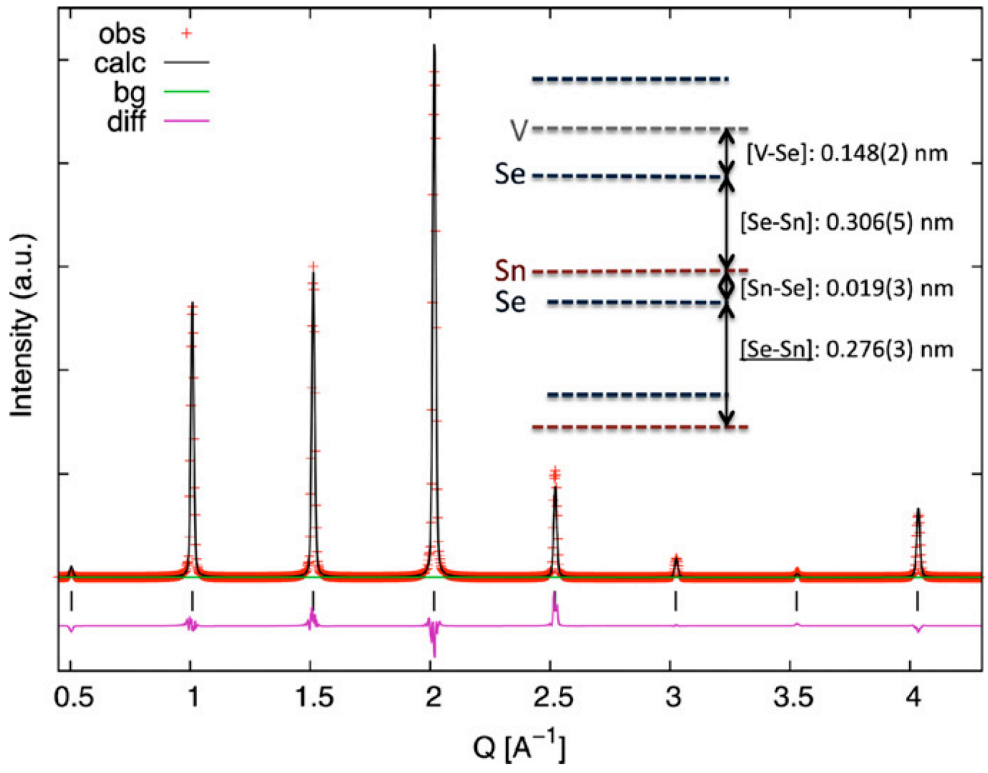

Figure V.5. Diffraction data and associated Rietveld refinement of a $(SnSe)_{1.15}(VSe_2)$ θ-2θ locked coupled X-ray diffraction scan, incident wavelength of 0.0992 nm. The observed, calculated, background, and difference patterns are represented. The inset is a line diagram indicating the distances between the refined atomic plane positions.

Table V.2. Results from Rietveld and LeBail refinements on $(SnSe)_{1.15}(VSe_2)$. The misfit parameter, 1.15, was calculated from in-plane parameters δ(*hk*0) and applied for δ(00*l*). Rietveld refinement of the (00*l*) XRD scan includes the *c*-lattice parameter of the $(SnSe)_{1.15}(VSe_2)$ intergrowth, *z*-positions for each atomic plane (*z*), site occupancies (occ.), and refinement residuals (Rp). Important inter-planer distances (*d*) derived from the refined atomic fractional coordinates are given below. *a*-lattice parameters for both constituents (SnSe and VSe_2) were obtained by a LeBail fit of the (*hk*0) XRD data.

Quantity		Refined Value
c-lattice parameter (00*l*) [nm]		1.2031(2)
V	z	0
	occ.	1
Se	z	0.123(2)
	occ.	1
Sn	z	0.377(3)
	occ.	0.573
Se	z	0.393(1)
	occ.	0.573
Uiso	($Å^2$)	0.058(1)
δ(00*l*)		0.146
Rp (12.501 KeV)		0.116
d (Sn-Se, puckering distortion) [nm]		0.019(3)
d (Sn-Se, bilayer separation) [nm]		0.296(3)
d (Sn-Se, interplanar) [nm]		0.306(5)
d (V-Se, dichalcogenide) [nm]		0.148(2)
a-lattice parameter (VSe_2) [nm]		0.3414(3)
a-lattice parameter (SnSe) [nm]		0.5934(4)
δ(*hk*0)		0.146(2)
Rp (12.501 KeV)		

the rock-salt and the Se plane of the dichalcogenide was found to be 0.306(5) nm. The interplanar distance between the V and Se planes in the dichalcogenide, 0.148(2) nm, is smaller than the 0.157 nm separation found in bulk VSe_2.[39] The refined model yielded a structure for $(SnSe)_{1.15}(VSe_2)$ which is consistent with prior studies of misfit layer compounds, despite the turbostratic disorder between constituents.

The lack of distinct (*hkl*) ($h,k \neq 0$; $l \neq 0$) reflections and the large amount of diffuse scattering from the turbostratic disorder prevents the determination of the three dimensional structure of the two constituent structures and the relationship between them. However, by assuming that the x and y atomic coordinates of both SnSe and VSe_2 are those found in their respective binary crystal structures and using both the in-plane lattice parameters and the *z* coordinates determined above, likely atomic distances within both the SnSe and VSe_2 constituents can be calculated. For the VSe_2 constituent, a V-Se bond distance of 0.246(2) nm is derived, comparable (0.2492 nm) to the bulk $V_{1.005}Se_2$ structure.[32] For the SnSe constituent, the in-plane Sn–Se atomic distance of 0.2974(3) nm deviates only slightly from one half of the *a*-lattice parameter (0.2968(2) nm) due to the 19(3) pm puckering distortion of the Se atoms. The Sn–Se atomic distance between atoms in each of the planes of the bilayer (0.276(3) nm) is considerably shorter than that found in the cubic thin-film form of SnSe,[38] which perhaps reflects the interlayer bonding between the SnSe and VSe_2 constituents.

Temperature-dependent resistivity was measured between room temperature and 20 K and below for two different $(SnSe)_{1.15}(VSe_2)$ samples on separate measurement systems. As shown in Figure V.6, both specimens have room temperature resistivity magnitudes and carrier concentrations characteristic of a metal. The resistivity decreases as temperature is lowered from room temperature to approximately 110 K, as expected for a metal. The slope, however, is much lower in magnitude than that found for VSe_2[3,32-34] or for other metallic MLCs.[4] In MLCs, it has been suggested that the incommensurate interfaces between the two constituents result in a significant contribution of scattering events, which raise the low-temperature residual resistivity, effectively reducing the

temperature dependence.[4] Turbostratic disorder also creates incommensurate interfaces and thereby further decreases the structural coherence in the *c*-direction in $(SnSe)_{1.15}(VSe_2)$. Perhaps the turbostratic disorder further increases the low-temperature residual resistivity, hence reducing the temperature dependence of the transport properties. At 110–120 K, the resistivity abruptly begins to increase, continuing to increase as temperature is decreased to 30 K, where it begins to drop again. This transition is reversible with temperature and reminiscent of a charge density wave (CDW) transition found at similar temperatures in the bulk transition metal dichalcogenide VSe_2.[3,32–34]

Literature suggests that the transport properties of MLCs whose TX_2 constituent contains a group V transition metal are dominated by the transition metal dichalcogenide component.[4] The magnitude of room temperature resistivity for NbX_2 and TaX_2 containing MLCs with divalent rock-salt MX constituents ranges from 0.8 to 21 uΩm.[4] The resistivity of both $(SnSe)_{1.15}(VSe_2)$ samples measured as part of this investigation are within this range, suggesting that the transport properties in $(SnSe)_{1.15}(VSe_2)$ are also dominated by the metallic dichalcogenide and that each vanadium atom contributes one delocalized electron. Bulk VSe_2 is metallic due to the delocalization of the electron on each of the V^{4+} ions and has a CDW transition identified by anomalies in the transport properties, with an onset temperature between 100 and 140 K depending on the $V_{1+x}Se_2$ composition.[3,32–34] The anomaly in the resistivity of $(SnSe)_{1.15}(VSe_2)$ is also in this temperature regime. However, we find an abrupt upturn and a doubling of the resistivity for $(SnSe)_{1.15}(VSe_2)$ in contrast to the subtle plateau in resistivity found for VSe_2.[3,32–34]

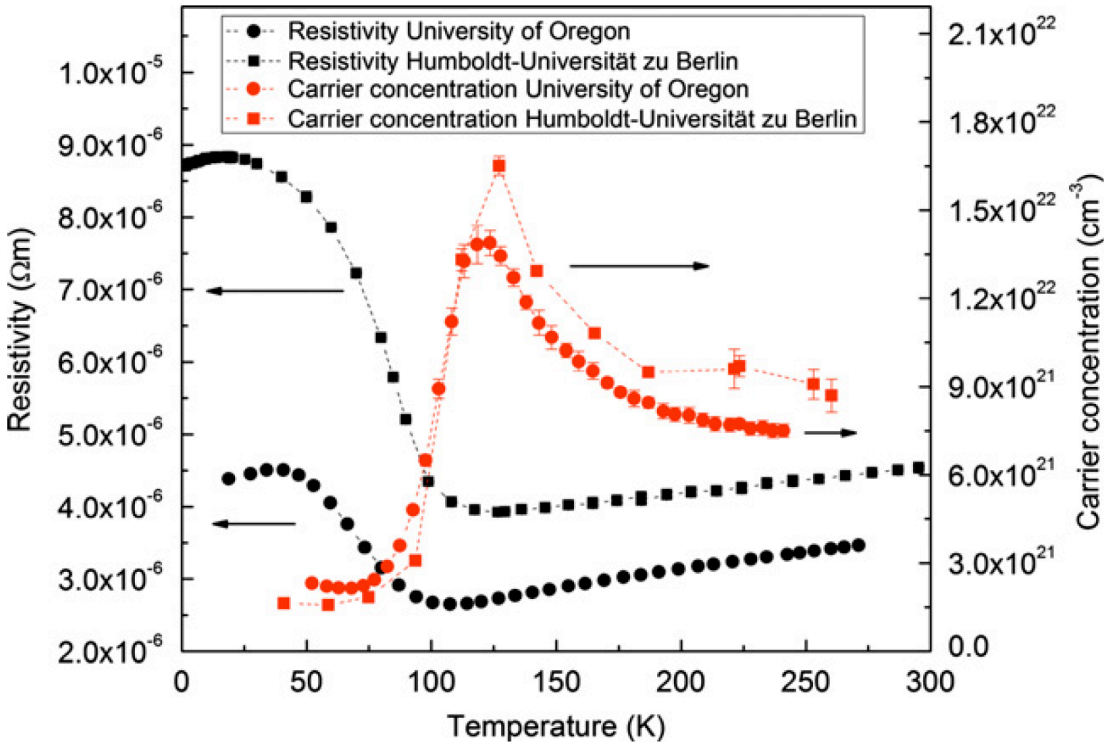

Figure V.6. Temperature-dependent resistivity and carrier concentration for two different $(SnSe)_{1.15}(VSe_2)$ samples.

To further understand the cause of this resistivity increase, the temperature-dependent carrier concentration was determined by measuring the Hall coefficient in both $(SnSe)_{1.15}(VSe_2)$ samples and assuming a single band model. As shown in Figure V.6, an abrupt drop in carrier concentration with decreasing temperature occurs at the same temperature as the upturn in resistivity, consistent with prior studies of CDWs in transition metal dichalcogenides.[3,32–34] The increase in carrier concentration as temperature is lowered from room temperature to approximately 100 K is probably a consequence of using a single band model to extract carrier concentration. Previous studies have explained both the surprising stability as well as unusual properties of MLCs as resulting from charge transfer between the constituents.[4,11,13] Previous electronic structure models have also suggested that both constituents are likely to have bands near

or at the Fermi level.[4,11,13] Assuming that the drop in carrier concentration during the upturn in resistivity corresponds to the localization of electrons in the VSe_2 constituent, then approximately one electron per V-atom is localized. Since the formal valance state of the vanadium in $(SnSe)_{1.15}(VSe_2)$ is V^{4+}, localizing one electron per vanadium would reduce the carrier concentration to zero. The system presumably remains metallic due to charge transfer between the SnSe and VSe_2 constituents, similar to that proposed by Giang, et al. to explain the metallic behavior of the misfit layer compound $(PbSe)_{1.18}(TiSe_2)_2$.[41]

Structural confirmation of CDW transitions in VSe_2 and other transition metal dichalcogenides has traditionally been obtained through temperature-dependent electron and X-ray diffraction studies.[40] In an attempt to see the structural distortion resulting from the potential CDW, we obtained (*hk*0) X-ray diffraction data at approximately 12 K and transmission electron diffraction data at 85 K. The low-temperature (*hk*0) X-ray diffraction data contained no changes in the number of reflections or peak broadening relative to the room temperature measurements. The electron diffraction data collected at 85 K also revealed no sign of supercell reflections, only a slight shrinkage (1–2%) of the lattice parameters. While further temperature-dependent diffraction studies are warranted at lower temperatures, the turbostratic disorder of the $(SnSe)_{1.15}(VSe_2)$ intergrowths will cause difficulties in observing supercell (*hkl*) reflections. A discontinuity in lattice parameters as a function of temperature at the transition might be the best evidence that could be expected from a more extensive investigation.

V.4. Bridge

During the synthesis of $(SnSe)_{1.15}(VSe_2)$, it was found that the calibrated parameters for creating the repeating sequence of one SnSe bilayer and one VSe_2 monolayer were sufficient to also create $[(SnSe)_{1.15}]_m(VSe_2)$ ferecrystals. Even more interesting was the trend in electrical transport properties as a function of *m*. The anomaly in the $(SnSe)_{1.15}(VSe_2)$ ferecrystal that was attributed to a charge density wave drastically changed between several $[(SnSe)_{1.15}]_m(VSe_2)$ samples. With the magnitude in resistivity upturn and the CDW transition temperature both increasing with increasing *m*. It appeared that the separation of VSe_2 monolayers had a drastic effect on the CDW transition; therefore, we synthesized several $[(SnSe)_{1.15}]_m(VSe_2)$ samples and characterized their structural and electrical properties as a function of *m*. These data are reported in chapter VI and are soon to be submitted to Chemistry of Materials.

CHAPTER VI

SYNTHESIS, STRUCTURE, AND ELECTRICAL CHARACTERIZATION OF $[(SnSe)_{1.15}]_m(VSe_2)$, m = 1, 2, 3, AND 4

This work is written for submission to Chemistry of Materials in 2013 with co-authors Michelle Dolgos, Andreas Fiedler, Corinna Grosse, Saskia F. Fischer, and David C. Johnson. Michelle Dolgos worked with the Rietveld Refinement, Andreas Fiedler and Corinna Grosse along with their advisor Saskia F. Fischer performed electrical measurements, David C. Johnson is my advisor and research group leader, and I am the primary author.

VI.1. Introduction

Layered compounds are very common, occurring both naturally and through many different synthetic techniques.[1,2] Their layered nature causes them to have a quasi-two-dimensional structure that produces largely anisotropic transport properties between down and across the layering. The layering also causes the structures to have very different interlayer and intralayer bonding environments, leading to a low-dimensionality that encourages phenomena such as charge density wave transitions.[3] A very well studied and large class of layered compounds is the transition metal dichalcogenides, with the general formula TX_2, where T is a transition metal and X is a chalcogen.[4,5] The TX_2 structure consists of repeating X-T-X trilayer sandwiches, with strong intralayer covalent

bonding and weak van der Waals interlayer interactions. The transition metal dichalcogenides have been studied for interesting phenomena such as superconductivity, magnetoresistance, intercalation, and charge density waves.[4-6] All of these phenomena can be manipulated by structural and compositional adjustments to the TX_2 structure; including doping, stoichiometry, polytype and intercalation.[6-10] In addition, transition metal dichalcogenides have been incorporated into composite crystals such as $(MX)_{1+y}(TX_2)$ misfit layer compounds.[9] Where their layered structure is ideal for intercalating an entire second crystal type, the MX constituent, and has resulted in misfit layer compounds with M = Sn, Pb, Sb, Bi, and rare earth metals; T = Ti, V, Cr, Nb, and Ta; and X = S and Se.[9] In this superlattice form, many of the bulk transition metal dichalcogenide characteristics remain; however, the MX constituent interacts with the TX_2 electronic structure through charge transfer and plays a role in the compound's electronic structure.[9,11,12] The composite crystal $(MX)_{1+y}(TX_2)$ is a potential tool for adjusting the TX_2 electronic structure while maintaining its bulk crystal structure and quasi-two-dimensionality.

Recently we synthesized the ferecrystalline composite crystal $(SnSe)_{1.15}(VSe_2)$ and showed that it contained a charge density wave (CDW) transition with onset temperature of 110 K.[13] A CDW transition is a modulation of a material's electron density and is usually more prevalent in low-dimensional solids.[3,14,15] VSe_2 is known to undergo a CDW transition with an equivalent onset temperature to that seen in $(SnSe)_{1.15}(VSe_2)$;[8,16-18] therefore the CDW in $(SnSe)_{1.15}(VSe_2)$ was attributed to the VSe_2 constituent. Until $(SnSe)_{1.15}(VSe_2)$, no CDW had been reported for a $(MX)_{1+y}(TX_2)$ misfit layer compound;[9] literature suggests that the periodic interlayer interactions of the MLCs

slightly distorts the TX_2 structure and thereby eliminates the CDW transition. The ferecrystalline $(SnSe)_{1.15}(VSe_2)$ composite crystal was created through the modulated elemental reactant (MER) synthetic approach[19] and contained turbostratic disorder[20] between the SnSe and VSe_2 constituents. This disorder disrupts the periodicity of interlayer interactions, potentially preserving the ideal conditions of the VSe_2 structure for undergoing a CDW transition. The MER synthetic approach also allows for creating $[(SnSe)_{1.15}]_m(VSe_2)$ intergrowths, where *m* is an integer value of SnSe bilayers; effectively increasing the distance between VSe_2 monolayers while not disturbing the VSe_2 structure. Increasing *m* provided an opportunity to increase the quasi-two-dimensionality of VSe_2 and investigate its effect on the CDW transition. This fundamental research is an extension on knowledge of CDW formation, because possible applications of CDW materials in transistors,[21,22] or electro-optical switches[23] have been proposed. Due to the large changes in resistivity and carrier density between the CDW state and normal state, an application of $[(SnSe)_{1.15}]_m(VSe_2)$ as thermal switches could also be possible.

Herein we report the synthesis of $[(SnSe)_{1.15}]_m(VSe_2)$ with m = 1-4, along with structural and electrical characterization. Taking advantage of the MER synthetic technique, we were able to prepare these new metastable $[(SnSe)_{1.15}]_m(VSe_2)$ structures from the calibration of the m = 1 ferecrystal.[13] Each integer increase of *m* represents an additional bilayer of SnSe atomic planes, linearly increasing the spacing between the VSe_2 layers. Structural information was obtained by analyzing the $[(SnSe)_{1.15}]_m(VSe_2)$ compounds with X-ray diffraction, through both Bragg-Brentano and in-plane scan geometries. For further insight into the atomic spacing of the layers and to confirm any

structural trends as a function of *m*, Rietveld refinement was performed on the (00*l*) reflections found in Bragg-Brentano X-ray diffraction data. Resistivity and Hall measurements of the $[(SnSe)_{1.15}]_m(VSe_2)$ ferecrystals show a reversible anomaly between 108 - 166 K with increasing resistivity and decreasing carrier density for decreasing temperatures, similar features to that found for the CDW transition in bulk VSe_2.[8,16-18] However, an equivalent magnitude of change in resistivity during the CDW transition was not observed in bulk VSe_2. Also, no anomalies were observed in electrical data gathered on the $[(SnSe)_{1.15}]_m(TaSe_2)$ ferecrystals,[19] even though binary $TaSe_2$ also exhibits charge density waves.[24-26] We find from resistivity and Hall measurements on $[(SnSe)_{1.15}]_m(VSe_2)$ that the onset temperature and transport property profiles change with stacking sequence, with a higher onset temperature with increasing *m*. We suggest that the additional SnSe layers cause the material to be more two-dimensional, encouraging the CDW transition to occur at higher temperatures.

VI.2. Experimental Details

The thin-film specimens studied in this work were created by physical vapor deposition using a custom-built vacuum deposition chamber.[27] The chamber was evacuated to a base pressure of 1×10^{-7} Torr before deposition and actively pumped by a cryogenic absorber during deposition. An effusion cell was used to evaporate Se (99.999% purity) while a Thermionics™ electron beam gun was used to evaporate Sn (99.98% purity) and V (99.7% purity). Substrates are positioned approximately 25 cm above the sources, with a pneumatic shutter in between them. Polished substrates, either (100) oriented silicon or fused quartz slides, are held upside down on a rotating carousel.

A quartz crystal monitoring system is used to monitor the deposition rates; an approximate rate of 0.04 nm/sec was used for each element. A custom LabVIEW program was used to maintain deposition rates, rotate substrates between sources, and deposit material.

The deposition of a layered $[(SnSe)_{1.15}]_m(VSe_2)$ intergrowth is a non-epitaxial process, instead sub-nanometer elemental layers are deposited onto an unheated substrate. Self-assembly, an amorphous precursor crystallizing into the $[(SnSe)_{1.15}]_m(VSe_2)$ intergrowth product, takes place during annealing; which is done on a hot plate under a nitrogen atmosphere (0.5 ppm O_2) to prevent excessive oxidation. Each crystallized SnSe and VSe_2 structural unit self-assembles from an as-deposited Sn-Se or V-Se amorphous bilayer. To self-assemble *m* layers of SnSe structural units, *m* Sn-Se amorphous bilayers are deposited in the precursor's repeating sequence. To determine the ideal deposition parameters that will self-assemble every Sn-Se and V-Se amorphous bilayer into a single sheet of crystalline SnSe and VSe_2 structural units requires an extensive calibration procedure.[19] Elemental composition of the thin-films was obtained through an electron probe microanalysis (EPMA) technique described elsewhere.[28]

In house X-ray reflection (XRR) and X-ray diffraction (XRD) data were gathered on a Bruker D8 Discover diffractometer, equipped with copper radiation (Kα, wavelength = 0.15418 nm) and Göbel mirror optics. Cross-plane XRR is gathered between 0-10 °2θ and XRD between 10-65 °2θ; both are done with a θ-2θ locked coupled scan geometry. Prior to scanning, the vertical X-ray beam is aligned parallel to the substrate so that the incident angle is normal to the substrate surface. In-plane XRD data, obtained with a low incident beam angle and the detector scanning angle parallel to the substrate, were

gathered at the advanced photon source (APS), Argonne National Labs (Beamline 33BM) and Lebail fits were performed to determine the *ab*-lattice parameters. Cross-plane XRD was also gathered at the APS, the high signal to background ratio was utilized for Rietveld refinement on the (00*l*) reflections. Lebail fits and Rietveld refinements were performed using the GSAS and EXPGUI software packages.[29,30]

High-resolution scanning transmission electron microscopy (HRSTEM) was performed on an objective lens c_s-corrected FEI Titan 80−300 TEM/STEM, equipped with a high angle annular dark field (HAADF) detector. HR-TEM samples were prepared at the Center for Advanced Materials Characterization in Oregon (CAMCOR) of the University of Oregon (UO) on a FEI Helios Nanolab D600 Dual Beam focused ion beam (FIB) by an in-situ lift-out and thinning method, followed by low voltage ion beam polishing.

In-plane resistivity and Hall measurements were carried out using the van der Pauw method.[31] The total film thickness, used for the resistivity and carrier density calculations, was determined by XRR measurements and was approximately 50 nm for all samples investigated in this study. Two sets of samples, which differ in shape and substrate material, were investigated. Using different contact masks, the precursors were deposited with variable shapes and sizes. Electrical measurements at the Humboldt-Universität zu Berlin used samples with a cloverleaf shape and 0.5 cm by 0.5 cm dimensions. They were deposited on a (100) silicon substrate with a thermally grown SiO_2 layer. Electrical contacts were made with thin gold wires, which were connected to the sample using indium. The electrical measurements were performed in a continuous-flow cryostat at temperatures between 4 K and 300 K. For the Hall measurements a

magnetic field of up to 0.6 T was applied perpendicular to the intergrowth layers. Electrical measurements at the University of Oregon used samples with a cross shape, 1 cm x 1 cm, deposited on fused quartz slides. Electrical measurements were performed between 20 and 290 K and Hall measurements used a magnetic field up to 2 T.

VI.3. Results and Discussion

The modulated elemental reactant (MER) synthetic technique requires calibrating deposition parameters to deposit sub-nanometer layers, whose composition and modulated layering sequence mimics that of the desired product. These as-deposited samples are referred to as precursors and if a precursor's repeating sequence contains an excess or lack of material compared to that which is required for crystallizing single structural units of $[(MX)_{1+y}]_m(TX_2)_n$ then layering defects will occur upon annealing. During the calibration procedure for synthesizing $(SnSe)_{1.15}(VSe_2)$, the deposition parameters for crystallizing single structural units of SnSe (a SnSe bilayer) and VSe_2 (a Se-V-Se trilayer sandwich, i.e. a VSe_2 monolayer) were determined.[13] Creating $[(SnSe)_{1.15}]_m(VSe_2)$ intergrowths required depositing *m* (Sn-Se) bilayers and one (V-Se) bilayer per repeating sequence, followed by low-temperature annealing to self-assemble the compound, maintaining the nano-architecture created in the precursor. X-ray reflection (XRR) patterns of the precursors contained (00*l*) reflections from the modulated amorphous layers that were used to determine the thickness of the [*m*(Sn-Se)] + (V-Se) repeating sequence. Plotting the thickness of the precursor's repeat unit vs. *m* provided the thickness of an as-deposited (Sn-Se) bilayer from the slope and the

thickness of the (V-Se) bilayer from the intercept. Our targeted values were 0.60 and 0.62 nm for the as-deposited (Sn-Se) and (V-Se) bilayers, respectively.

To promote the self-assembly of the as-deposited (Sn-Se) and (V-Se) bilayers into crystallized sheets of SnSe bilayers and VSe_2 monolayers, the precursors were annealed at 400 ˚C for 20 min; the optimal annealing conditions determined for $[(SnSe)_{1.15}]_1(VSe_2)$.[13] Figure VI.1 and VI.2 shows the Bragg-Brentano geometry X-ray diffraction (XRD) patterns of representative $[(SnSe)_{1.15}]_m(VSe_2)$ samples after annealing. The XRD patterns contain Bragg reflections, which can all be indexed as (00*l*) reflections coming from the targeted $[(SnSe)_{1.15}]_m(VSe_2)$ compound. The presence of only (00*l*) reflections reflects the preferred orientation of the layering, with layers parallel to the substrate surface. The *c*-lattice parameters of the $[(SnSe)_{1.15}]_m(VSe_2)$ compounds were determined from the (00*l*) reflections, reported within Figure VI.1 and VI.2 along with composition (2.93(1) nm for the $m = 4$ intergrowth). Plotting the *c*-lattice parameter vs. *m*, the increase in thickness of a single SnSe structural unit was determined to be 0.578(2) nm from the linear regression while the thickness of a single VSe_2 structural unit, 0.626(5) nm, was determined by the intercept. The increase per SnSe bilayer is equivalent to that expected for a bilayer spacing in the high-temperature tetragonal phase of SnSe (0.581 nm).[32] In literature examples, the *c*-lattice parameter of 1T $V_{1+x}Se_2$ ranges between 0.6105-0.5970 nm, with *c* increasing as *x* approaches zero.[8,16-18] Our value of 0.621(4) nm is significantly higher. These data confirm that the previously calibrated deposition parameters for the $(SnSe)_{1.15}(VSe_2)$ compound were also ideal for creating $[(SnSe)_{1.15}]_m(VSe_2)$ intergrowths.

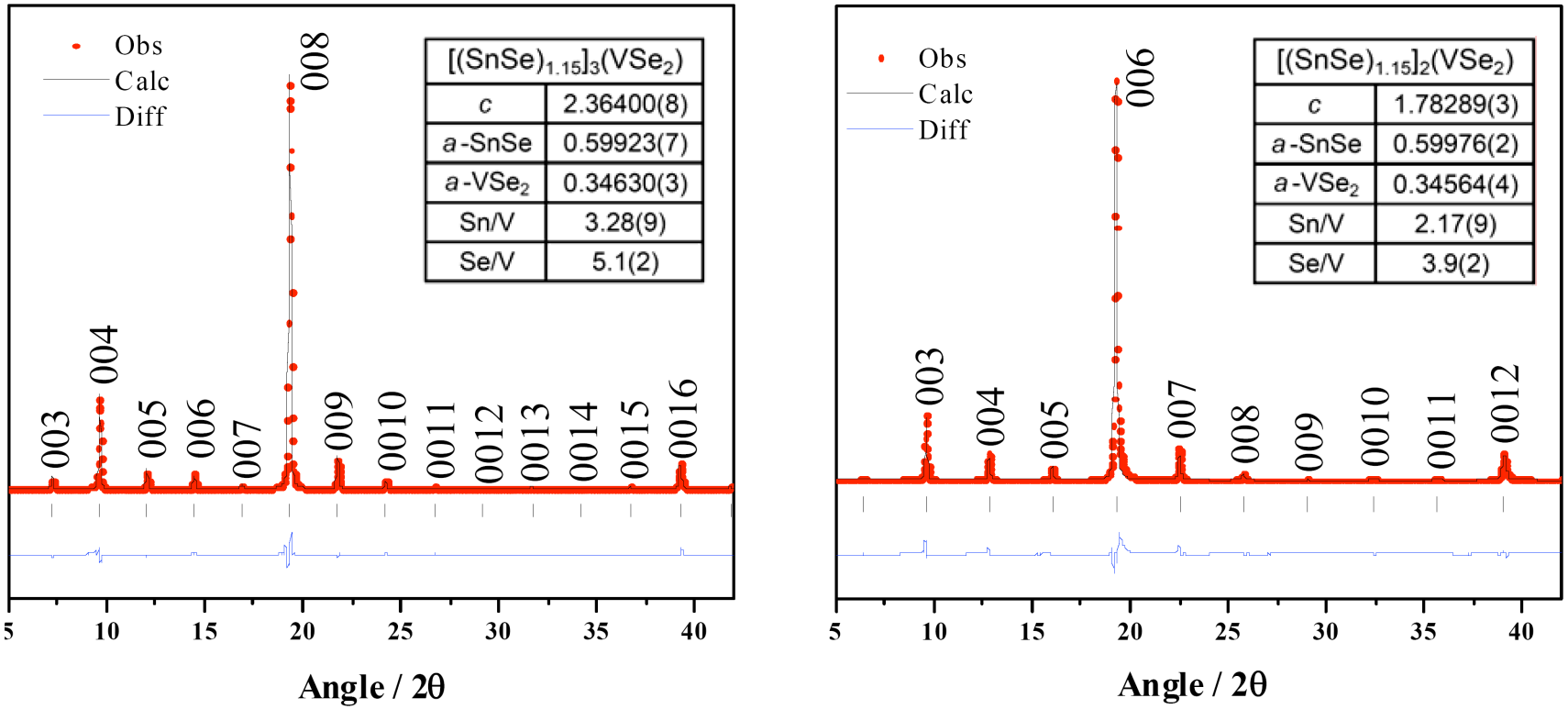

Figure VI.1. Bragg-Brentano X-ray diffraction patterns of (left) $[(SnSe)_{1.15}]_3(VSe_2)$ and (right) $[(SnSe)_{1.15}]_2(VSe_2)$ ferecrystals. Included with the XRD patterns is the Rietveld refinement calculated and difference patterns, indexing for the (00*l*) reflections, and an inserted table with relevant lattice parameters and composition (from EPMA).

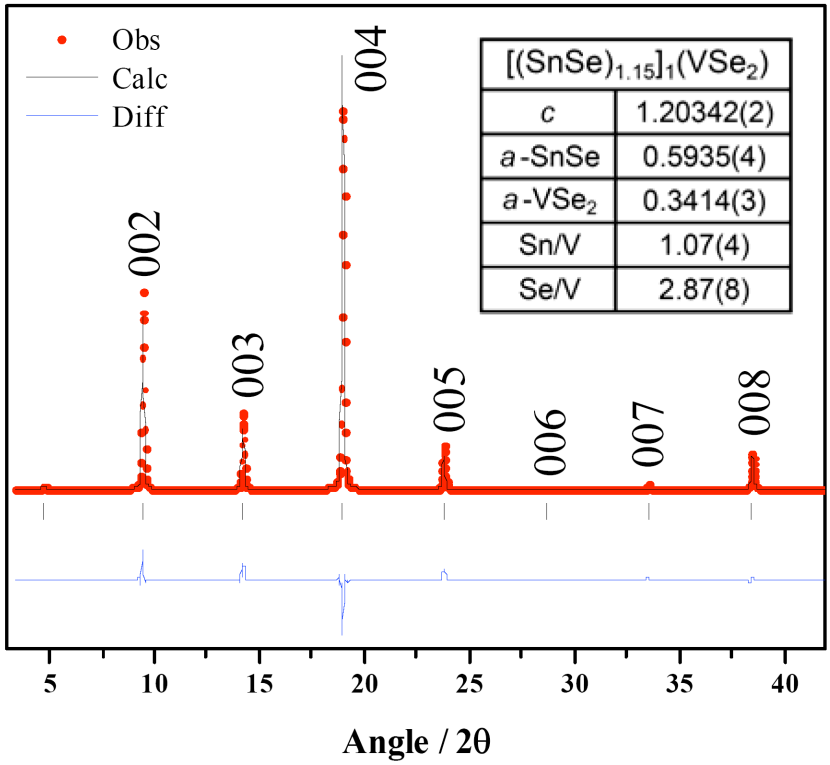

Figure VI.2. Bragg-Brentano X-ray diffraction patterns of $[(SnSe)_{1.15}]_1(VSe_2)$ ferecrystal. Included with the XRD pattern is the Rietveld refinement calculated and difference pattern, indexing for the (00*l*) reflections, and an inserted table with relevant lattice parameters and composition (from EPMA).

The preferred orientation of the $[(SnSe)_{1.15}]_m(VSe_2)$ layering requires that an alternate scan geometry be used to observe the *ab*-plane characteristics of the intergrowth. Using a low incident angle and scanning the detector parallel to the layers, the XRD patterns in Figure VI.3 of representative $[(SnSe)_{1.15}]_m(VSe_2)$ intergrowths were obtained; these data were not obtained for the $m = 4$ ferecrystal. In these patterns, all the diffraction maxima can be indexed as (*hk*0) reflections arising from two separate crystal lattices; representing the two independent constituents SnSe and VSe_2. This is an expected result for a $[(MX)_{1+y}]_m(TX_2)_n$ composite crystal, because the MX and TX_2 constituents maintain independent crystal lattices within the intergrowth. The (*hk*0)

reflections were indexed as arising from a square basal plane for SnSe and a hexagonal basal plane for VSe_2 and the resulting *a*-lattice parameters are given within Figure VI.1 and VI.2. The *a*-lattice parameter for the SnSe constituent varied from 0.5935(4), 0.59976(2), and 0.59923(7) nm for the m = 1, 2, and 3 compounds, respectively. A similar square basal plane of SnSe was reported for both $(SnSe)_{1.15}(VSe_2)$[13] and $(SnSe)_{1.15}(TaSe_2)$[19] and similar lattice parameter values were obtained. While bulk SnSe crystallizes in an orthorhombic crystal lattice under atmospheric conditions, a tetragonal phase does exist at high temperatures.[32] The *a*-lattice parameter for our VSe_2 constituent increases from 0.3414(3), 0.34564(4), and 0.34630(3) nm for the m = 1, 2, and 3 ferecrystals, respectively. The *a*-lattice parameter of bulk $V_{1+x}Se_2$ varies between 0.335 at $x = 0$ to 0.343 nm for $x = 0.18$, with *a* increasing approximately linearly as *x* increases due to interstitial vanadium in the van der Waals gap.[8,16-18] Since we have only one VSe_2 layer in the reported compounds, this most likely is not the cause of our increase in the *a*-lattice parameter. For the MLC $(La_{.95}Se)_{1.21}VSe_2$, a significantly larger *a*-lattice parameter of 0.3576(3) nm was found for the VSe_2 constituent, presumably due to charge donation from LaSe to the VSe_2 constituent.[33] This suggests that increasing charge donation from SnSe to VSe_2 could be responsible for the observed lattice parameter change. Using the *a*-lattice parameters for the SnSe and VSe_2 constituents the cation per area for each constituent was calculated and used to determine the misfit parameter of 1.15. Although, the compositions of the samples indicate that they are vanadium rich relative to this misfit parameter. We speculate that this excess vanadium is required to compensate for the oxygen found in the samples.

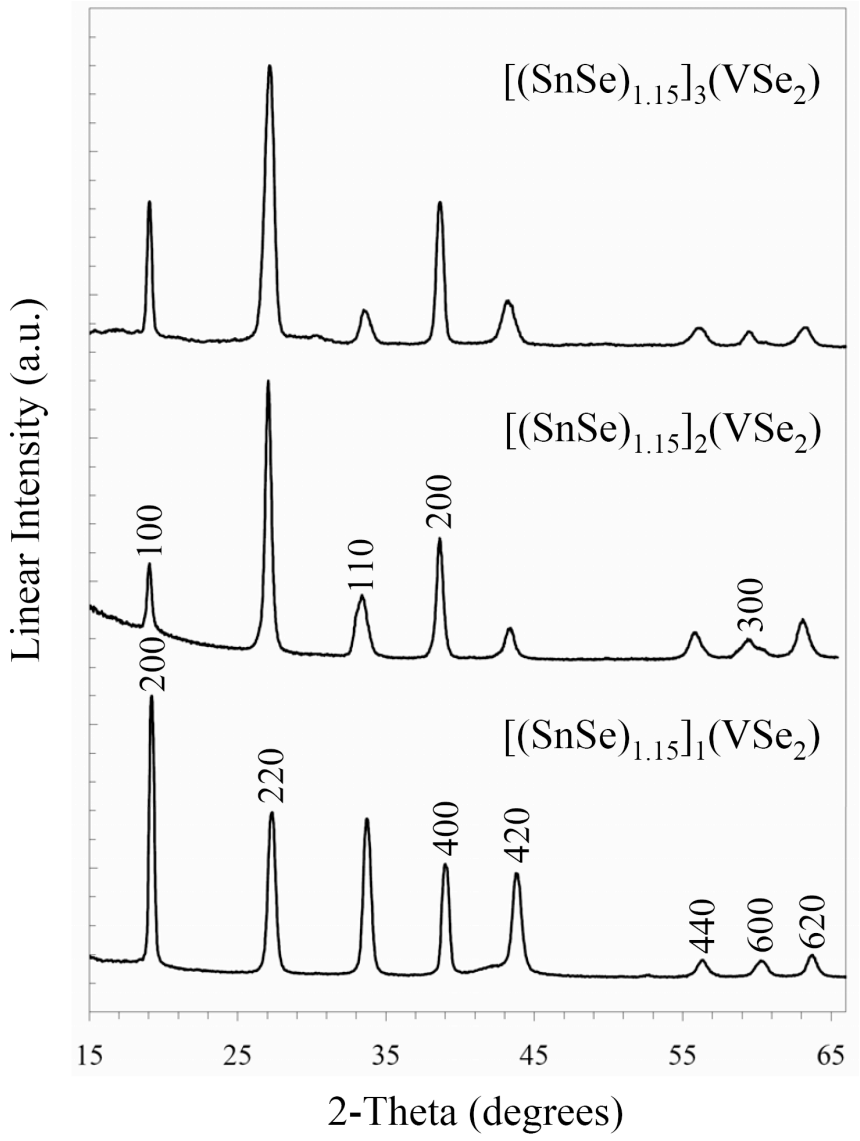

Figure VI.3. In-plane X-ray diffraction patterns of $[(SnSe)_{1.15}]_m(VSe_2)$ ferecrystals, incident x-ray wavelength is 0.0992 nm. The peaks are indexed for SnSe on the $[(SnSe)_{1.15}]_1(VSe_2)$ pattern and for VSe_2 on the $[(SnSe)_{1.15}]_2(VSe_2)$ pattern, the indexing applies to all three patterns.

To further investigate the crystallinity of the $[(SnSe)_{1.15}]_m(VSe_2)$ compounds, two dimensional XRD was gathered using an image plate area detector. Patterns from representative $[(SnSe)_{1.15}]_2(VSe_2)$ and $[(SnSe)_{1.15}]_3(VSe_2)$ samples are shown in Figure VI.4. There is a large amount of diffuse scattering, or intensity streaking, along the *l*

direction for particular (*hkl*) reflections ($l \neq 0$, $hk \neq 0$). Broadening of diffraction intensity can result from a shortened coherence length of the reflection. In the case of the $[(SnSe)_{1.15}]_m(VSe_2)$ intergrowths, the reflections are abrupt along (00*l*) and (*hk*0), representing the coherent *d*-spacing of the layering and the in-plane coherence of the individual layers but they are then broad along many (*hkl*) reflections. This combination of (*hkl*) reflection broadening but sharp (00*l*) and (*hk*0) is typical for turbostratic disorder,[20] where between layers there is a random rotational disorder of the *ab*-plane. The disorder constrains grain sizes to the individual layers, thereby extremely shortening the coherence length of particular (*hkl*) reflections ($l \neq 0$, $hk \neq 0$). Interestingly, there do appear to be satellite reflections along the (20*l*) line of SnSe constituent that increase in number between the $m = 2$ and $m = 3$ compounds (highlighted with white arrows in Figure VI.4). Anderson et. al. confirmed that these reflections arise from the isolated SnSe crystallites and increase with *m*.[34] These results confirm that $[(SnSe)_{1.15}]_m(VSe_2)$ intergrowths contain the structural characteristics of a ferecrystal, independent crystallographic *ab*-plane structures, regular spacing along the *c*-axis, and rotational disorder between the constituent layers.

In an effort to visually see and further characterize the layered structure of the $[(SnSe)_{1.15}]_m(VSe_2)$ ferecrystals, a cross-section specimen was cut out by focused ion beam (FIB) and examined by high-resolution transmission electron microscopy (HR-TEM) and scanning transmission electron microscopy (STEM) high-angle annular dark-field (HAADF) imaging. FigureVI.5 contains an HR-TEM image and Figure VI.6 a STEM-HAADF image of a representative $[(SnSe)_{1.15}]_3(VSe_2)$ ferecrystal. The HR-TEM and STEM-HAADF images clearly show a consistent layering of the expected repeating

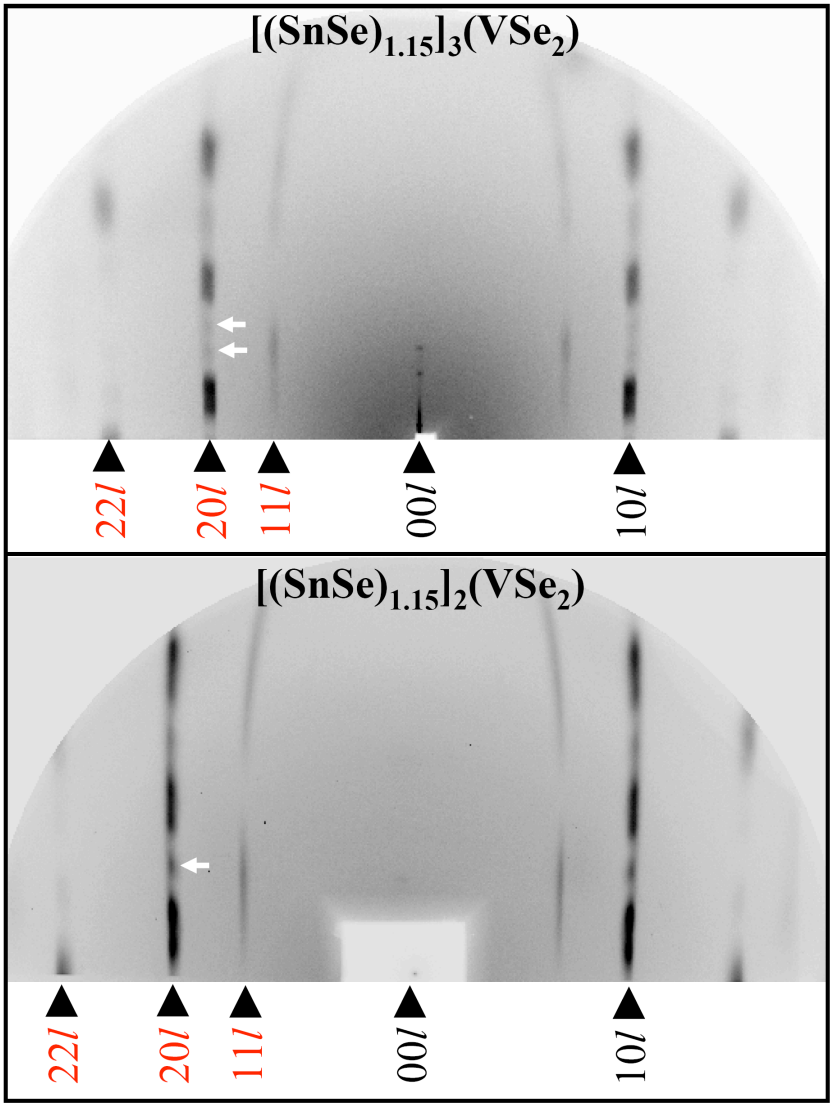

Figure VI.4. 2D X-ray diffraction pattern of representative $[(SnSe)_{1.15}]_m(VSe_2)$ ferecrystals. Families of reflections are indicated on the image's left side in red for the SnSe constituent and on the right side in black for the VSe_2 constituent. White arrows point to satellite reflections from the finite SnSe crystallites.

sequence, three SnSe bilayers and one VSe_2 monolayer. In the STEM-HAADF image, the *z*-contrast shows a darker contrast for the single VSe_2 monolayer and brighter for the three SnSe bilayers; as is expected for Sn has the highest *z*-value. Also, the STEM-HAADF image confirms the compositional abruptness of the layering, identifying this

intergrowth as a composite crystal of two separate crystal types. In the STEM-HAADF image the VSe_2 monolayer appears as a bilayer due to the smaller atomic number of V, which results in weaker scattering. In several areas amongst Figures VI.5 and VI.6 there are resolved atoms and particular zone axes are visible; however, there is no consistent zone axis across or down the layering. The randomly changing zone axes throughout the image is a result of turbostratic disorder and further identifies the $[(SnSe)_{1.15}]_3(VSe_2)$ intergrowth as a ferecrystal.

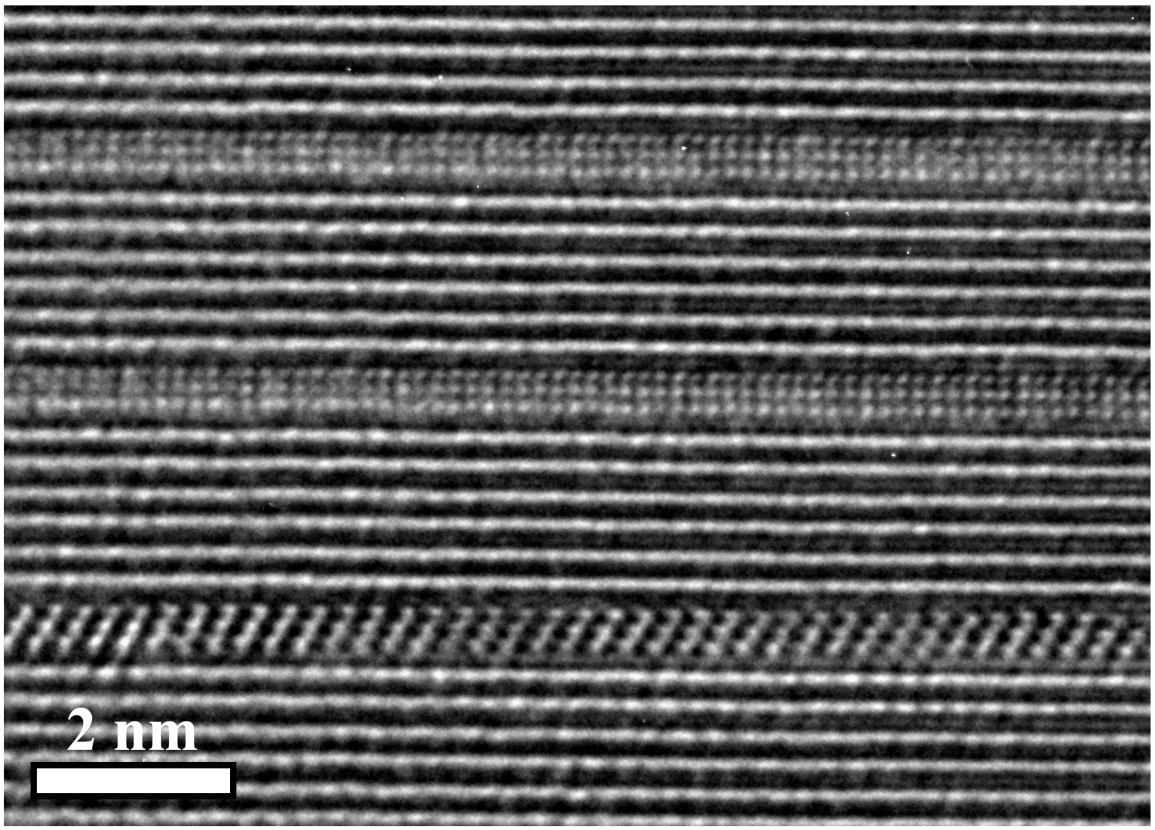

Figure VI.5. A cross-sectional HR-TEM image of a $[(SnSe)_{1.15}]_3(VSe_2)$ ferecrystal, the image clearly shows the expected repeating sequence (three SnSe bilayers and one VSe_2 monolayer).

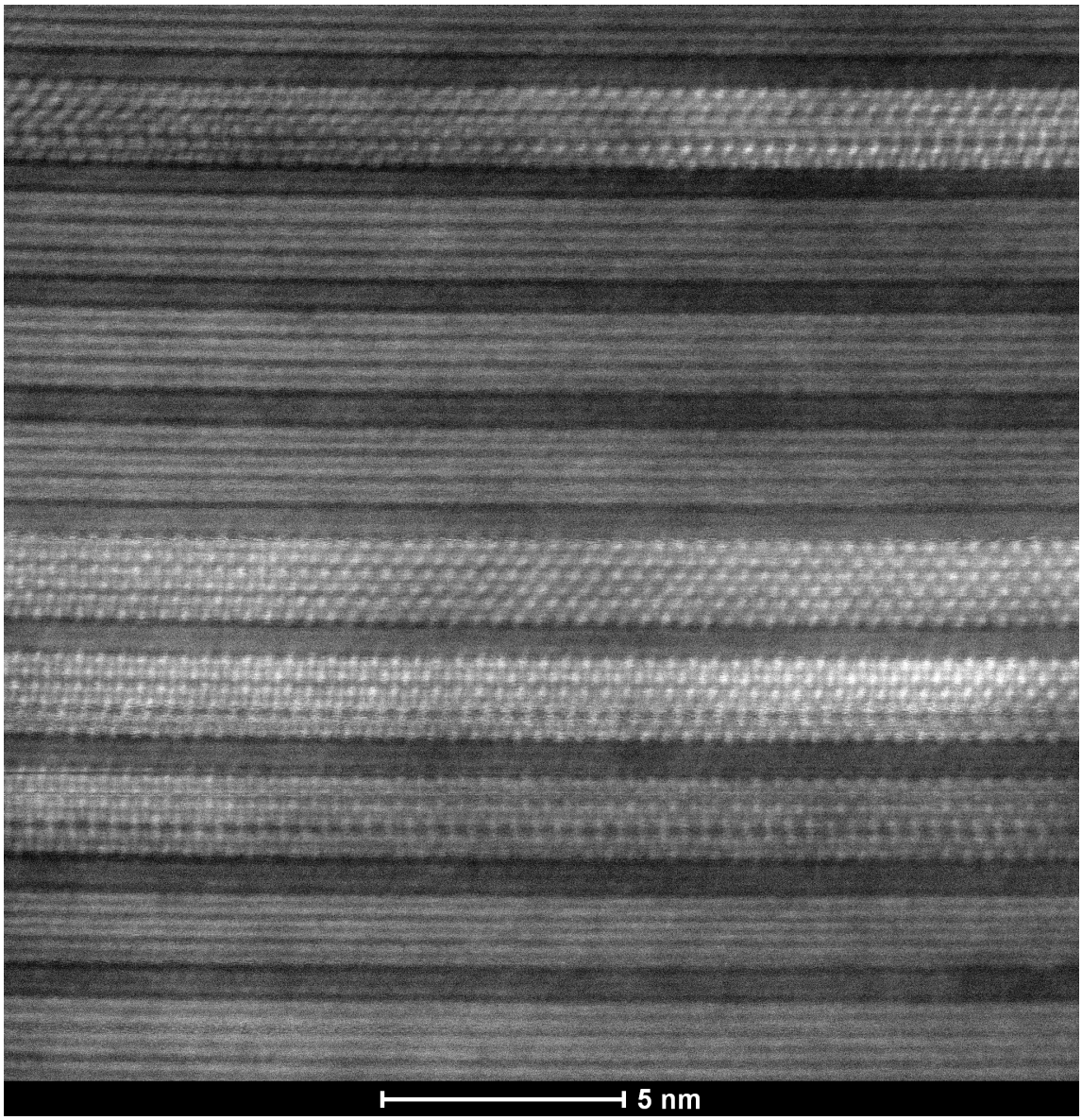

Figure VI.6. A cross-section STEM-HAADF image of a $[(SnSe)_{1.15}]_3(VSe_2)$ ferecrystal, the images *z*-contrast clearly shows a brighter set of three bilayers, the SnSe, and a darker monolayer, the VSe_2.

To gain further insight into the structural characteristics of the $[(SnSe)_{1.15}]_m(VSe_2)$ intergrowths, Rietveld refinements were performed on the (00*l*) reflections obtained from the Bragg-Brentano geometry X-ray diffraction measurements (Figures VI.1 and VI.2). The Rietveld refinement method originated as a bulk powder structural analysis and is

generally not applied to thin-films because most films are first made as a powder and the refinement is performed at that point. However, because ferecrystals are kinetically stable materials in thin-film form and are not thermodynamically stable when made using powder synthesis techniques, the Rietveld refinement is an invaluable tool for structural analysis of these films. The refinement of the (00*l*) pattern provides information about the spacing of the ferecrystal's planes along the *c*-axis. Figures VI.1 and VI.2 show the quality of fit for the model used in analyzing each of the $[(SnSe)_{1.15}]_m(VSe_2)$ ferecrystals with lattice parameters from the refinement in the inset of Figures VI.1 and VI.2 along with atomic spacing in Table VI.1. The layering sequence and distances based on the Rietveld refinement can be found in Figure VI.7.

Table VI.1. Atomic spacing along the *c*-axis using fractional coordinates from the Rietveld refinement.

Parameter	**$[(SnSe)_{1.15}]_1(VSe_2)_1$**	**$[(SnSe)_{1.15}]_2(VSe_2)_1$**	**$[(SnSe)_{1.15}]_3(VSe_2)_1$**
d (puckering distortion) [nm]			
Sn_1-Se_1	0.021	0.044	0.072
Sn_2-Se_2	NA	0.041	0.065
Sn_3-Se_3	NA	NA	0.028
d (dichalcogenide) [nm]			
V-Se	0.147	0.156	0.146
d (SnSe Bilayer(s)) [nm]			
Sn_1-Sn_1	0.312	NA	NA
Sn_1-Sn_2	NA	0.315	0.334
Sn_3-Sn_3	NA	NA	0.306

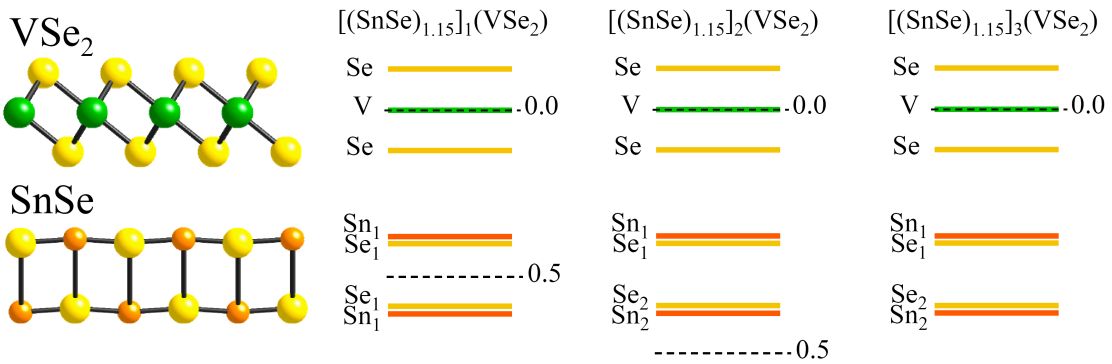

Refined Fractional Coordinates			
m:n	1:1	2:1	3:1
V	0.0	0.0	0.0
Se	0.1221(3)	0.0877(1)	0.0616(1)
Sn_1	0.3702(2)	0.2475(2)	0.1834(1)
Se_1	0.3876(2)	0.2723(3)	0.2139(2)
Se_2	NA	0.4010(1)	0.2972(1)
Sn_2	NA	0.4239(2)	0.3249(1)
Sn_3	NA	NA	0.4353(4)
Se_3	NA	NA	0.4471(2)

Figure VI.7. A visual representation of the atomic spacing for each $[(SnSe)_{1.15}]_m(VSe_2)$ ferecrystal. Also, a ball and stick model is provided for the bulk structure of SnSe and VSe_2 as well as an inserted table containing the *c*-lattice fractional coordinates from the Rietveld Refinement. The dashed lines indicate mirror planes used in the refinement model.

The spacing between the V-Se of the Se-V-Se trilayer is similar for the $m = 1$ and 3 ferecrystals but is much greater for the $m = 2$ ferecrystal. There is a puckering distortion of the SnSe monolayers in order to satisfy the coordination condition of the selenium in the transition metal dichalcogenide layer. This requirement results in the Sn atoms of the rock-salt layer moving closer to the Se of the dichalcogenide layer and the Se atoms of the rock-salt layer moving farther away. The puckering distortion increases by approximately 0.027 nm each time *m* increases by 1 from the $m = 1$ to 3 ferecrystal (Table VI.1). However, in the $m = 3$ material, the Sn and Se atomic planes on the interior of the three SnSe bilayers do not pucker to the same extent as the Sn and Se planes at the

SnSe-VSe_2 interface. This decrease in puckering is possibly due to an interlayer charge transfer between the SnSe and VSe_2 layers, the magnitude of which is reduced further from the interface, allowing the SnSe to assume a more bulk-like structure. The average intraplanar distance of the SnSe bilayers is similar between the m = 1, 2, and 3 ferecrystals; however, again the interior SnSe bilayer of the m = 3 ferecrystal is smaller than the exterior bilayer. These planar separations are consistent with the values found in the orthorhombic bulk phase of SnSe.

To investigate the electrical transport properties of $[(SnSe)_{1.15}]_m(VSe_2)$ as a function of m, we gathered temperature-dependent resistivity and Hall data on the m = 1, 2, 3, and 4 ferecrystals. Two different sets of samples with different shapes (cross and cloverleaf shape) and different substrate materials (quartz and silicon) were analyzed. All of them show the same trends in temperature-dependent resistivity and Hall coefficient. All the $[(SnSe)_{1.15}]_m(VSe_2)$ ferecrystals exhibit a metallic behavior between 170 K and room temperature (RT). In this temperature range the resistivity increases linearly with temperature and the Hall coefficient is nearly constant (Figures VI.8 and VI.9). The RT resistivity amounts to 3 μΩm for m = 1, 4 μΩm for m = 2, 6 μΩm for m = 3, and 10 μΩm for m = 4. These values are within the range of RT resistivities, ρ_{RT}, reported for conventional MLCs containing NbX_2 and TaX_2 and different rock-salt MX constituents ($\rho_{RT} \approx$ 0.8 μΩm to 21 μΩm).[9] The Hall measurements revealed a positive Hall coefficient. This would suggest positive charge carriers in a single band, single carrier type model. The charge carrier density p was determined from the Hall measurements, assuming a single band model and a single carrier type, i.e. $p=1/(R_H \cdot e)$ (with R_H=Hall coefficient). A RT charge carrier density of $p = 10^{21}$ cm^{-3} to 10^{22} cm^{-3} was determined

for the ferecrystals, also indicating a metal-like character. However, at temperatures of about 120 K – 170 K we find a reversible anomaly in resistivity and carrier density. Around these temperatures, the resistivity suddenly starts to increase as temperature is decreased (Figure VI.8). At 30 K the resistivity shows about twice the RT resistivity value. The Hall coefficient (Figure VI.9) increases for decreasing temperatures below about 150 K. The at 30 K is about of the RT value.

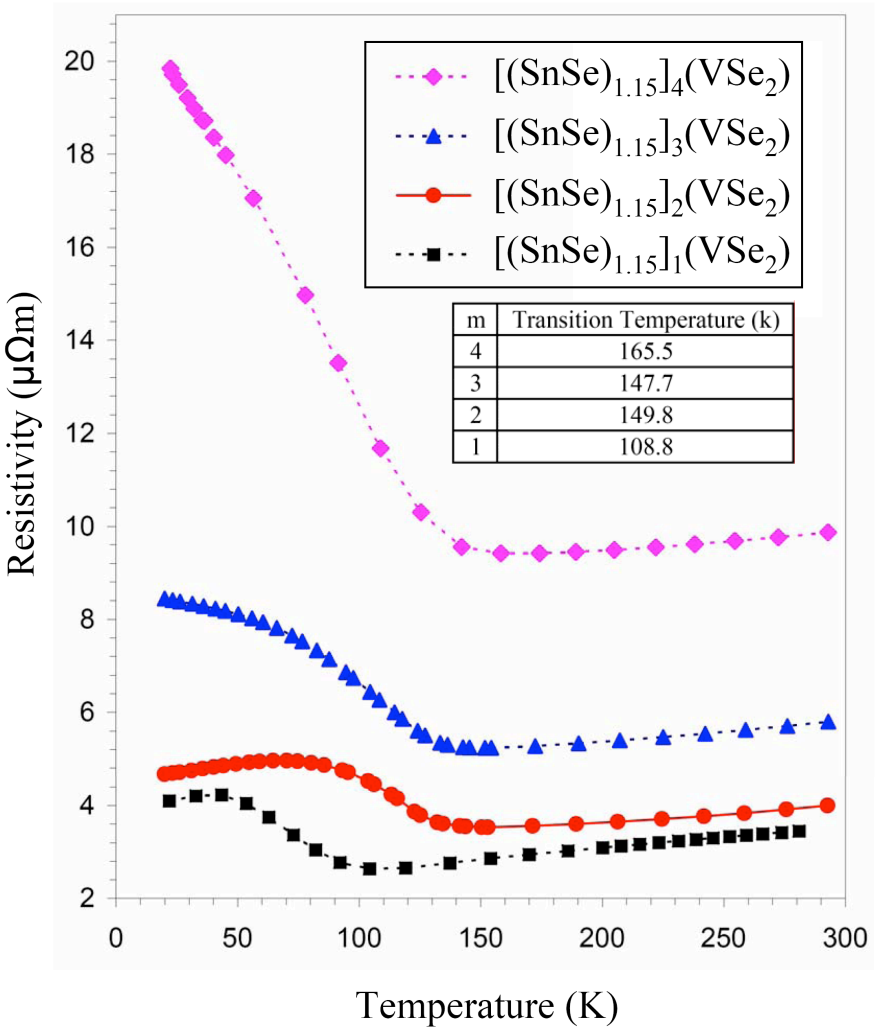

Figure VI.8. Temperature-dependent electrical resistivity for $[(SnSe)_{1.15}]_m(VSe_2)$ ferecrystals. The transition temperatures were determined by fitting the resistivity curves to a high order polynomial and selecting the lowest point in the transition zone.

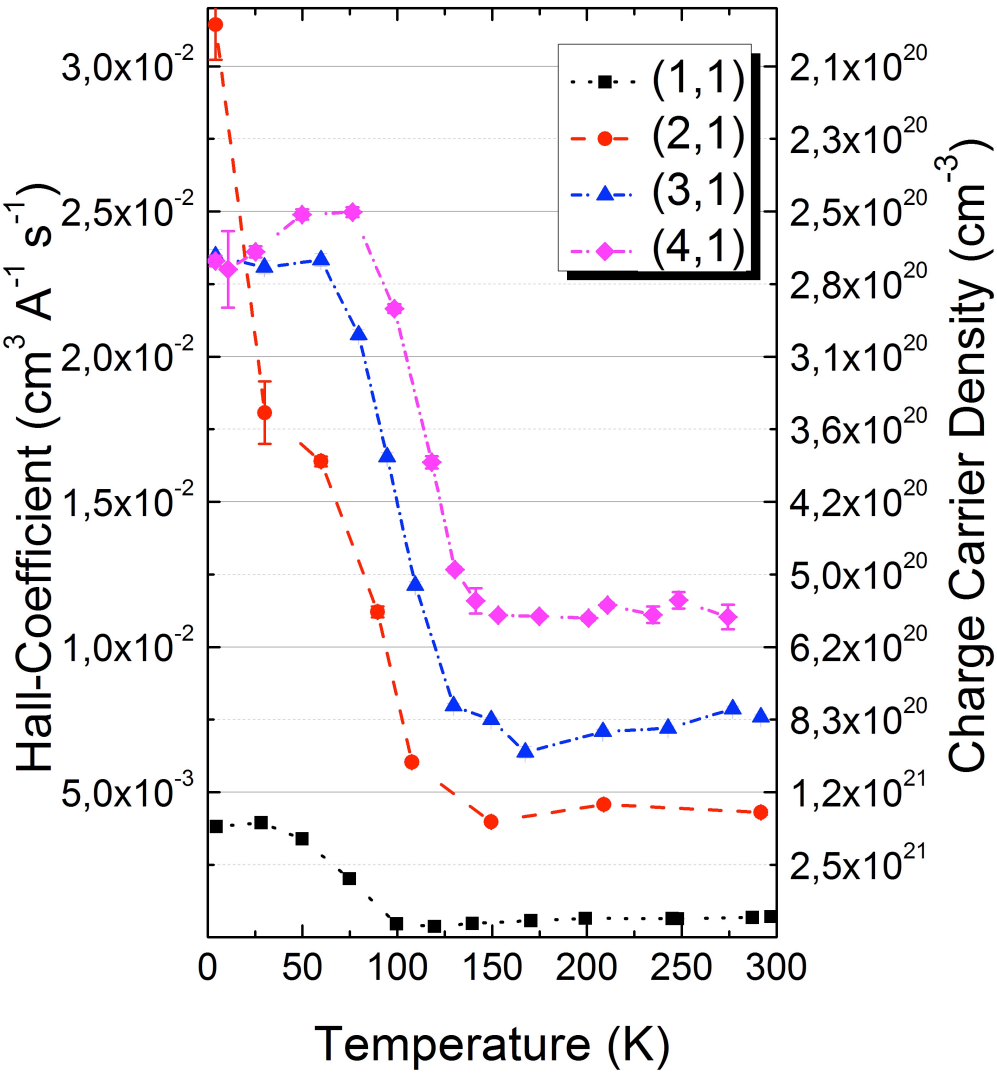

Figure VI.9. Temperature-dependent Hall coefficient and carrier concentration (assuming a single band model and a single carrier type) for the $[(SnSe)_{1.15}]_m(VSe_2)$ ferecrystals.

Binary VSe_2 has been reported to show two CDW transitions, an incommensurate one at about 117 K and a commensurate one at 75 K-85 K.[8,16-18,35-37] The incommensurate transition is accompanied by abrupt changes in electrical properties. The commensurate transition includes a change in structural properties. At around 100 K-110 K, VSe_2 exhibits discontinuities in resistivity, Hall coefficient, and magnetic properties, attributed

to the charge density wave transition.[8,16-18,35-37] Except for a discontinuity in resistivity between 50 K and 110 K, binary VSe_2 exhibits a metallic behavior for the rest of the temperature range between 4 K and 300 K. Binary SnSe, on the other hand, is a semiconductor with an increasing resistivity as temperature is lowered.[38-41] The RT resistivity of binary SnSe (e.g. ρ_{RT} = 0.1 -1 Ωm for polycrystalline SnSe films,[39,39] or ρ_{RT} = 0.04-2000 Ωm as reported for bulk single crystals)[40,41] is much higher in magnitude than the resistivity of VSe_2 (e.g. $\rho_{RT} \approx$ 2.2 μΩm or 3.2 μΩm).[16,17] Therefore, the resistivity of the $[(SnSe)_{1.15}]_m(VSe_2)$ ferecrystals is assumed to be ruled mainly by the resistivity of the VSe_2 subsystem.

Unlike the strong increase in resistivity for lowering temperatures, which we measured in our ferecrystals at the CDW transition temperature, the resistivity of binary VSe_2 only shows a plateau-like feature. Our measurement, on the other hand, shows that the resistivity increases drastically. Hence, if the VSe_2 is embedded in the ferecrystal, the different dimensions of the VSe_2 subsystem or an interaction with the adjacent SnSe layers lead to a different electrical behavior. The absolute value of the Hall coefficient for binary VSe_2 increases with decreasing temperatures when the temperature is decreased below the CDW transition temperature.[8,16-18] A similar effect is observed for the ferecrystals (Figure VI.9). Furthermore, the onset temperatures for the charge density wave formation were determined from the resistivity vs. temperature curves by determining the point at which the resistivity starts to increase with decreasing temperature, shown in the inset in Figure VI.8. The transition temperature in the ferecrystals clearly increases with increasing *m*. Hence, a larger spacing between the VSe_2 layers (filled with SnSe) seems to be favorable for the formation of a CDW at

higher temperatures. This might be due to an increased quasi-two-dimensional behavior of the VSe_2 inside the $[(SnSe)_{1.15}]_m(VSe_2)$ ferecrystals with increasing m. By preparing samples with different m values we are able to tune the electrical properties systematically.

It is interesting to note that for the ferecrystals which contain $TaSe_2$ instead of VSe_2 such discontinuities in resistivity or Hall coefficient have not been observed,[19] although $TaSe_2$ also has a CDW state with an incommensurate CDW transition at $T \approx$ 112-120 K and a commensurate one at $T \approx$ 85-110 K.[24-26] The ferecrystals $[(SnSe)_{1.15}]_m(TaSe_2)$ (m =1, 2) have exhibited metallic behavior with an approximately constant slope of the resistivity vs. temperature curve for the temperature range between 30-300 K.[19] Hence, the interaction between SnSe and $TaSe_2$ must be such that the CDW formation is suppressed, whereas for $[(SnSe)_{1.15}]_m(VSe_2)$ it is enhanced. Both, Ta and V, are group V transition metals. In MLCs containing VSe_2 or $TaSe_2$, the coordination of the Se atoms around V atoms is octahedral, whereas for $TaSe_2$ in $[(SnSe)_{1.15}]_m(TaSe_2)$ the coordination of the Se atoms around the Ta atoms is trigonal prismatic.[9,19] This structural difference might result in a different coupling between SnSe and $TaSe_2$ in $[(SnSe)_{1.15}]_m(TaSe_2)$ and SnSe and VSe_2 in $[(SnSe)_{1.15}]_m(VSe_2)$ ferecrystals; resulting in the observed differences.

CHAPTER VII

ABCB LAYERED FERECRYSTALS

VII.1. Introduction

When working with extended solids, chemical substitutions and solid solutions are traditional techniques used by materials scientists for the tuning of physical properties.[1,2] In this way, a single crystal type can be used for several applications; silicon is a very good example of this where, through doping, the majority carrier type is manipulated.[1,2] The high-temperature synthesis techniques most often used, result in random placement of the elements being alloyed on the available crystallographic positions within the structure. Mixed element solids typically have a miscible limit, where some materials can form completely miscible,[3] while other's potential tuning capabilities are limited.[4-6] In these solid solutions the lattice parameters are continuously variable as different sized atoms are substituted into the parent lattice and the resulting change in lattice parameters typically follow Vegard's law. As a result of continuous variation in lattice parameters it is expected that the properties of these compounds are typically a smooth function of the alloying as well.[1,2]

When using doping techniques, such as ion implantation, or when approaching the miscible limit, traditional techniques for mixed element solids can introduce defects or strain into the lattice and thereby lower mobility.[1,2] The ferecrystalline $[(MX)_{1+y}]_m(TX_2)_n$ composite crystals offer an opportunity to manipulate properties by changing composition of the intergrowth, with designed selection of m and n, while not straining

the crystal lattice or increasing defects.[7,8] The work on $[(SnSe)_{1.15}]_m(TaSe_2)_n$ and $[(SnSe)_{1.15}]_m(VSe_2)$ ferecrystals confirmed that the metallic conduction of the TX_2 constituent was preserved and is a sensitive function of the layering sequence.[7,8] Also, with the $[(SnSe)_{1.15}]_m(VSe_2)$ ferecrystals, a charge density wave transition occurred with a trending onset temperature, dependent on the value of m.[8] These data suggest that the ferecrystalline intergrowths can preserve bulk characteristics of the constituents, and that a CDW transition can be manipulated by increasing the quasi-two-dimensionality of the layered structure. With these promising results on the $[(MX)_{1+y}]_m(TX_2)_n$ ferecrystals an interesting next step is to attempt combining two separate $[(MX)_{1+y}]_m(TX_2)_n$ compounds, in order to test the capability of the modulated elemental reactant (MER) synthetic technique and to indirectly study the electronic structure through the resulting electrical properties. That is, to synthesize an ABCB layered intergrowth, $[(MX)_{1+y}]_m(TX_2)_n[(MX)_{1+y}]_p(T'X_2)_q$ where m, n, p, and q are integers and $T \neq T'$, as well as an alloyed intergrowth, $[(MX)_{1+y}]_m(T_xT'_{1-x}X_2)_n$, and compare the resulting combination of properties of these two doping styles (Figure VII.1).

Herein we report the synthesis of $[(SnSe)_{1.16}]_m(VSe_2)_n[(SnSe)_{1.16}]_p(TaSe_2)_q$ and $(SnSe)_{1+y}(V_xTa_{1-x}Se_2)$ ferecrystals along with a characterization of their structural and electrical properties. Using the modulated elemental reactant (MER) synthetic technique, we were able to take the calibrated parameters for the $[(SnSe)_{1.15}]_m(TaSe_2)_n$[7] and $[(SnSe)_{1.15}]_m(VSe_2)$[8] ferecrystals to create the $[(SnSe)_{1.16}]_m(VSe_2)_n[(SnSe)_{1.16}]_p(TaSe_2)_q$ ferecrystals. These deposition parameters were also used for creating the alloyed $(SnSe)_{1+y}(V_xTa_{1-x}Se_2)$ ferecrystals, by making estimations for the $V_xTa_{1-x}Se_2$ constituent followed by subsequent adjustments based on composition data from electron probe

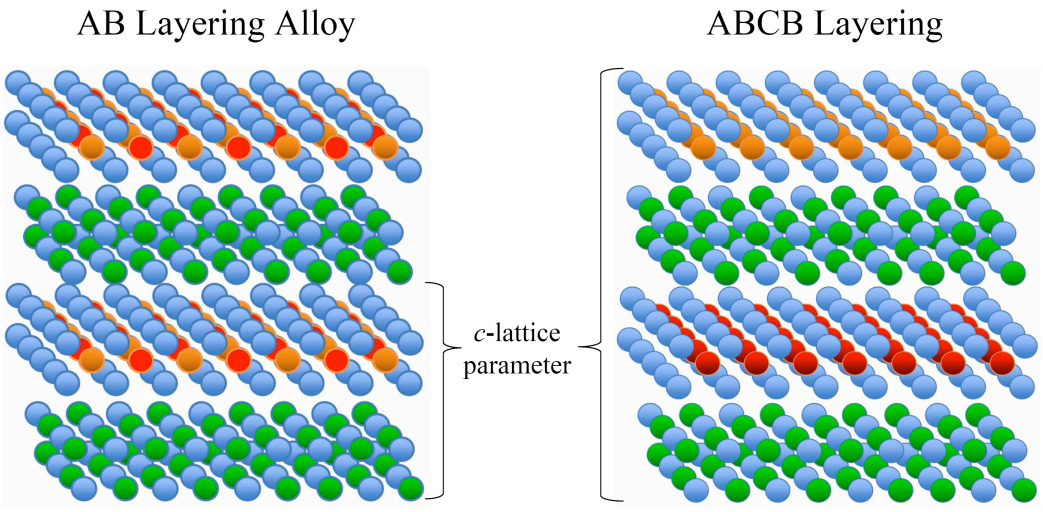

Figure VII.1. A theoretical image of a (left) alloyed $[(MX)_{1+y}]_1(T_{.5}T'_{.5}X_2)_1$ and (right) ABCB layered $[(MX)_{1+y}]_1(TX_2)_1[(MX)_{1+y}]_1(T'X_2)_1$ ferecrystal. The Alloyed *c*-lattice parameter is expected to be half that of the ABCB layered compound.

microanalysis (EPMA). Each integer increase of *m*, *n*, *p*, or *q* resulted in a linear increase of thickness, representing the addition of single structural units of SnSe, VSe_2, and $TaSe_2$. Structural characterization was primarily obtained through X-ray diffraction analysis, using Bragg-Brentano and in-plane scan geometries for studying the (00*l*) and (*hk*0) reflections, respectively. The chemical abruptness of the ABCB layering was confirmed by both the regular *d*-spacing of the superlattice layering, determined from XRD (00*l*) reflections, and by using the *z*-contrast difference between Ta and V in scanning transmission electron microscope (STEM) high angle annular dark-field (HAADF) imaging. The electrical transport properties of the $[(SnSe)_{1.16}]_m(VSe_2)_n[(SnSe)_{1.16}]_p(TaSe_2)_q$ and $(SnSe)_{1+y}(V_xTa_{1-x}Se_2)$ ferecrystals were studied by means of temperature-dependent resistivity and Hall measurements between room temperature and 20 K. Although the resistivity and carrier concentrations are of a metallic magnitude, there are anomalies in the electrical data between 100 and 150 K.

These anomalies are similar to those seen in the $[(SnSe)_{1.15}]_m(VSe_2)$ ferecrystals that arise from a CDW transition attributed to the VSe_2 constituent.[8] We speculate that a CDW transition is also present in the $[(SnSe)_{1.16}]_m(VSe_2)_n[(SnSe)_{1.16}]_p(TaSe_2)_q$ and $(SnSe)_{1+y}(V_xTa_{1-x}Se_2)$ ferecrystals.

VII.2. Results and Discussion

As described in Chapter III, creating a ferecrystalline $[(MX)_{1+y}]_m(TX_2)_n$, $[(MX)_{1+y}]_m(TX_2)_n[(MX)_{1+y}]_p(T'X_2)_q$, or $[(MX)_{1+y}]_m(T_xT'_{1-x}X_2)_n$ intergrowth compound first requires a calibrated as-deposited "precursor" that mimics the intergrowth's composition and absolute amount of materials. Any excess or lack of materials relative to what is required for forming single structural units of MX (two M/X atomic layers) or TX_2 (one TX_2 monolayer) will create defects in the final layering. To achieve a precursor of ideal materials requires an extensive calibration procedure. For the $[(SnSe)_{1.16}]_m(VSe_2)_n[(SnSe)_{1.16}]_p(TaSe_2)_q$ ferecrystals, the deposition parameters previously calibrated for the $[(SnSe)_{1.16}]_m(TaSe_2)_n$ and $[(SnSe)_{1.16}]_m(VSe_2)$ ferecrystals were used. For the $(SnSe)_{1+y}(V_xTa_{1-x}Se_2)$ ferecrystal, again the previously calibrated deposition parameters for creating SnSe structural units were used, but estimations based on the previous calibrations had to be made for creating $V_xTa_{1-x}Se_2$ structural units. Using electron probe microanalysis,[9] the composition of resulting $(SnSe)_{1+y}(V_xTa_{1-x}Se_2)$ precursors was analyzed and subsequent adjustments were made. The X-ray reflection (XRR) data showed weak and broad (00*l*) reflections at lower angles, representing the abrupt as-deposited layers.

To see if the as-deposited layers would self-assemble into the desired $[(SnSe)_{1.16}]_m(VSe_2)_n[(SnSe)_{1.16}]_p(TaSe_2)_q$ and $(SnSe)_{1+y}(V_xTa_{1-x}Se_2)$ ferecrystals, the precursors were annealed on a copper hot plate, under a nitrogen atmosphere to reduce oxidation (0.5 ppm O_2). Also, a representative precursor was annealed as a function of temperature to determine the ideal annealing temperature, the resulting Bragg-Brentano XRD patterns for a $[(SnSe)_{1.16}]_4(VSe_2)_4[(SnSe)_{1.16}]_4(TaSe_2)_4$ precursor are shown in Figure VII.2. The four XRD patterns in Figure VII.2 all contain Bragg reflections that can be indexed as (00*l*) reflections with a single *d*-spacing, representing the consistent layering of the $[(SnSe)_{1.16}]_4(VSe_2)_4[(SnSe)_{1.16}]_4(TaSe_2)_4$ intergrowth. The pattern resulting from a 450 ºC anneal resulted in the sharpest and most intense (00*l*) reflections,

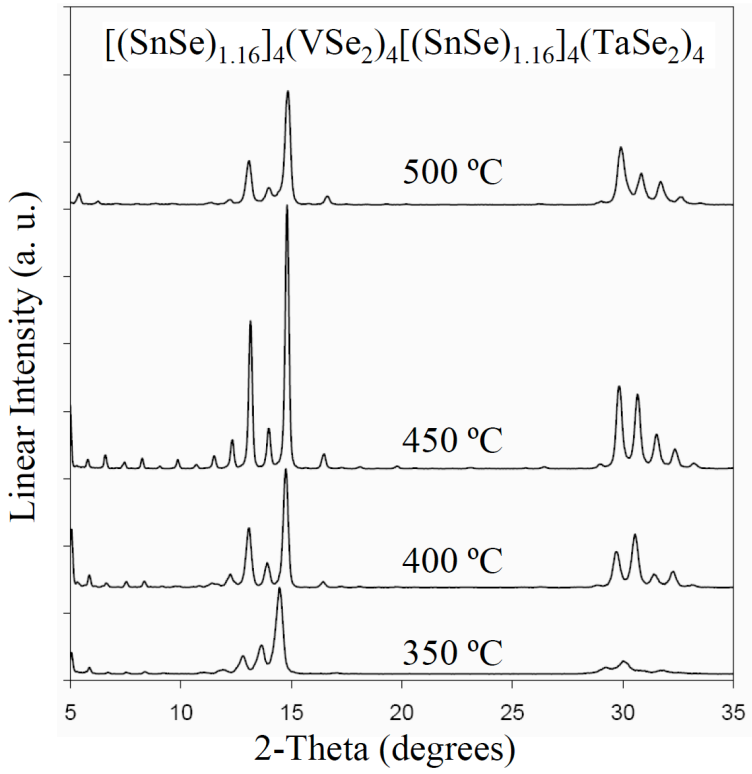

Figure VII.2. X-ray diffraction patterns, Bragg-Brentano scan geometry, of an ABCB layered precursor annealed at several different temperatures, 30 min anneal time.

this temperature was selected as the ideal annealing condition for the $[(SnSe)_{1.16}]_m(VSe_2)_n[(SnSe)_{1.16}]_p(TaSe_2)_q$ ferecrystals. A similar study was done for the $(SnSe)_{1+y}(V_xTa_{1-x}Se_2)$ ferecrystals, finding 400 ºC as the ideal annealing temperature (Figure III.19).

All of the $[(SnSe)_{1.16}]_m(VSe_2)_n[(SnSe)_{1.16}]_p(TaSe_2)_q$ ferecrystals made in this work were analyzed by Bragg-Brentano geometry XRD scans; also a $(SnSe)_{1.16}(V_{.51}Ta_{.49}Se_2)$ ferecrystal was studied. Figure VII.3 contains XRD patterns of two representative $[(SnSe)_{1.16}]_m(VSe_2)_n[(SnSe)_{1.16}]_p(TaSe_2)_q$ ferecrystals; one with *m*, *n*, *p*, and *q* all equal to 1 and the other equal to 3. Prior to starting Bragg-Brentano geometry XRD scans, the

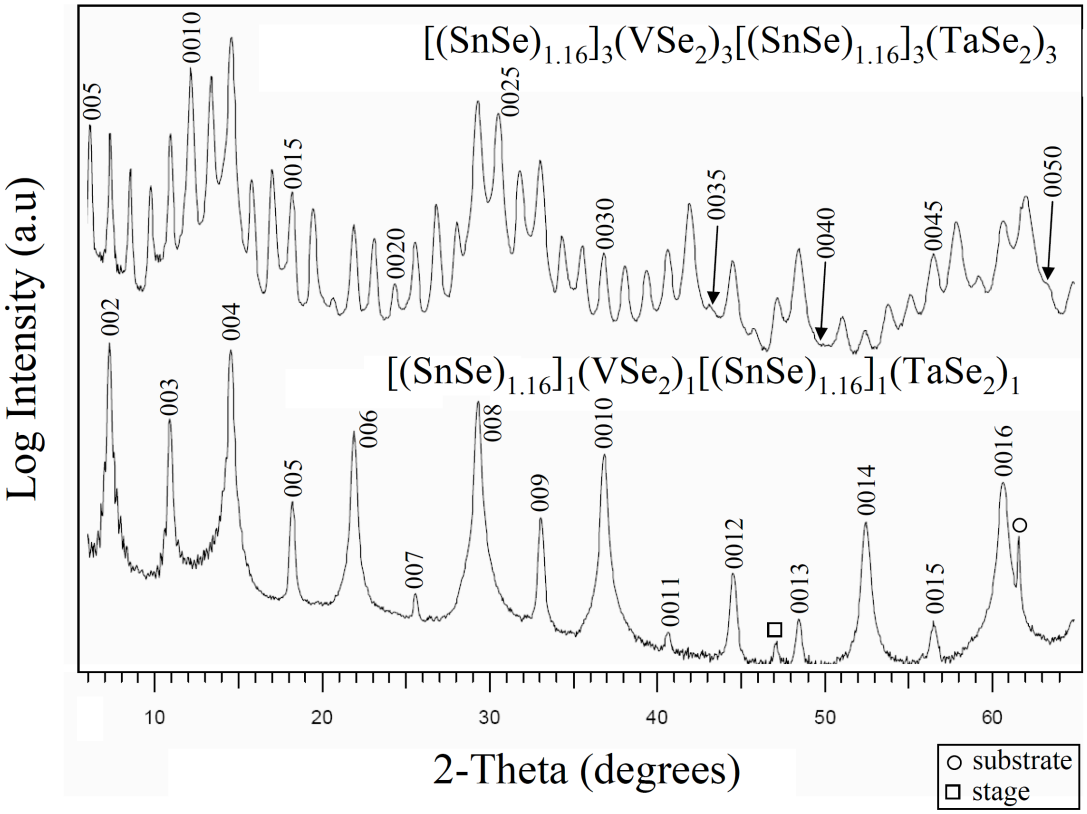

Figure VII.3. X-ray diffraction patterns, Bragg-Brentano scan geometry, of two ABCB layered ferecrystals. The (00*l*) reflections are indexed for the bottom pattern and every fifth (00*l*) reflection is indexed on the top pattern.

vertical incident beam was aligned such that the incident and detector angles are normal to the substrate surface. The resulting XRD patterns contained Bragg maxima that could all be indexed as (00*l*) reflections from a single *d*-spacing, representing the *c*-lattice parameter of the intergrowth layering; *c*-lattice parameters are compiled in Table VII.1. The presence of only (00*l*) reflections identifies the intergrowth layering as preferentially oriented with the (00*l*) planes of the layers parallel to the substrate surface. Also, this confirms that the nano-architecture laid down in the deposition is maintained through the

Table VII.1. A compilation of *c*-lattice parameters, determined from the positions of (00*l*) reflections in Bragg-Brentano XRD patterns.

m*:*n*:*p*:*q	**Thickness (nm)**	**Error (nm)**
1:1:1:1	2.42	0.01
1:2:1:2	3.64	0.01
	3.63	0.01
	3.64	0.01
2:1:2:1	3.57	0.01
	3.57	0.01
2:2:2:2	4.79	0.01
	4.80	0.02
	4.80	0.03
	4.81	0.01
	4.81	0.01
	4.80	0.03
3:1:3:1	4.72	0.03
3:2:3:2	5.95	0.01
	5.96	0.01
	5.97	0.05
	5.96	0.02
4:1:4:1	5.88	0.02
4:2:4:2	7.12	0.01
	7.11	0.01
	7.08	0.08
3:3:3:3	7.19	0.02
	7.19	0.02
4:4:4:4	9.57	0.03
	9.57	0.02
$(SnSe)_{1.15}(VSe_2)$	1.2030	0.0002
$(SnSe)_{1.15}(TaSe_2)$	1.238	0.001
$(SnSe)_{1.16}(V_{.51}Ta_{.49}Se_2)$	1.215	0.001

self-assembly process. For comparison the *c*-lattice parameters of $(SnSe)_{1.15}(TaSe_2)$,[7] $(SnSe)_{1.15}(VSe_2)$,[8] and $(SnSe)_{1.16}(V_{.51}Ta_{.49}Se_2)$ ferecrystals are reported in Table VII.1.

Due to the preferred orientation of the layers, a different XRD scan geometry was required to observe the in-plane or *ab*-plane diffraction characteristics of the $[(SnSe)_{1.16}]_m(VSe_2)_n[(SnSe)_{1.16}]_p(TaSe_2)_q$ and $(SnSe)_{1+y}(V_xTa_{1-x}Se_2)$ ferecrystals. Using a low incident angle, ~0.3 ºθ, and scanning the detector parallel to the layering, the XRD patterns in Figure VII.4 were obtained. In these patterns, the diffraction maxima can be indexed as belonging to either a SnSe constituent, with a square basal plane, or a TSe_2 constituent, with a hexagonal basal plane. This is an expected result for a $[(MX)_{1+y}]_m(TX_2)_n$ composite crystal, where the two constituents maintain independent crystal types.[10] In the XRD patterns several of the (*hk*0) reflections for the SnSe and TSe_2 constituents overlap, making it difficult to identify peak positions. However, for the $[(SnSe)_{1.16}]_1(VSe_2)_1[(SnSe)_{1.16}]_1(TaSe_2)_1$ ferecrystal, using the peak positions of the SnSe (220) and (420) and the TSe_2 (110) reflections, *a*-lattice parameters of 0.602 and 0.348 nm were determined for the SnSe and TSe_2 constituents, respectively. For the $(SnSe)_{1.15}(TaSe_2)$ and $(SnSe)_{1.15}(VSe_2)$ ferecrystals,[7,8] *a*-lattice parameters for SnSe = 0.6015(8) nm,[7] or 0.5935(4) nm,[8] $TaSe_2$ = 0.3456(4), and VSe_2 = 0.3414(3) were found. For the $(SnSe)_{1.16}(V_{.51}Ta_{.49}Se_2)$ ferecrystal, an *a*-lattice parameter of 0.602 and 0.3485 nm was found for the SnSe and $V_{.51}Ta_{.49}Se_2$ constituents, respectively.

To further investigate the $[(SnSe)_{1.16}]_m(VSe_2)_n[(SnSe)_{1.16}]_p(TaSe_2)_q$ ferecrystals' 3D crystallinity, 2D X-ray diffraction patterns were gathered using an image plate detector. The resulting pattern for a $[(SnSe)_{1.16}]_1(VSe_2)_1[(SnSe)_{1.16}]_1(TaSe_2)_1$ ferecrystal is shown in Figure VII.5. The pattern contains intensity maxima from diffraction off the

ferecrystal; however, the maxima are not sharp points of intensity as would be expected from a single crystal and they are not rings as would be expected for a powder sample. Instead the maxima contain a great deal of broadening along *l*, so much so that individual peak positions cannot be identified and only (*hkl*) families are identified. The combination of results from Bragg-Brentano, in-plane, and 2D X-ray diffraction studies have identified abrupt layering with a consistent *d*-spacing, in-plane crystallinity, but an extreme lack of coherence in axes that traverse through the layering (except for (00*l*)). These results are consistent with turbostratic disorder, where a random rotational

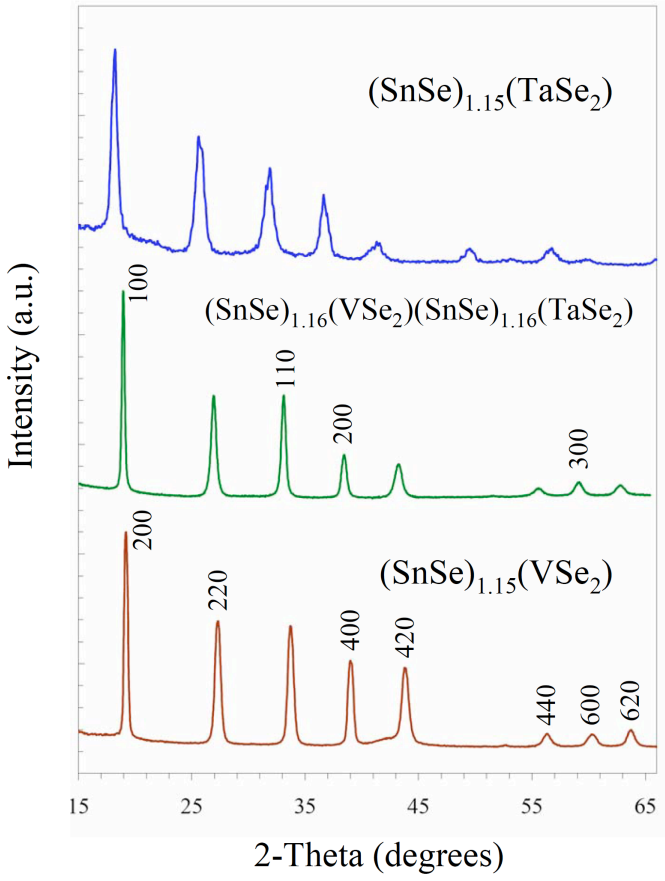

Figure VII.4. X-ray diffraction patterns from in-plane scan geometries for several ferecrystals. The (*hk*0) reflections are indexed for the SnSe reflections in the $(SnSe)_{1.15}(VSe_2)$ pattern and the TSe_2 reflections are indexed in the $[(SnSe)_{1.16}]_1(VSe_2)_1[(SnSe)_{1.16}]_1(TaSe_2)_1$ pattern; the indexing applies to all three patterns. X-ray wavelength, (top) 0.0946 nm, (middle and bottom) 0.0992 nm.

disorder between the layers disrupts periodic interlayer modulations. This disorder eliminates translational symmetry across the layers, causing an extremely short coherence length of particular (*hkl*) reflections ($l \neq 0$, $hk \neq 0$) and thereby the streaking of intensity present in Figure VII.5. These data also confirm the $[(SnSe)_{1.16}]_m(VSe_2)_n[(SnSe)_{1.16}]_p(TaSe_2)_q$ and $(SnSe)_{1+y}(V_xTa_{1-x}Se_2)$ intergrowths as ferecrystals.

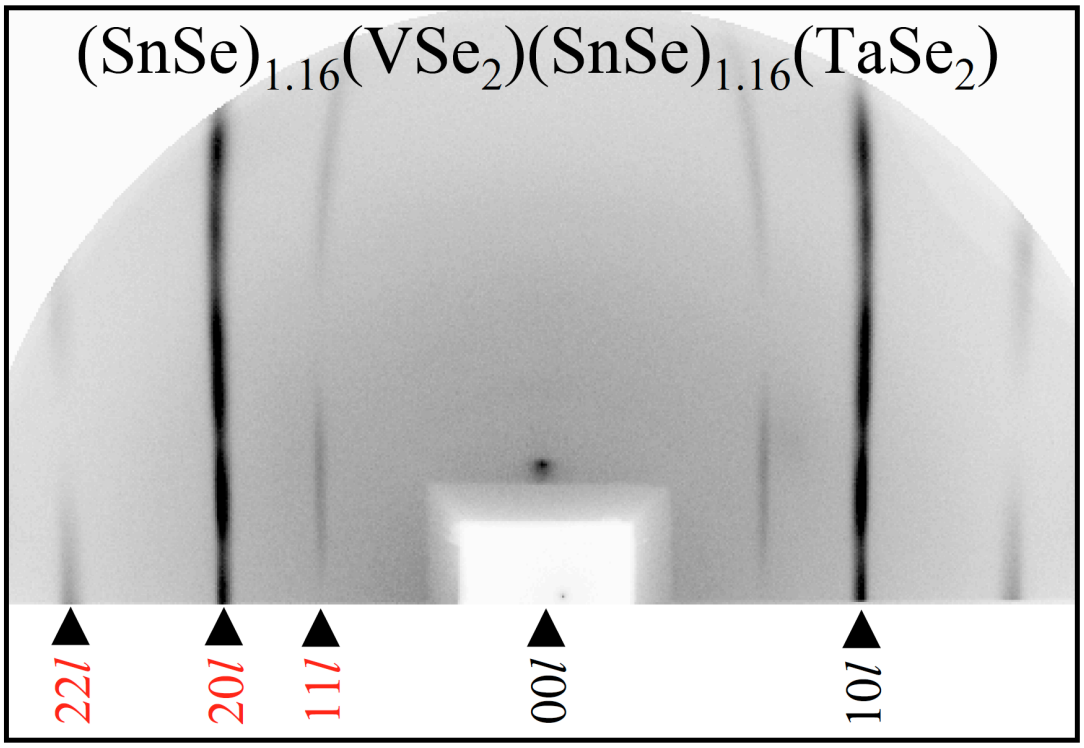

Figure VII.5. 2D X-ray diffraction pattern of an ABCB layered ferecrystal.

When synthesizing the $[(SnSe)_{1.16}]_m(VSe_2)_n[(SnSe)_{1.16}]_p(TaSe_2)_q$ ferecrystals, there was some thought as to whether the VSe_2 and $TaSe_2$ would remain chemically abrupt, as ABCB layering, or alloy, as $(A_{.5}C_{.5})B$ layering, (Figure VII.1). To investigate the chemical abruptness of the ABCB layering, we examined the *c*-lattice parameters of

the resulting ferecrystals and studied a representative $[(SnSe)_{1.16}]_4(VSe_2)_4[(SnSe)_{1.16}]_4(TaSe_2)_4$ ferecrystal by STEM-HAADF imaging. In Figure VII.6 the *c*-lattice parameters from Table VII.1 have been plotted vs. *m* (only for intergrowths where $m = n = p = q$). The slope of the linear regression in this graph is equal to the thickness of a single $[(SnSe)_{1.16}]_1(VSe_2)_1[(SnSe)_{1.16}]_1(TaSe_2)_1$ unit, 2.3840(2) nm. This value is slightly smaller in comparison to adding the *c*-lattice parameters of the $(SnSe)_{1.15}(TaSe_2)$ and $(SnSe)_{1.15}(VSe_2)$ ferecrystals (2.441(6) nm);[7,8] however, the near equivalency confirms the chemical abruptness of the ABCB layering. For if we created $(A_{.5}C_{.5})B$ instead of ABCB layering, the *c*-lattice parameter would be equivalent to the $(SnSe)_{1.16}(V_{.51}Ta_{49}Se_2)$ ferecrystal. Figure VII.7 contains a STEM-HAADF image of a representative $[(SnSe)_{1.16}]_4(VSe_2)_4[(SnSe)_{1.16}]_4(TaSe_2)_4$ ferecrystal. The *z*-contrast of the image means that the brightest intensity areas correspond to the atoms with the highest atomic number, in this case the Ta atoms, and the darkest areas are the V atoms. Although the image is not high resolution, using the *z*-contrast, it is clear that three separate areas of layering are present; representing the $(SnSe)_4$, $(VSe_2)_4$, and $(TaSe_2)_4$ sections. Also, the TSe_2 sections clearly show monolayers while the SnSe sections appear as bilayers; as is expected for the two crystal types. The *z*-contrast of the image clearly shows a chemical distinction between the VSe_2 and $TaSe_2$ layers. These data confirm that the ABCB layering maintains a high level of chemical abruptness.

The electrical transport properties of the $[(SnSe)_{1.15}]_m(TaSe_2)_n$ (Chapter IV) and $[(SnSe)_{1.15}]_m(VSe_2)$ (Chapter V and VI) ferecrystals were previously studied by means of temperature-dependent resistivity and Hall measurements (Hall coefficient data for the $(SnSe)_{1.15}(TaSe_2)$ ferecrystal was not obtained previously and is reported here (Figure

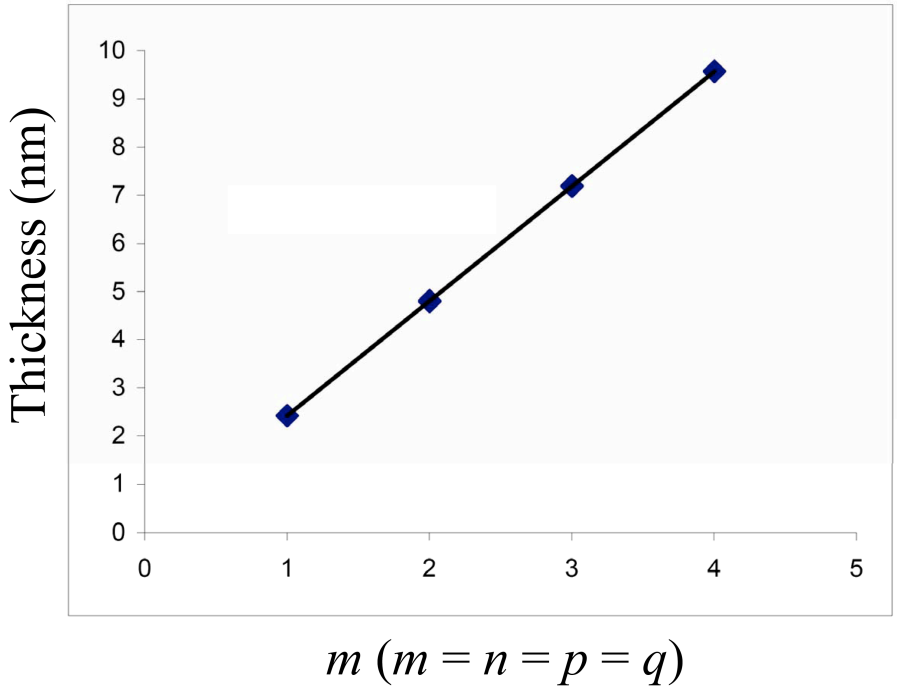

Figure VII.6. *c*-lattice parameters of several $[(SnSe)_{1.16}]_m(VSe_2)_n[(SnSe)_{1.16}]_p(TaSe_2)_q$ ferecrystals plotted as a function of *m*. Only *c*-lattice parameters from ferecrystals with $m = n = q = p$ were used.

VII.9). Both of these two systems showed metallic-like electrical properties, with electrical resistivity in the μΩm regime. The $[(SnSe)_{1.15}]_m(VSe_2)$ ferecrystal contained anomalies in its resistivity and Hall coefficient data characteristic of a CDW transition, which were attributed to a CDW transition arising from the VSe_2 constituent.[8] Although $TaSe_2$ is known to undergo a CDW transition, with a polytype dependent CDW onset temperature, no anomalies were seen in the $(SnSe)_{1.15}(TaSe_2)$ electrical data.[7,11] The same analysis techniques were used to investigate the $[(SnSe)_{1.16}]_m(VSe_2)_n[(SnSe)_{1.16}]_p(TaSe_2)_q$ and $(SnSe)_{1+y}(V_xTa_{1-x}Se_2)$ ferecrystals. Temperature-dependent resistivity is given for a $[(SnSe)_{1.16}]_1(VSe_2)_1[(SnSe)_{1.16}]_1(TaSe_2)_1$ and $(SnSe)_{1.16}(V_{.51}Ta_{.49}Se_2)$ ferecrystal in

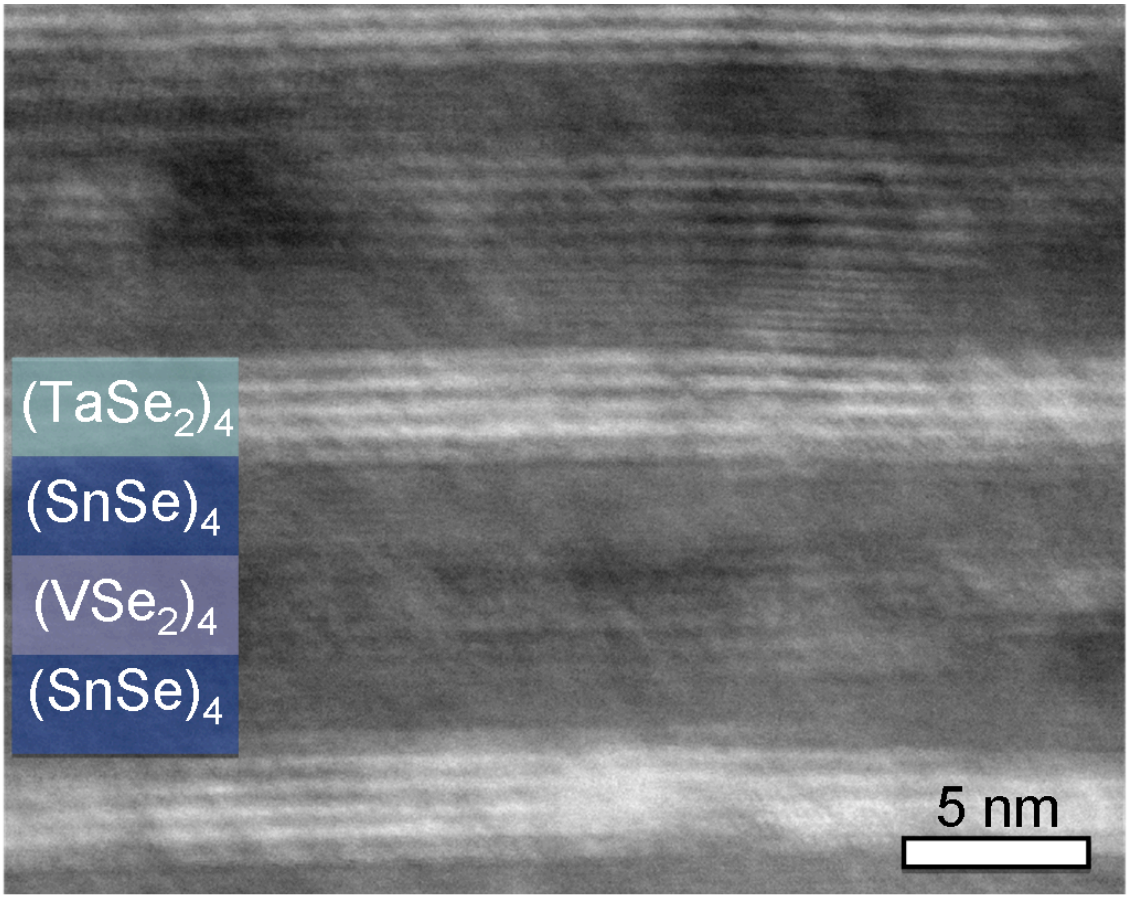

Figure VII.7. A STEM-HAADF image of a $[(SnSe)_{1.16}]_4(VSe_2)_4[(SnSe)_{1.16}]_4(TaSe_2)_4$ ferecrystal. Due to the *z*-contrast of the image, the brightest areas are those corresponding to Ta atoms and the darkest are V.

Figure VII.8 and Hall coefficient in Figure VII.9. The room temperature resistivity of the ABCB layered and alloyed ferecrystals (7.2 and 8.4 μΩm) is above the range (0.8 – 4.0 μΩm, at 300 K) previously reported for single crystal $(MX)_{1+y}(TX_2)_n$ MLCs containing TaX_2 or NbX_2 constituents (M = Sn, Pb, and Bi; X = S and Se).[10]

For both the $[(SnSe)_{1.16}]_1(VSe_2)_1[(SnSe)_{1.16}]_1(TaSe_2)_1$ and $(SnSe)_{1.16}(V_{.51}Ta_{.49}Se_2)$ ferecrystals the temperature-dependent resistivity profile contains a non-linear increase with decreasing temperature followed by the beginning of a plateau at approximately 20

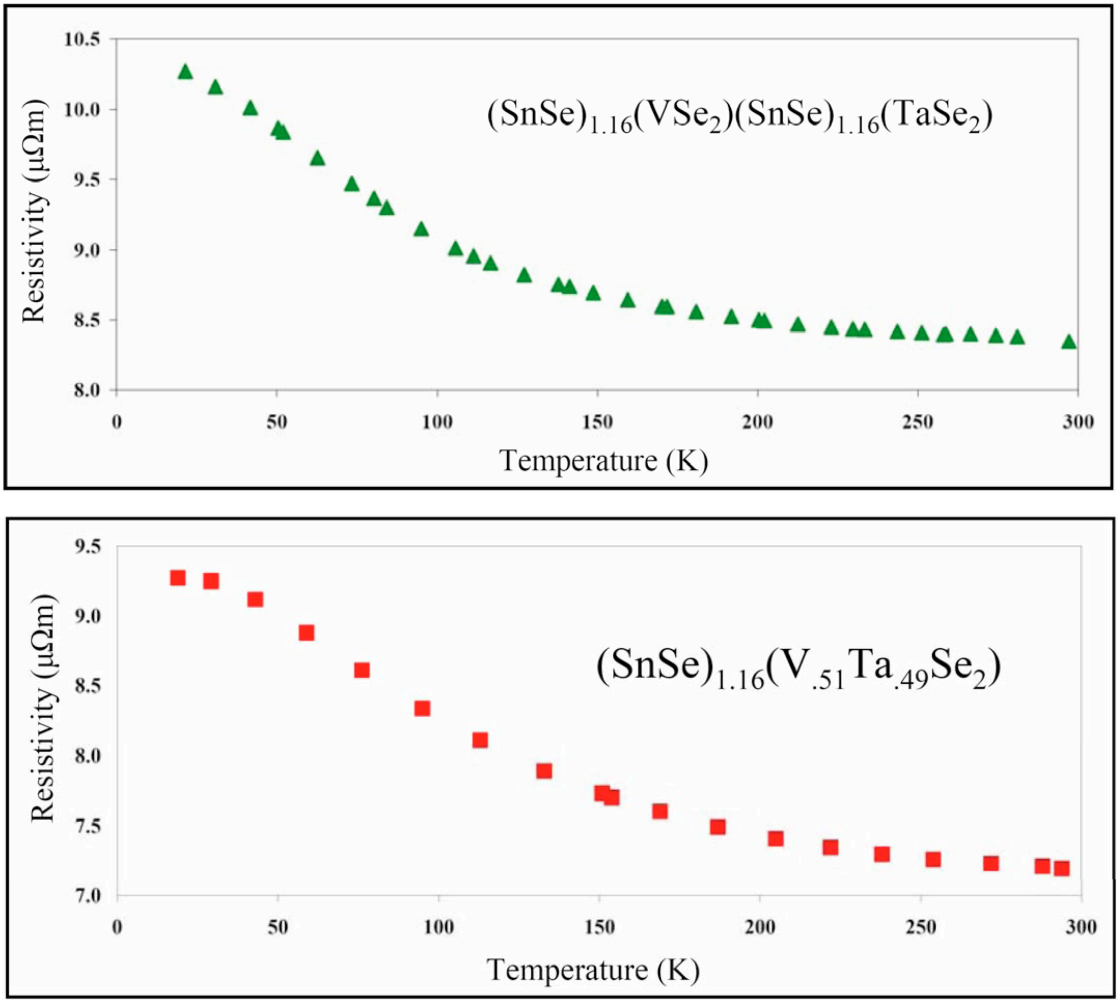

Figure VII.8. Temperature-dependent electrical resistivity from a $(SnSe)_{1.16}(V_{.51}Ta_{.49}Se_2)$ and $[(SnSe)_{1.16}]_1(VSe_2)_1[(SnSe)_{1.16}]_1(TaSe_2)_1$ ferecrystal.

K. These trends are similar to that seen in the electrical properties of $(SnSe)_{1.15}(VSe_2)$,[8] where the anomalies where attributed to a CDW transition arising from the VSe_2 constituent. When observing the Hall coefficient temperature dependence, the profiles are very different between the $[(SnSe)_{1.16}]_1(VSe_2)_1[(SnSe)_{1.16}]_1(TaSe_2)_1$ and $(SnSe)_{1.16}(V_{.51}Ta_{.49}Se_2)$ ferecrystals. The temperature dependence of the $[(SnSe)_{1.16}]_1(VSe_2)_1[(SnSe)_{1.16}]_1(TaSe_2)_1$ ferecrystal's Hall coefficient changes in magnitude less than it does for the $(SnSe)_{1.16}(V_{.51}Ta_{.49}Se_2)$ ferecrystal (0.0008 vs 0.002

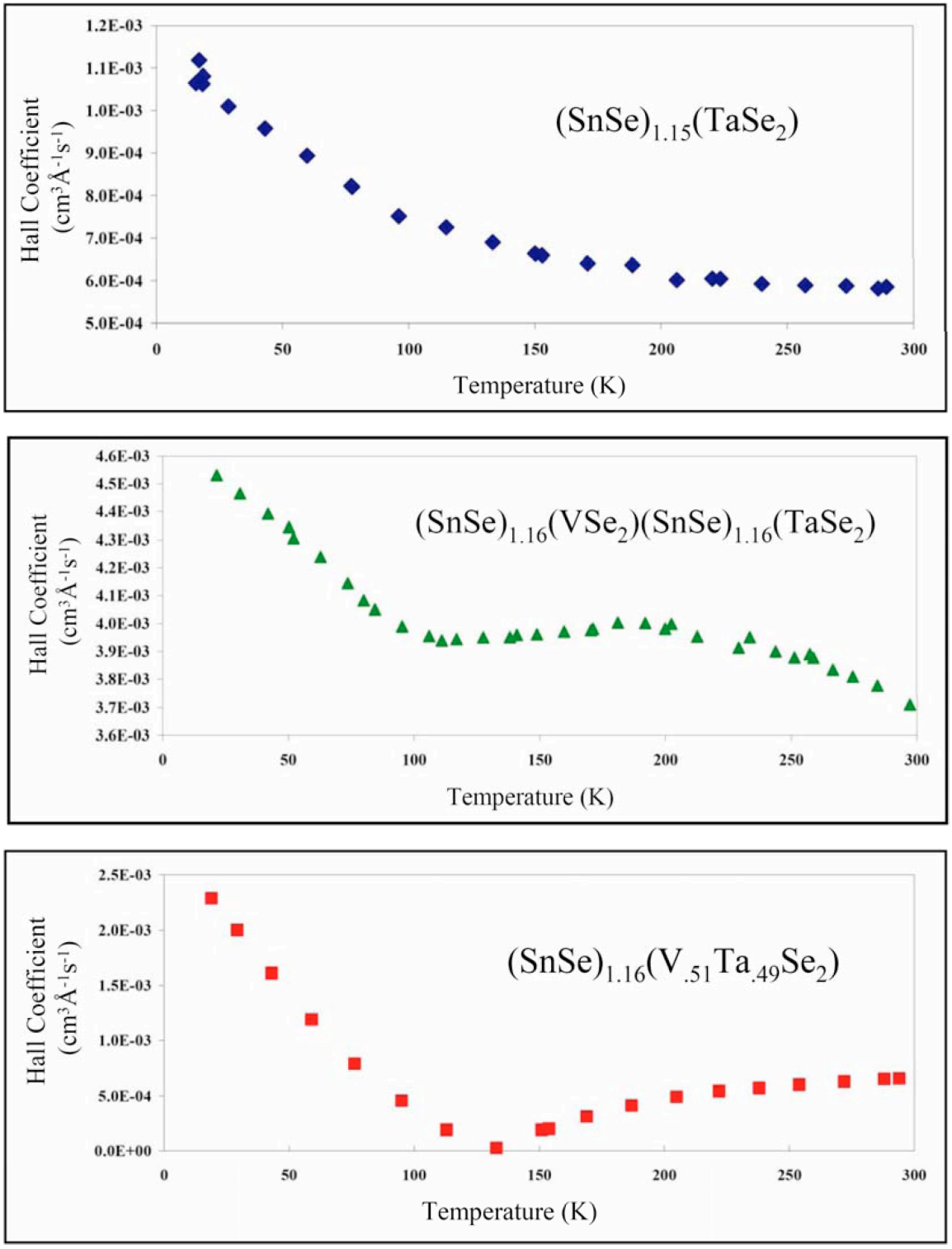

Figure VII.9. Temperature-dependent absolute Hall coefficient data.

$cm^3Å^{-1}s^{-1}$ between room temperature and 20 K). In comparison to literature values, the Hall coefficient changes in bulk VSe_2 by approximately 0.002 $cm^3Å^{-1}s^{-1}$ between room temperature and 1.5 K, while crossing over the CDW transition.[12] Also, the CDW transition in VSe_2 disrupts the linear profile of the temperature-dependent resistivity with a small bump or plateau. These data suggest that the $(SnSe)_{1.16}(V_{.51}Ta_{.49}Se_2)$ ferecrystal contains a similar transition to the CDW found in bulk VSe_2. For the $[(SnSe)_{1.16}]_1(VSe_2)_1[(SnSe)_{1.16}]_1(TaSe_2)_1$ ferecrystal, the temperature dependence of the Hall coefficient does not gradually trend as it does in the $(SnSe)_{1.15}(TaSe_2)$ ferecrystal but contains abrupt transitions. Possibly the VSe_2 constituent within $[(SnSe)_{1.16}]_1(VSe_2)_1[(SnSe)_{1.16}]_1(TaSe_2)_1$ still undergoes a transition but since carriers are also conducting through the $TaSe_2$ constituent, the effect on the Hall coefficient is less in magnitude.

For transition metal dichalcogenides that undergo a CDW transition, such as TaS_2 and VSe_2, alloying typically lowers the onset temperature followed by complete elimination of the CDW transition. This has been investigated for $Ta_{1-x}V_xS_2$, $V_{1-x}Ti_xSe_2$, and $V_{1-x}Fe_xSe_2$; all these compounds showed a loss of CDW transition at x values 0.15 or less.[4,5] However, it appears that a CDW transition occurs in both the $[(SnSe)_{1.16}]_1(VSe_2)_1[(SnSe)_{1.16}]_1(TaSe_2)_1$ and $(SnSe)_{1.16}(V_{.51}Ta_{.49}Se_2)$ ferecrystal, even though $x = 0.49$ in the alloy. Possibly the presence of turbostratic disorder in these intergrowths encourages the onset of a CDW transition. It has been suggested that the random rotational disorder between the constituent layers eliminates the periodic interlayer interactions that disrupt CDW transitions in misfit layer compounds.[8,10] Also, CDW transitions are more prevalent in low-dimensional solids and the $(MX)_{1+y}(TX_2)$

intergrowth effectively increases the TX_2 quasi-two-dimensionality. Further studies are warranted to investigate the possible CDW transition in $(SnSe)_{1+y}(V_xTa_{1-x}Se_2)$ and $[(SnSe)_{1.16}]_m(VSe_2)_n[(SnSe)_{1.16}]_p(TaSe_2)_q$ as a function of both alloy composition and ABCB layering sequence.

VII.3. Bridge

The $[(SnSe)_{1.15}]_m(TaSe_2)_n$, $[(SnSe)_{1.15}]_m(VSe_2)$, $(SnSe)_{1+y}(V_xTa_{1-x}Se_2)$, and $[SnSe)_{1.16}]_m(VSe_2)_n[(SnSe)_{1.16}]_p(TaSe_2)_q$ ferecrystals have been synthesized and structurally characterized. Studying their electrical transport properties revealed not only trending properties but a potential CDW transition. The magnitude of properties and the CDW transition were both suggested to exist because of the turbostratic disorder's presence in the intergrowths. Therefore, there is great interest in understanding the growth mechanism that creates turbostratically disordered misfit layered compounds; i.e. ferecrystals. Chapter IX investigates the self-assembly growth mechanism of $[(MX)_{1+y}]_m(TX_2)_n$ ferecrystals through a study on self-assembled TX_2 ferecrystals.

CHAPTER VIII

INSIGHTS INTO THE SELF-ASSEMBLY OF FERECRYSTALLINE COMPOUNDS FROM DESIGNED AMORPHOUS PRECURSORS

This work was accepted for publication by Chemistry of Materials in 2013 with co-authors Daniel B. Moore and David C. Johnson. Daniel B. Moore provided work on the $TiSe_2$ system, David C. Johnson is my advisor and research group leader, and I am the primary author.

VIII.1. Introduction

We have demonstrated that designed thin-film precursors, prepared by sequentially layering repeating patterns of sub-nanometer thick amorphous elemental layers, will self-assemble into targeted compounds preserving the nano-architecture of the precursor.[1,2] By controlling the repeating sequence in the precursor, this kinetically driven synthetic approach permits the targeted synthesis of new solids with designed nano-architecture. Figure VIII.1 shows a representative scanning transmission electron microscope (STEM) image from one of these new compounds: an $m = 3$, $n = 1$ layering sequence from the $[(PbSe)_{1.00}]_m[MoSe_2]_n$ family of materials. The structure consists of alternating layers of two different constituents, distorted rock-salt structured PbSe layers and transition metal dichalcogenide structured $MoSe_2$ layers, with a structurally and chemically abrupt interface between them. The (00*l*) plane of the PbSe is always adjacent

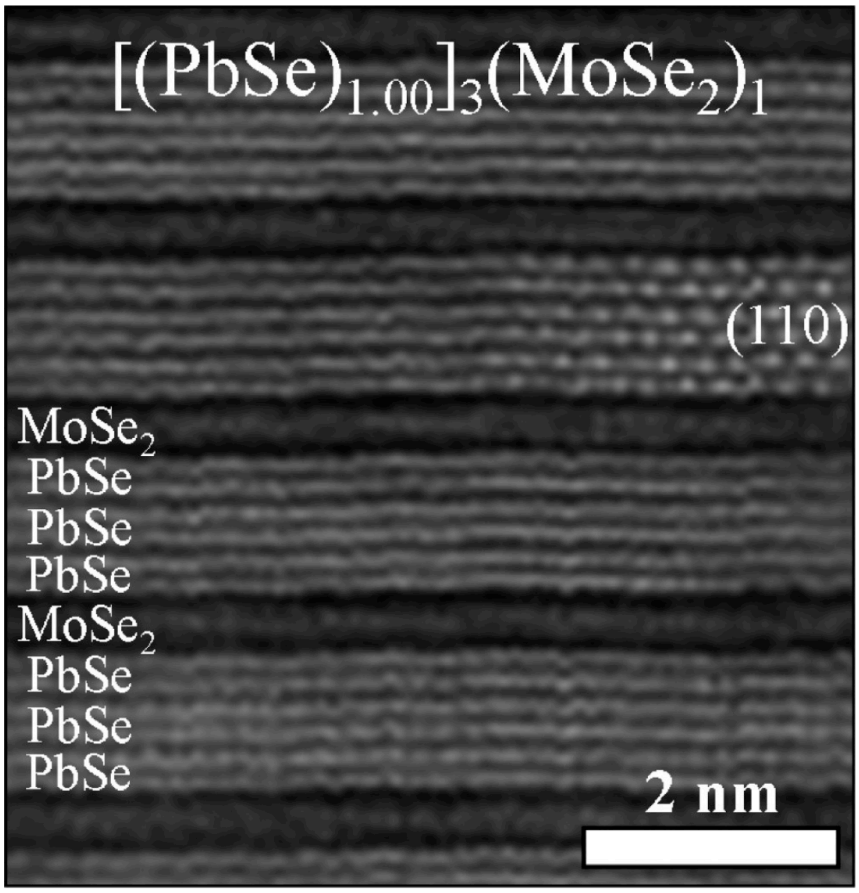

Figure VIII.1. High resolution STEM *z*-contrast image of $[(PbSe)_{1.00}]_3(MoSe_2)_1$.[7] The rock-salt structured PbSe and transition metal dichalcogenide structured $MoSe_2$ layers are distinct and regularly ordered. A (110) zone axis of the PbSe constituent is visible among non-major zone axes, (*hk*0). Random structural alignment between the different layers and even between grains in the same layer is found throughout. This turbostratic disorder is the defining characteristic of a ferecrystal.

to the (001) selenium planes of the transition metal dichalcogenide. The two constituents are independent of each other, maintaining nonequivalent in-plane lattice parameters and a random interlayer orientation. While in this particular example both constituents have the same cation per area, typically the difference in the constituents *ab*-plane cation per area results in a non-integer stoichiometry $(1 + y)$ in the formula unit. The constituents also have an arbitrary rotational orientation with respect to one another. This type of rotational disorder is known as turbostratic disorder.[3] We have referred to materials in

this new state of matter (layered structures with in-plane crystallinity, abrupt interfaces, layer-to-layer misregistration, and turbostratic disorder) as ferecrystals (from Latin *fere*, meaning almost).[2] The disorder in these compounds produce very unusual properties, including the lowest thermal conductivity every reported for a fully dense solid and higher mobility values for charge transport than those observed for crystalline misfit layer compounds prepared through high-temperature synthetic techniques.[4,5] The main differentiator between ferecrystalline and crystalline misfit layer compounds is turbostratic disorder. It eliminates interlayer epitaxial relationships in either one or both in-plane directions that would typically be found in the crystalline misfit layer compounds, where the unit cells of the two constituents distort to conform to one another.[6]

In contrast to traditional solid-state synthetic approaches, designed to yield thermodynamic products, the self-assembly of designed precursors is kinetically controlled and able to prepare multiple compounds with the same stoichiometry but different nanoarchitectures, such as the $[(PbSe)_{0.99}]_m(WSe_2)_n$ series, produced with m = 1−8.[1] Gaining an understanding of the mechanism by which these precursors self-assemble into their targeted structures is important, both to optimize the synthetic procedure, as well as successfully extend this approach to new constituent structure combinations. Initially we hypothesized that local composition controls the structure of the compounds that nucleate in each region of the precursor. We expected that each nucleation event would have a random orientation. A sequence of randomly oriented nucleation events would explain the observed turbostratic disorder between both the two different constituent structures and between adjacent Se-T-Se trilayers of the transition

metal dichalcogenide constituent (when *n* is 2 or greater). In this hypothesis, crystallographic alignment between the constituents, the (00*l*) plane of the MSe constituent parallel with the (00*l*) plane of the TSe_2, would be a consequence of the system minimizing interfacial free energy by aligning low energy surfaces toward one another via an Ostwald ripening mechanism. An alternative hypothesis is nucleation of one of the constituents followed by the templated growth of the second constituent off of the first during the self-assembly process. In this second hypothesis, the templated growth process would dictate the crystallographic alignment between layers, and the turbostratic disorder would be the consequence of a random selection between different layer-to-layer orientations during growth.

To investigate these different mechanisms and determine if either of them was plausible, we synthesized $TiSe_2$, VSe_2, and $TaSe_2$ via self-assembly of designed precursors. We chose these transition metal dichalcogenides because they stabilize with different numbers of polytypes in their bulk form.[8–12] VSe_2 and $TiSe_2$ form only a 1T polytype in bulk form, where the Se-T-Se trilayer sandwich has an A-b-C stacking arrangement resulting in octahedral coordination of the transition metal by selenium. These basal plane structural units stack directly on top of each other, in an AAA stacking arrangement in the 1T polytype. $TaSe_2$ forms several polytypes, depending on subtly different synthesis conditions, which have both A-b-C and A-b-A stacking arrangements of the Se-T-Se trilayer sandwich, resulting in octahedral and trigonal prismatic coordination of Ta, respectively. These basal plane structural units stack in a variety of ways to create the large number of different polytypes observed for $TaSe_2$, including the AAA stacking arrangement with octahedral coordination of Ta leading to the 1T

polytype, an AB stacking of Se-Ta-Se structural units with trigonal prismatic coordination of Ta leading to the 2H polytype, and an ABC stacking of layers with trigonal prismatic coordination of Ta leading to the 3R polytype. Our two proposed self-assembly mechanisms would result in different outcomes for these different transition metal dichalcogenides. Random nucleation and growth of each Se-T-Se trilayer would result in a ferecrystalline polytype being formed for all three compounds. Nucleation of an initial Se-T-Se trilayer followed by the templated growth of the following basal plane units would result in only a 1T polytype for both VSe_2 and $TiSe_2$ as only an AA stacking would be expected on the basis of the structure of the bulk compounds. $TaSe_2$, on the other hand, would be expected to form a ferecrystalline polytype because once an initial layer forms (say an "A" layer), there are two potential orientations for nucleation and growth of the next layer crystallizing (either B or C), which have very similar energies. Since there is always a random selection between two potential next layers, templated growth would result in random orientations between layers creating turbostratic disorder.

In this study, we will show that VSe_2 and $TiSe_2$ both form the ordered 1T polytype and that $TaSe_2$ formed a turbostratically disordered, ferecrystalline polytype. These results suggest that nucleation and subsequent templated growth is the self-assembly growth mechanism rather than distinct, random nucleation events in each layer. Also, compounds prepared via self-assembly of designed precursors will have different structures depending on the element used in the transition metal dichalcogenide. For elements that preferentially form only a 1T polytype, then the resulting compound will consist of crystalline TX_2 layers with the expected 1T polytype interlayer modulation. If the transition metal dichalcogenide can form polytypes with more than one basal plane

unit in the unit cell, then the resulting compound will consist of nanocrystalline TX_2 layers but will have turbostratic disorder between the Se-T-Se structural units.

VIII.2. Experimental Details

The transition metal dichalcogenide samples investigated in this study were formed through physical vapor deposition using a custom built high-vacuum deposition system[13] evacuated to a base pressure of 1×10^{-7} mbar before deposition. Elemental sources were purchased from Alfa Aesar. Selenium (99.999% purity) was evaporated using an effusion cell. Titanium (99.99% purity), tantalum (99.95% purity), and vanadium (99.7% purity) were evaporated using a Thermionics electron beam gun. The films were deposited on (100) oriented, polished silicon substrates positioned above the evaporating sources. Pneumatic powered shutters, located between each source and the substrate, were used to control the deposition. A custom LabVIEW program controlled the position of the shutters and the order in which elements were deposited. A quartz microbalance crystal monitoring system was used to control deposition rates. Se, Sn, and V were deposited at rates below 0.5 Å/s.

The deposition of TSe_2 specimens was not an epitaxial process. Instead, individual elemental layers were amorphously deposited onto a nominally room temperature substrate. Ideally each amorphous T-Se bilayer within the precursor will self-assemble a plane of Se-T-Se structural units on annealing. Calibration of the deposition times was necessary to determine this ideal amount of material per T-Se bilayer. Annealing was performed on a hot plate, under a nitrogen atmosphere to reduce oxidation (~0.5 O_2 ppm). Composition of the films was analyzed by electron probe microanalysis

(EPMA) using a thin-film technique described elsewhere.[14] The total film thickness was determined by the number of layers deposited. In this study approximately 50 nm was targeted, as this was a sufficient thickness for our analytical techniques.

X-ray reflection (XRR) and X-ray diffraction (XRD) data were obtained on a Bruker D8 Discover diffractometer, using Cu Kα radiation and Göbel mirror optics. θ-2θ locked coupled scan geometry was used to acquire XRR scans (between 0° and 10° 2θ) and XRD scans (between 10° and 65° 2θ) of the precursors and annealed samples. High-resolution synchrotron X-ray diffraction data were acquired on beamline 33-BM of the Advanced Photon Source (APS), Argonne National Laboratory. A point detector was used for acquisition of diffraction scans in (*hk*0) direction (in-plane diffraction) using an X-ray energy of 12.501 keV. An image plate detector (mar345) was used for collection of (*hkl*) reflection data.

High-resolution transmission electron microscopy (HR-TEM) and selected area electron diffraction (SAED) were obtained on an objective lens c_s-corrected FEI Titan 80-300 kV TEM, equipped with a high angle annular dark field (HAADF) detector. HR-TEM samples were prepared at the Center for Advanced Materials Characterization in Oregon (CAMCOR) of the University of Oregon (UO) on a FEI Helios Nanolab D600 Dual Beam focused ion beam (FIB) by an in situ lift-out and thinning method, followed by low voltage ion beam polishing.

VIII.3. Results and Discussion

The modulated elemental reactant synthetic technique requires that the correct ratio of elements is deposited to provide local compositions in the precursor that will

nucleate into the desired constituents. For intergrowth structures, it also is necessary that the amount of material deposited per elemental sequence correspond to the number of atoms required to self-assemble a single crystallographic unit of the desired intergrowth compound. To determine the shutter times required for creating stoichiometric ratios of V:Se, Ti:Se, and Ta:Se, we deposited a series of samples for each system, holding the Se shutter time constant while varying the amount of time each shutter over the appropriate transition metal source was kept open. Using EPMA to determine composition, the resulting graph of composition versus shutter time provided a linear trend that was interpolated to determine the T and Se deposition time ratio that produced the ideal composition. The final sets of samples were prepared with approximately 5% excess Se to compensate for Se loss to evaporation during the annealing process, which was determined by analyzing the composition of pre- and post-annealed samples. The deposition times of both sources were then simultaneously varied while holding the previously calibrated T:Se ratio constant to adjust the deposited bilayer thickness while maintaining constant composition to determine if the kinetics of the self-assembly process was a function of bilayer thickness. X-ray reflection (XRR) analysis of the as-deposited films revealed Kiessig fringing and (00*l*) reflection maxima between 0 and 10 °2θ, suggesting that the elemental layers have not completely interdiffused on deposition and that the repeating elemental bilayers in each sample have consistent thicknesses. X-ray diffraction (XRD) analysis of the as-deposited films contain broad weak (0*0l*) reflection maxima at higher angles, with positions consistent with that expected for the transition metal dichalcogenides, suggesting that some nucleation has occurred either during deposition or while the samples were stored at room temperature. The precursors

were studied as a function of annealing temperature and time in order to probe when the as-deposited films would self-assemble into the targeted transition metal dichalcogenides. Figure VIII.2 contains the resulting XRD patterns of VSe_2 annealed at several different temperatures (for 30 min), and Table VIII.1 contains the unit cell sizes, compositions, and line widths of the (001) reflection for each annealing temperature. Annealing temperatures as low as 200 °C result in an enhancement of the (00*l*) reflections' intensity and a decrease in their line width; representing progressive crystallization of the targeted Se-T-Se basal plane units with a consistent spacing between them along the *c*-axis. This low-temperature self-assembly is a consequence of the very short diffusion length required for appropriate atoms to attach to the growing edges of nucleated crystallites. XRD rocking curves about the (00*l*) reflections reveal that these Bragg reflections narrow with increasing annealing temperature, indicating that the planes of Se-T-Se structural units become more aligned as the samples are annealed. Equivalent annealing studies on $TaSe_2$ and $TiSe_2$ produced similar data, suggesting that all these transition metal dichalcogenides nucleate and grow Se-T-Se structural units crystallographically aligned with their *c*-axis perpendicular to the substrate. The annealing conditions that produced the most intense (00*l*) X-ray reflections varied for the studied compounds, with 350 °C for 30 min required for both VSe_2 and $TiSe_2$, and 450 °C for 30 min required for $TaSe_2$. As the annealing temperature is raised above their respective ideal annealing conditions, the diffraction patterns of all of the compounds degrade in intensity, probably due to Se loss through sublimation. Oxidation also occurs at surprisingly low-temperatures, evidenced by the increased oxygen content with annealing temperature, despite the samples being annealed in an inert (0.5 ppm or less oxygen) atmosphere. The formation

of X-ray amorphous transition metal oxides at the higher annealing temperatures results in lower selenium to metal ratios than expected for the diffraction patterns obtained.

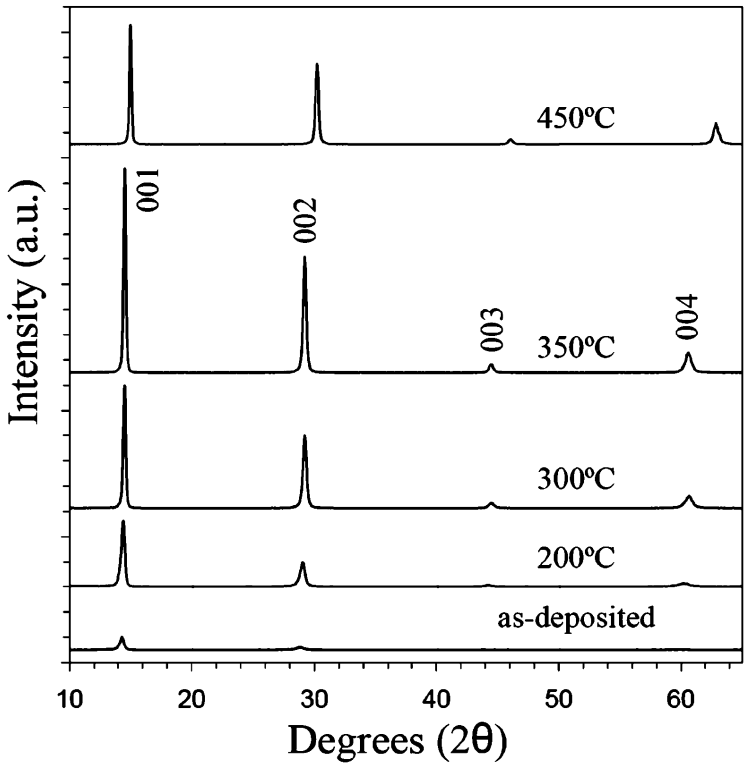

Figure VIII.2. X-ray diffraction patterns (θ-2θ locked coupled scan geometry) collected as a function of temperature for a representative precursor containing modulated V-Se bilayers, showing the low-temperature formation of VSe_2. The (00*l*) reflections are indexed for the 350 °C scan.

Over the course of this investigation, we discovered that the absolute amount of material deposited in each repeating Se-T bilayer had a surprisingly large effect on the kinetics of the self-assembly and coherent organization of the desired Se-T-Se transition metal dichalcogenide structural units. Figure VIII.3 contains a graph of the (001) reflection intensity of different VSe_2 and $TaSe_2$ samples annealed at the ideal conditions discussed above, as a function of the deposition time. The deposition time on the x axis of

Table VIII.1. Summary of composition, unit cell size perpendicular to the substrate, and line width collected as a function of annealing temperature for a representative precursor containing modulated V-Se bilayers.

annealing temp (°C)	Se/V composition	oxygen (%)	(001) fwhm (°2θ)	(00l) d-spacing (nm)
as-deposited	2.14(4)	3.1(5)	0.31(1)	0.6184(5)
150	2.18(5)	2.6(4)	0.26(1)	0.6167(5)
200	2.09(5)	4.0(5)	0.19(1)	0.6139(5)
250	1.90(5)	3.7(5)	0.168(9)	0.6115(2)
300	1.84(4)	3.2(4)	0.141(7)	0.6103(1)
350	1.81(4)	3.2(5)	0.128(6)	0.6103(5)
450	1.49(4)	6.0(7)	0.130(7)	0.5906(2)
500	1.31(3)	8.1(6)	0.129(7)	0.5908(1)

Figure VIII.3 is proportional to the thickness of the T-Se bilayers deposited in each sample, while the ratio of deposition times for the two elements was kept constant to maintain the ratio of T:Se at the desired 1:2 ratio with a 5% excess selenium. The data presented in Figure VIII.3 clearly suggest that there is an ideal bilayer thickness, which we postulate is the thickness that contains the amount of material in each bilayer to self-assemble a single plane of Se-T-Se transition metal dichalcogenide structural units. The measured thickness of the as-deposited bilayers supports this idea. We speculate that if each as-deposited Se-T bilayer contains more or less material than the ideal amount, then significantly larger diffusion paths are required to either remove or gain material at the growth front to continue the growth of each Se-T-Se plane. Since the annealing temperature is low, resulting in low diffusion rates, this would have a drastic effect on the time required to crystallize each sample. The VSe_2, $TaSe_2$, and $TiSe_2$ samples discussed

in the remainder of this article were deposited with deposition times calibrated to produce this ideal amount of material per layer.

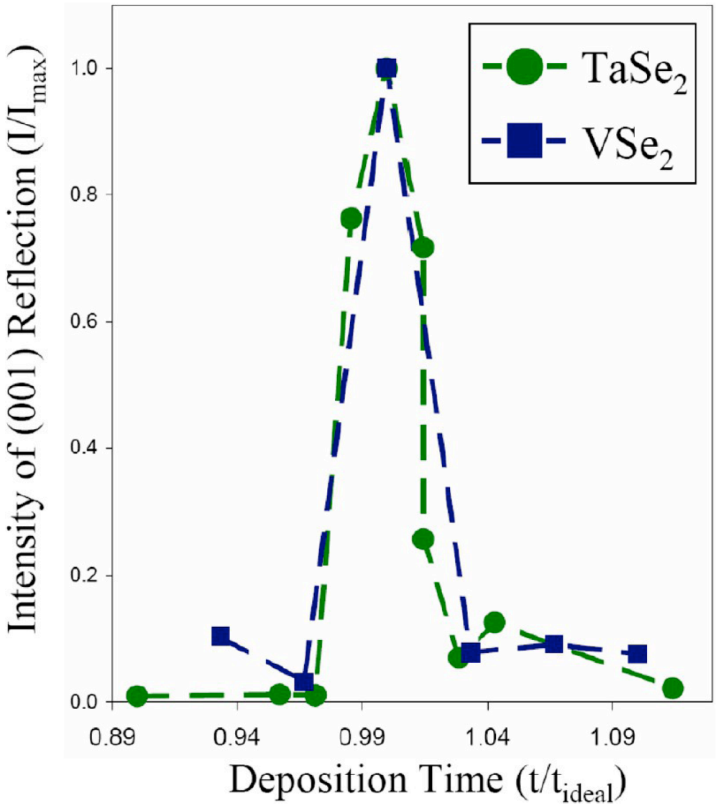

Figure VIII.3. Diffraction intensity of the (001) reflection for VSe_2 and $TaSe_2$ films as a function of the deposition time, which is proportional to the T-Se bilayer thickness of the precursor.

Figure VIII.4 contains the diffraction patterns of $TiSe_2$, VSe_2, and $TaSe_2$ samples prepared with ideal bilayer thickness in their precursors and annealed under their respective optimum annealing conditions. The Bragg maxima in the XRD patterns can all be indexed as (00*l*) reflections coming from the expected planes of Se-T-Se structural units forming with their *c*-axis perpendicular to the substrate. Indexing the peaks, as indicated in Figure VIII.4, allowed us to determine the thickness of a single Se-T-Se structural unit in each of these compounds and compare to that reported previously in the

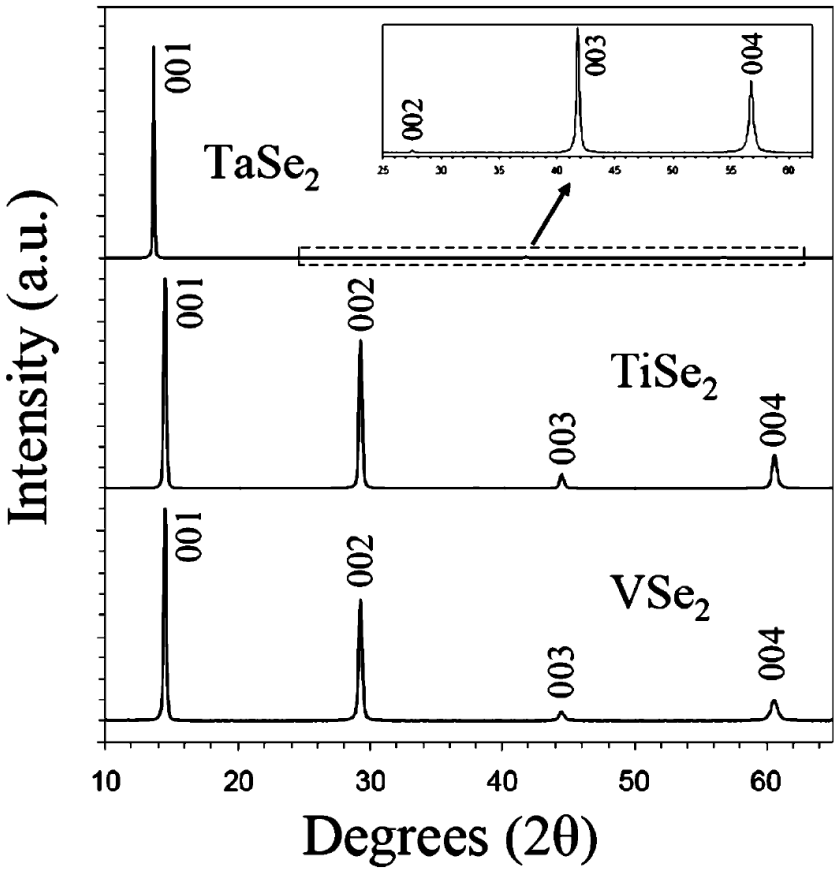

Figure VIII.4. X-ray diffraction patterns (θ-2θ locked coupled scan geometry) obtained for $TaSe_2$, $TiSe_2$, and VSe_2 samples. The precursors of these samples contained ideal thicknesses of their T-Se bilayers and were annealed at the respective optimum annealing temperatures and times for transition metal dichalcogenide formation. The (00*l*) reflections are indexed in each pattern. The higher angle reflections of $TaSe_2$ are only visible in the expanded box.

literature for bulk compounds. The *c*-lattice parameter of 0.6103(5) nm for VSe_2 is at the high end of the reported range for 1T $V_{1+x}Se_2$ (0.6105−0.5970 nm, with *c* increasing as *x* approaches zero),[8–10] suggesting that our VSe_2 is close to stoichiometric. The *c*-lattice parameter of 0.6036(2) nm for $TiSe_2$ is slightly larger than the *c*-lattice parameter reported for stoichiometric 1T $TiSe_2$, c = 0.6008(3) nm.[11] The *c*-lattice parameter of 0.6478(3) nm for $TaSe_2$, however, is significantly higher than any of the *c*-lattice

parameters (0.6272−0.6392 nm) reported for different polytypes in the literature.[12] The ratio of diffraction intensities between (00*l*) reflections for the self-assembled $TiSe_2$ and VSe_2 compounds is similar to that reported for their 1T polytypes. However, the intensities of higher order (00*l*) reflections for $TaSe_2$ are an order of magnitude lower relative to the (001) reflection than expected for any of the known $TaSe_2$ polytypes.

In-plane XRD patterns were collected, using a grazing incidence scan geometry, to determine the *a*-lattice parameters of our $TiSe_2$, VSe_2, and $TaSe_2$ samples, and a representative XRD pattern for VSe_2 is shown in Figure VIII.5. All of the diffraction maxima in the patterns can be indexed as (*hk*0) reflections for the expected hexagonal lattices, confirming the preferred orientation seen in standard specular XRD scans, and *a*-lattice parameters were calculated from these data. The calculated *a*-lattice parameter a = 0.3361(3) nm for VSe_2 is at the low end of the reported range for 1T $V_{1+x}Se_2$, 0.335−0.343 nm, with a decreasing as x approaches zero,[8−10] suggesting that our VSe_2 is close to stoichiometric composition. The *a*-lattice parameter calculated for $TiSe_2$, 0.3563(5) nm, is also close to that reported for stoichiometric 1T $TiSe_2$, c = 0.3553 nm.[11] The calculated *a*-lattice parameter of 0.3441(6) nm for $TaSe_2$ is in the middle of a range (0.34348−0.34769 nm) reported in the literature for the different $TaSe_2$ polytypes.[12] The in-plane X-ray diffraction patterns collected confirm that Se-T-Se structural units have self-assembled upon annealing of the precursors, that they are preferentially oriented with their *c*-axis perpendicular to the substrate, and that the structures are similar to those reported previously for these compounds.

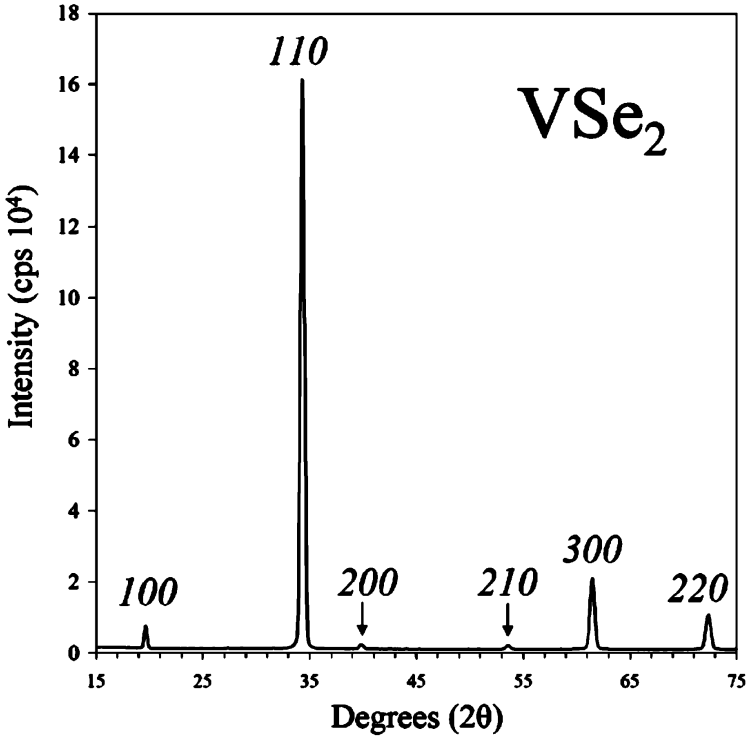

Figure VIII.5. In-plane grazing incidence diffraction pattern obtained for a representative VSe_2 sample. Reflections are indexed as (*hk*0) reflections for a hexagonal in-plane transition metal dichalcogenide structure. The incident X-ray wavelength was 0.0992 nm.

Cross-section transmission electron microscopy (TEM) studies were conducted on representative samples of VSe_2 and $TaSe_2$ to investigate the relative orientation of the Se-T-Se structural units in each layer. Figure VIII.6 contains representative cross section TEM images of VSe_2 and $TaSe_2$. Both images clearly show the layered structure expected for transition metal dichalcogenides with Se-T-Se structural units parallel to the substrate, in agreement with the XRD data discussed earlier. Averaging the intensity profile across the images, the planes of atoms are spaced by *d*-values in agreement with the *c*-lattice parameters calculated from the X-ray diffraction data. While both images clearly show the expected Se-T-Se structural units, the two images in Figure VIII.6 are different in the degree of consistent correlation and modulation between the layers of Se-T-Se structural

units. The different Se-V-Se layers in the VSe_2 image are all arranged in an identical orientation, down a (120) zone axis, and are stacked on top of one another as expected for a 1T polytype, with a grain size larger than the image shown. This information is consistent with our diffraction studies and supports the formation of a 1T polytype of VSe_2. In the $TaSe_2$ image the layers appear less correlated. Throughout the image there is no consistent zone axis and the spacing between layers appears variable. These observations are consistent with $TaSe_2$ having turbostratic disorder between layers and provide an explanation for the rapid decay of the (00*l*) reflection intensity with increasing *l* observed in the $TaSe_2$ diffraction pattern in Figure VIII.4.

To further characterize the degree of structural coherence between Se-T-Se structural units and hence the degree of turbostratic disorder within these transition metal dichalcogenide compounds, we collected XRD and transmission electron diffraction (TED) data throughout reciprocal space on several samples. The resulting images of (*hkl*) reflections from representative samples for each compound are shown in Figure VIII.7. The (*hkl*) reflections of VSe_2 and $TiSe_2$ contain the expected diffraction pattern of a 1T polytype with distinct and relatively sharp maxima, reflecting the long coherence length visually evident in the cross-section TEM image in Figure VIII.6. The small amount of streaking along *l* of the (*hkl*) ($h,k \neq 0$) reflections in the VSe_2 and $TiSe_2$ XRD patterns is likely caused by the approximately 50 nm total film thickness of the samples studied, as the electron diffraction patterns do not contain any streaking along the *l* direction for VSe_2. The X-ray diffraction pattern for the $TaSe_2$ sample, however, has very pronounced streaking along the *l* direction indicating a very short coherence length between Se-Ta-Se structural units, consistent with the turbostratic disorder seen in the TEM images of

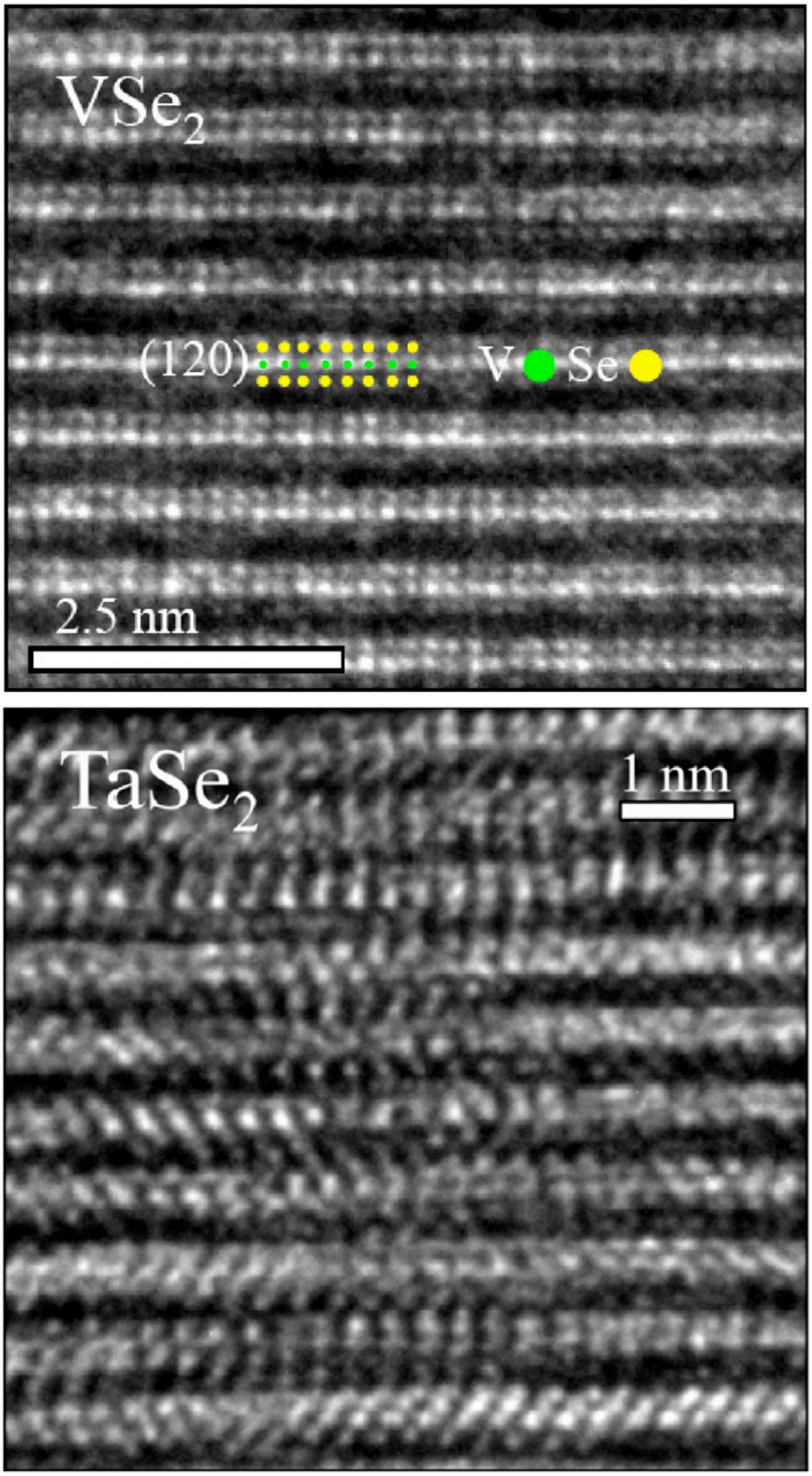

Figure VIII.6. Cross-sectional transmission electron microscope image of VSe_2 (top) and $TaSe_2$ (bottom). A (120) zone axis is clearly visible in the VSe_2 image while no consistent zone axis is visible within $TaSe_2$.

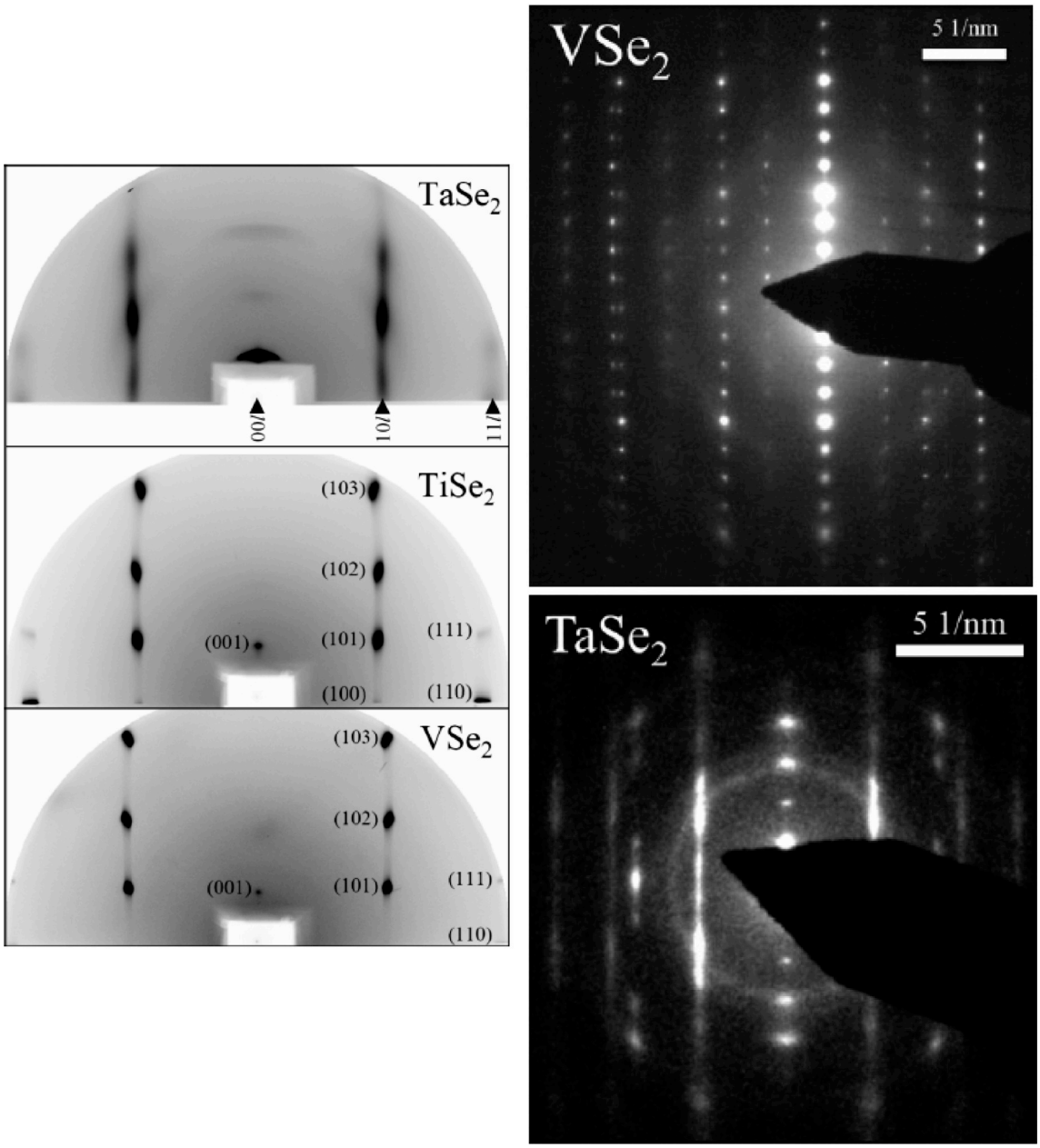

Figure VIII.7. (left) Grazing incidence X-ray diffraction by representative $TaSe_2$, $TiSe_2$, and VSe_2 specimens. (right) Transmission electron diffraction images taken through a cross section of representative VSe_2 and $TaSe_2$ specimens. The pronounced streaking of $TaSe_2$ reflections in the *c*-direction indicates extremely short coherence lengths reflecting the disorder between layers.

Figure VIII.6. A transmission electron diffraction pattern collected on a $TaSe_2$ sample showed similar streaking, confirming short coherence lengths along (*hkl*) ($h,k \neq 0$; $l \neq 0$)

directions. These data support our conclusion that VSe_2 and $TiSe_2$ form 1T polytypes, while $TaSe_2$ self-assembles into a disordered, ferecrystalline polytype.

Our results clearly differentiate between the two proposed self-assembly mechanisms. The data are not consistent with random nucleation and growth of each Se-T-Se layer, because the ordered 1T polytypes would not be expected to form by this mechanism. The diffraction data are consistent with nucleation and growth of an initial Se-T-Se layer, followed by templated growth of new layers during the self-assembly process. This would result in the observed 1T polytypes for VSe_2 and $TiSe_2$, with the formation of a ferecrystalline $TaSe_2$ polytype resulting from the random orientation of A, B, and C layers during templated growth. This growth mechanism is also consistent with a prior literature report on the synthesis of turbostratic disordered WSe_2 using the same procedure.[4] Bulk WSe_2 forms only the 2H polytype when prepared via traditional approaches, which contains an ordered AB stacking sequence of Se-W-Se layers with trigonal prismatic coordination of W. Nucleation followed by templated growth of subsequent layers would lead to a turbostratically disordered polytype, because once the initial layer nucleates and grows there are two options for orientation of the next layer crystallizing. Both arrangements have very similar energies and result in a random selection of the two possible modulations as additional layers are templated. It appears that, within the transition metal dichalcogenide compounds, self-assembly of turbostratic polytypes is dictated by having bulk polytypes with more than one Se-T-Se unit per unit cell.

The data obtained in this study also explain the turbostratic disorder found in many new $[(MSe)_{1+y}]_m(TSe_2)_n$ intergrowth compounds (M = Pb, Bi, Ce, and Sn; T = W,

Mo, Nb, Ta, and Ti; $y = -0.1$ to 0.18; and $m,n = 1-14$)[1,2,5,15–22] prepared using the self-assembly of designed MER precursors. In all of these ferecrystalline intergrowth compounds, there is rotational disorder between the MSe and TSe_2 units due to the structural misfit between them. The structural misfit results in no favored orientation for nucleation of the next constituent layer, which encourages random rotational disorder. $[(MSe)_{1+y}]_m(MoSe_2)_n$ where M = Pb and Sn, $[(PbSe)_{1+y}]_m(WSe_2)_n$, and $[(SnSe)_{1.15}]_m(TaSe_2)_n$ intergrowth compounds were found to form ferecrystals[1,15–17,21] with random rotational disorder at the MSe-TSe_2 interfaces and between Se-T-Se structural units. This is consistent with our findings reported here, since both $MoSe_2$ and WSe_2 form 2H polytypes as bulk compounds and bulk $TaSe_2$ forms several polytypes. Few $[(MSe)_{1+y}]_m(TiSe_2)_n$ intergrowth compounds have been reported to date, but $[(PbSe)_{1.18}]_1(TiSe_2)_2$ was recently reported as the first example in this family to be self-assembled from a designed MER precursor.[22] In this ferecrystal, there is turbostratic disorder at PbSe-$TiSe_2$ interfaces but each $TiSe_2$-$TiSe_2$ pair forms the 1T polytype. This is also consistent with nucleation followed by interlayer templating of subsequent layers as the self-assembly growth mechanism because bulk $TiSe_2$ only forms the 1T polytype.

The proposed self-assembly mechanism of nucleation followed by templated growth explains both the crystallographic alignment of constituents at the interface and the turbostratic disorder between them. The disorder in both binary TSe_2 compounds and in the TSe_2 constituent in $[(MSe)_{1+y}]_m(TSe_2)_n$ intergrowth compounds is dictated by the polytypes found for the bulk TSe_2 compound. This proposed template nucleation mechanism implies, however, that the disorder in the TSe_2 layers of the reported ferecrystal is not locally random as previously suggested. Instead of each subsequent Se-

T-Se layer being rotated at an arbitrary angle with respect to its neighbors, the proposed mechanism predicts that locally there is a random stacking of A, B, and C layers, each rotated 120° from the other two. This remains to be experimentally determined.

CHAPTER IX

CONCLUSION

An enhancement of the modulated elemental reactant synthetic technique successfully produced TSe_2, $[(SnSe)_{1+y}]_m(TSe_2)_n$, $(SnSe)_{1+y}(T_{1-x}T'_xSe_2)$, and $[(SnSe)_{1+y}]_m(TSe_2)_n[(SnSe)_{1+y}]_p(T'Se_2)_q$ layered compounds (where T = V, Ta, and Ti). The structural data presented here show that precursor films of sub-nanometer, modulated amorphous layers designed to mimic a layered compound will self-assemble into that product upon low temperature annealing. The layering of these compounds is highly oriented, with regular, abrupt stacking along their *c*-axis, evident by (00*l*) reflections in Bragg-Brentano X-ray diffraction studies. The two constituents, SnSe and TSe_2, are independently crystalline in their *ab*-plane, evident by (*hk*0) reflections from in-plane X-ray diffraction studies that indexed to a square SnSe basal plane and a hexagonal TSe_2. For the composite crystals, X-ray diffraction and transmission electron microscopy studies revealed a similar structure to that found in misfit layer compounds; with alternating SnSe bilayers and TSe_2 monolayers. Each integer increase of *m*, *n*, *p*, or *q* resulted in a linear increase in thickness, representing the addition single structural units of SnSe and TSe_2. Although the layering contained regular spacing along *l* and in-plane crystallinity, turbostratic disorder between the layers was confirmed by XRD and TEM studies. This disorder causes random rotation of the crystal lattices at SnSe-TSe_2 interfaces and depending on T, at TSe_2-TSe_2 interfaces as well; eliminating translational symmetry of the continuous lattice in three dimensions. This combination of independently crystalline layers and turbostratic disorder identifies these compounds as

ferecrystals. A self-assembly growth mechanism based on the templated nucleation of subsequent layers is presented to explain this structural data. The formation of turbostratically disordered layered compounds using the modulated elemental reactant synthetic technique is dictated by the energetics of nucleating subsequent structural units in a crystal growth front, which can be predicted from the polytypes observed in the bulk TSe_2 compound. For the $[(SnSe)_{1.15}]_m(VSe_2)$ ferecrystal, anomalies in temperature-dependent resistivity and Hall data were found and attributed to a charge density wave transition in the VSe_2 constituent. Anomalies were also found in the electrical data of $(SnSe)_{1+y}(V_{1-x}Ta_xSe_2)$, and $[(SnSe)_{1.15}]_m(VSe_2)_n[(SnSe)_{1.15}]_p(TaSe_2)_q$ ferecrystals. To our knowledge this is the first observation of a possible CDW in a $(MX)_{1+y}(TX_2)$ intergrowth compound. The CDW transition onset temperature was found to be a sensitive function of m, suggesting that increasing the quasi-two-dimensionality of VSe_2 encourages the CDW transition.

APPENDIX A

LIST OF MISFIT LAYER COMPOUNDS

Appendix A contains a list of all misfit layer compounds (MLCs) and compilation of relevant structural information from current literature reports. In the following tables, a "*" indicates that separate sources report different misfit parameters for the particular MLC. A reported misfit parameter of "*y*" not accompanied by a "*" indicates that no misfit parameter was calculated. Several MLCs have different lattice parameters reported by separate sources, this is indicated by "n)" where n is the corresponding source. For several MLCs, only the *c*-lattice parameter of the superlattice was reported; this is indicated by "Superlattice *c*-lattice parameter (nm)".

Table A.1. $[(MS)_{1+y}]_{1.5}(TS_2)$ misfit layer compounds

Compound	Source
$[(EuS)_{1.5}]_{1.15}(NbS_2)$	1
$[(EuS)_{1.15}]_{1.5}(NbS_2)$	9
$[(Pb_{2/3}Fe_{1/3}S)_{1.16}]_{1.5}(NbS_2)$	3
$[(Pb_{2/3}(Nb,Mn)_{1/3}S)_{1.16}]_{1.5}(NbS_2)$	3
$[(Nb_{1-y-z}Pb_yBi_zS)_{1+y}]_{1.5}(NbS_2)$	3

Table A.1. $[(MS)_{1+y}]_2(TS_2)$ misfit layer compounds

Compound	Source
$[(Pb_{3/4}Sb_{1/4}S)_{1.18}]_2(TiS_2)$	3
$[(Pb_{.83}Sb_{.17}S)_{1.14}]_2(NbS_2)$	3

Table A.3. $(MS)_{1+y}(TS_2)$ misfit layer compounds

Compound Source		*a* -lattice parameter (nm)	*b* -lattice parameter (nm)	*c* -lattice parameter (nm)	Space Group
$(BiS)_{1+y}(TaS_2)$* 2, 5, 8, 11, 12	BiS TaS_2	2) 0.6101 11) 0.5732 2) 0.3300, 0.3301 11) 0.57243	2) 0.5725, 0.5732 11) 1.5368 2) 0.5732, 0.5724 11) 0.33006	2) 2.307, 2.314 11) 2.3135 2) 2.314, 2.312 11) 2.3119	 2) Fm2m
$(BiS)_{1.11}(NbS_2)$ 2, 19, 8, 24	BiS NbS_2	19, 24) 0.5752 19, 24) .57504	19, 24) 3.6156 19, 24) 0.33306	19, 24) 2.3001 19, 24) 2.30001	19) F2mm 19) F2mm
$(BiS)_{1.24}(CrS_2)$ 2	BiS CrS_2	2) 0.5582 2) 0.3470	2) 0.5899 2) 0.5904	2) 1.098 2) 1.098	 2) C2/m
$(BiS)_{1+y}(TiS_2)$ 8		Superlattice c-lattice parameter (nm) 2, 8, 12) 1.131			
$(BiS)_{1.16}(VS_2)$ 21	BiS VS_2	21) 0.5670 21) 0.5670	21) 0.5643 21) 0.3261	21) 1.1354 21) 1.1354	
$(CeS)_{1+y}(NbS_2)$* 1,2,4, 5	CeS NbS_2	2,4) 0.5728 2) 0.3295 4) 0.3309	2, 4) 0.5767 2, 4) 0.5767	2, 4) 1.141 2, 4) 2.281	2, 4) Cm2a 2, 4) Fm2m
$(CeS)_{1.14}(TaS_2)$ 1, 2	CeS TaS_2	2) 0.5737 2) 0.3293	2) 0.5743 2) 0.5743	2) 1.144 2) 2.289	2) Cm2a 2) Fm2m
$(CeS)_{1.19}(TiS_2)$ 1					
$(CeS)_{1.19}(VS_2)$ 1, 5					
$(CeS)_{1.20}(CrS_2)$ 1					
$(DyS)_{1.22}(NbS_2)$ 1, 2	DyS NbS_2	2) 0.5435 2) 0.3309	2) 0.5681 2) 0.5681	2) 2.228 2) 1.114	
$(DyS)_{1.22}(TaS_2)$ 1, 2	DyS TaS_2	2) 0.5441 2) 0.3300	2) 0.5671 2) 0.5671	2) 2.240 2) 1.120	

Table A.4. $(MS)_{1+y}(TS_2)$ misfit layer compounds

Compound Source		*a* -lattice parameter (nm)	*b* -lattice parameter (nm)	*c* -lattice parameter (nm)	Space Group
$(ErS)_{1.23}(NbS_2)$	ErS	2) 0.5354	2) 0.5662	2) 2.215	
2	NbS_2	2) 0.3319	2) 0.5662	2) 1.108	
$(ErS)_{1.23}(TaS_2)$	ErS	2) 0.5365	2) 0.5645	2) 2.221	
1, 2	TaS_2	2) 0.3293	2) 0.5645	2) 1.111	
$(GdS)_{1.20}(TaS_2)$	GdS	2) 0.5515	2) 0.5680	2) 2.250	
1, 2	TaS_2	2) 0.3294	2) 0.5680	2) 2.250	
$(GdS)_{1.21}(NbS_2)$	GdS	2, 4) 0.5518	2, 4) 0.5708	2, 4) 2.253	4) Fm2m
1, 2, 4, 5	NbS_2	2, 4) 0.3311	2, 4) 0.5708	2, 4) 2.253	4) Cm2m
$(GdS)_{1.27}(VS_2)$ 1					
$(GdS)_{1.27}(CrS_2)$	GdS	2) 0.5454	2) 0.5810	2) 2.146	2) Cmca
1, 5	CrS_2	2) 0.3451	2) 0.5802	2) 2.146	2) C2/m
$(HoS)_{1.23}(NbS_2)$	HoS	2) 0.5396	2) 0.5661	2) 2.219	2) F2
1, 2	NbS_2	2) 0.3312	2) 0.5661	2) 1.112	2) C2
$(HoS)_{1.23}(TaS_2)$ 1					
$(LaS)_{1.13}(TaS_2)$	LaS	2, 7) 0.5813	2, 7) 0.5775	2, 7) 1.153	2) Cm2a
1, 2, 7	TaS_2	2, 7) 0.3295	2, 7) 0.5775	2) 2.306 7) 1.153	2) Fm2m
$(LaS)_{1.14}(NbS_2)$	LaS	2, 4, 5) 0.5828	2, 4, 5) 0.5797	2, 4, 5) 1.152	2) Cm2m 2, 4) Cm2a
1, 2, 4,5	NbS_2	2, 4, 5) 0.331	2, 4, 5) 0.5797	2, 4) 2.304 5) 2.394	2, 4) Fm2m
$(LaS)_{1.16}(VS_2)$ 1					
$(LaS)_{1.19}(CrS_2)$	LaS	2) 0.5752 26) 0.5934	2)0.5936 26) 0.5765	2) 1.1036 26) 1.1047	2) C-1
1, 2, 26	CrS_2	2) 0.3435 26) 0.5936	2) 0.5936 26) 0.34311	2) 1.105 26) 1.1067	2) C-1
$(LaS)_{1.19}(TiS_2)$ 5					
$(NdS)_{1.17}(TaS_2)$	NdS	2) 0.568	2) 0.5725	2) 2.273	
1, 2	TaS_2	2) 0.3315	2) 0.5725	2) 2.273	

Table A.5. $(MS)_{1+y}(TS_2)$ misfit layer compounds

Compound Source		*a* -lattice parameter (nm)	*b* -lattice parameter (nm)	*c* -lattice parameter (nm)	Space Group
$(NdS)_{1.18}(NbS_2)$	NdS	2, 4) 0.5635	2, 4) 0.5742	2, 4) 2.2663	2, 4) Fm2m
1, 2, 4	NbS_2	2, 4) 0.3331	2, 4) 0.5742	2, 4) 2.2663	2, 4) Fm2m
$(NdS)_{1.23}(CrS_2)$					
6					
$(NdS)_{1.23}(VS_2)$					
1					
$(PbS)_{1.12}(VS_2)$	PbS	2) 0.5789 28) 0.5720	2) 0.5728 28) 0.5766	2) 2.394 28) 2.3896	2) C2/m and F2
2, 28	VS_2	2) 0.3256 28) 0.572	2) 0.5727 28) 0.328	2) 1.197	2) F2/m and C2
$(PbS)_{1.13}(TaS_2)$	PbS	2, 7) 0.5825	2, 7) 0.5779	2, 7) 2.396	2) Fm2m
2, 5, 7, 12	TaS_2	2, 7) 0.3304	2, 7) 0.5779	2, 7) 2.396	2) Fm2m
$(PbS)_{1.14}(NbS_2)$	PbS	2, 7) 0.5834	2, 7) 0.5801	7) 2.38 2, 14) 1.1902	2) Cm2a
2, 5, 7, 15	NbS_2	2, 7) 0.3313	2, 7) 0.5801	2, 7) 2.38	2) Fm2m
$(PbS)_{1.18}(TiS_2)$	PbS	2, 5, 14) 0.5800 (M)	2, 5, 14) 0.5881 (M)	2, 5, 14) 1.1759 (M)	2,14) C2/m (M)
2, 5, 14		2) 0.5802 (O)	2) 0.5882 (O)	2) 2.341 (O)	2,14) Cmna (O)
	TiS_2	2, 5, 14) 0.3409 (M,O)	2, 5, 14) 0.5881 (M)	2, 5, 14) 1.176 (M)	2) F2/m 2,14) C2/m (M)
			2) 0.5882 (O)	2) 2.341 (O)	2,14) Cmca (O)
$(PrS)_{1.16}(TaS_2)$	PrS	2) 0.570	2) 0.5735	2) 2.284	
1, 2	TaS_2	2) 0.330	2) 0.5725	2) 2.273	
$(PrS)_{1.22}(CrS_2)$					
1					
$(SbS)_{1.15}(TiS_2)$	SbS	2, 22) 0.5908	2, 22) 0.5936	2, 22) 1.1311	2) C-1
1, 2, 12, 22	TiS_2	2, 22) 0.3403	2, 22) 0.5911	2) 1.138 22) 1.0385	2) C-1
$(SbS)_{1+y}(TaS_2)$		Superlattice c-lattice parameter (nm)			
12		2, 12) 1.151			
$(SmS)_{1.19}(NbS_2)$	SmS	1, 2, 4, 20) 0.557	2, 4, 20) 0.5714	2, 4, 20) 2.251	2, 4, 20) Fm2m
1, 2, 4, 20	NbS_2	1, 2, 4, 20) 0.3314	2, 4, 20) 0.5714	2, 4, 20) 2.2511	2, 4, 20) Fm2m
$(SmS)_{1.19}(TaS_2)$	SmS	2, 7) 0.552	2, 7) 0.5679	2, 7) 2.250	2) Fm2m
1,2,5, 7	TaS_2	2, 7) 0.3293	2, 7) 0.5679	2, 7) 2.250	2) Fm2m

Table A.6. $(MS)_{1+y}(TS_2)$ misfit layer compounds

Compound Source		*a* -lattice parameter (nm)	*b* -lattice parameter (nm)	*c* -lattice parameter (nm)	Space Group
$(SmS)_{1.23}(VS_2)$ 1, 5					
$(SmS)_{1.25}(TiS_2)$ 1					
$(SnS)_{1.16}(TaS_2)$ 2, 7	SnS TaS_2	2) 0.5737 7) 0.572 2) 0.3308 7) 0.3316	2) 0.5749 7) 0.5742 2) 0.5750 7)0.5742	2) 1.188 7) 2.376 2, 7) 2.376	2) Cm2a 2) Fm2m
$(SnS)_{1.17}(NbS_2)$ 1, 2, 5, 7, 17, 18	SnS NbS_2	2, 5, 7, 17, 18) 0.5673 2, 5, 7, 17, 18) 0.3321	2, 5, 7, 17, 18) 0.5751 2, 5, 7, 17, 18) 0.5751	2, 5, 7, 17, 18) 1.1761 2, 5, 7, 17, 18) 1.1761	2, 18) C2mb2) Cm2a 2, 18) Cm2m
$(SnS)_{1.20}(TiS_2)$ 2, 5, 13, 14	SnS TiS_2	2, 13, 14) 0.5683 2, 13, 14) 0.3412	2, 13, 14) 0.5832 2, 13, 14) 0.5835	2, 13, 14) 1.168 2, 13, 14) 2.3289	2, 13, 14) C-1 2, 13, 14) F-1
$(TbS)_{1.20}(TaS_2)$ 1, 2	TbS TaS_2	2) 0.5478 2) 0.3293	2) 0.5671 2) 0.5671	2) 2.240 2)1.120	
$(TbS)_{1.21}(NbS_2)$ 1,2,7	TbS NbS_2	2, 7) 0.5467 2, 7) 0.331	2, 7) 0.5695 2, 7) 0.5695	2) 2.235 7) 1.118 2, 7) 1.118	
$(YbS)_{1.23}(NbS_2)$ 1, 2, 4, 5	YbS NbS_2	2, 4) 0.5379 2, 4) 0.3309	2, 4) 0.5637 2, 4) 0.5637	2, 4) 2.230 2, 4) 1.115	4) Fm2m 4) Cm2m
$(YS)_{1.23}(NbS_2)$ 1, 2, 4	YS NbS_2	2, 4) 0.5393 2, 4) 0.3322	2, 4) 0.5658 2, 4) 0.5662	2, 4) 2.2284 2, 4) 1.113	2) F24) Fm2m 2, 4) C2
$(YS)_{1.28}(CrS_2)$ 2, 6	YS CrS_2	2) 0.5409 2) 0.3460	2) 0.5788 2) 0.5788	2) 1.070 2) 1.070	2) C2/m 2) C2/m
$(YbS)_{1.25}(CrS_2)$ 9	YbS CrS_2	9) 0.531 9) 0.332	9) 0.575 9) 0.575	9) 1.063 9)1.063	

Table A.7. $(MSe)_{1+y}(TSe_2)$ misfit layer compounds

Compound Source		*a* -lattice parameter (nm)	*b* -lattice parameter (nm)	*c* -lattice parameter (nm)	Space Group
$(BiSe)_{1.09}(TaSe_2)$	BiSe	2) 0.6270 25) 0.3135	2) 0.5967 25) 0.2984	2) 2.434 25) 1.2174	25) Pm2m
5, 8, 25	$TaSe_2$	2, 25) 0.3421	2, 25) 0.5970	2, 25) 2.4341	25) Fm2m
$(BiSe)_{1+y}(TiSe_2)$	BiSe	Superlattice c-lattice parameter (nm)			
8	$TiSe_2$	2, 8) 1.184			
$(BiSe)_{1+y}(VSe_2)$	BiSe	Superlattice c-lattice parameter (nm)			
8	VSe_2	2, 8) 1.192			
$(BiSe)_{1.10}(NbSe_2)$	BiSe	2, 24) 0.6255	2, 24) 0.5983	2, 24) 2.4203	
2, 24, 27, 5, 8	$NbSe_2$	2, 24) 0.3437	2, 24) 0.5983	2, 24) 2.4203	2) Fm2m
$(GdSe)_{2.15}NbSe_2$					
1					
$(LaSe)_{1.14}(NbSe_2)$	LaSe	2) 0.6016	2) 0.6070	2) 2.407	
2, 5. 6	$NbSe_2$	2) 0.3429	2) 0.6070	2) 2.407	
$(LaSe)_{1.21}(VSe_2)$	LaSe	2, 23) 0.5911	2, 23) 0.6101	2, 23) 1.1684	2, 23) C-1
2, 23	VSe_2	2, 23) 0.3576	2, 23) 0.6100	2, 23) 1.1690	2,23) C-1
$(PbSe)_{1.14}(NbSe_2)$	PbSe	2) 0.6202 15) 0.6013	2, 15) 0.6058	2) 2.495 15) 2.491	2) Fm2m
2, 15	$NbSe_2$	2) 0.3442 15) 0.6015	2) 0.6056 15) 0.3456	2) 2.494 15) 2.490	2) Cm2m
$(SnSe)_{1+y}(VSe_2)$	SnSe	Superlattice c-lattice parameter (nm)			
16	VSe_2	16) 2.420			
$(SnSe)_{1.16}(NbSe_2)$	SnSe	2, 10) 0.5928	2, 10) 0.597	2, 10) 1.2282	2, 10) Cm2a
2, 10	$NbSe_2$	2, 10) 0.3441	2, 10) 0.5971	2, 10) 2.4572	2, 10) Fm2m

Table A.8. $[(MS)_{1+y}(TS_2)_2$ misfit layer compounds

Compound Source		*a* -lattice parameter (nm)	*b* -lattice parameter (nm)	*c* -lattice parameter (nm)	Space Group
$(BiS)_{1.08}(TaS_2)_2$ 2, 12	BiS TaS_2	2) 0.6123 2) 0.3313	2) 0.5744 2) 0.5745	2) 1.755 2) 1.755	
$(BiS)_{1+y}(TiS_2)_2$ 2		Superlattice c-lattice parameter (nm) 2) 1.699			
$(BiS)_{1+y}(NbS_2)_2$ 12		Superlattice c-lattice parameter (nm) 2,12) 1.744			
$(CeS)_{1.16}(NbS_2)_2$ 1	CeS NbS_2	2) 0.5761 2) 0.3334	2) 0.5761 2) 0.5761	2) 3.498 2) 3.498	
$(CeS)_{1.19}(TiS_2)_2$ 1					
$(ErS)_{1.21}(NbS_2)_2$ 1	ErS NbS_2	2) 0.5359 2) 0.3318	2) 0.5592 2) 0.5592	2) 3.429 2) 3.429	
$(GdS)_{1.21}(NbS_2)_2$ 1					
$(LaS)_{1.20}(TiS_2)_2$ 1					
$(LaS)_{1.14}(NbS_2)_2$ 2, 5, 6	LaS NbS_2	2) 0.5895 2) 0.3349	2) 0.5763 2) 0.5763	2) 3.517 2) 3.517	
$(NdS)_{1.17}(NbS_2)_2$ 1, 6	NdS NbS_2	2) 0.5683 2) 0.3339	2) 0.5759 2) 0.5759	2) 3.464 2) 3.464	
$(PbS)_{1.14}(NbS_2)_2$ 2, 5, 15	PbS NbS_2	2) 0.5829 (O) 0.5837 (M) 15) 0.5775 2) 0.3326 (O) 0.3320 (M) 15) 0.5776	2) 0.5775 (O) 0.5788 (M) 15) 0.5829 2) 0.5775 (O) 0.5781(M) 15) 0.33263	2) 3.586 (O) 3.604 (M) 15) 3.586 2) 3.587 (O) 3.604(M) 15) 3.588	2) $Cmc2_1$ (O) $F2_1/m$ (M) 2) $Cmc2_1$ (O) Cm (M)
$(PbS)_{1.18}(TiS_2)_2$ 5	PbS TiS_2	2) 0.5761 2) 3.390	2) 0.5873 2) 0.5873	2) 1.746 2) 1.746	2) C2/m 2) $C2_1/m$
$(SbS)_{1.15}(TiS_2)_2$ 22, 23	SbS TiS_2	2, 22) 0.5902 2, 22) 0.3405	2, 22) 0.5924 2, 22) 0.5898	2, 22) 1.7019 2, 22) 1.7030	2) C-1 2)C-1
$(SbS)_{1+y}(TaS_2)_2$ 12		Superlattice c-lattice parameter (nm) 2, 12) 1.753			
$(SbS)_{1+y}(NbS_2)_2$ 12		Superlattice c-lattice parameter (nm) 2, 12) 1.731			

Table A.9. $[(MS)_{1+y}(TS_2)_2$ misfit layer compounds

Compound Source		*a* -lattice parameter (nm)	*b* -lattice parameter (nm)	*c* -lattice parameter (nm)	Space Group
$(SmS)_{1.18}(NbS_2)_2$ 1	SmS NbS_2	2) 0.5617 2) 0.3314	2) 0.5763 2) 0.5763	2) 3.457 2) 3.457	
$(SmS)_{1.25}(TiS_2)_2$ 1					
$(SnS)_{1.17}(NbS_2)_2$ 1, 2, 5, 7					
$(SnS)_{1.20}(TiS_2)_2$ 5					
$(YS)_{1.21}(NbS_2)_2$ 2, 6	YS NbS_2	2) 0.5474 2) 0.3222	2) 0.5637 2) 0.5637	2) 3.441 2) 0.3441	

Table A.10. $[(MSe)_{1+y}(TSe_2)_2$ misfit layer compounds

Compound Source		*a* -lattice parameter (nm)	*b* -lattice parameter (nm)	*c* -lattice parameter (nm)	Space Group
$(BiSe)_{1+y}(TaSe_2)_2$ 2				Superlattice c-lattice parameter (nm) 2) 1.833	
$(LaSe)_{1.14}(NbSe_2)_2$ 1, 5, 6	LaSe $NbSe_2$	2) 0.6019 2) 0.3437	2) 0.5998 2) 0.6004	2) 3.654 2) 3.653	2) C1 2) C2221
$(LaSe)_{1.20}(TiSe_2)_2$ 1					
$(NdSe)_{1.17}(NbSe_2)_2$ 1, 2					
$(PbSe)_{1.14}(NbSe_2)_2$ 15	PbSe $NbSe_2$	0.5991(3) 0.5990(4)	0.6025(6) 0.3449(2)	1.8752(6) 1.8746(8)	
$(PbSe)_{1.16}(TiSe_2)_2$ 29	PbSe $TiSe_2$	0.614(2) 0.3533(1)		Superlattice c-lattice parameter (nm) 1.8247(1)	
$(SnSe)_{1+y}(NbSe_2)_2$ 16				Superlattice c-lattice parameter (nm) 16) 3.705	

Table A.11. $[(MX)_{1+y}(TX_2)_3$ misfit layer compounds

Compound Source		*a* -lattice parameter (nm)	*b* -lattice parameter (nm)	*c* -lattice parameter (nm)	Space Group
$(PbSe)_{1.14}(NbSe_2)_3$	PbSe	2) 0.6011 15) 0.5986	2) 0.5986 15) 0.6011	2, 15) 2.5087	
2, 15	$NbSe_2$	2) 0.3441 15) 0.5986	2) 0.5986 15) 0.3441	2, 15) 2.5086	
$(SnS)_{1.16}(NbS_2)_3$	SnS	2) 0.5688	2) 0.5757	2) 2.359	2) Cm2a
2	NbS_2	2) 0.3324	2) 0.5657	2) 2.359	2) Cm2m

Table A.12. Alloy misfit layer compounds

Compound Source		*a* -lattice parameter (nm)	*b* -lattice parameter (nm)	*c* -lattice parameter (nm)	Space Group
$[(Bi,Ca)S]_{1.20}(TiS_2)$	(Bi,Ca)S	2) 0.5683	2) 0.5852	2) 2.296	
2	TiS_2	2) 0.3410	2) 0.5852	2) 2.296	
$[(Pb,Sb)S]_{1.18}(TiS_2)$ 3					
$[(Pb,Sb)S]_{1.14}(NbS_2)$ 3					
$Pb(Nb_{1-x}Ta_x)S_3$		Superlattice c-lattice parameter (nm)			
2			2) 1.191-1.197		

APPENDIX B

LIST OF FERECRYSTALS

Appendix B contains a compilation of $[(MX)_{1+y}]_m(TX_2)_n$ ferecrystals and structural data from literature accounts. Sources are cited to Chapter II under references cited.

Table B.1. A compilation of structural data from $[(MX)_{1+y}]_m(TX_2)_n$ ferecrystals reported in literature accounts and synthesized by the Dave Johnson Lab.

Sample	*c*-lattice parameter (nm)		*a*-lattice parameter (nm)	
$[(BiSe)_{1.10}]_m(NbSe_2)_n$ [9,10]	1:1	1.2047(8)		
	BiSe	0.507-0.548		
	$NbSe_2$	0.632		
$[(CeSe)_{1.14}]_m(NbSe_2)_n$ [9,10]	CeSe	0.566		
	$NbSe_2$	0.641		
$[(PbSe)_{1.00}]_m(MoSe_2)_n$ [5,6,9,14,15]	1:1	1.246(1)-1.275(5)	PbSe	0.6163(3)-0.6182(2)
			$MoSe_2$	0.3308(4)-0.3310(9)
$[(PbSe)_{1.10}]_m(NbSe_2)_n$ [10]	1:1	1.2439(7)		
	PbSe	0.633-0.634		
	$NbSe_2$	0.613		
$[(PbSe)_{1.12}]_m(TaSe_2)_n$ [9,10]	1:1	1.249(1)		
	PbSe	0.600-0.628		
	$TaSe_2$	0.640-0.641		
$(PbSe)_{1+y}(TiSe_2)_n$ [7,16]	1:1	1.2174(2)	PbSe	0.6122(4)-0.6133(3)
y = 7) 0.18 16) 0.16	$TiSe_2$	0.6083	$TiSe_2$	0.3552(7)-0.3568(2)
$[(PbSe)_{0.99}]_m(WSe_2)_n$ [5,11]	1:1	1.2697(3)	PbSe	0.618(2)
	PbSe	0.612-0.615	WSe_2	0.331(1)
	WSe_2	0.654-0.656		
$[(SnSe)_{1+y}]_m(MoSe_2)_n$ [5,8]	1:1	1.2425(6)	SnSe	0.6003(1)-0.608(2)
y = 5) 0.03 8) 0.06	SnSe	0.5806(2)	$MoSe_2$	0.3308(4)-0.3320(1)
$[(SnSe)_{1.15}]_m(TaSe_2)_n$ [12]	1:1	1.238(1)	SnSe	0.60(1)-0.605(9)
	SnSe	0.579(1)	$TaSe_2$	0.345(3)-0.346(3)
	$TaSe_2$	0.649(1)		
$(SnSe)_{1.15}(VSe_2)$ [13]	1:1	1.2028(9)-1.2032(7)	SnSe	0.5935(4)
			VSe_2	0.3414(3)

Table B.2. A compilation of $[(MX)_{1+y}]_m(TX_2)_n$ ferecrystals reported in literature and synthesized by the Dave Johnson Lab.

Sample	m	n
$[(BiSe)_{1.10}]_m(NbSe_2)_n$ [9,10]	1	1
	1	2
	1	3
	1	4
	1	5
	3	1
	3	3
	4	1
	4	2
	5	1
	5	2
	5	3
	5	4
	5	5
	6	1
	6	1
	6	2
	6	3
	6	4
	6	5
	7	4
	8	1
	8	4
	8	4
	9	3
	10	4
	11	3
	11	4
	13	4
	14	4
	15	4
$[(CeSe)_{1.14}]_m(NbSe_2)_n$ [9,10]	1	4
	1	8
	2.5	4
	2.5	6
	2.5	8
	2.5	10
	4	4
	4	8

Sample	m	n
$[(PbSe)_{1.00}]_m(MoSe_2)_n$ [5,6,9,14,15]	1	1
	1	2
	1	3
	1	5
	2	1
	2	2
	2	3
	3	1
	3	3
	4	4
	4.5	1
	5	1
	5	5
$[(PbSe)_{1.10}]_m(NbSe_2)_n$ [10]	1	1
	1	2
	1	3
	1	5
	2	1
	2	2
	3	1
$[(PbSe)_{1.12}]_m(TaSe_2)_n$ [9,10]	1	1
	1	2
	1	5
	2	1
	2	2
	2	3
	2	4
	3	1
	3	2
	3	3
	4	4
$(PbSe)_{1+y}(TiSe_2)_n$ [7,16]	1	1
y = 7) 0.18 16) 0.16	1	2
$[(PbSe)_{0.99}]_m(WSe_2)_n$ [5,11]	1	1
	1	2
	1	3
	1	4
	1	5
	1	6

Table B.3. A compilation of $[(MX)_{1+y}]_m(TX_2)_n$ ferecrystals reported in literature and synthesized by the Dave Johnson Lab.

Sample	m	n
$[(PbSe)_{0.99}]_m(WSe_2)_n$ [5,11]	1	7
	1	8
	2	1
	2	2
	2	3
	2	4
	2	5
	2	6
	2	7
	2	8
	3	1
	3	2
	3	3
	3	4
	3	5
	3	6
	3	7
	3	8
	4	1
	4	2
	4	3
	4	4
	4	5
	4	6
	4	7
	4	8
	5	1
	5	2
	5	3
	5	4
	5	5
	5	6
	5	7
	5	8
	6	1
	6	2
	6	3
	6	4
	6	5
$[(PbSe)_{0.99}]_m(WSe_2)_n$ [5,11]	6	6
	6	7
	6	8
	7	1
	7	2
	7	3
	7	4
	7	5
	7	6
	7	7
	7	8
	8	1
	8	2
	8	3
	8	4
	8	5
	8	6
	8	7
	8	8
$[(SnSe)_{1+y}]_m(MoSe_2)_n$ [5,8]	1	1
y = 5) 0.03 8) 0.06	1	3
	1	4
	2	1
	3	1
	4	1
	4	4
$[(SnSe)_{1.15}]_m(TaSe_2)_n$ [12]	1	1
	1	2
	1	3
	1	4
	1	5
	1	6
	2	1
	3	1
	4	1
	5	1
	6	1
$(SnSe)_{1.15}(VSe_2)$ [13]	1	1

REFERENCES CITED

CHAPTER I

1. Palewski, T. Rare Earth Compounds with Incommensurate Layered Structures. *Wiadomości Chemiczne* **2003**, 57, 9-10, 827-854.

2. Wiegers, G.A. Misfit Layer Compounds: Structures and Physical Properties. *Progress in Solid State Chemistry*, **1996**, 24, 1-139.

3. Ohno, Y. Electron Tunneling from a Metallic TS_2 Layer Underneath an Ultra-Thin MS Layer with Semiconducting Properties for Misfit-Layer Compounds. *Surface Science* **2006**, 600, 598-609.

4. Peña, O.; Rabu, P.; Meerschaut, A. Magnetic Properties of Rare-Earth-Based Misfit Layered Materials of Formula $(LnS)_nNbS_2$ (Ln ≡ Lanthanides, Y). *Journal of Physics: Condensed Matter*, **1991**, 3, 9929-9940.

5. Rouxel, J.; Meerschaut, A.; Wiegers, G.A. Chalcogenide Misfit Layer Compounds. *Journal of Alloys and Compounds*, **1995**, 229, 144-157.

6. Roesky, R.; Gressier, P.; Meerschaut, A.; Widder, K.; Geserich, H.P.; Scheiber, G. Optical Properties and Electronic Structure of the Misfit Layered Compounds '$LnNb_2X_5$' (Ln ≡ Y, La or Nd; X ≡ S or Se). *Journal of Physics: Condensed Matter*, **1994**, 6, 3437-3442.

7. Rüscher, C.H.; Haas, C.; van Smaalen, S.; Wiegers, G.A. Investigation of the Optical Reflectivity of Misfit Layer Compounds: $(MS)_nTS_2$ (T = Ta, Nb; M = Sn, Pb, Sm, Tb, La; $1.08 < n < 1.23$). *Journal of Physics: Condensed Matter*, **1994**, 6, 2117-2128.

8. Gotoh, Y.; Onoda, M.; Uchida, K.; Tanaka, Y.; Iida, T.; Hayakawa, H.; Oosawa, Y. Preperation and Characterization of $BiMX_3$ (M = Ti, V, Nb, Ta; X = S, Se), New Composite-Layered Chalcogenides. *Chemistry Letters*, **1989**, 1559-1562.

9. Ohno, Y.; Yamaguchi, T. Electrical and Optical Properties of the Mixed-Valence Misfit-Layer Compound $(YbS)_{1.25}CrS_2$. *Journal of Alloys and Compounds*, **2008**, 455, 10-16.

10. Wiegers, G.A.; Zhou, W.Y. The Misfit Layered Compound $(SnSe)_{1.16}NbSe_2$. *Materials Research Bulletin*, **1991**, 26, 879-885.

11. Gotoh, Y.; Onoda, M.; Akimoto, J.; Goto, M.; Oosawa, Y. The Layered Composite Crystal Structure of the Ternary Sulfide $(BiS)_{1.07}TaS_2$ "$BiTaS_3$". *Japan Journal of Applied Physics*, **1992**, 31, 3946-3950.

12. Gotoh, Y.; Onoda, M.; Akimoto, J.; Oosawa, Y. Preparation and Characterization of New Sb-Containing Ternary Sulfides with Layered Composite Crystal Structure. *Japan Journal of Applied Physics* **1991**, 30, 6A, 1039-1041.

13. Ettema, A.R.H.F.; Wiegers, G.A.; Haas, C.; Turner, T.S. Resonant and Core Level Photoemission Spectroscopy of the Misfit Layer Compound $(SnSe)_{1.20}TiS_2$. *Physica Scripta* **1992**, 41, 265-268.

14. Wiegers, G.A.; Haange, R.J. Electrical Transport Properties of the Misfit Layer Compounds $(SnS)_{1.20}TiS_2$ and $(PbS)_{1.18}TiS_2$. *European Journal of Solid State Inorganic Chemistry* **1991**, 28, 1071-1078.

15. Oosawa, Y.; Gotoh, Y.; Akimoto, J.; Tsunoda, T.; Sohma, M.; Onoda, M. Three Types of Ternary Selenides with Layered Composite Crystal Structures Formed in the Pb-Nb-Se System. *Japan Journal of Applied Physics* **1992**, 31, 2, 1096-1099.

16. Hernan, L.; Morales, J.; Pattanayak, J.; Tirado, J.L. Preperation and Characterization of New Misfit Layere Selenides $SnVSe_3$ and $SnNb_2Se_5$. *Chemistry Letters* **1991**, 11, 1981-1984.

17. Kuypers, S.; Van Tendeloo, G.; Van Landuyt, J.; Amelinckx, S. The Incommensurate Misfit Layer Structure of $(SnS)_{1.17}NbS_2$ '$SnNbS_3$'. II. A Study by Means of Electron Microscopy. *Acta Crystallographica Section A* **1989**, 45, 291-296.

18. Meetsma, A.; Wiegers, G.A.; Haange, R.J.; de Boer, J.L. The Incommensurate Misfit Layer Structure of $(SnS)_{1.17}NbS_2$ '$SnNbS_3$'. I. A Study by Means of X-ray Diffraction. *Acta Crystallographica Section A* **1989**, 45, 285-291.

19. Gotoh, Y.; Akimoto, J.; Goto, M.; Oosawa, Y.; Onoda, M. The Layered Composite Crystal Structure of the Ternary Sulfide $(BiS)_{1.11}NbS_2$. *Journal of Solid State Chemistry* **1995**, 116, 61-67.

20. Meerschaut, A.; Auriel, C.; Lafond, A.; Deudon, C.; Gressier, P.; Rouxel, J. Crystal Structure Determinatino and Physical Properties of the Misfit Compound $(SmS)_{1.19}NbS_2$. *European Journal of Solid State Inorganic Chemistry* **1991**, 28, 581-595.

21. Gotoh, Y.; Akimoto, J.; Oosawa, Y.; Onoda, M. Synthesis and Characterization of Mutually Incommensurate $(BiS)_{1.16}VS_2$ with Layered Composite Crystal Structure. *Japan Journal of Applied Physics* **1995**, 34, 2, 1662-1665.

22. Ren, Y.; Haas, C.; Wiegers, G.A. Photoelectron Spectroscopy Study of the Electronic Structure of the Incommensurate Intergrowth Compounds $(SbS)_{1.15}(TiS_2)_n$ with n = 1, 2. *Journal of Physics: Condensed Matter* **1995**, 7, 5949-5958.

23. Ren, Y.; Baas, J.; Meetsma, A.; de Boer, J.L.; Wiegers, G.A. Vacancies and Electron Localization in the Incommensurate Intergrowth Compound $(La_{0.95}Se)_{1.21}VSe_2$. *Acta Crystallographica Section B* **1996**, 52, 398-405.

24. Nader, A.; Briggs, A.; Gotoh, Y. Superconductivity in the Misfit Layer Compounds $(BiSe)_{1.10}(NbSe_2)$ and $(BiS)_{1.11}(NbS_2)$. *Solid State Communications* **1997**, 101, 3, 149-153.

25. Petricek, V.; Cisarova, I. The Modulated Structure of the Commensurate Misfit-Layer Compound $(BiSe)_{1.09}TaSe_2$. *Acta Crystallographica Section B* **1993**, 49, 258-266.

26. Otero-Diaz, L.; FitzGerald, J.D.; Williams, T.B.; Hyde, B.G. On the Monoclinic Binary-Layer Compound 'LaCrS$_3$'. *Acta Crystallographica Section B* **1985**, 41, 405-410.

27. Nader, A. Resistivity Anisotropy of the Bi-based Misfit Layer Compounds $(BiS)_{1.11}(NbS_2)$ and $(BiSe)_{1.10}(NbSe_2)$ Down to the Liquid Nitrogen Temperature. *Physica Status Solidi C* **2006**, 3, 9, 2972-2974.

28. Gotoh, Y.; Onoda, M.; Goto, M.; Oosawa, Y. Preparation and Characterization of "PbVS$_3$" a New Composite Layered Compound. *Chemistry Letters* **1989**, 1281-1282.

29. Giang, N.; Xu, Q.; Hor, Y.S.; Williams, A.J.; Dutton, S.E.; Zandbergen, H.W.; Cava, R.J. Superconductivity at 2.3 K in the Misfit Compound $(PbSe)_{1.16}(TiSe_2)_2$. *Physical Review B: Condensed Matter* **2010**, 82, 024503-(1-5).

30. Smeller, M.M.; Heideman, C.L.; Lin, Q.; Beekman, M.; Anderson, M.D.; Zschack, P.; Anderson, I.M; Johnson, D.C. Structure of Turbostratically Disordered Misfit Layer Compounds $[(PbSe)_{0.99}]_1[WSe_2]_1$, $[(PbSe)_{1.00}]_1[MoSe_2]_1$, and $[(SnSe)_{1.03}]_1[MoSe_2]_1$. *Zeitschrift für anorganische and allgemeine Chemie* **2012**, 638, 15, 2632-2639.

31. Heideman, C.L.; Rostek, R.; Anderson, M.D.; Herzing, A.A.; Anderson, I.M.; Johnson, D.C. Synthesis and Electronic Properties of the Misfit Layered Compound $[(PbSe)_{1.00}]_1[MoSe_2]_1$. *Journal of Electronic Materials* **2010**, 39, 9, 1476-1481.

32. Moore, D.B.; Beekman, M.; Disch, S.; Zschack, P.; Häusler, I.; Neumann, W.; Johnson, D.C. Synthesis, Structure and Properties of Turbostratically Disordered $(PbSe)_{1.18}(TiSe_2)_2$. *submitted to Chemistry of Materials* **2013**.

33. Beekman, M.; Cogburn, G.; Heideman, C.; Rouvimov, S.; Zschack, P.; Neumann, W.; Johnson, D.C. New Layered Intergrowths in the Sn-Mo-Se System. *Journal of Electronic Materials* **2012**, 41, 6, 1476-1480.

34. Lin, Q.; Heideman, C.L.; Nguyen, N.; Zschack, P.; Christescu, C.; Cahill, D.G.; Johnson, D.C. Designed Synthesis of Families of Misfit-Layered Compounds. *European Journal of Inorganic Chemistry* **2008**, 15, 382-2385.

35. Heideman, C.; Nyugen, N.; Hanni, J.; Lin, Q.; Duncombe, S.; Johnson, D.C.; Zschack, P. The Synthesis and Characterization of New $[(BiSe)_{1.10}]_m[NbSe_2]_n$, $[(PbSe)_{1.10}]_m[NbSe_2]_n$, $[(CeSe)_{1.14}]_m[NbSe_2]_n$, and $[(PbSe)_{1.12}]_m[TaSe_2]_n$ Misfit Layered Compounds. *Journal of Solid State Chemistry* **2008**, 181, 1701-1706.

36. Lin, Q.; Smeller, M.; Heideman, C.; Zschack, P.; Koyano, M.; Anderson, M.D.; Kykyneshi, R.; Keszler, D.A.; Anderson, I.M.; Johnson, D.C. Rational Synthesis and Characterization of a New Family of Low Thermal Conductivity Misfit Layered Compounds $[(PbSe)_{.99}]_m[WSe_2]_n$. *Chemistry of Materials* **2010**, 22, 1002-1009.

37. Atkins, R.; Wilson, J.; Zschack, P.; Grosse, C.; Neumann, W.; Johnson, D.C. Synthesis of $[(SnSe)_{1.15}]_m(TaSe_2)_n$ Ferecrystals: Structurally Tunable Metallic Compounds. *Chemistry of Materials* **2012**, 24, 4594-4599.

38. Atkins, R.; Disch, S.; Jones, Z.; Häusler, I.; Grosse, C.; Fischer, S.F.; Neumann, W.; Zschack, P.; Johnson, D.C. Synthesis, Structure, and Electrical Properties of a New Tin Vanadium Selenide. *Journal of Solid State Chemistry* **2013**, 202, 128-133.

39. Anderson, M.D.; Heideman, C.L.; Smeller, M.; Kokenyesi, R.; Herzing, A.A.; Anderson, I.M.; Keszler, D.A.; Zschack, P.; Johnson, D.C. Size-Dependent Structural Distortion in One-Dimensional Nanostructures. *Angewandte Chemie International Edition* **2013**, 52, 1982-1985.

40. Chiritescu, C.; Cahill, D.G.; Heideman, C.; Lin, Q.; Mortensen, C.; Nguyen, N.T.; Johnson, D.; Rostek, R.; Böttner, H. Low Thermal Conductivity in Nanoscale Layered Materials Synthesized by the Method of Modulated Elemental Reactants. *Journal of Applied Physics* **2008**, 104, 033533.

41. Moore, D.; Stolt, M.; Atkins, R.; Sitts, L.; Jones, Z.; Disch, S.; Beekman, M.; Johnson, D.C. Structural and Electrical Properties of $(PbSe)_{1.16}TiSe_2$. *Emerging Materials Research* **2012**, 1, 292-298.

42. Beekman, M.; Heideman, C.; Anderson, M.; Smeller, M.; Atkins, R.; Lin, Q.; Nguyen, N.; Johnson, D.C. Modules, Systems, and Applications in Thermoelectrics, *CRC Press Boca Raton* **2012**, 2.1-19.

43. Onoda, M.; Kato, K. Structure of the Incommensurate Composite Crystal $(PbS)_{1.12}VS_2$. *Acta Crystallographica Section B* **1990**, 46, 487-492.

44. van Smaalen, S.; Meetsma, A.; Wiegers, G.A.; de Boer, J.L. Determination of the Modulated Structure of the Inorganic Misfit Layer Compound $(PbS)_{1.18}TiS_2$. *Acta Crystallograhpica Section B* **1991**, 47, 314-325.

45. Ren, Y.; Meetsma, A.; Wiegers, G.A.; van Smaalen, S. (3+2)-Dimensional Superspace Approach to the structure of the Stage-2 Misfit Layer Compound $(SbS)_{1.15}(TiS_2)_2$. *Acta Crystallographica Section B* **1996**, 52, 389-397.

46. Berner, D.; Leihenseder, H.; Widder, K.; Geserich, H.P.; Burlakov, V.M.; Mavrin, B.N.; Denisov, V.N.; Roesky, R.; Gressier, P.; Meerschaut, A. $(LaSe)_{1.14}(NbSe_2)_2$ – A Metal-Insulator Quantum Well Crystal? *Journal of Physics: Condensed Matter* **1997**, 9, 10545-10553.

47. Brandt, J.; Kipp, L.; Skibowski, M.; Krasovskii, E.E.; Schattke, W.; Spiecker, E.; Dieker, C.; Jäger, W. Charge Transfer in Misfit Layered Compounds. *Surface Science* **2003**, 532-5, 705-710.

48. Ettema, A.R.H.F.; Haas, C. An X-ray Photoemission Spectroscopy Study of Interlayer Charge Transfer in Some Misfit Layer Compounds. *Journal of Physics: Condensed Matter* **1993**, 5, 3817-3826.

49. Fang, C.M.; Ettema, A.R.H.F.; Haas, C.; Wiegers, G.A.; van Leuken, H.; de Groot, R.A. Electronic Structure of the Misfit-Layer Compound $(SnS)_{1.17}NbS_2$ Deduced from Band-Structure Calculations and Photoelectron Spectra. *Physical Review B: Condensed Matter* **1995**, 52, 4, 2336-2347.

50. Fang, C.M.; de Groot, R.A.; Wiegers, G.A.; Haas, C. Electronic Structure of the Misfit Layer Compound $(SnS)_{1.20}TiS_2$: Band Structure Calculations and Photoelectron Spectra. *Journal of Physics: Condensed Matter* **1996**, 8, 1663-1676.

51. Kisoda, K.; Hangyo, M.; Nakashima, S.; Terashima, T.; Kojima, N. Charge Transfer and Phonons in Misfit Layer Compounds $(RS)_xNbS_2$ (R = rare earth; $x \approx 1.2$). *Physica B* **1996**, 219-220, 565-567.

52. Shirai, K.; Kisoda, K.; Hangyo, M.; Nakashima, S. On the Raman Shift in Misfit Layer Compounds of Metal-Dichalcogenides $(MX)(TX_2)$ – An Effect of the Charge Transfer on the Intralayer Noncentral Forces. *Solid State Communications* **1997**, 103, 3, 131-135.

53. Wiegers, G.A. Charge Transfer Between Layers in Misfit Layer Compounds. *Journal of Alloys and Compounds* **1995**, 219, 152-156.

54. Abramov, S.P. Varieties of Charge Transfer and Bonding Between Layers in Misfit Layer Compounds $(MX)_xTX_2$. *Journal of Alloys and Compounds* **1997**, 259, 212-218.

55. Friend, R.H. Yoffe, A.D. Electronic Properties of Intercalation Complexes of the Transition Metal Dichalcogenides. *Advances in Physics* **1987**, 36 (1), 1-94.

CHAPTER II

1. Wiegers, G.A. Misfit Layer Compounds: Structures and Physical Properties. *Progress in Solid State Chemistry*, **1996**, 24, 1-139.

2. Beekman, M.; Heideman, C.; Anderson, M.; Smeller, M.; Atkins, R.; Lin, Q.; Nguyen, N.; Johnson, D.C. Modules, Systems, and Applications in Thermoelectrics, *CRC Press Boca Raton* **2012**, 2.1-19.

3. Nguyen, N.T.; Howe, B.; Hash, J.R.; Liebrecht, N.; Zschack, P.; Johnson, D.C. Synthesis of a Family of $\{[(VSe_2)_n]_{1.06}(TaSe_2)_m\}_z$ Compounds. *Chemistry of Materials* **2007**, 19, 1923-1930.

4. Ufer, K.; Roth, G.; Kleeberg, R.; Stanjek, H.; Dohrmann, R.; Bergmann, J. Description of X-ray Powder Pattern of Turbostratically Disordered Layer Structures with a Rietveld Compatible Approach. *Zeitschrift für Kristallographie* **2004**, 219, 519-527.

5. Smeller, M.M.; Heideman, C.L.; Lin, Q.; Beekman, M.; Anderson, M.D.; Zschack, P.; Anderson, I.M; Johnson, D.C. Structure of Turbostratically Disordered Misfit Layer Compounds $[(PbSe)_{0.99}]_1[WSe_2]_1$, $[(PbSe)_{1.00}]_1[MoSe_2]_1$, and $[(SnSe)_{1.03}]_1[MoSe_2]_1$. *Zeitschrift für anorganische and allgemeine Chemie* **2012**, 638, 15, 2632-2639.

6. Heideman, C.L.; Rostek, R.; Anderson, M.D.; Herzing, A.A.; Anderson, I.M.; Johnson, D.C. Synthesis and Electronic Properties of the Misfit Layered Compound $[(PbSe)_{1.00}]_1[MoSe_2]_1$. *Journal of Electronic Materials* **2010**, 39, 9, 1476-1481.

7. Moore, D.B.; Beekman, M.; Disch, S.; Zschack, P.; Häusler, I.; Neumann, W.; Johnson, D.C. Synthesis, Structure and Properties of Turbostratically Disordered $(PbSe)_{1.18}(TiSe_2)_2$. *submitted to Chemistry of Materials* **2013**.

8. Beekman, M.; Cogburn, G.; Heideman, C.; Rouvimov, S.; Zschack, P.; Neumann, W.; Johnson, D.C. New Layered Intergrowths in the Sn-Mo-Se System. *Journal of Electronic Materials* **2012**, 41, 6, 1476-1480.

9. Lin, Q.; Heideman, C.L.; Nguyen, N.; Zschack, P.; Chiristescu, C.; Cahill, D.G.; Johnson, D.C. Designed Synthesis of Families of Misfit-Layered Compounds. *European Journal of Inorganic Chemistry* **2008**, 15, 382-2385.

10. Heideman, C.; Nyugen, N.; Hanni, J.; Lin, Q.; Duncombe, S.; Johnson, D.C.; Zschack, P. The Synthesis and Characterization of New $[(BiSe)_{1.10}]_m[NbSe_2]_n$, $[(PbSe)_{1.10}]_m[NbSe_2]_n$, $[(CeSe)_{1.14}]_m[NbSe_2]_n$, and $[(PbSe)_{1.12}]_m[TaSe_2]_n$ Misfit Layered Compounds. *Journal of Solid State Chemistry* **2008**, 181, 1701-1706.

11. Lin, Q.; Smeller, M.; Heideman, C.; Zschack, P.; Koyano, M.; Anderson, M.D.; Kykyneshi, R.; Keszler, D.A.; Anderson, I.M.; Johnson, D.C. Rational Synthesis and Characterization of a New Family of Low Thermal Conductivity Misfit Layered Compounds $[(PbSe)_{.99}]_m[WSe_2]_n$. *Chemistry of Materials* **2010**, 22, 1002-1009.

12. Atkins, R.; Wilson, J.; Zschack, P.; Grosse, C.; Neumann, W.; Johnson, D.C. Synthesis of $[(SnSe)_{1.15}]_m(TaSe_2)_n$ Ferecrystals: Structurally Tunable Metallic Compounds. *Chemistry of Materials* **2012**, 24, 4594-4599.

13. Atkins, R.; Disch, S.; Jones, Z.; Häusler, I.; Grosse, C.; Fischer, S.F.; Neumann, W.; Zschack, P.; Johnson, D.C. Synthesis, Structure, and Electrical Properties of a New Tin Vanadium Selenide. *Journal of Solid State Chemistry* **2013**, 202, 128-133.

14. Anderson, M.D.; Heideman, C.L.; Smeller, M.; Kokenyesi, R.; Herzing, A.A.; Anderson, I.M.; Keszler, D.A.; Zschack, P.; Johnson, D.C. Size-Dependent Structural Distortion in One-Dimensional Nanostructures. *Angewandte Chemie International Edition* **2013**, 52, 1982-1985.

15. Chiritescu, C.; Cahill, D.G.; Heideman, C.; Lin, Q.; Mortensen, C.; Nguyen, N.T.; Johnson, D.; Rostek, R.; Böttner, H. Low Thermal Conductivity in Nanoscale Layered Materials Synthesized by the Method of Modulated Elemental Reactants. *Journal of Applied Physics* **2008**, 104, 033533.

16. Moore, D.; Stolt, M.; Atkins, R.; Sitts, L.; Jones, Z.; Disch, S.; Beekman, M.; Johnson, D.C. Structural and Electrical Properties of $(PbSe)_{1.16}TiSe_2$. *Emerging Materials Research* **2012**, 1, 292-298.

17. Ludemann, M.; Gordan, O.D.; Zahn, D.R.T.; Beekman, M.; Atkins, R.; Johnson, D.C. Observation by Raman Spectroscopy of Systematic Structural Changes in Two-Dimensional Confined Layers of SnSe as a Function of Layer Thickness. *To Be Submitted* **2013**.

18. Chattopadhyay, T.; Pannetier, J.; von Schnering, H. G. Neutron Diffraction Study of the Structural Phase Transition in SnS and SnSe. *Journal of Physics and Chemistry of Solids* **1986**, 47, 9, 879−885.

19. Grosse, C.; Atkins, R.; Kirmse, H.; Mogilatenko, A.; Neumann, W.; and Johnson, D.C. Local Structure and Defect Chemistry of $[(SnSe)_{1.15}]_m(TaSe_2)$ Ferecrystals – A New Type of Layered Intergrowth Compound. *Submitted to Journal of Alloys and Compounds* **2013**.

CHAPTER III

1. Fister, L.; Li, X.; McConnell, J.; Novet, T.; Johnson, D.C. Deposition System for the Synthesis of Modulated, Ultrathin-film Composites. *Journal of Vacuum Science and Technology A* **1993**, 11, 3014-3019.

2. Phung, T. M.; Jensen, J. M.; Johnson, D. C.; Donovan, J. J.; McBurnett, B. G. Determination of the Composition of Ultra-thin Ni-Si Films on Si: Constrained Modeling of Electron Probe Microanalysis and X-ray Reflectivity Data. *X-Ray Spectrometry* **2008**, 37, 608−614.

CHAPTER IV

1. Wiegers, G.A. Misfit Layer Compounds: Structures and Physical Properties. *Progress in Solid State Chemistry*, **1996**, 24, 1-139.

2. Gotoh, Y.; Onoda, M.; Akimoto, J.; Goto, M.; Oosawa, Y. The Layered Composite Crystal Structure of the Ternary Sulfide, $(SnS)_{1.15}TaS_2$ "$SnTaS_3$". *Japan Journal of Applied Physics* **1993**, 32-3, 760-762.

3. Wiegers, G.A.; Zhou, W.Y. The Misfit Layered Compound $(SnSe)_{1.16}NbSe_2$. *Materials Research Bulletin*, **1991**, 26, 879-885.

4. Rouxel, J.; Meerschaut, A.; Wiegers, G.A. Chalcogenide Misfit Layer Compounds. *Journal of Alloys and Compounds* **1995**, 229, 144-157.

5. Wiegers, G.A.; Meetsma, A.; van Smaalen, S.; Haange, R.J.; Wulff, J.; Zeinstra, T.; de Boer, J.L. Misfit Layer Compounds $(MS)_nTS_2$ (M = Sn, Pb, Bi, Rare Earth Elements; T = Nb, Ta; n = 1.08-1.19), A New Class of Layer Compounds. *Solid State Communications* **1989**, 70, 4, 409-413.

6. Brandt, J.; Kipp, L.; Skibowski, M.; Krasovskii, E.E.; Schattke, W.; Spiecker, E.; Dieker, C.; Jäger, W. Charge Transfer in Misfit Layered Compounds. *Surface Science* **2003**, 532-5, 705-710.

7. Moëlo, Y.; Meerschaut, A.; Rouxel, J.; Auriel, C. Precise Analytical Characterization of Incommensurate Sandwiched Layered Compounds $[(Pb,Sn)S]_{1+x}[(Nb,Ti)S_2]_m$ ($0.08 \leq x \leq 0.28$, m = 1-3). Role of Cationic Coupling on the Properties and the Structural Modulation. *Chemistry of Materials* **1995**, 7, 1759-1771.

8. Ettema, A.R.H.F.; Haas, C. An X-ray Photoemission Spectroscopy Study of Interlayer Charge Transfer in Some Misfit Layer Compounds. *Journal of Physics: Condensed Matter* **1993**, 5, 3817-3826.

9. Chiritescu, C.; Cahill, D.G.; Nguyen, N.; Johnson, D.; Bodapati, A.; Keblinski, P.; Zschack, P. Ultralow Thermal Conductivity in Disordered, Layered WSe_2 Crystals. *Science* **2007**, 315, 351-353.

10. Chiritescu, C.; Cahill, D.G.; Heideman, C.; Lin, Q.; Mortensen, C.; Nguyen, N.T.; Johnson, D.; Rostek, R.; Böttner, H. Low Thermal Conductivity in Nanoscale Layered Materials Synthesized by the Method of Modulated Elemental Reactants. *Journal of Applied Physics* **2008**, 104, 033533.

11. Heideman, C.; Nyugen, N.; Hanni, J.; Lin, Q.; Duncombe, S.; Johnson, D.C.; Zschack, P. The Synthesis and Characterization of New $[(BiSe)_{1.10}]_m[NbSe_2]_n$, $[(PbSe)_{1.10}]_m[NbSe_2]_n$, $[(CeSe)_{1.14}]_m[NbSe_2]_n$, and $[(PbSe)_{1.12}]_m[TaSe_2]_n$ Misfit Layered Compounds. *Journal of Solid State Chemistry* **2008**, 181, 1701-1706.

12. Lin, Q.; Smeller, M.; Heideman, C.; Zschack, P.; Koyano, M.; Anderson, M.D.; Kykyneshi, R.; Keszler, D.A.; Anderson, I.M.; Johnson, D.C. Rational Synthesis and Characterization of a New Family of Low Thermal Conductivity Misfit Layered Compounds $[(PbSe)_{.99}]_m[WSe_2]_n$. *Chemistry of Materials* **2010**, 22, 1002-1009.

13. Moss, S.; Noh, M.; Jeong, K.H.; Kim, D.H.; Johnson, D.C. Synthesis of Designed W-Wse_2 Heterostructures from Superlattice Reactants. *Chemistry of Materials* **1996**, 8, 1853-1857.

14. Heideman, C.L.; Rostek, R.; Anderson, M.D.; Herzing, A.A.; Anderson, I.M.; Johnson, D.C. Synthesis and Electronic Properties of the Misfit Layered Compound $[(PbSe)_{1.00}]_1[MoSe_2]_1$. *Journal of Electronic Materials* **2010**, 39, 9, 1476-1481.

15. Lin, Q.; Heideman, C.L.; Nguyen, N.; Zschack, P.; Christescu, C.; Cahill, D.G.; Johnson, D.C. Designed Synthesis of Families of Misfit-Layered Compounds. *European Journal of Inorganic Chemistry* **2008**, 15, 382-2385.

16. Phung, T. M.; Jensen, J. M.; Johnson, D. C.; Donovan, J. J.; McBurnett, B. G. Determination of the Composition of Ultra-thin Ni-Si Films on Si: Constrained Modeling of Electron Probe Microanalysis and X-ray Reflectivity Data. *X-Ray Spectrometry* **2008**, 37, 608−614.

17. Bjerkelund, E.; Kjekshus, A. On the Structural Properties of the $Ta_{1+x}Se_2$ Phase. *Acta Chemica Scandinavica* **1967**, 21, 513−526.

18. Mariano, A. N.; Chopra, K. L. Polymorphism in Some IV-VI Compounds Induced by High Pressure and Thin-Film Epitaxial Growth. *Applied Physics Letters* **1967**, 10, 10, 282−284.

19. Okazaki, A. The Crystal Structure of Stannous Selenide SnSe. *Journal of the Physical Society of Japan* **1956**, 11, 470.

20. Chattopadhyay, T.; Pannetier, J.; von Schnering, H. G. Neutron Diffraction Study of the Structural Phase Transition in SnS and SnSe. *Journal of Physics and Chemistry of Solids* **1986**, 47, 9, 879−885.

CHAPTER V

1. Rossnagel, K. On the Origin of Charge-Density Waves in Select Layered Transition-Metal Dichalcogenides. *Journal of Physics: Condensed Matter* **2011**, 23, 213001/1-24.

2. Di Salvo, F.J.; Wilson, J.A.; Bagley, B.G.; Waszczak, J.V. Effects of Doping on Charge-Density Waves in Layer Compounds. *Physical Review B: Condensed Matter* **1975**, 12, 6, 2220-2235.

3. Schneemeyer, L.F.; Stacy, A.; Sienko, M.J. Effect of Nonstoichiometry on the Periodic Lattice Distortion in Vanadium Diselenide. *Inorganic Chemistry* **1980**, 19, 9, 2659-2662.

4. Wiegers, G.A. Misfit Layer Compounds: Structures and Physical Properties. *Progress in Solid State Chemistry*, **1996**, 24, 1-139.

5. Friend, R.H. The Electronic and Magnetic Properties of Transition Metal Dichalcogenide Intercalation Complexes. *Physica B+C* **1983,** 117-118, 593-598.

6. Wilson, J.A.; Di Salvo, F.J.; Mahajan, S. Charge-Density Waves in Metallic, Layered, Transition-Metal Dichalcogenides. *Physical Review Letters* **1974**, 32, 16, 882-885.

7. Makovicky, E.; Hyde, B.G. Incommensurate, Two-Layer Structures With Complex Crystal Chemistry: Minerals and Related Synthetics. *Materials Science Forum* **1992**, 100-101, 1-100.

8. van Smaalen, S. Incommensurate Crystal Structures. *Crystallography Reviews* **1995**, 4, 79-202.

9. Gotoh, Y.; Onoda, M.; Akimoto, J.; Goto, M.; Oosawa, Y. The Layered Composite Crystal Structure of the Ternary Sulfide, $(SnS)_{1.15}TaS_2$ "$SnTaS_3$". *Japan Journal of Applied Physics* **1993**, 32-3, 760-762.

10. Wiegers, G.A.; Zhou, W.Y. The Misfit Layered Compound $(SnSe)_{1.16}NbSe_2$. *Materials Research Bulletin*, **1991**, 26, 879-885.

11. Rouxel, J.; Meerschaut, A.; Wiegers, G.A. Chalcogenide Misfit Layer Compounds. *Journal of Alloys and Compounds*, **1995**, 229, 144-157.

12. Wiegers, G.A.; Meetsma, A.; van Smaalen, S.; Haange, R.J.; Wulff, J.; Zeinstra, T.; de Boer, J.L. Misfit Layer Compounds $(MS)_nTS_2$ (M = Sn, Pb, Bi, Rare Earth Elements; T = Nb, Ta; n = 1.08-1.19), A New Class of Layer Compounds. *Solid State Communications* **1989**, 70, 4, 409-413.

13. Brandt, J.; Kipp, L.; Skibowski, M.; Krasovskii, E.E.; Schattke, W.; Spiecker, E.; Dieker, C.; Jäger, W. Charge Transfer in Misfit Layered Compounds. *Surface Science* **2003**, 532-5, 705-710.

14. Wiegers, G.A.; Meetsma, A.; de Boer, J.L.; van Smaalen, S.; Haange, R.J. The Incommensurate Misfit Layer Structure of $(PbS)_{1.14}NbS_2$, 'PbNbS$_3$' and $(LaS)_{1.14}NbS_2$, 'LaNbS$_3$': an X-ray Diffraction Study. *Acta Crystallographica Section B* **1990**, 46, 324-332.

15. Wiegers, G.A.; Meetsma, A.; de Boer, J.L.; van Smaalen, S.; Haange, R.J. X-ray Crystal Structure Determination of the Triclinic Misfit Layer Compound $(SnS)_{1.20}TiS_2$. *Journal of Physics: Condensed Matter* **1991**, 3, 2603-2612.

16. Meerschaut, A.; Guemas, L.; Auriel, C.; Rouxel, J. Preparation, Structure Determination and Transport Properties of a New Misfit Layer Compound: $(PbS)_{1.14}(NbS_2)_2$. *European Journal of Solid State and Inorganic Chemistry* **1990**, 27, 557-570.

17. de Boer, J.L.; Meetsma, A.; Zeinstra, J.; Haange, R.J.; Wiegers, G.A. Structures of the Misfit Layer Compounds $(LaS)_{1.13}TaS_2$, 'LaTaS$_3$' and $(CeS)_{1.15}TaS_2$, 'CeTaS$_3$'. *Acta Crystallographica Section C* **1991**, 47, 924-930.

18. van Smaalen, S.; Meetsma, A.; Wiegers, G.A.; de Boer, J.L. Determination of the Modulated Structure of the Inorganic Misfit Layer Compound $(PbS)_{1.18}TiS_2$. *Acta Crystallographica Section B* **1991**, 47, 314-325.

19. Nader, A.; Lafond, A.; Briggs, A.; Meerschaut, A. Critical Magnetic Field Measurements of the Misfit Layer Compound $(SnS)_{1.17}(NbS_2)$ Down to 50 mK. *Physica Scripta* **1998**, 57, 310-312.

20. Nader, A.; Briggs, A.; Gotoh, Y. Superconductivity in the Misfit Layer Compounds $(BiSe)_{1.10}(NbSe_2)$ and $(BiS)_{1.11}(NbS_2)$. *Solid State Communications* **1997**, 101, 3, 149-153.

21. Ren, Y.; Baas, J.; Meetsma, A.; de Boer, J.L.; Wiegers, G.A. Vacancies and Electron Localization in the Incommensurate Intergrowth Compound $(La_{0.95}Se)_{1.21}VSe_2$. *Acta Crystallographica Section B* **1996**, 52, 398-405.

22. Wan, C.; Wang, Y.; Wang, N.; Koumoto, K. Low-Thermal-Conductivity $(MS)_{1+x}(TiS_2)_2$ (M = Pb, Bi, Sn) Misfit Layer Compounds for Bulk Thermoelectric Materials. *Materials* **2010**, 3, 2606-2617.

23. Hernán, L.; Morales, J.; Pattanayak, J.; Tirado, J.L. Lithium Intercalation into $PbNb_2S_5$, $PbNbS_3$, $SnNb_2Se_5$, $BiVS_3$, $SnVSe_3$, and $PbNb_2Se_5$ Misfit Layer Chalcogenides. *Journal of Solid State Chemistry* **1992**, 100, 262-271.

24. Moore, D.; Stolt, M.; Atkins, R.; Sitts, L.; Jones, Z.; Disch, S.; Beekman, M.; Johnson, D.C. Structural and Electrical Properties of $(PbSe)_{1.16}TiSe_2$. *Emerging Materials Research* **2012**, 1, 292-298.

25. Chiritescu, C.; Cahill, D.G.; Heideman, C.; Lin, Q.; Mortensen, C.; Nguyen, N.T.; Johnson, D.; Rostek, R.; Böttner, H. Low Thermal Conductivity in Nanoscale Layered Materials Synthesized by the Method of Modulated Elemental Reactants. *Journal of Applied Physics* **2008**, 104, 033533.

26. Heideman, C.; Nyugen, N.; Hanni, J.; Lin, Q.; Duncombe, S.; Johnson, D.C.; Zschack, P. The Synthesis and Characterization of New $[(BiSe)_{1.10}]_m[NbSe_2]_n$, $[(PbSe)_{1.10}]_m[NbSe_2]_n$, $[(CeSe)_{1.14}]_m[NbSe_2]_n$, and $[(PbSe)_{1.12}]_m[TaSe_2]_n$ Misfit Layered Compounds. *Journal of Solid State Chemistry* **2008**, 181, 1701-1706.

27. Lin, Q.; Smeller, M.; Heideman, C.; Zschack, P.; Koyano, M.; Anderson, M.D.; Kykyneshi, R.; Keszler, D.A.; Anderson, I.M.; Johnson, D.C. Rational Synthesis and Characterization of a New Family of Low Thermal Conductivity Misfit Layered Compounds $[(PbSe)_{.99}]_m[WSe_2]_n$. *Chemistry of Materials* **2010**, 22, 1002-1009.

28. Beekman, M.; Heideman, C.; Anderson, M.; Smeller, M.; Atkins, R.; Lin, Q.; Nguyen, N.; Johnson, D.C. Modules, Systems, and Applications in Thermoelectrics, *CRC Press Boca Raton* **2012**, 2.1-19.

29. Heideman, C.L.; Rostek, R.; Anderson, M.D.; Herzing, A.A.; Anderson, I.M.; Johnson, D.C. Synthesis and Electronic Properties of the Misfit Layered Compound $[(PbSe)_{1.00}]_1[MoSe_2]_1$. *Journal of Electronic Materials* **2010**, 39, 9, 1476-1481.

30. Lin, Q.; Heideman, C.L.; Nguyen, N.; Zschack, P.; Chiristescu, C.; Cahill, D.G.; Johnson, D.C. Designed synthesis of families of misfit-layered compounds. *European Journal of Inorganic Chemistry* **2008**, 15, 382-2385.

31. Atkins, R.; Wilson, J.; Zschack, P.; Grosse, C.; Neumann, W.; Johnson, D.C. Synthesis of $[(SnSe)_{1.15}]_m(TaSe_2)_n$ Ferecrystals: Structurally Tunable Metallic Compounds. *Chemistry of Materials* **2012**, 24, 4594-4599.

32. Bayard, M.; Sienko, M.J. Anomalous Electrical and Magnetic Properties of Vanadium Diselenide. *Journal of Solid State Chemistry* **1976**, 19, 325-329.

33. van Bruggen, C.F.; Haas, C. Magnetic Susceptibility and Electrical Properties of VSe_2 Single Crystals. *Solid State Communications* **1976**, 20, 251-254.

34. Thompson, A.H.; Silbernagle, B.G. Correlated Magnetic and Transport Properties in the Charge-Density-Wave Sates of VSe_2. *Physical Review B: Condensed Matter* **1979**, 19, 7, 3420-3426.

35. Hernan, L.; Morales, J.; Pattanayak, J.; Tirado, J.L. Preperation and Characterization of New Misfit Layere Selenides $SnVSe_3$ and $SnNb_2Se_5$. *Chemistry Letters* **1991**, 11, 1981-1984.

36. Fister, L.; Li, X.; McConnell, J.; Novet, T.; Johnson, D.C. Deposition System for the Synthesis of Modulated, Ultrathin-film Composites. *Journal of Vacuum Science and Technology A* **1993**, 11, 3014-3019.

37. Phung, T. M.; Jensen, J. M.; Johnson, D. C.; Donovan, J. J.; McBurnett, B. G. Determination of the Composition of Ultra-thin Ni-Si Films on Si: Constrained Modeling of Electron Probe Microanalysis and X-ray Reflectivity Data. *X-Ray Spectrometry* **2008**, 37, 608−614.

38. Mariano, A. N.; Chopra, K. L. Polymorphism in Some IV-VI Compounds Induced by High Pressure and Thin-Film Epitaxial Growth. *Applied Physics Letters* **1967**, 10, 10, 282−284.

39. Rigoult, J.; Guidi-Moroshini, C.; Tomas, A.; Molinie, P. An Accurate Refinement of 1*T*-VSe_2 at Room Temperature. *Acta Crystallographica Section B* **1982**, 38, 1557-1559.

40. Eaglesham, D.J.; Withers, R.L.; Bird, D.M. Charge-Density-Wave Transitions in 1T-VSe_2. *Journal of Physics C: Solid State Physics* **1986**, 19, 359-367.

41. Giang, N.; Xu, Q.; Hor, Y.S.; Williams, A.J.; Dutton, S.E.; Zandbergen, H.W.; Cava, R.J. Superconductivity at 2.3 K in the Misfit Compound $(PbSe)_{1.16}(TiSe_2)_2$. *Physical Review B: Condensed Matter* **2010**, 82, 024503-(1-5).

CHAPTER VI

1. Makovicky, E.; Hyde, B.G. Incommensurate, Two-Layer Structures with Complex Crystal Chemistry: Minerals and Related Synthetics. *Materials Science Forum* **1992**, 100-101, 1-100.

2. van Smallen, S. Incommensurate Crystal Structures. *Crystallography Reviews* **1995**, 4, 79-202.

3. Thorne, R.E. Charge-Density Wave Conductors. *Physics Today* **1996**, 49, 5, 42-47.

4. Wilson, J.A.; Di Salvo, F.J.; Mahajan, S. Charge-Density Waves and Superlattices in the Metallic Layered Transition Metal Dichalcogenides. *Advances in Physics* **1975**, 24, 2, 117-201.

5. Friend, R.H.; Yoffe, A.D. Electronic Properties of Intercalation Complexes of the Transition Metal Dichalcogenides. *Advances in Physics* **1987**, 36, 1, 1-94.

6. Friend, R.H. The Electronic and Magnetic Properties of Transition Metal Dichalcogenide Intercalation Complexes. *Physica B&C* **1983**, 117-118, 2, 593-598.

7. Di Salvo, F.J.; Wilson, J.A.; Bagley, B.G.; Waszczak, J.V. Effects of Doping on Charge-Density Waves in Layer Compounds. *Physical Review B: Condenses Matter* **1975**, 12, 6, 2220-2235.

8. Schneemeyer, L.F.; Stacy, A.; Sienko, M.J. Effect of Nonstoichiometry on the Periodic Lattice Distortion in Vanadium Diselenide. *Inorganic Chemistry* **1980**, 19, 2659-2662.

9. Wiegers, G.A. Misfit Layer Compounds: Structures and Physical Properties. *Progress in Solid State Chemistry* **1996**, 24, 1-139.

10. Wilson, J.A.; Di Salvo, F.J.; Mahajan, S. Charge-Density Waves in Metallic, Layered, Transition-Metal Dichalcogenides. *Physical Review Letters* **1974**, 32, 16, 882-885.

11. Brandt, J.; Kipp, L.; Skibowski, M.; Krasovskii, E.E.; Schattke, W.; Spiecker, E.; Dieker, C.; Jäger, W. Charge Transfer in Misfit Layered Compounds. *Surface Science* **2003**, 532-5, 705-710.

12. Wiegers, G.A. Charge Transfer Between Layers in Misfit Layer Compounds. *Journal of Alloys and Compounds* **1995**, 219, 152-156.

13. Atkins, R.; Disch, S.; Jones, Z.; Haeusler, I.; Grosse, C.; Fischer, S.F.; Neumann, W.; Zschack, P.; Johnson, D.C. Synthesis, structure, and electrical properties of new tin vanadium selenide. *Journal of Solid State Chemistry* 2013, 202, 128-133.

14. Brown, S.; Grüner, G. Charge and Spin Density Waves. *Scientific American* **1994**, 270, 4, 50-56.

15. Peierls, R.E. Quantum Theory of Solids. *Oxford University Press, London* **1955**.

16. Bayard, M.; Sienko, M.J. Anomalous Electrical and Magnetic Properties of Vanadium Diselenide. *Journal of Solid State Chemistry* **1976**, 19, 325-329.

17. van Bruggen, C.F.; Haas, C. Magnetic Susceptibility and Electrical Properties of VSe_2 Single Crystals. *Solid State Communications* **1976**, 20, 251-254.

18. Thompson, A.H.; Silbernagle, B.G. Correlated Magnetic and Transport Properties in the Charge-Density-Wave Sates of VSe_2. *Physical Review B: Condensed Matter* **1979**, 19, 7, 3420-3426.

19. Atkins, R.; Wilson, J.; Zschack, P.; Grosse, C.; Neumann, W.; Johnson, D.C. Synthesis of $[(SnSe)_{1.15}]_m(TaSe_2)_n$ Ferecrystals: Structurally Tunable Metallic Compounds. *Chemistry of Materials* **2012**, 24, 4594-4599.

20. Ufer, K.; Roth, G.; Kleeberg, R.; Stanjek, H.; Dohrmann, R.; Bergmann, J. Description of X-ray Powder Pattern of Turbostratically Disordered Layer Structures with a Rietveld Compatible Approach. *Zeitschrift für Kristallographie* **2004**, 219, 519−527.

21. Kurita, R. Current Modulation of Charge-Density-Wave Field-Effect Transistors with $NbSe_3$ Channel. *Journal of the Physical Society of Japan* **2000**, 69, 8, 2604-2608.

22. Marković, N.; Dohmen, M.A.H.; van der Zant, H.S.J. Tunable Charge-Density Wave Transport in a Current Transistor. *Physical Review Letters*, **2000**, 84, 3, 534-537.

23. Ogawa, N.; Miyano, K. Charge-Density Wave as an Electro-Optical Switch and Memory. *Applied Physics Letters* **2002**, 80, 17, 3225-3227.

24. Leininger, Ph.; Chernyshov, D.; Bosak, A.; Berger, H.; Inosov, D.S. Competing Charge Density Waves and Temperature-Dependent Nesting in 2*H*-$TaSe_2$. *Physical Review B: Condensed Matter* **2011**, 83, 233101.

25. Craven, R. A.; Meyer, S.F. Specific Heat and Resistivity Near the Charge-Density-Wave Phase Transitions in 2H-$TaSe_2$ and 2H-TaS_2. *Physical Review B: Condensed Matter* **1977**, 16, 10, 4583-4593.

26. Walker, M. B.; Jacobs, A. E. Distinct Commensurate Charge-Density-Wave Phases in the 2H-$Tase_2$ Structure. *Physical Review B: Condensed Matter* **1981**, 21, 11, 6770-6772.

27. Fister, L.; Li, X.; McConnell, J.; Novet, T.; Johnson, D.C. Deposition System for the Synthesis of Modulated, Ultrathin-film Composites. *Journal of Vacuum Science and Technology A* **1993**, 11, 3014-3019.

28. Phung, T. M.; Jensen, J. M.; Johnson, D. C.; Donovan, J. J.; McBurnett, B. G. Determination of the Composition of Ultra-thin Ni-Si Films on Si: Constrained Modeling of Electron Probe Microanalysis and X-ray Reflectivity Data. *X-Ray Spectrometry* **2008**, 37, 608−614.

29. Larson, A.C.; Von Dreel, R.B. General Structure Analysis System (GSAS). *Los Alamos National Laboratory Report* **2000**, LAUR 86-748.

30. Toby, B.H. *EXPGUI*, A Graphical User Interface for GSAS. *Journal of Applied Crystallography* **2001**, 34, 210-213.

31. Van der Pauw, L.J. A Method of Measuring Specific Resistivity and Hall Effect of Discs of Arbitrary Shape. *Philips Research Reports* **1958**, 13, 1, 1-9.

32. Chattopadhyay, T.; Pannetier, J.; von Schnering, H. G. Neutron Diffraction Study of the Structural Phase Transition in SnS and SnSe. *Journal of Physics and Chemistry of Solids* **1986**, 47, 9, 879−885.

33. Ren, Y.; Baas, J.; Meetsma, A.; de Boer, J.L.; Wiegers, G.A. Vacancies and Electron Localization in the Incommensurate Intergrowth Compound $(La_{0.95}Se)_{1.21}VSe_2$. *Acta Crystallographica Section B* **1996**, 52, 398-405.

34. Anderson, M.D.; Heideman, C.L.; Lin, Q.; Smeller, M.; Kokenyesi, R.; Herzing, A.A.; Anderson, I.M.; Keszler, A.; Zschack, P.; Johnson, D.C. Size-Dependent Structural Distortions in One-Dimensional Nanostructures. *Angewandte Chemie International Edition* **2013**, 52, 1982-1985.

35. Tsutsumi, K. X-ray-Diffraction Study of the Periodic Lattice Distortion Associated with a Charge-Density wave in 1T-VSe_2. *Physical Review B: Condensed Matter* **1982**, 26, 10 , 5756- 5759.

36. Eaglesham, D.J.; Withers, R.L.; Bird, D.M. Charge-Density-Wave Transitions in 1T-VSe_2. *Journal of Physics C: Solid State Physics* **1986**, 19, 359-367.

37. Di Salvo, F. J.; Waszczak, J.V. Magnetic Studies of VSe_2. *Physical Review B*: *Condensed Matter* **1981**, 23, 2, 457-461.

38. Kumar, N.; Sharma, V.; Padha, N.; Shah, N. M.; Desai, M. S.; Panchal, C. J; Protsenko I. Y. Influence of the Substrate Temperature on the Structural, Optical, and Electrical Properties of Tin Selenide Thin Films Deposited by Thermal Evaporation Method. *Crystal Research and Technology* **2010**, 45, 1, 53-58.

39. Singh, J. P.; Bedi, R. K. Tin Selenide Films Grown by Hot Wall Epitaxy. *Journal of Applied Physics* **1990**, 68, 2776-2779.

40. Abraham, T.; Juhasz, C.; Silver, J. A; Donaldson, J. D.; Thomas, M. J. K. Tin-119 Mössbauer and Electrical Conductivity Study of the System $Sn_xGe_{1-x}Se$ ($0 \leq x \leq 1$). *Solid State Communications* **1978**, 27, 1185-1187.

41. Agarwal, A.; Vashi, M. N.; Lakshminarayana, D.; Batra, N.M. Electrical Resistivity Anisotropy in Layered p-SnSe Single Crystals. *Journal of materials science: materials in electronics* **2000**, 11, 67-71.

CHAPTER VII

1. Sze, S.M. Semiconductor Devices: Physics and Technology. *John Wiley & Sons* **2002**, 2nd Edition.

2. Wolf, S.; Tauber, R.N. Silicon Processing: for the VLSI Era; Volume 1: Process Technology. *Lattice Press* **2000**, 2nd Edition.

3. Liu, Q.L.; Rao, G.H.; Yang, H.F.; Liang, J.K. Formation of Completely Miscible Solid-Solution $Gd_5(Si_{1-x}Ge_x)_4$ Induced by Ferromagnetic Exchange Interaction. *Journal of Alloys and Compounds* **2001**, 325, 50-53.

4. Di Salvo, F.J.; Waszczak, J.V. The Effect of Fe Substitution on the Charge Density Wave in VSe_2. *Journal de Physique* **1976**, 37, 157-161.

5. Di Salvo, F.J.; Wilson, J.A.; Bagley, B.G.; Waszczak, J.V. Effects of Doping on Charge-Density Waves in Layer Compounds. *Physical Review B: Condensed Matter* **1975**, 12, 6, 2220-2235.

6. Schneemeyer, L.F.; Stacy, A.; Sienko, M.J. Effect of Nonstoichiometry on the Periodic Lattice Distortion in Vanadium Diselenide. *Inorganic Chemistry* **1980**, 19, 9, 2659-2662.

7. Atkins, R.; Wilson, J.; Zschack, P.; Grosse, C.; Neumann, W.; Johnson, D.C. Synthesis of $[(SnSe)_{1.15}]_m(TaSe_2)_n$ Ferecrystals: Structurally Tunable Metallic Compounds. *Chemistry of Materials* **2012**, 24, 4594-4599.

8. Atkins, R.; Disch, S.; Jones, Z.; Haeusler, I.; Grosse, C.; Fischer, S.F.; Neumann, W.; Zschack, P.; Johnson, D.C. Synthesis, Structure, and Electrical Properties of New Tin Vanadium Selenide. *Journal of Solid State Chemistry* **2013**, 202, 128-133.

9. Phung, T. M.; Jensen, J. M.; Johnson, D. C.; Donovan, J. J.; McBurnett, B. G. Determination of the Composition of Ultra-thin Ni-Si Films on Si: Constrained Modeling of Electron Probe Microanalysis and X-ray Reflectivity Data. *X-Ray Spectrometry* **2008**, 37, 608−614.

10. Wiegers, G.A. Misfit Layer Compounds: Structures and Physical Properties. *Progress in Solid State Chemistry*, **1996**, 24, 1-139.

11. Di Salvo, F.J.; Moncton, D.E.; Wilson, J.A.; Mahajan, S. Coexistence of Two Charge-Density Waves of Different Symmetry in 4*H*b-$TaSe_2$. *Physical Review B: Condensed Matter* **1976**, 14, 4, 1543-1546.

12. Bayard, M.; Sienko, M.J. Anomalous Electrical and Magnetic Properties of Vanadium Diselenide. *Journal of Solid State Chemistry* **1976**, 19, 325-329.

CHAPTER VIII

1. Lin, Q.; Smeller, M.; Heideman, C.; Zschack, P.; Koyano, M.; Anderson, M.D.; Kykyneshi, R.; Keszler, D.A.; Anderson, I.M.; Johnson, D.C. Rational Synthesis and Characterization of a New Family of Low Thermal Conductivity Misfit Layered Compounds $[(PbSe)_{.99}]_m[WSe_2]_n$. *Chemistry of Materials* **2010**, 22, 1002-1009.

2. Beekman, M.; Heideman, C.; Anderson, M.; Smeller, M.; Atkins, R.; Lin, Q.; Nguyen, N.; Johnson, D.C. Modules, Systems, and Applications in Thermoelectrics, *CRC Press Boca Raton* **2012**, 2.1-19.

3. Ufer, K.; Roth, G.; Kleeberg, R.; Stanjek, H.; Dohrmann, R.; Bergmann, J. Description of X-ray Powder Pattern of Turbostratically Disordered Layer Structures with a Rietveld Compatible Approach. *Zeitschrift für Kristallographie* **2004**, 219, 519-527.

4. Chiritescu, C.; Cahill, D.G.; Nguyen, N.; Johnson, D.; Bodapati, A.; Keblinski, P.; Zschack, P. Ultralow Thermal Conductivity in Disordered, Layered WSe_2 Crystals. *Science* **2007**, 315, 351-353.

5. Moore, D.; Stolt, M.; Atkins, R.; Sitts, L.; Jones, Z.; Disch, S.; Beekman, M.; Johnson, D.C. Structural and Electrical Properties of $(PbSe)_{1.16}TiSe_2$. *Emerging Materials Research* **2012**, 1, 292-298.

6. Wiegers, G.A. Misfit Layer Compounds: Structures and Physical Properties. *Progress in Solid State Chemistry* **1996**, 24, 1-139.

7. Anderson, M. D. Novel Misfit Layer Systems: Synthesis and Characterization. *Unpublished Doctoral Dissertation*, *University of Oregon*, **2011**.

8. Bayard, M.; Sienko, M.J. Anomalous Electrical and Magnetic Properties of Vanadium Diselenide. *Journal of Solid State Chemistry* **1976**, 19, 325-329.

9. van Bruggen, C.F.; Haas, C. Magnetic Susceptibility and Electrical Properties of VSe_2 Single Crystals. *Solid State Communications* **1976**, 20, 251-254.

10. Schneemeyer, L.F.; Stacy, A.; Sienko, M.J. Effect of Nonstoichiometry on the Periodic Lattice Distortion in Vanadium Diselenide. *Inorganic Chemistry* **1980**, 19, 9, 2659-2662.

11. Riekel, C. J. Structure Refinement of $TiSe_2$ by Neutron Diffraction. *Journal of Solid State Chemistry*, **1976**, 17, 389−392.

12. Bjerkelund, E.; Kjekshus, A. On the Structural Properties of the $Ta_{1+x}Se_2$ Phase. *Acta Chemica Scandinavica* **1967**, 21, 513−526.

13. Fister, L.; Li, X.; McConnell, J.; Novet, T.; Johnson, D.C. Deposition System for the Synthesis of Modulated, Ultrathin-film Composites. *Journal of Vacuum Science and Technology A* **1993**, 11, 3014-3019.

14. Phung, T. M.; Jensen, J. M.; Johnson, D. C.; Donovan, J. J.; McBurnett, B. G. Determination of the Composition of Ultra-thin Ni-Si Films on Si: Constrained Modeling of Electron Probe Microanalysis and X-ray Reflectivity Data. *X-Ray Spectrometry* **2008**, 37, 608−614.

15. Beekman, M.; Cogburn, G.; Heideman, C.; Rouvimov, S.; Zschack, P.; Neumann, W.; Johnson, D.C. New Layered Intergrowths in the Sn-Mo-Se System. *Journal of Electronic Materials* **2012**, 41, 6, 1476-1480.

16. Smeller, M.M.; Heideman, C.L.; Lin, Q.; Beekman, M.; Anderson, M.D.; Zschack, P.; Anderson, I.M; Johnson, D.C. Structure of Turbostratically Disordered Misfit Layer Compounds $[(PbSe)_{0.99}]_1[WSe_2]_1$, $[(PbSe)_{1.00}]_1[MoSe_2]_1$, and $[(SnSe)_{1.03}]_1[MoSe_2]_1$. *Zeitschrift für anorganische and allgemeine Chemie* **2012**, 638, 15, 2632-2639.

17. Heideman, C.L.; Rostek, R.; Anderson, M.D.; Herzing, A.A.; Anderson, I.M.; Johnson, D.C. Synthesis and Electronic Properties of the Misfit Layered Compound $[(PbSe)_{1.00}]_1[MoSe_2]_1$. *Journal of Electronic Materials* **2010**, 39, 9, 1476-1481.

18. Chiritescu, C.; Cahill, D.G.; Heideman, C.; Lin, Q.; Mortensen, C.; Nguyen, N.T.; Johnson, D.; Rostek, R.; Böttner, H. Low Thermal Conductivity in Nanoscale Layered Materials Synthesized by the Method of Modulated Elemental Reactants. *Journal of Applied Physics* **2008**, 104, 033533.

19. Heideman, C.; Nyugen, N.; Hanni, J.; Lin, Q.; Duncombe, S.; Johnson, D.C.; Zschack, P. The Synthesis and Characterization of New $[(BiSe)_{1.10}]_m[NbSe_2]_n$, $[(PbSe)_{1.10}]_m[NbSe_2]_n$, $[(CeSe)_{1.14}]_m[NbSe_2]_n$, and $[(PbSe)_{1.12}]_m[TaSe_2]_n$ Misfit Layered Compounds. *Journal of Solid State Chemistry* **2008**, 181, 1701-1706.

20. Lin, Q.; Heideman, C.L.; Nguyen, N.; Zschack, P.; Chiristescu, C.; Cahill, D.G.; Johnson, D.C. Designed Synthesis of Families of Misfit-Layered Compounds. *European Journal of Inorganic Chemistry* **2008**, 15, 382-2385.

21. Atkins, R.; Wilson, J.; Zschack, P.; Grosse, C.; Neumann, W.; Johnson, D.C. Synthesis of $[(SnSe)_{1.15}]_m(TaSe_2)_n$ Ferecrystals: Structurally Tunable Metallic Compounds. *Chemistry of Materials* **2012**, 24, 4594-4599.

22. Moore, D.B.; Beekman, M.; Disch, S.; Zschack, P.; Häusler, I.; Neumann, W.; Johnson, D.C. Synthesis, Structure and Properties of Turbostratically Disordered $(PbSe)_{1.18}(TiSe_2)_2$. *submitted to Chemistry of Materials* **2013**.